Εθνικο Μετσοβιο
Πολυτεχνειο
Σχολη Εφαρμοσμενων
Μαθηματικων & Φυσικων
Επιστημων

Ε.Κ.Ε.Φ.Ε Δημοκριτος

Ινστιτουτο Πυρηνικης &
Σωματιδιακης
Φυσικης

Έρευνα για Υπερσυμμετρία με το πείραμα CMS σε τελικές καταστάσεις φωτονίων, πιδάκων και εγκάρσιας ελλείπουσας ενέργειας και ανάπτυξη οργανολογίας για τα πειράματα του LHC

ΔΙΔΑΚΤΟΡΙΚΗ ΔΙΑΤΡΙΒΗ

της

Ελένης Β. Ντόμαρη

ΕΠΙΒΛΕΠΩΝ: Θεόδωρος Γέραλης
Κύριος Ερευνητής Ε.Κ.Ε.Φ.Ε Δημόκριτος

National Technical
University Of Athens
School Of Applied
Mathematical &
Physical Sciences

NCSR Demokritos
Institute Of
Nuclear &
Particle
Physics

SUSY Search in Photon(s)+jets+MET final state with the Jet-Gamma Balance method in CMS at the LHC and development of instrumentation for the LHC experiments

DOCTORAL OF PHILOSOPHY
PHYSICS

by

Eleni V. Ntomari

SUPERVISOR: Theodoros Geralis
Senior Researcher N.C.S.R. Demokritos

Εθνικο Μετσοβιο Πολυτεχνειο
ΣΧΟΛΗ ΕΦΑΡΜΟΣΜΕΝΩΝ ΜΑΘΗΜΑΤΙΚΩΝ & ΦΥΣΙΚΩΝ ΕΠΙΣΤΗΜΩΝ
ΤΟΜΕΑΣ ΦΥΣΙΚΗΣ
ΕΡΓΑΣΤΗΡΙΟ ΠΕΙΡΑΜΑΤΙΚΗΣ ΦΥΣΙΚΗΣ ΥΨΗΛΩΝ ΕΝΕΡΓΕΙΩΝ

Έρευνα για Υπερσυμμετρία με το πείραμα CMS σε τελικές καταστάσεις φωτονίων, πιδάκων και εγκάρσιας ελλείπουσας ενέργειας και ανάπτυξη οργανολογίας για τα πειράματα του LHC

ΔΙΔΑΚΤΟΡΙΚΗ ΔΙΑΤΡΙΒΗ

της

Ελένης Β. Ντόμαρη

ΕΠΙΒΛΕΠΩΝ: Θεόδωρος Γέραλης, Κύριος Ερευνητής Ε.Κ.Ε.Φ.Ε Δημόκριτος

ΕΓΚΡΙΘΗΚΕ ΑΠΟ ΤΗΝ ΤΡΙΜΕΛΗ ΕΞΕΤΑΣΤΙΚΗ ΕΠΙΤΡΟΠΗ:

....	....	....
Θεόδωρος Αλεξόπουλος	Θεόδωρος Γέραλης	Γεώργιος Τσιπολίτης
Καθηγητής	Κύριος Ερευνητής	Αναπληρωτής Καθηγητής
ΕΜΠ	Ε.Κ.Ε.Φ.Ε. Δημόκριτος	ΕΜΠ

ΑΘΗΝΑ, ΔΕΚΕΜΒΡΙΟΣ 2012.

NATIONAL TECHNICAL UNIVERSITY OF ATHENS
SCHOOL OF APPLIED MATHEMATICAL & PHYSICAL SCIENCIES
PHYSICS DEPARTMENT

SUSY Search in Photon(s)+jets+MET final state with the Jet-Gamma Balance method in CMS at the LHC and development of instrumentation for the LHC experiments

DOCTORAL OF PHILOSOPHY
PHYSICS

by

Eleni V. Ntomari

SUPERVISOR: Theodoros Geralis, Senior Researcher N.C.S.R. Demokritos

ACCEPTED BY THE COMMITTEE:

....	....	....
Theodoros Alexopoulos	Theodoros Geralis	Yorgos Tsipolitis
Professor	Senior Researcher	Associate Professor
NTUA	NCSR Demokritos	NTUA

ATHENS, DECEMBER 2012.

....

Ελένη Β. Ντόμαρη
Διπλωματούχος Φυσικός Εφαρμογών Ε.Μ.Π

Aknowledgements

Preparing a PHD thesis is the conclusion of many years of experience; both exciting and difficult.. So many things I have seen, so much information gathered, so many wonderful people I would like to mention...

I have to start this part expressing my gratefulness and deepest gratitude to my supervisor Senior Researcher Theodoros Geralis. I would not have gone all the way without his guidance and generous support during these years. He is an example of a hard worker, always available for questions providing help when needed and driving me to advance and progress. I also want to thank him for the trust he has shown to my person and for his big efforts to supply me with the best conditions to work (including trying to find the funds for giving me the opportunity to spend as much time as possible of my PHD at CERN or sending me to conferences). And of course for his assistance in reading and correcting this thesis.

I am indeed indebted to Dr. Konstantinos Theofilatos for his precious help, support and guidance all this period!! His deep enthusiasm about the field was an inspiring factor from the first time. He was patiently teaching me every single technical detail of the CMS software and providing me great help and advice each time I needed! I really thank you so much!

I would also like to express my deep gratitude to my professors at the National Technical University of Athens and especially to Theodoros Alexopoulos and Yorgos Tsipolitis for introducing me to this field, for trusting me and supporting me since my undergraduate studies and for having drawn my path to this work. I must also acknowledge Prof. Evagelos Gazis, for giving me the chance to be a summer student at CERN; that was the beginning of my journey in particle physics!!

I must also thank George Fanourakis for his guidance on micromegas detectors and for the pleasure to work with him during the test beams at CERN and Demokritos as well. Many thanks belongs to Assistant Professor Michalis Kokoris for all the conversations on nuclear physics throughout my studies on micromegas detector and for all the helpful and inspiring discussions during my undergraduate studies. A thank you for the help on nuclear physics also belongs to Dr. Tasos Lagoyannis. I could not forget the remarkable guidance of Georgios Daskalakis on the ECAL studies, but also for all the fruitful discussions on the field in general.

Of course, my very special thanks go to Dr. Stilianos Kessisoglou for being always very helpful and an endless source of knowledge! His passion for work and learning was something more than just an inspiring factor. Thanks belongs also to Victoria Giakoumopoulou for always being very polite, encouraging and helpful each time I needed something and for all her precious comments on this thesis.

My thanks should also go to all the people in the collaboration that I have met, for everything I have learned from them and especially to Dongwook Jang for his help with the group's tools on the exclusion limits calculation and Ulla Gebbert for being always willing to answer my questions.

I owe many thanks to all of the friends I made at CERN and helped me feel like home..

Thanks to Vaso and Vasilis for their hospitality when I couldn't find room in the hostel and also to Panos and Nikos for going out with me, when I was tired of just seeing the CERN campus.

Many thanks goes to Gitsa for the delicious cheesecakes! Especially those for my birthdays..

Thanks to Kostas for the delicious meals (especially those without cream fresh) and of course for the perfect cooperation during the micromegas testbeams. We were a great team!!! Just remember how fast we could mount and dismount everything!!! :-)

I shouldn't forget Manos for being my PC-doctor, for all the lifts to the supermarket (and in general) and for being a friend especially at the times at CERN when I was feeling down. I won't forget it!

Special thanks goes to Christos, for his precious help concerning technical issues such as CMSSW and ROOT at the beginning of my analysis, but mostly for all the times he made my eyes smile more than my lips.

I can't say anything else but "thank you" to my officemates Eleni, Lilia and Iasonas. Eleni for all her support and all the good advice, Lilia for all the beautiful breaks, chats and for the room-service (water, food...) and of course Iasonas for being patient to hearing me in our office at Demokritos and especially at CERN! Thank you guys so much!!!!

Georgia Kareli for being always helpful and with a smile in her face.

Chara and Eleana for being the sisters I never had.. For our unforgettable childhood, the sofa-movie-gossip nights all these years and of course Christos who tried to add some fitness days to our program (it doesn't matter if in the end he was the only one jogging...) and of course for the theater nights (remember Epidavros) and excursions to the beach!!!!!! Nikos for standing by me all these years and for all the beautiful moments we shared. Aristi for reminding me the child that will never grow up (something like PeterPan) and Sofia for understanding my inner thoughts.. Lastly but not least I want to thank Natasoula and Magdalene for being by my side since our childhood, giving me courage to follow my dreams and for their opposite way of thinking helping me to see different prospects of each situation.. But most of all for helping me overcome all the difficulties I had to face...and for listening.. and listening.. and listening me talking for hours.. Thank you so much!

My utmost respect, love and gratitude belongs to my parents Vlasis and Sofia for all of their support and patience during all these years! It is them I owe who I am... Also many thanks to my brothers; my twin Dimitris and our little Panagiotis (who is not that little any more), for being in my life.

Ευχαριστώ!!

To my family

Περίληψη

Το Καθιερωμένο Πρότυπο (ΚΠ) -Standard Model- της σωματιδιακής φυσικής έχει προκύψει μέσα από διαχρονικές επιτυχίες της πειραματικής και θεωρητικής φυσικής στην περιγραφή της πολυπλοκότητας που μας περιβάλλει, χρησιμοποιώντας θεμελιώδη σωματίδια και αλληλεπιδράσεις. Αποτελεί τη συμπαγή διατύπωση μιας σειράς θεωριών οι οποίες ερμηνεύουν και περιγράφουν τη συμπεριφορά της ύλης σε επίπεδο στοιχειωδών σωματιδίων. Οι προβλέψεις του είναι μεγάλης σημασίας καθώς πολλά σωματίδια ανακαλύφθηκαν μετά την πρόβλεψή τους. Εξακολουθεί να παραμένει το πιο ολοκληρωμένο μοντέλο που συμβάλλει στην κατανόηση του σύμπαντός μας. Περιγράφει τις τρεις από τις τέσσερις γνωστές θεμελιώδεις αλληλεπιδράσεις μεταξύ των στοιχειωδών σωματιδίων, την ηλεκτρομαγνητική, την ασθενή και την ισχυρή αλληλεπίδραση, στα πλαίσια μιας θεωρίας κβαντικών πεδίων της οποίας η θεμελιώδης ποσότητα (Lagrangian) είναι αναλλοίωτη κάτω από μια κατηγορία συνεχών τοπικών μετασχηματισμών (Gauge Theory). Δεν συμβαίνει όμως το ίδιο και με τη βαρυτική αλληλεπίδραση.

Παράλληλα η συμμετρία βαθμίδας στην οποία στηρίζεται το ΚΠ, έχει ένα αναπάντητο ερώτημα: "Γιατί τα στοιχειώδη σωματίδια φέρουν μάζα;". Το ΚΠ στηρίζεται σε μια θεωρία βαθμίδας (gauge group theory) η οποία απαγορεύει την ύπαρξη μάζας σε όλα τα σωματίδια. Η εισαγωγή του μηχανισμού Higgs στο ΚΠ, δίνει μάζες στα διανυσματικά μποζόνια (Vector Bosons: W, Z) καθώς επίσης και σε ολόκληρο το φάσμα των στοιχειωδών σωματιδίων, ενώ παράλληλα αφήνει το φωτόνιο χωρίς μάζα. Παρά το γεγονός ότι πρόκειται για μια πολύ κομψή θεωρία, το σωματίδιο αυτό δεν έχει ακόμα επιβεβαιωθεί (αν και η τελευταία ανακοίνωση της 4ης Ιουλίου 2012 στο CERN μιλά για ένα καινούριο μποζόνιο με ιδιότητες παρόμοιες του σωματιδίου Higgs) και παραμένει ως το πιο συναρπαστικό κίνητρο για τα πείραματα του LHC. Ακόμη και αν τελικά επιβεβαιωθεί η ανακάλυψη του σωματιδίου Higgs, το Καθιερωμένο Πρότυπο πιστεύεται ότι αποτελεί απλά ένα μέρος της ευρύτερης εικόνας. Απέχει από το να χαρακτηριστεί ως μια πλήρης θεωρία των θεμελιωδών αλληλεπιδράσεων, διότι δεν περιλαμβάνει τη φυσική της σκοτεινής ύλης και ενέργειας, ούτε την πλήρη θεωρία της βαρύτητας, όπως περιγράφεται από τη γενική σχετικότητα. Η θεωρία δεν περιέχει οποιοδήποτε βιώσιμο σωματίδιο σκοτεινής ύλης, που να διαθέτει όλες τις απαιτούμενες ιδιότητες, όπως συνάγονται από την παρατηρη -σιακή κοσμολογία. Επίσης, δεν αντιπροσωπεύει σωστά τις ταλαντώσεις των

νετρίνων (και των μη μηδενικών μαζών τους). Παρά το γεγονός ότι το Καθιερωμένο Πρότυπο πιστεύεται ότι είναι θεωρητικά αυτο-συνεπές, έχει αρκετές αφύσικες ιδιότητες που δημιουργούν γρίφους, όπως το πρόβλημα της ιεραρχίας (hierarchy problem).

Εντούτοις το ΚΠ είναι πολύ σημαντικό εξίσου για τη θεωρητική όσο και για την πειραματική σωματιδιακή φυσική. Οι θεωρητικοί το χρησιμοποιούν ως βάση για το σχεδιασμό πιο εξωτικών μοντέλων που εμπεριέχουν υποθετικά σωματίδια, επιπλέον διαστάσεις και πραγματεύονται συμμετρίες (όπως για παράδειγμα την Υπερσυμμετρία) σε μια προσπάθεια να ερμηνεύσουν πειραματικές παρατηρήσεις που δεν ερμηνεύονται από το Καθιερωμένο Πρότυπο, όπως για παράδειγμα η ύπαρξη της σκοτεινής ύλης και ενέργειας και οι ταλαντώσεις των νετρίνων. Από την αντίπερα όχθη, οι πειραματικοί φυσικοί, έχουν ενσωματώσει το ΚΠ σε προσομοιωτές ώστε να ερευνήσουν τη φυσική πέρα από το Καθιερωμένο Πρότυπο. Παράλληλα το ΚΠ ελέγχεται εξονυχιστικά από τους πειραματικούς σε διάφορες ενέργειες και πειράματα.

Ο Μεγάλος Επιταχυντής Αδρονίων (Large Hadron Collider, LHC), χτίστηκε στο Ευρωπαϊκό Συμβούλιο Πυρηνικής Έρευνας (CERN) στη Γενεύη, και θα λειτουργήσει σε ενέργεια κέντρου μάζας έως 14 TeV, ώστε να δώσει τη δυνατότητα διερεύνησης και επιβεβαίωσης θεμελιωδών θεωριών των στοιχειωδών σωματιδίων. Τα αποτελέσματα από προηγούμενα πειράματα καθώς επίσης και οι νέες θεωρητικές προβλέψεις συνηγορούν στη νέα γενιά πειραμάτων. Η μελέτη ενεργειακών κλιμάκων μιας πιθανής νέας φυσικής μπορεί να πραγματοποιηθεί με τη δημιουργία επιταχυντών υψηλής ενέργειας και φωτεινότητας για τη συλλογή όσο το δυνατόν περισσότερων ενδιαφέροντων γεγονότων ως προς τη μελέτη της νέας φυσικής. Ο LHC αποτελεί το εργαλείο για την αναζήτηση του σωματιδίου Higgs καθώς και για τη μελέτη της δομής της ύλης στη μικρότερη κλίμακα που έχει επιτευχθεί μέχρι σήμερα. Ο LHC είναι σχεδιασμένος έτσι ώστε να επιταχύνει δύο δέσμες πρωτονίων σε ενέργειες 7 TeV η κάθε μία, προσφέροντας ενέργεια 14 TeV στο κέντρο της μάζας. Η μέγιστη αναμενόμενη στιγμιαία φωτεινότητα (instantaneous luminosity) των δεσμών πρωτονίων είναι 10^{34} cm^{-2}s^{-1}, ποσότητα που αντιστοιχεί κατά μέσο όρο σε 10^{12} αλληλεπιδράσεις το δευτερόλεπτο, ενώ στην περίπτωση δεσμών ιόντων μολύβδου μπορεί να φτάσει τα 10^{27} cm^{-2}s^{-1}. Οι παραπάνω αριθμοί μαρτυρούν τον υψηλό ρυθμό συγκρούσεων στον LHC, που συνοδεύονται από πολλά δευτερογενή σωματίδια τα οποία παράγονται μετά από κάθε σύγκρουση. Αυτά τα γεγονότα απαιτούν εξελιγμένους ανιχνευτές και αλγορίθμους ανακατασκευής γεγονότων, καθώς επίσης και γρήγορη επεξεργασία και συλλογή δεδομένων. Ο Μεγάλος Επιταχυντής Αδρονίων σχεδιάστηκε έτσι ώστε να εκπληρώσει τις απαιτήσεις αυτές.

Ένας από τους δύο ανιχνευτές γενικού ενδιαφέροντος στον LHC είναι το Συμπαγές Σωληνοειδές Μιονίων (Compact Muon Solenoid, CMS) και η διατριβή αυτή βασίζεται στην ανάλυση των δεδομένων που συλλέγονται από τον ανιχνευτή αυτό.

Η πιο δημοφιλής επέκταση του ΚΠ είναι η Υπερσυμμετρία (Supersymmetry, SUSY). Διπλασιάζει τον αριθμό των σωματιδίων, προβλέποντας υπερσυμμετρικά σωματίδια για κάθε ένα από τα σωματίδια του ΚΠ, και μπορεί να λύσει πολλά από τα προβλήματα του ΚΠ με ένα κομψό τρόπο. Η συγκεκριμένη διατριβή παρουσιάζει έρευνα για Υπερσυμμετρία, η οποία βασίζεται στη θεωρία General Gauge-Mediation (GGM), σε τελικές καταστάσεις με φωτόνια, πίδακες αδρονίων και ελλείπουσα εγκάρσια ενέργεια ($\mathrm{E}_{\mathrm{T}}^{\mathrm{miss}}$) που παράγονται σε γεγονότα που προέρχονται από συγκρούσεις πρωτονίων (pp) με ενέργεια κέντρου μάζας ίση με 7 TeV. Αυτή είναι μια πολύ προσιτή πειραματική υπογραφή (ή κανάλι όπως αλλιώς ονομάζεται), διότι τα φωτόνια μπορούν να προσδιοριστούν με υψηλή απόδοση και καθαρότητα στα πειράματα επιταχυντών. Ένας πρόσθετος παράγοντας είναι ότι σε περίπτωση μεγάλης ελλείπουσας εγκάρσιας ενέργειας, όπως αναμένεται από τις διάφορες Υπερσυμμετρικές θεωρίες, τα υπόβαθρα που προέρχονται από το Καθιερωμένο Πρότυπο μειώνονται αισθητά, σε σχέση με πιθανά σήματα από Υπερσυμμετρικά μοντέλα.

Στο Κεφάλαιο 1, περιγράφεται το Καθιερωμένο Πρότυπο και η θεωρία της Υπερσυμμετρίας και στη συνέχεια ακολουθεί σύντομη περιγραφή του LHC και του πειράματος CMS (Κεφάλαιο 2) δίνοντας έμφαση στην περιγραφή του προσομοιωτή του συστήματος σκανδαλισμού (Global Trigger Processor emulator), σύστημα το οποίο αναπτύχθηκε και ελέχθηκε στο Ινστιτούτο Πυρηνικής και Σωματιδιακής Φυσικής του ΕΚΕΦΕ "Δημόκριτος". Στο Κεφάλαιο 3 παρατίθεται περίληψη της ιστορίας των ανιχνευτών αερίων και της αρχής λειτουργίας τους, με ιδιαίτερη έμφαση στον ανιχνευτή micromegas και τη δυνατότητά του να χρησιμοποιηθεί στην αναβάθμιση του LHC. Ακολούθως (Κεφάλαιο 4) παρουσιάζονται λεπτομέρειες σχετικά με την προσομοίωση γεγονότων τα οποία και χρησιμοποιούνται για το έλεγχο της μεθόδου που περιγράφεται στη διατριβή αυτή και η οποία αφορά την ανάδειξη της παρουσίας σήματος Υπερσυμμετρικών Σωματιδίων ως προς το υπόβαθρο. Στο Κεφάλαιο 5 γίνεται η περιγραφή των αντικειμένων (object definition) που χρησιμοποιούνται στη συγκεκριμένη ανάλυση καθώς επίσης και η διαδικασία επιλογής των υποψήφιων γεγονότων. Αμέσως μετά περιγράφεται η μεθοδολογία προσδιορισμού του υποβάθρου μαζί με ελέγχους για την επιβεβαίωση της εγκυρότητας της μεθόδου (Monte Carlo closure tests) και φυσικά ακολουθεί η παρουσίαση των αποτελεσμάτων της μεθόδου χρησιμοποιώντας δεδομένα που συλλέχθηκαν από τον ανιχνευτή CMS (Κεφάλαιο 7). Η διατριβή ολοκληρώνεται συνοψίζοντας τα αποτελέσματα. Επιπροσθέτως, στο τέλος επισυνάπτονται παραρτήματα σχετικά με συγκριτικές μελέτες διαφόρων ποσοτήτων όπως η ορμή των φωτονίων, για δεδομένα που προέρχονται από προσομοίωση (MC) και από αληθινά γεγονότα (Παράρτημα A). Ακολουθεί σχηματική αναπαράσταση (event display) των πιο ενδιαφερόντων γεγονότων στο Παράρτημα B, ενώ στο επόμενο γίνεται αναφορά στα φίλτρα που χρησιμοποιηθήκαν προκειμένου να απομακρυνθούν τα προβληματικά γεγονότα από τη λίστα των γεγονότων που μελετήθηκαν. Στο τελευταίο παράρτημα παρουσιάζεται μία μελέτη που πραγματοποιήθηκε στα πλαίσια αυτής της διατριβής και που αφορά την εύρεση αλγορίθμου για την διόρθωση της ενέργειας των προβληματικών κρυστάλλων του ηλεκτρομαγνητικού θερμιδομέτρου του ανιχνευτή CMS.

Θεωρητική Προσέγγιση

Όπως προαναφέρεται, ένας από τους κυριότερους ερευνητικούς στόχους της φυσικής στοιχειωδών σωματιδίων είναι η ενοποίηση των θεμελιωδών αλληλεπιδράσεων της φύσης (ηλεκτρομαγνητική, ισχυρή, ασθενής και βαρύτητα). Η προσπάθεια αυτή οδήγησε στη δημιουργία μιας θεωρίας που περιγράφει όλες τις θεμελιώδεις δυνάμεις εκτός από τη βαρύτητα. Αυτή η θεωρία περιγράφει τις τρεις αλληλεπιδράσεις με τη βοήθεια της τοπικά αναλλοίωτης θεωρίας βαθμίδας η οποία περιλαμβάνει την κβαντική ηλεκτροδυναμική, την ηλεκτρασθενή αλληλεπίδραση και τη κβαντική χρωμοδυναμική και είναι γνωστή ως το Καθιερωμένο Πρότυπο. Οι θεωρίες βαθμίδας χαρακτηρίζονται από την αναλλοιώτητα των αποτελεσμάτων τους κάτω από συγκεκριμένους μετασχηματισμούς οι οποίοι είναι γνωστοί ως *μετασχηματισμοί βαθμίδας*. Η ηλεκτρασθενής θεωρία και η κβαντική χρωμοδυναμική ενοποιούνται σε μια θεωρία αναλλοίωτη κάτω από την ομάδα μετασχηματισμών βαθμίδας $SU(3)_C \bigotimes SU(2)_L \bigotimes U(1)_Y$.

Σύμφωνα με το ΚΠ, φορείς των αλληλεπιδράσεων που περιγράφει, είναι τα μποζόνια βαθμίδας με σπιν 1. Τα μποζόνια προκύπτουν από την απαίτηση να είναι η συμμετρία βαθμίδας που εφαρμόζεται στα φερμιονικά πεδία τοπικά αναλλοίωτη. Τα φερμιόνια διακρίνονται στα λεπτόνια και τα κουάρκ (quarks). Στους παρακάτω πίνακες φαίνονται οι γενιές των φερμιονίων.

Πίνακας 1: Οι γενιές των Κουάρκ

	Quarks	
1η γενιά	up (u)	down (d)
2η γενιά	charm (c)	strange (s)
3η γενιά	top (t)	bottom (b)

Πίνακας 2: Οι γενιές των Λεπτονίων

	Leptons	
1η γενιά	electron (e)	electron neutrino (ν_e)
2η γενιά	muon (μ)	muon neutrino (ν_μ)
3η γενιά	tau (τ)	tau neutrino (ν_τ)

Η ομάδα συμμετρίας $SU(2)_L \bigotimes U(1)_Y$, περιγράφει την ηλεκτρασθενή αλληλεπίδραση και σπάει αυθόρμητα από την ύπαρξη ενός υποτιθέμενου πεδίου

Higgs με μη μηδενική τιμή κενού. Αυτό έχει σαν αποτέλεσμα τη δημιουργία διανυσματικών μποζονίων που διαθέτουν μάζα, τα W και Z, τα οποία είναι διαδότες της ασθενούς αλληλεπίδρασης, ενώ το φωτόνιο αποτελεί τον διαδότη της ηλεκτρομαγνητικής αλληλεπίδρασης και παραμένει χωρίς μάζα.

Η ομάδα $SU(3)_C$ περιγράφει την ισχυρή αλληλεπίδραση (κβαντική χρωμοδυναμική, QCD) και έχει ως διαδότες οχτώ διανυσματικά γκλουόνια.

Στον πίνακα που ακολουθεί φαίνονται οι θεμελιώδεις αλληλεπιδράσεις του καθιερωμένου προτύπου καθώς επίσης και οι φορείς (διαδότες) των αλληλεπιδράσεων αυτών [4].

Πίνακας 3: Περιγραφή των θεμελιωδών αλληλεπιδράσεων

Αλληλεπίδραση	**Ένταση**	**Θεωρία**	**Διαδότης**	**Φορτίο**
Ισχυρή	1	Χρωμοδυναμική	8 διαν. γκλουόνια	0
Ηλεκτρομαγνητική	10^{-2}	Ηλεκτροδυναμική	γ	0
Ασθενής	10^{-7}	Flavordynamics	W^+	+1
			W^-	-1
			Z	0
Βαρυτική	10^{-42}	Γενική Σχετικότητα	γκραβιτόνιο	0

Το καθιερωμένο πρότυπο που περιγράψαμε συνοπτικά, έχει τρία βασικά ανοιχτά ερωτήματα:

- Το πρόβλημα της ιεραρχίας σύμφωνα με το οποίο δεν μπορεί να ερμηνευτεί η μεγάλη διαφορά ανάμεσα πχ στις μάζες των σωματιδίων W και Z και στην κλίμακα Planck.
- Το πρόβλημα της ενοποίησης των δυνάμεων συμπεριλαμβανομένης και της βαρυτικής αλληλεπίδρασης.
- Το πρόβλημα των γεύσεων ή με άλλα λόγια η έλλειψη εξήγησης σχετικά με τις γενιές και τον αριθμό των λεπτονίων και των quark που παρατηρούμε.

Σε μια προσπάθεια απάντησης στα ερωτήματα αυτά, αναπτύχθηκε μια νέα συμμετρία γνωστή και ως Υπερσυμμετρία (Supersymmetry, SUSY). Η θεωρία αυτή προβλέπει για κάθε γνωστό (σύμφωνα με το Καθιερωμένο Πρότυπο) σωματίδιο, ένα αντίστοιχο Υπερσυμμετρικό το οποίο θα έχει ίδιους όλους τους κβαντικούς αριθμούς εκτός από το σπιν που θα πρέπει να είναι διαφορετικό κατά 1/2. Αυτό γίνεται με τη χρήση ενός γεννήτορα (Q) ο οποίος μετατρέπει ένα μποζόνιο σε φερμιόνιο και το αντίθετο. Με αυτόν τον τρόπο επιτυγχάνεται μια σχέση συμμετρίας μεταξύ ύλης και δυνάμεων. Τα Υπερσυμμετρικά σωματίδια της ύλης έχουν ένα "s" μπροστά από το όνομά τους (για παράδειγμα το υπερσυμμετρικό σωματίδιο του ηλεκτρονίου-electron είναι το "selectron"), ενώ τα Υπερσυμμετρικά σωματίδια των δυνάμεων λαμβάνουν ως κατάληξη "ino" (πχ το γκλουόνιο-gluon έχει σαν Υπερσυμμετρικό σωματίδιο το "gluino").

Εδώ τίθεται το ερώτημα "Γιατί δεν έχει παρατηρηθεί κανένα Υπερσυμμετρικό σωματίδιο μέχρι σήμερα;". Έτσι εύλογα προκύπτει η απάντηση ότι η Υπερσυμμετρία, αν υπάρχει, θα πρέπει να είναι "σπασμένη" (broken) επιτρέποντας έτσι σε κάθε Υπερσυμμετρικό σωματίδιο να έχει πολύ μεγαλύτερη μάζα από το αντίστοιχο που προβλέπει το ΚΠ.

Πίνακας 4: Σωματίδια του ΚΠ μαζί με τα αντίστοιχα Υπερσυμμετρικά τους

	Καθιερωμένο Πρότυπο				**Υπερσυμμετρία**		
	Σπιν	**Όνομα**	**Σύμβολα**		**Όνομα**	**Σύμβολα**	**Σπιν**
Φερμιόνια	1/2	leptons	e, ν_e μ, ν_μ τ, ν_τ	**Μποζόνια**	sleptons	$\tilde{e}$, $\tilde{\nu}_e$ $\tilde{\mu}$, $\tilde{\nu}_\mu$ $\tilde{\tau}$, $\tilde{\nu}_\tau$	0
	1/2	quarks	u,d c,s t,b		squarks	$\tilde{u}$, $\tilde{d}$ $\tilde{c}$, $\tilde{s}$ $\tilde{t}$, $\tilde{b}$	0
Μποζόνια	1	gluons	g	**Φερμιόνια**	gluinos	$\tilde{g}$	1/2
	1	EW bosons	γ,Z^0,W$^\pm$		winos	$\tilde{W}^\pm$, $\tilde{W}^0$	1/2
					bino	$\tilde{B}^0$	1/2
	0	higgs	H$_u$, H$_d$		higgsinos	$\tilde{H}_u$, $\tilde{H}_d$	1/2

Η ανάλυση που περιγράφεται στη διατριβή αυτή βασίζεται στην έρευνα για Υπερσυμμετρία σε τελικές καταστάσεις με φωτόνια, πίδακες αδρονίων και ελλείπουσα εγκάρσια ενέργεια ($\mathrm{E}_{\mathrm{T}}^{\mathrm{miss}}$). Οι διασπάσεις τις οποίες πραγματοποιούν τα Υπερσυμμετρικά σωματίδια, όπως και οι ρυθμοί παραγωγής τους, εξαρτώνται από τις μάζες τους. Οι μάζες εξαρτώνται από τον τρόπο που η Υπερσυμμετρία παραβιάζεται, και ο μηχανισμός αυτός δεν είναι γνωστός. Ως εκ τούτου δεν είναι δυνατός ο ακριβής υπολογισμός των ακολουθιών διασπάσεων που πραγματοποιούν τα sparticles. Επομένως είναι αναγκαία η θεώρηση όλων των δυνατών περιπτώσεων. Στην διατριβή αυτή θα μελετήσουμε την Υπερσυμμετρία μέσα από το πρίσμα της General Gauge-Mediation (GGM). Σύμφωνα με τη θεωρία της GGM, το γκραβιτίνο (gravitino) είναι το Υπερσυμμετρικό σωματίδιο με τη χαμηλότερη μάζα (lowest mass SUSY particle, LSP) ενώ το αμέσως επόμενο (next-to-lowest mass SUSY particle, NLSP) είναι το neutralino. Στη συγκεκριμένη μελέτη θα μας απασχολήσουν τα bino και wino-like neutralinos.

Στην περίπτωση ενός bino-like neutralino, η διάσπαση με τη μεγαλύτερη πιθανότητα (branching ratio) είναι σε ένα gravitino και ένα φωτόνιο ($\sim \cos^2\theta_{\mathrm{w}}$)

και ακολουθεί η διάσπαση σε ένα gravitino και ένα μποζόνιο Z ($\sim \sin^2\theta_\mathrm{w}$). Από την άλλη πλευρά, ο διαχωρισμός μεταξύ φορτισμένου και ουδέτερου wino σε γενικές γραμμές είναι μικρός και ως εκ τούτου τα ουδέτερα και τα φορτισμένα winos γίνονται co-NLSPs. Το φορτισμένου wino διασπάται απευθείας σε $\mathrm{W}^+/\mathrm{W}^-$, ενώ το ουδέτερο wino (wino-like neutralino) διασπάται πρωτίστως σε ένα gravitino και ένα μποζόνιο Z ($\sim \cos^2\theta_\mathrm{w}$) και δευτερευόντως σε ένα gravitino και ένα φωτόνιο ($\sim \sin^2\theta_\mathrm{w}$).

Η διατριβή αυτή πραγματεύεται μόνο περιπτώσεις στις οποίες τουλάχιστον ένα από τα neutralinos διασπάται κυρίως σε ένα gravitino και ένα φωτόνιο. Το gravitino διαφεύγει από το σύστημα ανίχνευσης και ως εκ τούτου οδηγεί στην ύπαρξη ελλείπουσας εγκάρσιας ενέργειας. Υποθέτωντας διατήρηση της R-parity, τα Υπερσυμμετρικά σωματίδια παράγονται ανά ζεύγη. Αυτά τα σωματίδια κατά κύριο λόγο αλληλεπιδρούν ισχυρά, με αλυσίδες διάσπασης που συμπεριλαμβάνουν ένα ή περισσότερα quarks/gluons. Κατά συνέπεια, γεγονότα με αμιγώς bino-like neutralino αναμένεται να έχουν σαν τελική κατάσταση δύο φωτόνια, δύο gravitons και σωματίδια που προβλέπει το ΚΠ. Τα σωματίδια του ΚΠ μπορεί να είναι είτε φωτόνια, είτε μποζόνια Z, είτε μποζόνια Higgs αν το επιτρέπει κινηματικά η διαφορά μάζας μεταξύ NLSP και LSP. Μια δεύτερη "υπογραφή" αποτελείται από ένα μόνο φωτόνιο όταν το ένα από τα NLSP διασπάται σε ένα μποζόνιο Z αντί για ένα φωτόνιο. Τέλος στην περίπτωση wino-like neutralino, η τελική κατάσταση με δύο φωτόνια είναι αρκετά σπάνια, αλλά η περίπτωση ενός μόνο φωτονίου μπορεί να είναι αρκετά σημαντική.

Το πείραμα CMS

Η διατριβή αυτή στηρίζεται στην ανάλυση δεδομένων που συγκεντρώθηκαν από τον ανιχνευτή του πειράματος Compact Muon Solenoid (CMS). Το CMS αποτελεί, όπως προαναφέρεται, ένα από τα τέσσερα πειράματα του LHC. Η εγκατάσταση του LHC έγινε στην ήδη υπάρχουσα υπόγεια κυκλική σήραγγα του επιταχυντή ηλεκτρονίων-ποζιτρονίων LEP. Η σήραγγα αυτή έχει περιφέρεια περίπου 27 km και διασχίζει τα σύνορα Γαλλίας-Ελβετίας σε βάθος μεταξύ 45 και 175 m.

Η εισαγωγή των πρωτονίων στον δακτύλιο επιτάχυνσης του LHC γίνεται με χρήση μιας σειράς άλλων επιταχυντών που λειτουργούν στις εγκαταστάσεις του CERN. Τα πρωτόνια που δημιουργούνται μέσω ιονισμού υδρογόνου ξεκινούν από τετράπολα ραδιοσυχνότητας (Radio Frequency Quadrupole) έχοντας ενέργεια 750 keV. Ακολούθως επιταχύνονται αποκτώντας ενέργεια 50 MeV με τη βοήθεια του γραμμικού επιταχυντή LINAC και κατευθύνοται στον προωθητή (Booster) όπου αναπτύσσουν ενέργεια ίση με 1.4 GeV. Στη συνέχεια οδηγούνται στο σύγχροτρο πρωτονίων (Proton Synchrotron) όπου και επιταχύνονται μέχρι την ενέργεια 25 GeV και κατόπιν στο μεγάλο σύγχροτρο πρωτονίων (Super Proton Synchrotron), όπου και καταλήγουν στην ενέργεια των 450 GeV. Από εκεί κατευθύνονται προς τους δύο ομόκεντρους δακτυλίους του LHC [18, 19, 20, 21], με αντίθετες κατευθύνσεις μέχρι να αποκτήσουν την επιθυμητή ενέργεια των 7 TeV (3.5 TeV για τα δεδομένα που ελήφθηκαν το 2011, τα οποία και επεξεργάστηκαν στην παρούσα διατριβή). Κατόπιν συγκρούνονται στα σημεία που είναι εγκατεστημένοι οι ανιχνευτές των τεσσάρων πειραμάτων ATLAS [52], CMS[53], ALICE [54] και LHCb [55].

Πολύ συνοπτικά, ο ανιχνευτής CMS σχεδιάστηκε με στόχο τη μελέτη των προϊόντων σύγκρουσης πρωτονίων-πρωτονίων και ως εκ τούτου δύναται να ανιχνεύει φωτόνια, ηλεκτρόνια, αδρόνια και μιόνια μετρώντας με ακρίβεια την ενέργειά τους. Παράλληλα καταγράφει έμμεσα τα παράγωγα που δεν αλληλεπιδρούν με τα υλικά του ανιχνευτή, μετρώντας το έλλειμμα στην εγκάρσια συνιστώσα της ορμής ή αλλιώς μετρώντας την ελλείπουσα εγκάρσια ενέργεια. Χαρακτηρίζεται από την ακριβή μέτρηση στην ορμή των μιονίων, από υψηλή διακριτική ικανότητα του ηλεκτρομαγνητικού καλοριμέτρου και από ισχυρό ανιχνευτή τροχιών.

Το σύστημα συντεταγμένων που έχει υιοθετηθεί από το πείραμα CMS, έχει την αρχή του (0,0) στο κέντρο του ανιχνευτή, στο σημείο σύγκρουσης. Ο άξονας y δείχνει κάθετα προς τα πάνω, ενώ ο άξονας x δείχνει προς το κέντρο του LHC. Ως εκ τούτου, ο άξονας z δείχνει κατά μήκος της δέσμης προς τα βουνά Jura. Η αζιμουθιακή γωνία ϕ μετράται από τον άξονα x στο επίπεδο xy, ενώ η πολική γωνία θ μετράται από τον άξονα z. Από τα παραπάνω προκύπτει ότι η εγκάρσια ορμή ($\mathrm{p_T}$) και η εγκάρσια ενέργεια ($\mathrm{E_T}$), υπολογίζονται χρησιμοποιώντας τις συντεταγμένες x και y. Επιπροσθέτως, το έλλειμμα ενέργειας, όπως υπολογίζεται στο εγκάρσιο επίπεδο, συμβολίζεται ως $\mathrm{E_T^{miss}}$.

Οι διαστάσεις του ανιχνευτή CMS είναι 21.6 m μήκος, 14.6 m διάμετρος και συνολικό βάρος 12500 t. Το βασικό χαρακτηριστικό του είναι ο υπεραγώγιμος μαγνήτης (superconducting solenoid) εσωτερικής διαμέτρου 6 m, ο οποίος δημιουργεί αξονικό μαγνητικό πεδίου έντασης 3.8 T κατά μήκος της κατεύθυνσης της δέσμης. Οι τροχιές των φορτισμένων σωματιδίων μετρώνται από το εσωτερικό σύστημα τροχιάς (inner tracking system), το οποίο αποτελείται από έναν ανιχνευτή pixel (pixel detector) κι έναν ανιχνευτή τροχιάς πυριτίου (silicon strip tracker), καλύπτοντας $0 < \phi < 2\pi$ και $|\eta| < 2.5$, όπου η είναι η ψευδοωκύτητα[1]. Το σύστημα τροχιάς περικλείεται από το ηλεκτρομαγνητικό θερμιδόμετρο (ECAL) και από το αδρονικό θερμιδόμετρο (HCAL). Το ECAL αποτελείται από 61200 κρυστάλλους βολφραμικού μολύβδου ($\mathrm{PbWO_4}$) οι οποίοι είναι εγκατεστημένοι στο κεντρικό μέρος του βαρελιού (ECAL Barrel, EB) και 7324 που βρίσκονται τοποθετημένοι στις άκρες (ECAL Endcap, EE). Επιπλέον ένας ανιχνευτής προκαταιγισμού (preshower detector) έχει τοποθετηθεί μπροστά από τους κρυστάλλους στο EE, με σκοπό την αναγνώριση των ουδέτερων πιονίων στην περιοχή $1.653 < |\eta| < 2.6$. Συντελεί επίσης στο διαχωρισμό των ηλεκτρονίων από τα

---

[1] $\eta = -\ln[\tan(\theta/2)]$, όπου θ είναι η πολική γωνία της τροχιάς του σωματιδίου ως προς την κατεύθυνση της δέσμης.

σωματίδια που είναι γνωστά ως minimum bias ionizing και επιτρέπει τον προσδιορισμό της θέσης των ηλεκτρονίων και των φωτονίων. Το σύστημα σκανδαλισμού (trigger system) είναι οργανωμένο σε δύο επίπεδα και έχει ως στόχο την επιλογή των πιο ενδιαφέροντων γεγονότων όπως προκύπτουν μετά από τις συγκρούσεις μεταξύ των πρωτονίων. Σε αυτό ακριβώς το σύστημα θα πρέπει να αναφερθεί και η συνεισφορά του ερευνητικού κέντρου "Δημόκριτος" με το σύστημα Global Trigger emulator (GTPe). Το σύστημα αυτό σχεδιάστηκε στο Δημόκριτο και στα πλαίσια αυτής της διατριβής πραγματοποιήθηκαν έλεγχοι για τη σωστή λειτουργία του πριν την αποστολή του στο CERN. Ο GTPe παράγει τυχαίους σκανδαλισμούς (pseudo-random triggers) για το πρώτο επίπεδο σκανδαλισμού (Level-1) ενώ παράλληλα ανταλλάσσει πληροφορίες με άλλα μέρη του συστήματος λήψης δεδομένων (DAQ). Ο προορισμός του συστήματος αυτού είναι η αποσύνδεση του Πρώτου επιπέδου σκανδαλισμού (Level-1 trigger system) από το συστημα readout, κάτι που το καθιστά ένα πολύ σημαντικό συστατικό για την εγκατάσταση, τον έλεγχο και τη συντήρηση του συστήματος λήψης δεδομένων.

Μελέτη του ανιχνευτή micromegas για το sLHC

Ο ανιχνευτής Micromegas, ανήκει στην ευρύτερη κατηγορία των ανιχνευτών αερίου. Έχει δυνατότητα ανίχνευσης ποικίλων ειδών σωματιδίων (φωτόνια, φορτισμένα σωματίδια, νετρόνια) εφόσον γίνουν οι απαραίτητες προσαρμογές, γι' αυτό και παρουσιάζει μεγάλη ποικιλία εφαρμογών.

Κατά τη διάρκεια του δεύτερου μισού του 20ου αιώνα, αναπτύχθηκαν τρεις βασικοί τύποι ανιχνευτών, ο θάλαμος ιονισμού (ionization chamber), ο αναλογικός απαριθμητής (proportional counter) και ο απαριθμητής Geiger-Muller (Geiger-Muller counter). Οι θάλαμοι ιονισμού ήταν οι πρώτες συσκευές που αναπτύχθηκαν για την ανίχνευση της ακτινοβολίας. Αυτές οι συσκευές στηρίζονται στην απευθείας συγκέντρωση των ιονισμένων ηλεκτρονίων και των ιόντων που παράχθηκαν σε ένα αέριο καθώς το διαπερνούσε ακτινοβολία. Χρησιμοποιούνται ευρέως στα εργαστήρια σαν συσκευές μέτρησης και ελέγχου της ακτινοβολίας. Είναι οικονομικοί, χειρίζονται με απλό τρόπο και συντηρούνται εύκολα. Στην πραγματικότητα, ο βασικός σχεδιασμός και η κατασκευή τους δεν έχουν αλλάξει πολύ από τα τέλη της δεκαετίας του 1940.

Συνέχεια των τριών αυτών βασικών τύπων ανιχνευτών, αποτέλεσε μια πολύ σημαντική ανακάλυψη που τιμήθηκε και με βραβείο Nobel το 1992. Η ανακάλυψη αυτή ήταν ο θάλαμος που είναι γνωστός με την ονομασία Πολυσυρματικός Αναλογικός θάλαμος (MultiWire Proportional Chamber-MWPC) από τον G. Charpak το 1968 [47]. Τα βασικά χαρακτηριστικά των MWPC είναι η καλή χωρική διακριτική ικανότητα (μερικές εκατοντάδες μm), η πολύ καλή ενεργειακή διακριτική ικανότητα και ο αρκετά ικανοποιητικός ρυθμός μέτρησης 10^4 counts

$mm^{-2}s^{-1}$. Ένα άλλο είδος ανιχνευτή που αναπτύχθηκε τότε ήταν ο θάλαμος ολίσθησης (drift cell). Ο θάλαμος ολίσθησης καθορίζεται στο ένα άκρο του από ένα ηλεκτρόδιο υψηλής τάσης (High Voltage) και στο άλλο άκρο του από την άνοδο ένας απλού αναλογικού απαριθμητή. Προκειμένου να δημιουργηθεί ένα σταθερό ηλεκτρικό πεδίο, χρησιμοποιούνται σειρές συρμάτων καθόδου (series of cathode field wires) τα οποία κρατώνται στο κατάλληλο δυναμικό, διαμορφώνοντας την περιοχή ολίσθησης. Προκειμένου να δοθεί το σήμα για την άφιξη του σωματιδίου, ένας απαριθμητής σπινθηρισμών που καλύπτει όλη την ευαίσθητη περιοχή, τοποθετείται πριν ή μετά από τον θάλαμο (chamber). Ένα σωματίδιο το οποίο διαπερνά τον θάλαμο και τον σπινθηριστή (scintillator), απελευθερώνει στο αέριο ηλεκτρόνια τα οποία τότε αρχίζουν να ολισθαίνουν στην άνοδο. Την ίδια στιγμή, ένα γρήγορο σήμα από τον σπινθηριστή ξεκινά τη λειτουργία σε ένα χρονόμετρο. Το σήμα που δημιουργείται στην άνοδο καθώς τα ολισθαίνοντα ηλεκτρόνια φτάνουν, σταματάει τότε το χρονόμετρο αποδίδοντας με τον τρόπο αυτό τον χρόνο ολίσθησης.

Τρισδιάστατες πληροφορίες για τα σωματίδια, έγιναν εφικτές με την κατασκευή των θαλάμων προβολής χρόνου (Time Projection Chamber, TPC). Οι θάλαμοι αυτοί αποτελούν μια εκλεπτυσμένη συσκευή που συνδυάζει τα χαρακτηριστικά του θαλάμου ολίσθησης και των MWPC. Ο θάλαμος προβολής χρόνου είναι λοιπόν ένας θάλαμος ολίσθησης ο οποίος παρέχει χωρική πληροφορία στις τρεις διαστάσεις, όπως επίσης και μετρήσεις του ρυθμού απώλειας ενέργειας (dE/dx) για ταυτοποίηση των σωματιδίων. Το βασικό χαρακτηριστικό ενός TPC είναι ότι το ηλεκτρικό πεδίο στον θάλαμο είναι παράλληλο στο μαγνητικό πεδίο από ένα μαγνητικό φασματόμετρο. Αυτή η διευθέτηση μειώνει την διάχυση των ηλεκτρονίων στο αέριο επειδή το μαγνητικό πεδίο αναγκάζει το ηλεκτρόνιο που ολισθαίνει να καμπυλωθεί γύρω απ' τις γραμμές του ηλεκτρικού πεδίου. Σαν επακόλουθο, το ηλεκτρόνιο μπορεί να ολισθήσει σε μια μεγάλη απόσταση και ακόμα όμως να παρέχει καλή χωρική διακριτική ικανότητα. Ο ανιχνευτής μπορεί να έχει μεγάλη γεωμετρική αποδοχή και μπορεί ταυτόχρονα να μετράει έναν μεγάλο αριθμό τροχιών. Όσο επιτυχείς κι αν ήταν όμως οι θάλαμοι αυτοί, μοιραία βρέθηκαν αντιμέτωποι με στοιχειώδεις περιορισμούς όταν εμφανίστηκαν στο προσκήνιο ερωτήσεις ως προς την καλύτερη χωρική ανάλυση και μεγαλύτερο ρυθμό καταμέτρησης. Τα σύρματα δεν μπορούσαν να τοποθετηθούν κοντά χωρίς να συναντήσουν λειτουργικά προβλήματα και όσο είχαν ενδιαφέρον οι ρυθμοί, τα θετικά ιόντα δεν απομακρύνονταν αρκετά γρήγορα. Προκειμένου να καλυφθούν αυτοί οι περιορισμοί, ο A. Oed επινόησε τους Micro-Strip Gas Chambers (MSGC) [49, 50], σηματοδοτώντας μια καινούρια στιγμή στην ιστορία των ανιχνευτών αερίου. Παίρνοντας πλεονέκτημα από την βελτίωση των μικροηλεκτρονικών και την ανάπτυξη διαδικασιών φωτολιθογραφίας, πολύ λεπτά strips αποτυπώθηκαν σε μια άδεια πλακέτα, σαν συνέχεια στενών ανόδων και πιο πλατιών καθόδων, πιο κοντά από τα σύρματα σε ένα MWPC (τυπικές αποστάσεις είναι περίπου 50-100mm). Εξαιτίας της μορφής του ηλεκτρικού

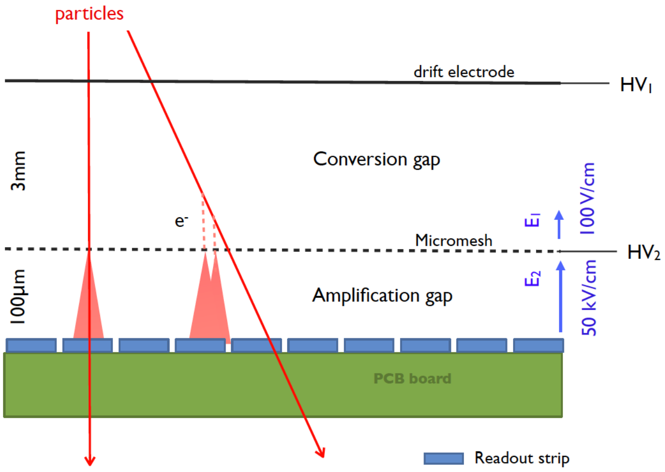

Σχήμα 1: Σχηματική αναπαράσταση του ανιχνευτή micromegas.

πεδίου, τα ιόντα που παράγονται από το φαινόμενο της χιονοστιβάδας, απομακρύνονται γρήγορα, αυξάνοντας έτσι την ικανότητα μέτρησης (counting capacity) του θαλάμου 100 φορές πάνω από την αντίστοιχη του MWPC, φτάνοντας τα 10^6 counts $mm^{-2}s^{-1}$. Οι MSGC έγιναν γρήγορα ευπρόσδεκτοι και αναπτύχθηκαν έτσι ώστε να συμπεριληφθούν σε πειράματα υψηλής φωτεινότητας. Βέβαια οι ανιχνευτές αυτοί ήταν ευάλωτοι στη γήρανση και σε βλάβες εκφόρτισης κι έτσι ακολουθήθηκαν από μια σειρά άλλων ανακαλύψεων που οδήγησαν στο σχεδιασμό των ανιχνευτών "Micro-Pattern", οι οποίοι επωφελήθηκαν από τη νέα τεχνολογία στα μικροηλεκτρονικά και τη φωτολιθογραφία. Τη χρονική αυτή περίοδο έκανε την εμφάνισή του και ο micromegas (MICROMEsh GAsous Structure). Ο ανιχνευτής αυτός προτάθηκε αρχικά για την ανίχνευση φορτισμένων σωματιδίων της τάξης των 1-10 keV, από τους Γ.Γιοματάρη και J.Collar στα μέσα της δεκαετίας του ’90 [34, 40].

Ο ανιχνευτής αυτός υπερτερεί έναντι των υπολοίπων ανιχνευτών αερίου, ως προς το γεγονός ότι έχει πολύ μικρό υπόβαθρο και ως εκ τούτου είναι ιδανικός για μετρήσεις πολύ μικρών φορτίων και άρα μικρής ενέργειας. Η διαφορά του από τους ανιχνευτές που έχουμε αναφέρει ως τώρα είναι οι δύο καλά διαχωρισμένες περιοχές οι οποίες δεν διαχωρίζονται πια από ένα επίπεδο με σύρματα, αλλά από ένα πλέγμα το οποίο είναι γνωστό με την ονομασία micromesh.

Η αρχή λειτουργίας του μπορεί να περιγραφεί πολύ απλά από τα επιμέρους εξαρτήματά του (βλ. Σχήμα 1). Το πρώτο τμήμα που θα πρέπει να διασχίσει ένα σωματίδιο είναι το ηλεκτρόδιο ολίσθησης (drift electrode). Καθώς περάσει το ηλεκτρόδιο ολίσθησης, το σωματίδιο βρίσκεται ήδη στην περιοχή απογύμνωσης (conversion region), η οποία απλώνεται μέχρι μερικά mm μέχρι το πλέγμα. Έχει ένα πολύ ασθενές ηλεκτρικό πεδίο της τάξεως του 1 kV/cm και είναι το μέρος όπου γίνεται η πρώτη αλληλεπίδραση του σωματιδίου με τον ανιχνευτή.

Ο ρόλος του πλέγματος (micromesh) είναι πολλαπλός και είναι κάτι περισσότερο από το να «σημειώνει» το τέλος της περιοχής απογύμνωσης (conversion gap) και την αρχή της περιοχής ενίσχυσης (amplification). Στις πρώτες εκδοχές του micromegas είναι κατασκευασμένος από χαλκό (5 μm) με μία διαδικασία η οποία βασίζεται στην τεχνική της φωτολιθογραφίας και επιτρέπει την χάραξη σε αυτόν ανοιγμάτων 25 μm με βήμα 50 μm. Η τάση που εφαρμόζεται είναι γύρω στα 500 V και είναι τόση ώστε ο λόγος του ηλεκτρικού πεδίου στην περιοχή ενίσχυσης και της περιοχής απογύμνωσης να είναι μεγάλος. Η τιμή του επιλέγεται κατάλληλα ώστε να επιτυγχάνουμε μέγιστη διείσδυση των ηλεκτρονίων προς την περιοχή καταιγισμού. Άπαξ και στην περιοχή απογύμνωσης ξεκινήσει η διαδικασία της χιονοστιβάδας, το χάσμα είναι τόσο μικρό (της τάξης των 50-100 μm) κι έτσι το ηλεκτρικό πεδίο που επιτυγχάνεται είναι πολύ μεγάλο (μέχρι 50 kV/cm). Την ίδια στιγμή, καθώς παρέχεται ένας ομαλός δρόμος για τα ηλεκτρόνια στην περιοχή ενίσχυσης, το πλέγμα αποτρέπει τα ιόντα που παράγονται από τη χιονοστιβάδα να εισέλθουν στην περιοχή απογύμνωσης. (Οι προαναφερθείσες τιμές για τις διαστάσεις του micromegas είναι ενδεικτικές και διαφέρουν από ανιχνευτή σε ανιχνευτή.)

Το ηλεκτρόδιο ανόδου αποτελείται από λωρίδες χαλκού, πλάτους της τάξεως των 150-350 μm και ενδιάμεσου κενού περίπου 100 μm. Το ηλεκτρόδιο ανόδου είναι γειωμένο διαμέσου ενός προενισχυτή χαμηλού θορύβου και μεγάλης ενίσχυσης σε ένα απομονωμένο στρώμα (kapton).

Συνοψίζοντας τα σημαντικότερα πλεονεκτήματα της τεχνικής που εισήχθη με τους Micromegas είναι τα εξής:

- Πολύ καλή χωρική ανάλυση (spatial resolution).
- Γρήγορη απόκριση (response).
- Μεγάλοι ρυθμοί μέτρησης (counting rates).
- Αντοχή στην ακτινοβολία (radiation hardness).
- Καλή ανάλυση ενέργειας (energy resolution).
- Αντοχή (robustness).
- Δυνατότητα για κάλυψη μεγάλων επιφανειών.

Οι ανιχνευτές Micromegas έχουν χρησιμοποιηθεί σε διάφορες εφαρμογές, όπως στη φυσική υψηλών ενεργειών (COMPASS, nTOF, NA48, TESLA, CAST, HELLAZ) [34, 35, 36, 37, 38, 39, 40], και είναι υπό μελέτη ώστε να χρησιμοποιηθούν ως ανιχνευτές τροχιάς (όπως για παράδειγμα οι μιονικοί ανιχνευτές) στα πειράματα για το super LHC. Μπορούν επίσης να χρησιμοποιηθούν σε ιατρικές εφαρμογές (π.χ. κρυσταλλογραφία πρωτεϊνών, ιατρική ραδιολογία, ακτινογραφία-β).

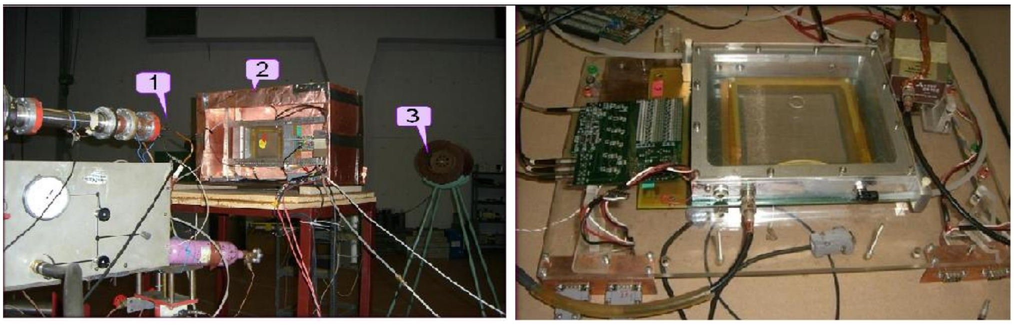

Σχήμα 2: Μέρος της πειραματικής διάταξης. Το δοχείο αερίου του δευτερίου (1), ο κλωβός Faraday, ο ανιχνευτής micromegas (2) και ο μετρητής νετρονίων BF3 (3) είναι ορατά στη φωτογραφία (αριστερά). Ο ανιχνευτής micromegas, ο προενισχυτής, οι σωλήνες εισόδου και εξόδου του αερίου, οι παροχές υψηλής τάσης και οι κάρτες gassiplex για την ανάγνωση των δεδομένων είναι επίσης ορατά στην εικόνα (δεξιά).

Στα πλαίσια της διατριβής αναπτύχθηκε σύστημα λήψης δεδομένων βασισμένο στο λογισμικό πακέτο Labview [46], το οποίο και χρησιμοποιήθηκε για τη μελέτη του ανιχνευτή micromegas σε δοκιμαστικές δέσμες νετρονίων στο Δημόκριτο αλλά και αδρονίων στο CERN.

Η λειτουργία του ανιχνευτή micromegas στο sLHC απαιτεί και καλή λειτουργία σε περιβάλλον υψηλής ροής νετρονίων. Σε αντίθεση με τα σωματίδια ελάχιστου ιονισμού, τα νετρόνια εναποθέτουν μεγάλες ποσότητες φορτίου και προκαλούν εκσπάσεις (sparks) ακόμα και σε μικρές ενισχύσεις (gain). Η μελέτη του ανιχνευτή σε υπόβαθρο νετρονίων είχε ως στόχο να καταδείξει την καταλληλότητά του και να μελετήσει το πρόβλημα των εκσπάσεων. Τα νετρόνια παρέχονταν από τον ανιχνευτή Tandem στο ΕΚΕΦΕ "Δημόκριτος", ο οποίος και δύναται να παράγει νετρόνια με ενέργειες έως 25.7 MeV. Τα νετρόνια παράγονταν μέσω της αντίδρασης [D(d,n)^{3}He] και οι ενέργειες Δευτερίου που χρησιμοποιήθηκαν ήταν 2.8 MeV, 3.2 MeV, 3.7 MeV, 4 MeV και 4.3 MeV οι οποίες αντιστοιχούν σε ενέργειες νετρονίων: 5.5 MeV, 5.9 MeV, 6.5 MeV, 6.8 MeV και 7.1 MeV. Η ροή νετρονίων ήταν μεταξύ 2.4×10^{5} cm^{-2} s^{-1} και 7.7×10^{5} cm^{-2} s^{-1}. Ο ανιχνευτής που απεικονίζεται στην παρακάτω εικόνα αποτελείται από ένα πλαίσιο αλουμινίου και ενεργό περιοχή 10×10 cm^2 η οποία δημιουργείται από μία μονοδιάστατη δομή 96 λωρίδων με βήμα 1 mm. Ο ανιχνευτής ήταν έγκλειστος σε κλωβό Faraday κατά το βομβαρδισμό του με τη δέσμη νετρονίων. Στην ίδια εικόνα είναι ορατό ένα μεγάλο μέρος της πειραματικής διάταξης.

Από τα αποτελέσματα της μελέτης αυτής φάνηκε οτι οι αρχικοί ανιχνευτές micromegas, είχαν πρόβλημα να λειτουργήσουν σε περιβάλλον με μεγάλες ροές νετρονίων και χρειάστηκε περαιτέρω μελέτη και νέα σχεδίαση βασισμένη σε επικάλυψη με υλικά μεγάλης αντίστασης ωστε να λυθούν τα προβλήματα εκσπάσεων. Παρόλα αυτά μετρήθηκαν οι παράγοντες αποδιέγερσης (de-excitation components) μετά την ακτινόβοληση με τα νετρόνια (βλ. Σχήμα3) ήταν σε πολύ καλή συμφωνία με τη θεωρία. Συγκεκριμένα, οι παράγοντες αποδιέγερσης που προέκυψαν από το fit (δύο εκθετικές κατανομές) ήταν 2.33±0.20 min και 10.18±1.37 min, ενώ οι αντίστοιχες θεωρητικές τιμές ήταν: 2.24 min (^{27}Al(n,g)^{28}Al) και 9.46 min (^{27}Al(n,p)^{27}Mg).

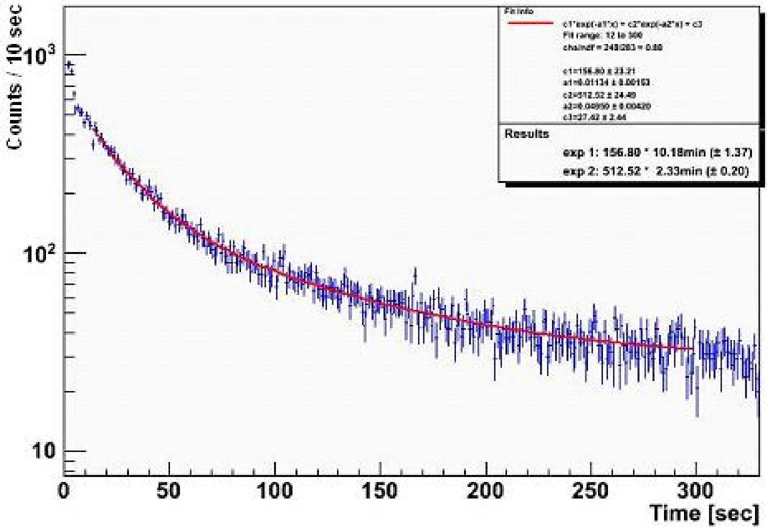

Σχήμα 3: Μετρήσεις του ανιχνευτή micromegas κατά τη διάρκεια του χρόνου "αποδιέγερσης". Οι παράγοντες αποδιέγερσης του fit (κόκκινη γραμμή) 2.33±0.20 min και 10.18±1.37 min, βρίσκονται σε συμφωνία με την αποδιέγερση των ^{27}Al(n,g)^{28}Al (2.24 min) και ^{27}Al(n,p)^{27}Mg (9.46 min).

Στους πρωτότυπους ανιχνευτές micromegas, όπως ήδη συζητήθηκε, εφαρμόζεται ένα πολύ υψηλό πεδίο ενίσχυσης σε ένα πολύ μικρό κενό (gap). Στο περιβάλλον του super LHC, η μεγάλη ροή των αδρονίων μπορεί να οδηγήσει σε γεγονότα μεγάλου ιονισμού που συνεπάγεται μεγάλη εναπόθεση ενέργειας και ως εκ τούτου αυξανόμενη πιθανότητα δημιουργίας εκσπάσεων. Το πρόβλημα με τις εκσπάσεις δεν έγκειται την ανθεκτικότητα του ανιχνευτή ή τα ηλεκτρονικά στα οποία είναι εφικτή η τοποθέτηση κατάλληλης προστασίας, αλλά στο νεκρό χρόνο που προκαλείται από την αποφόρτιση όλου του πλέγματος (micromesh). Ο νεκρός χρόνος ποικίλει μεταξύ 1 και 2 ms ώστε να αποκατασταθεί η σωστή τάση. Για το σκοπό αυτό ανάλογα τεστ πραγματοποιήθηκαν στο CERN σε περιβάλλον αδρονίων (π^+ στον SPS) αυτή τη φορά. Μελετήθηκαν διάφοροι πρωτότυποι ανιχνευτές διαστάσεων 10×10 cm^2, με διαφορετικά pitches (0.5 - 2 mm) και διαφορετικές τεχνολογίες ανόδων με resistive layers και όλες έδειξαν πολύ καλή συμπεριφορά με καλή χωρική ανάλυση, καλή αποδοτικότητα

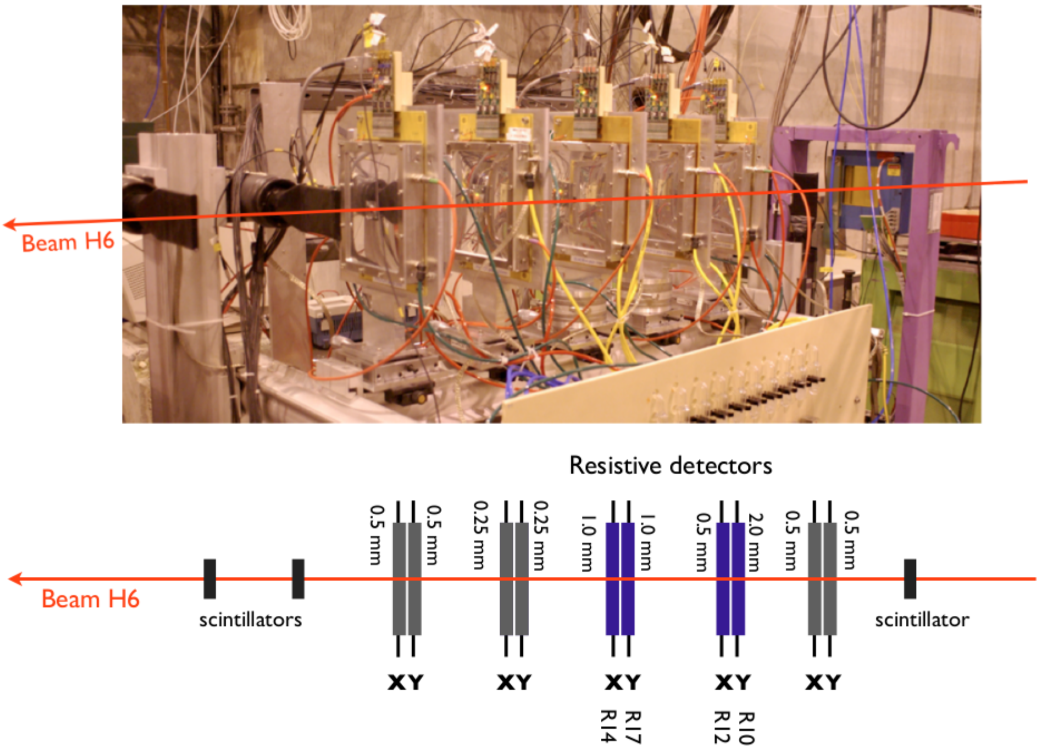

Σχήμα 4: Φωτογραφία μέρους της πειραματικής διάταξης στο CERN, όπου επισημαίνεται και η κατεύθυνση της δέσμης. Το τηλεσκόπιο αποτελείται από 3 ζεύγη ανιχνευτών (X-Y) και 4 ανιχνευτές ελέγχονται.

(efficiency) και μείωση των εκσπάσεων.

Η ακόλουθη εικόνα περιέχει τη γεωμετρία των διαφορετικών τεχνολογιών resistive ανόδων που ελέγχθηκαν. Συνοπτικά οι διαφορετικοί ανιχνευτές είναι οι ακόλουθοι:

- **Carbon-Loaded Kapton**: Το επίπεδο των strips καλύπτεται από ένα μονωτικό στρώμα πάχους 75 μm, στο οποίο προσκολλάται ένα λεπτό στρώμα carbon-loaded kapton. Το βήμα μεταξύ των strips είναι 2.0 mm (Σχήμα 5 -R10)

- **Resistive strip to ground**: Το επίπεδο των strips καλύπτεται από ένα μονωτικό στρώμα πάχους 64 μm, στο οποίο εναποτίθενται μονωτικά strips χρησιμοποιώντας μονωτικό μελάνι (resistive ink), τα οποία ταιριάζουν με τη γεωμετρία. Κάθε ένα από τα strips (βήμα μεταξύ των strips: 1.0 mm) γειώνεται με τη βοήθεια αντίστασης 30 MΩ και η αντίσταση κατά μήκος των strips είναι 250 MΩ (Σχήμα 5-R17)

- **Resistive strips**: Σε κάθε ένα από τα χάλκινα strips της ανόδου εναποτίθεται ωμική κάλυψη (resistive coating). Η αντίσταση κατά μήκος των strips είναι 300 kΩ (Σχήμα 5R12 (βήμα μεταξύ των strips: 0.5 mm) και R14 (βήμα μεταξύ των strips: 1.0 mm))

Η επεξεργασία των πειραματικών δεδομένων έδειξε ότι η ωμική κάλυψη (resistive coating) ήταν η πιο πετυχημένη μέθοδος στη μείωση της επίδρασης των εκσπάσεων στην αποδοτικότητα (efficiency) του ανιχνευτή micromegas. Καλή χωρική ανάλυση της τάξης των $\sim 80\mu$m μπορεί να επιτευχθεί με τη χρήση ωμικής κάλυψης (resistive strip coating) και υψηλή αποδοτικότητα (>98%) επιτυγχάνεται με ανιχνευτές micromegas εφοδιασμένους με ωμικές ανόδους (resistive anode). Η τεχνολογία με τα γειωμένα ωμικά strips (R17) φαίνεται να είναι h καλύτερη υποψήφια για το περιβάλλον υψηλής φωτεινότητας sLHC διότι παρουσιάζει καλύτερη αποδοτικότητα, πολύ ικανοποιητική μείωση των εκσπάσεων, πολύ καλή χωρική ανάλυση και καλύτερη ανθεκτικότητα σε σχέση με την απλή ωμική επένδυση (resistive coating) και καθόλου επίδραση φορτίου (charging effect) συγκριτικά με την τεχνολογία Carbon-Loaded-Kapton.

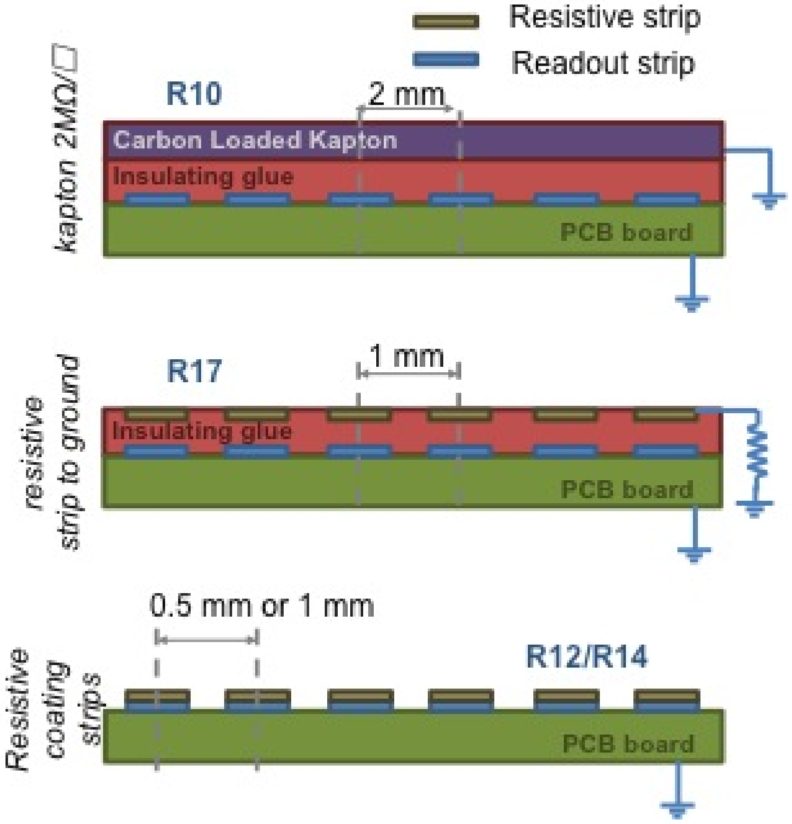

Σχήμα 5: Γεωμετρία των διαφορετικών τεχνολογιών ανόδων (resistive anodes).

Μελέτη για Υπερσυμμετρία σε τελικές καταστάσεις με φωτόνια

Προσομοίωση δεδομένων

Η προσομοίωση των δεδομένων είναι υψίστης σημασίας στον έλεγχο και τη διόρθωση πολύπλοκων φυσικών καταστάσεων, αλλά και για τη σύγκριση της απόδοσης ενός ανιχνευτή με τις προβλέψεις. Τα γεγονότα προσομοίωσης θα πρέπει να συμφωνούν όσο πιο πολύ γίνεται με τα πραγματικά δεδομένα. Ως εκ τούτου, ο πρωταρχικός ρόλος ενός προγράμματος προσομοίωσης είναι η πιο κοντινή πρόβλεψη των εμπλεκόμενων φυσικών διεργασιών, της επίδοσης του ανιχνευτή.

Η προσομοίωση γεγονότων μπορεί να διακριθεί σε τρία βασικά στάδια: παραγωγή των γεγονότων, προσομοίωση του ανιχνευτή και ψηφιοποίηση (προσομοίωση της απόκρισης των ηλεκτρονικών του ανιχνευτή).

Η παραγωγή των γεγονότων γίνεται με διάφορους γεννήτορες οι οποίοι μπορούν να κατανεμηθούν σε δύο κατηγορίες: Automatized Matrix Element generators και Parton Shower MC event generators. Στην πρώτη κατηγορία ανήκει και ο γεννήτορας MadGraph [28] με τον οποίο δημιουργήθηκαν τα υπόβαθρα που χρησιμοποιήθηκαν στην διατριβή αυτή. Στην δεύτερη κατηγορία ανήκουν τα υποτιθέμενα Υπερσυμμετρικά σήματα που χρησιμοποιηθήκαν για τις πρώτες δοκιμές της μεθόδου που αναπτύχθηκε για την ανάδειξη του σήματος σε τελικές καταστάσεις με φωτόνια, πίδακες αδρονίων (jets) και ελλείπουσα εγκάρσια ενέργεια.

Η προσομοίωση του ανιχνευτή βασίζεται στο λογισμικό πακέτο Geant4 και χρησιμοποιήθηκε για την αναπαράσταση των διεργασιών που διαδραματίζονται από τις αλληλεπιδράσεις των σωματιδίων με το υλικό του ανιχνευτή. Ο αλγόριθμος βασίζεται σε εκτενή περιγραφή της ιεραρχίας μεταξύ των υποανιχνευτών, των υλικών από τα οποία αποτελούνται αλλά και από τα εφαρμοζόμενα μαγνητικά πεδία. Γνωρίζει ποιος είναι ο ενεργός όγκος του ανιχνευτή (sensitive detector) και ποια είναι τα "νεκρά" μέρη (πχ καλώδια ή συστήματα ψύξης) και χρησιμοποιεί όλες αυτές τις πληροφορίες για να αποφασίσει την απόκριση του ανιχνευτή στα προσομοιωμένα σωματίδια.

Στην υπό μελέτη τελική κατάσταση (κανάλι) τα υπόβαθρα που προβλέπονται από το Καθιερωμένο Πρότυπο είναι τα ακόλουθα:

- **γ + jets**: Αποτελεί το κύριο υπόβαθρο σύμφωνα με το Καθιερωμένο Πρότυπο, καθώς τα γεγονότα ενδεχομένως να συνοδεύονται με την ύπαρξη ελλείπουσας εγκάρσιας ενέργειας. Η $\mathrm{E_T^{miss}}$ δεν πρόερχεται από τη φυσική διαδικασία, αλλά από την ικανότητα ανακατασκευής (jet energy scale) του ανιχνευτή γι'αυτό και ονομάζεται "φαινομενική $\mathrm{E_T^{miss}}$ ".

- **W + jets**: Αυτό το υπόβαθρο μαζί με τα $t\bar{t}$ + jets και Drell-Yan αποτελούν τα αμέσως επόμενα σημαντικά υπόβαθρα και εμπεριέχουν διεργασίες με πραγματική $\mathrm{E_T^{miss}}$. Οι διασπάσεις των φορτισμένων μποζονίων $\mathrm{W}^{+/-}$ τα οποία είναι πιθανόν να συνεισφέρουν στο υπόβαθρο που προβλέπει το ΚΠ είναι: $\mathrm{W} \rightarrow \mathrm{e}\nu$ όπου το ηλεκτρόνιο μπορεί να προσδιοριστεί λαθεμένα ως φωτόνιο και $\mathrm{W} \rightarrow \tau\nu$ όπου $\tau \rightarrow e\nu\nu$, ή $\tau \rightarrow h \geq 1\pi^0\nu$, ($h$: αδρόνιο)
- **$\mathbf{t\bar{t}}$ + jets**: Ο μόνος γνωστός τρόπος που το top quark μπορεί να διασπαστεί είναι μέσω της ασθενούς αλληλεπίδρασης παράγοντας ένα μποζόνιο W και ένα down-type quark (κατά κύριο λόγο bottom αλλά επίσης και down και strange quark)[24]. Τα παραγόμενα μποζόνια W είναι πιθανόν να εισάγουν υπόβαθρο στο σήμα μας εξαιτίας της λαθεμένης αναγνώρισης ενός ηλεκτρονίου για φωτόνιο και εξαιτίας των νετρίνων που διαφεύγουν εμφανίζοντας έτσι $\mathrm{E_T^{miss}}$ στο γεγονός.
- **γ + W/Z + jets**: Η παρουσία μποζονίων W/Z θα μπορούσε επίσης να συνεισφέρει στο υπόβαθρο, διότι ελλείπουσα εγκάρσια ενέργεια παράγεται εξαιτίας των νετρίνων.
- **Drell Yan + jets**: Στις συγκρούσεις μεταξύ πρωτονίων, η αλληλεπίδραση μεταξύ $q\bar{q}$ ίσως παράγει Z^0 ή $\gamma^{\star}$ τα οποία με τη σειρά τους διασπώνται σε ζεύγος λεπτονίου-αντιλεπτονίου. Αυτή η διεργασία η οποία είναι γνωστή ως Drell-Yan αποτελεί ένα ακόμα πιθανό υπόβαθρο στο υπό μελέτη κανάλι.

Για τη μελέτη του καναλιού αυτού χρησιμοποιήθηκαν τρία διαφορετικά αντιπροσωπευτικά σενάρια δύο bino-like και ένα wino-like neutralino, τα οποία και περιγράφονται στον πίνακα που ακολουθεί.

Πίνακας 5: Summary of studied GGM benchmark scenarios

	$\mathrm{m_{neutralino}}$ [GeV]	$\mathrm{m_{squark}}$ [GeV]	$\mathrm{m_{gluino}}$ [GeV]
bino-like	375	400-2000	400-2000
bino-like	150-1050	2500	160-2000
wino-like	375	400-2000	400-2000

Επιλογή των ενδιαφέροντων γεγονότων

Τα δεδομένα που χρησιμοποιήθηκαν σε αυτή την ανάλυση συγκεντρώθηκαν χρησιμοποιώντας ένα σύνολο από σκανδαλιστές (triggers) που απαιτούν τουλάχιστον ένα φωτόνιο με εγκάρσια ενέργεια >70 GeV και ελάχιστη αδρονική εγκάρσια ενέργεια ($\mathrm{H_T}$) η μέγιστη τιμή της οποίας (κατά τη διάρκεια των μετρήσεων) ήταν 400 GeV. Ως $\mathrm{H_T}$ ορίζεται το βαθμωτό άθροισμα της εγκάρσιας ορμής ($\mathrm{p_T}$) όλων των πιδάκων που ανιχνεύονται στο αδρονικό θερμιδόμετρο

(HCAL) με p_T >40 GeV, $|\eta| < 3$ και ικανοποιούν διάφορες άλλες απαιτήσεις ως προς την ποιότητα των πιδάκων (quality requirements). Η εφαρμογή περιορισμών (cuts) που γίνεται μετά τη λήψη των δεδομένων (offline) είναι πιο αυστηρή από τα cuts που εφαρμόζονται από το σύνολο των triggers, έτσι ώστε να επιτυγχάνεται η μεγαλύτερη δυνατή αποδοτικότητα. Η αντίστοιχη φωτεινότητα (integrated luminosity) των γεγονότων που αναλύθηκαν είναι 4.7 fb^{-1}.

Στις επόμενες παραγράφους ακολουθεί σύντομη περιγραφή των αντικειμένων (objects) που χρησιμοποιήθηκαν. Τα υποψήφια φωτόνια ανακατασκευάστηκαν από συλλογές (clusters) ενέργειας στο ηλεκτρομαγνητικό θερμιδόμετρο του CMS (ECAL). Το ECAL σχεδιάστηκε έτσι ώστε να παρέχει εξαιρετική ακρίβεια στη μέτρηση της ενέργειας, γεγονός που το καθιστά ένα ισχυρό εργαλείο για τη μέτρηση φωτονίων με υψηλή ακρίβεια στον LHC. Τα αντικείμενα που αναγνωρίζονται ως φωτόνια δημιουργήθηκαν από αποθέσεις ενέργειας στο ηλεκτρομαγνητικό θερμιδόμετρο. Εξαιτίας του υλικού των ανιχνευτών τροχιάς μπροστά από το θερμιδόμετρο, είναι πιθανό το φαινόμενο μετατροπής φωτονίου (photon conversion), καθώς και το φαινόμενο bremsstrahlung από ηλεκτρόνια και ποζιτρόνια. Το ισχυρό μαγνητικό πεδίο οδηγεί συχνά τη ροή της ενέργειας που συνδέεται με τα πρωτογενή (primary) ηλεκτρόνια ή τα converted primary φωτόνια να εξαπλωθεί ως προς την κατεύθυνση ϕ. Για να υπολογιστεί η ενέργεια ενός φωτονίου στο ECAL, αθροίζονται τοπικές εναποθέσεις (local deposits) σε υπερομάδες (superclusters) που εκτείνονται σε μία στενή ζώνη στην διεύθυνση η. Ένα supercluster αφού περάσει μια λίστα από κριτήρια αναγνώρισης και ποιότητας (π.χ. ως προς το σχήμα του καταιγισμού-shower), προάγεται σε φωτόνιο, όπως περιγράφεται και στην [64]. Επιπλέον, η απουσία ίχνους στον ανιχνευτή τροχιάς που να συμφωνεί με το supercluster χρησιμοποιείται για το διαχωρισμό των φωτονίων από τα ηλεκτρόνια. Για να αυξηθεί ο αριθμός των απομονωμένων φωτονίων, τα κριτήρια απομόνωσης εφαρμόζονται χρησιμοποιώντας συνδυασμένες πληροφορίες από τα θερμιδόμετρα (ECAL, HCAL) και τον ανιχνευτή τροχιάς (tracker). Συνολικά, η ενέργεια που συγκεντρώνεται σε ένα κώνο $\Delta R = \sqrt{\Delta\phi^2 + \Delta\eta^2} = 0.3$ (αφού έχουμε αφαιρέσει και τη συνεισφορά από τα "pileup") δεν θα πρέπει να υπερβαίνει τα 6 GeV.

Ο ορισμός του ηλεκτρονίου είναι όμοιος με τον αντίστοιχο του φωτονίου, εκτός από την επιπλέον απαίτηση για την ύπαρξη ίχνους στον ανιχνευτή τροχιών που να ταιριάζει με το supercluster. Τα ηλεκτρόνια χρησιμοποιούνται για τον υπολογισμό των διεργασιών όπου το ηλεκτρόνιο θα μπορούσε να αναγνωριστεί λαθεμένα ως φωτόνιο ενώ παράλληλα υπάρχει ελλείπουσα έγκαρσια ενέργεια (πχ. $W \rightarrow e\nu$).

Οι πίδακες αδρονίων ομαδοποιούνται με χρήση του αλγορίθμου anti-k_T με παράμετρο R=0.5 [25] και ανακατασκευάζονται με τον αλγόριθμο ανακατασκευής Particle-Flow [68]. Προκειμένου να συμπεριληφθεί η μη-γραμμική απόκριση της ενέργειας τω πιδάκων, εφαρμόζονται διορθώσεις κλίμακας ενέργειας (energy scale corrections). Για τον υπολογισμό της ποσότητας H_T που χρησιμοποιείται από το σύστημα σκανδαλισμού, οι πίδακες αδρονίων ανακατασκευάζονται κάνοντας χρήση πληροφοριών από το αδρονικό θερμιδόμετρο (calorimeter jets).

Η εγκάρσια ελλείπουσα ενέργεια είναι το αρνητικό διανυσματικό άθροισμα της εγκάρσιας ορμής $\mathrm{p_T}$, όλων των ανακατασκευασμένων σωματιδίων.

Τελικά επιλέγουμε γεγονότα που αποτελούνται από τουλάχιστον ένα φωτόνιο και τουλάχιστον τρεις πίδακες αδρονίων:

- τουλάχιστον ένα φωτόνιο εγκάρσιας ορμής $\mathrm{p_T} > 80$ GeV, $|\eta| < 1.4442$,
- τουλάχιστον τρεις πίδακες αδρονίων εγκάρσιας ορμής $\mathrm{p_T} > 100$ GeV, $|\eta| < 2.6$ και με απόσταση $\Delta R > 0.4$ από τα υποψήφια φωτόνια,
- $\mathrm{H_T} > 460$ GeV.

Προσδιορισμός του υποβάθρου

Πριν την εφαρμογή της μεθόδου σε πραγματικά δεδομένα, πραγματοποιήθηκαν έλεγχοι με χρήση δεδομένων προσομοίωσης (MC closure tests) για τα υποθετικά σενάρια υπάρξης μόνο υποβάθρου (background only) ή και σήματος (signal+background). Όπως έχει ήδη αναφερθεί ο γεννήτορας που παρήγαγε τα δεδομένα του υποβάθρου ήταν ο MadGraph και τα γεγονότα αυτά χρησιμοποιήθηκαν για τη μελέτη της μεθόδου πρόβλεψης υποβάθρου αλλά και τη μελέτη της συστηματικής αβεβαιότητας (systematic uncertainties) που την συνοδεύει. Τα δείγματα προσομοίωσης κανονικοποιήθηκαν με βάση τη φωτεινότητα των πραγματικών δεδομένων και τις συνθήκες της δέσμης εξαιτίας των αλληλεπιδράσεων "pileup".

Η μέθοδος εύρεσης υποβάθρου και κατά συνέπεια ανάδειξης του υποθετικού Υπερσυμμετρικού σήματος βασίζεται στη μεταβλητή JGB η οποία ορίζεται ως:

$$JGB = |\sum \overrightarrow{\mathrm{p_T}, jets}| - |\overrightarrow{\mathrm{p_T}, \gamma}| = |\overrightarrow{\mathrm{E_T^{miss}}} + \overrightarrow{\mathrm{p_T}, \gamma}| - |\overrightarrow{\mathrm{p_T}, \gamma}| \tag{1}$$

Η μεταβλητή JGB θα μπορούσε να παρομοιαστεί με τη $\mathrm{E_T^{miss}}$ με την επιπλέον πληροφορία θετικού ή αρνητικού προσήμου. Γεγονότα με μεγάλες θετικές τιμές JGB αφορούν κατά κύριο λόγο γεγονότα που βρίσκονται στο τέλος της αλυσίδας διάσπασης (decay chain) όπως για παράδειγμα περιπτώσεις Υπερσυμμετρίας. Τα φωτόνια που δημιουργούνται πιο κοντά στο primary vertex βρίσκονται σε κινηματική ισορροπία με τους πίδακες αδρονίων και επομένως τελικές καταστάσεις (φωτονίων και πιδάκων) με μικρό decay chain τείνουν να έχουν τιμές JGB κοντά στο μηδέν. Το υπόβαθρο που αντιστοιχεί στην περίπτωσή μας, μπορεί να ταξινομηθεί σε συμμετρικό και ασύμμετρο (ως προς τη JGB).

- Συμμετρικό υπόβαθρο: Το υπόβαθρο αυτό αφορά διεργασίες με φαινομενική E_T^{miss} (εξαιτίας της διακριτικής ικανότητας του ανιχνευτή - jet energy scale). Οι διεργασίες αυτές έχουν συμμετρική κατανομή JGB κι έτσι η περιοχή JGB < 0 δίνει με πολύ καλή προσέγγιση το υπόβαθρο που προβλέπεται στην περιοχή JGB > 0. Αυτού του είδους οι διεργασίες αποτελούν το μεγαλύτερο ποσοστό του συνολικού υποβάθρου.

- Ασύμμετρο υπόβαθρο: Στην κατηγορία αυτή συγκαταλέγονται διεργασίες του ΚΠ με πραγματική E_T^{miss} και ασύμμετρη κατανομή JGB, όπως για παράδειγμα W+jets και $t\bar{t}$ οι οποίες τείνουν να έχουν περισσότερα γεγονότα στην θετική ουρά. Η συνεισφορά του υποβάθρου στην περιοχή με μεγάλες τιμές JGB (περιοχή σήματος-signal region) υπολογίζεται χρησιμοποιώντας μια μέθοδο βασισμένη σε αληθινά δεδομένα (data-driven) και η οποία χρησιμοποιεί γεγονότα με τελικές καταστάσεις ηλεκτρονίων, πιδάκων και ελλείπουσας ενέργειας. Στηρίζεται στο ρυθμό λαθεμένης αναγνώρισης ηλεκτρονίων ως φωτονίων ($f_{e\rightarrow\gamma}$) ο οποίος για ηλεκτρόνια (περιορισμένα στο ECAL barrel) με $p_T > 80\ GeV$ είναι $\sim 0.006\pm0.0025$, όπου η αβεβαιότητα οφείλεται κατά κύριο λόγο στη στατιστική. Όπως φαίνεται και στις δημοσιεύσεις [89, 92] υπάρχει καλή συμφωνία μεταξύ δεδομένων και MC ως προς το $f_{e\rightarrow\gamma}$. Για τα γεγονότα αυτά υπολογίζεται η κατανομή JGB και η διαφορά μεταξύ του πληθυσμού της αρνητικής από της θετικής τιμής JGB δίνει την επιπλέον συνεισφορά στο υπόβαθρο που αντιστοιχεί στο υπό μελέτη κανάλι.

Από την άλλη πλευρά, σε περίπτωση Υπερσυμμετρικών διεργασιών, η περιοχή JGB >0 έχει πολύ μεγαλύτερο πληθυσμό από την περιοχή JGB <0. Αυτό επιβεβαιώνεται από την προσομοίωση MC για το υπόβαθρο και διάφορα υποθετικά σήματα όπως φαίνεται και στο Σχήμα 6.

Σε γεγονότα με ένα μόνο πίδακα, το σχήμα της κατανομής JGB αντιπροσωπεύει την απόκριση της ενέργειας του πίδακα (jet energy response) ως προς το p_T φάσμα του φωτονίου. Γεγονότα με υπερεκτιμημένη ενέργεια πίδακα εγκαθίστανται στην περιοχή JGB >0, ενώ γεγονότα με υποτιμημένη ενέργεια πίδακα εγκαθίστανται στην περιοχή JGB <0. Το σχήμα της κατανομής JGB σε γεγονότα με πολλούς πίδακες αποτελεί τη συνέλιξη της ενέργειας των πιδάκων και του φωτονίου και σε αυτή την περίπτωση δεν είναι απαραίτητο ότι γεγονότα με υποτιμημένους πίδακες θα βρίσκονται στην περιοχή JGB <0 κι αυτό εξαιτίας του διανυσματικού αθροίσματος της ορμής των πιδάκων.

Συνοψίζοντας, η μεταβλητή JGB έχει διτή συνεισφορά. Καταρχάς μπορεί να χρησιμοποιηθεί σαν μια απλή μεταβλητή όπως η E_T^{miss} ως προς την απόρριψη του υποβάθρου. Θυσιάζοντας 30% του σήματος μειώνουμε 50% το υπόβαθρο. Κατά δεύτερον η μέθοδος JGB παρέχει μια καλή προσέγγιση του συνολικού υποβάθρου που αναμένεται στην περιοχή JGB >0, χωρίς να βασίζεται σε προσομοίωση MC. Για το σκοπό αυτό, όπως προαναφέρεται, υπολογίζουμε ξεχωριστά

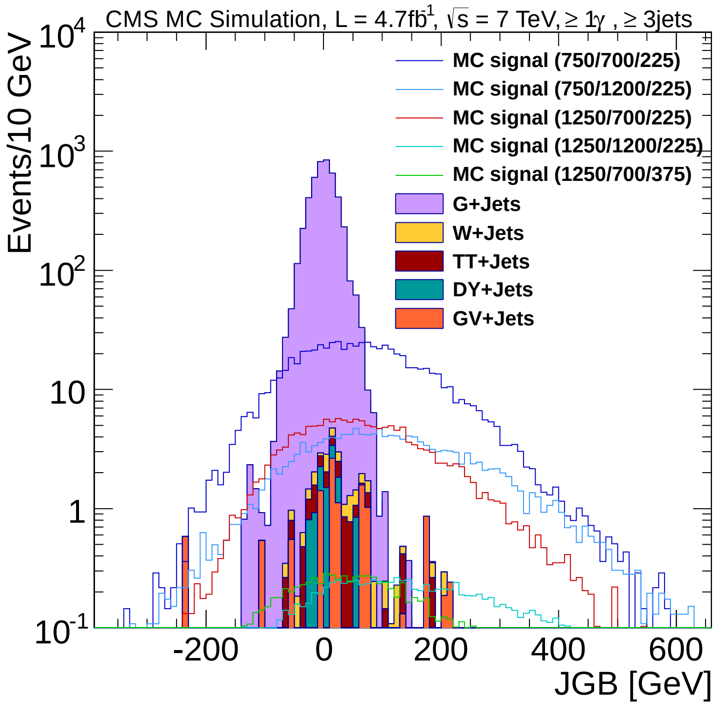

Σχήμα 6: Η κατανομή JGB χρησιμοποιώντας δεδομένα προσομοίωσης για πέντε διαφορετικά σήματα ((m$_{squark}$/m$_{gluino}$/m$_{neutralino}$) και τα πιο σημαντικά υπόβαθρα που προβλέπει το ΚΠ ($\geq 1\gamma, \geq 3jets$).

τη συνεισφορά του συμμετρικού και του ασύμμετρου υποβάθρου. Για τη συνεισφορά του συμμετρικού, βρίσκουμε την ανεστραμένη κατανομή JGB <0 για τα γεγονότα με τουλάχιστον ένα φωτόνιο. Έπειτα προσθέτουμε στο αποτέλεσμα αυτό, τη συνεισφορά του ασύμμετρου υποβάθρου, η οποία υπολογίζεται με χρήση των δεδομένων με τουλάχιστον ένα ηλεκτρόνιο. Συγκεκριμένα αφού κανονικοποιήσουμε την κατανομή JGB με βάση το f$_{e\to\gamma}$, αφαιρούμε την ανεστραμένη JGB <0 από τη JGB >0 κι έτσι έχουμε την συνεισφορά του ασύμμετρου υποβάθρου.

Η σύγκριση μεταξύ προβλεπόμενων και παρατηρηθέντων JGB κατανομών απεικονίζεται στο Σχήμα 7, όπου και αποδεικνύεται η πολύ καλή συμφωνία μεταξύ του προβλεπόμενου υποβάθρου και των τιμών που πράγματι παρατηρούνται από τα προσομοιωμένα γεγονότα. Μικρές διακυμάνσεις οφείλονται στη συστηματική αβεβαιότητα η οποία για μεγάλες τιμές της JGB μπορεί να φτάνει μέχρι και 40% με βάση τα δείγματα MC (τα οποία και αναλύονται με ακριβώς τον ίδιο τρόπο όπως και τα αληθινά γεγονότα). Οι διαμερίσεις που έχουν χρησιμοποιηθεί έχουν επιλεγεί με γνώμονα την ακρίβεια μέτρησης των πιδάκων αδρονίων (jet resolution) η οποία στην περιοχή του βαρελιού και των endcaps είναι:

$$\left(\frac{\sigma}{E}\right)^2 = \left(\frac{90\%}{\sqrt{E}}\right)^2 + (4.5\%)^2$$

.

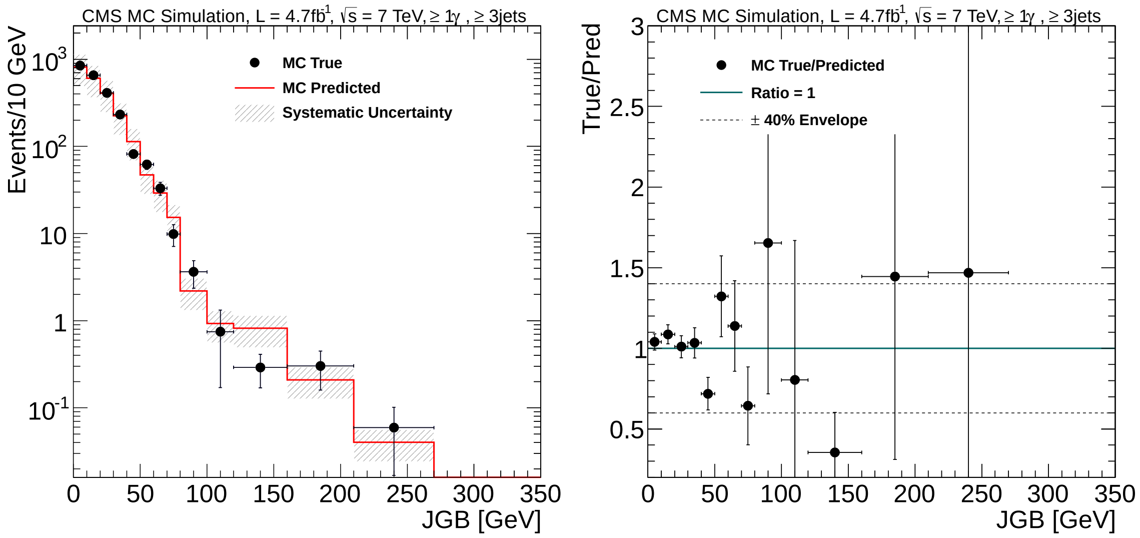

Σχήμα 7: Μελέτη αποδοτικότητας της μεθόδου με χρήση δεδομένων προσομοίωσης (MC closure test), για την περίπτωση ύπαρξης υποβάθρου με βάση το ΚΠ (SM background only hypothesis) ($\geq 1\gamma, \geq 3jets$). Σύγκριση μεταξύ των προβλεπόμενων και παρατηρούμενων JGB κατανομών (αριστερά) και ο λόγος των παρατηρούμενων τιμών προς τις προβλεπόμενες (δεξιά).

Το ίδιο τεστ επαναλαμβάνεται χρησιμοποιώντας ένα μίγμα υποβάθρου και Υπερσυμμετρικού σήματος (m_{squark}:750 GeV / m_{gluino}:700 GeV / $m_{neutralino}$:225 GeV, cross section: 0.3844 pb). Με αυτόν τον τρόπο προσδοκάται η απόδειξη ότι η μέθοδος JGB δύναται να αναδείξει την ύπαρξη ενός υποτιθέμενου σήματος και δεν θα το αφήσει να αποκρυφθεί από το γεγονός ότι η περιοχή που χρησιμοποιείται για την πρόβλεψη του υποβάθρου (JGB < 0, control region) θα έχει νοθευτεί με σήμα. Τα ακόλουθα διαγράμματα δείχνουν εμφανώς την ύπαρξη σήματος το οποίο αναδεικνύεται (ύπαρξη γεγονότων πάνω από το προβλεπόμενο υπόβαθρο) και ως εκ τούτου αποδεικνύεται ποιοτικά η ευαισθησία της μεθόδου (Σχήμα 8).

Ανάλυση

Η ίδια ακριβώς διαδικασία ακολουθείται και στα δεδομένα που συγκεντρώθηκαν από τον ανιχνευτή CMS. Το Σχήμα 9 δείχνει την εφαρμογή της μεθόδου JGB στα δεδομένα. Σε γενικές γραμμές παρατηρείται καλή συμφωνία μεταξύ παρατήρησης και πρόβλεψης. Το αριστερό σχεδιάγραμμα δείχνει τη σύγκριση μεταξύ του αριθμού των γεγονότων που παρατηρούνται (observed) και της πρόβλεψης του υποβάθρου στην περιοχή JGB > 0, ενώ στο διάγραμμα στα δεξιά απεικονίζεται ο λόγος μεταξύ των γεγονότων που παρατηρούνται και αυτών που προβλέπονται.

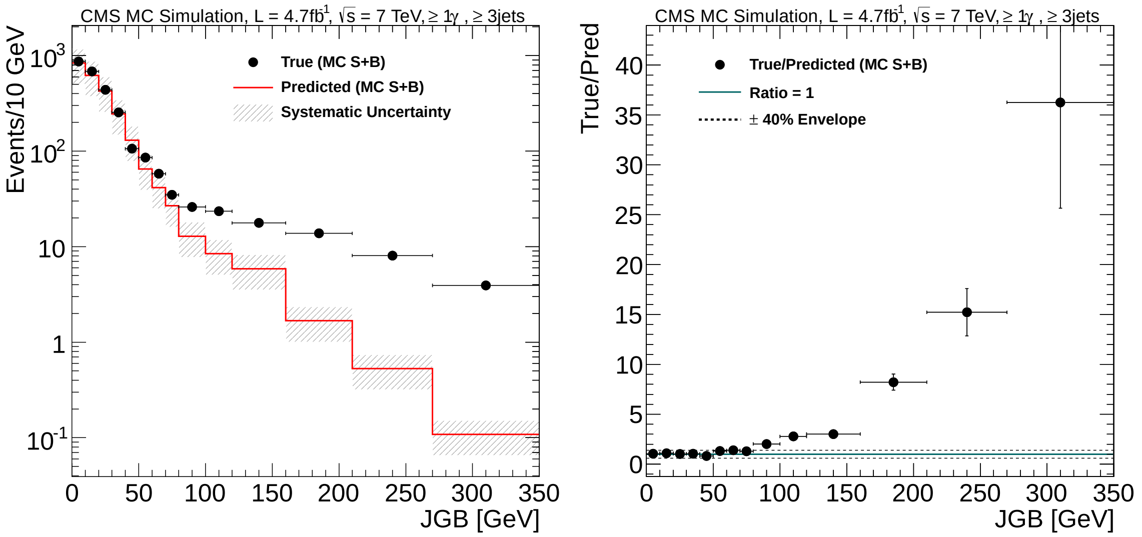

Σχήμα 8: Η κατανομή JGB για την υπόθεση υποβάθρου+σήματος (MC backgrounds + signal) (αριστερά) και ο λόγος μεταξύ των παρατηρηθέντων τιμών και των αντίστοιχων όπως προβλέπονται από τη μέθοδο JGB (δεξιά) $(\geq 1\gamma, \geq 3jets)$.

Ο ακόλουθος πίνακας περιέχει τον αριθμό των γεγονότων για τα πειραματικά δεδομένα και την πρόβλεψη του υποβάθρου (ξεχωριστά και συγκεντρωτικά) για τρεις διαφορετικές περιοχές σήματος που αντιστοιχούν σε φωτεινότητα 4.7 fb^{-1}.

Πίνακας 6: Συνολικός αριθμός των δεδομένων που παρατηρούνται και η αντίστοιχη πρόβλεψη του υποβάθρου, σε διαμερίσεις της JGB

4.7 fb^{-1}	**80-100 GeV**			**100-120 GeV**			**>120 GeV**		
$\geq 1\gamma, \geq$ 3jets		**stat.**	**sys.**		**stat.**	**sys.**		**stat.**	**sys.**
Πρόβλεψη ΚΠ (JGB<0)	9	$^{+4.1}_{-2.9}$	±3.6	5	$^{+3.4}_{-2.2}$	±2.0	3	$^{+2.9}_{-1.6}$	±1.2
Πρόβλεψη ΚΠ ($f_{e\to\gamma}$)	0.3	±0.04	±0.1	0.3	±0.04	±0.1	0.9	±0.07	±0.4
Συνολική πρόβλεψη	9.3	$^{+4.1}_{-2.9}$	±3.6	5.3	$^{+3.4}_{-2.2}$	±2.0	3.9	$^{+2.9}_{-1.6}$	±1.3
Δεδομένα	16			8			8		

Η συστηματική αβεβαιότητα που αντιστοιχεί στη συνεισφορά του υποβάθρου είναι ±40% και έχει υπολογιστεί συγκρίνοντας τον αριθμό των παρατηρηθέντων και των προβλεπόμενων γεγονότων στις περιοχές σήματος, χρησιμοποιώντας το MC closure test. Λαμβάνοντας υπόψην τα σφάλματα, τα πειραματικά δεδομένα βρίσκονται σε ικανοποιητική συμφωνία με την πρόβλεψη σύμφωνα με το Καθιερωμένο Πρότυπο και ως εκ τούτου επόμενο βήμα ήταν ο προσδιορισμός των σχετικών ορίων.

Οι συστηματικές αβεβαιότητες που λήφθηκαν υπόψην στον υπολογισμό των ορίων (experimental error band) συνοψίζονται στον ακόλουθο πίνακα. Η συ-

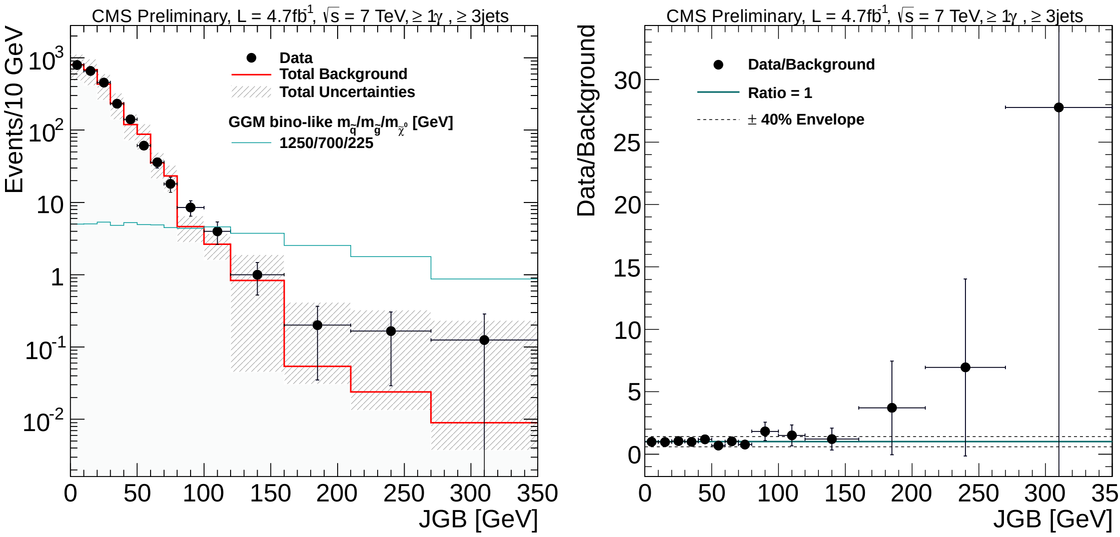

Σχήμα 9: Η κατανομή JGB για τα δεδομένα του πειράματος ($\geq 1\gamma, \geq 3jets$). Σύγκριση μεταξύ πρόβλεψης και παρατήρησης (αριστερά) και ο σχετικός τους λόγος (δεξιά).

στηματική αβεβαιότητα που αντιστοιχεί στη φωτεινότητα είναι 2.2% [84] ενώ η αντίστοιχη αβεβαιότητα στην κλίμακα της ενέργειας των πιδάκων (Jet energy scale) είναι 2%. Πιθανές διαφορές στην αποδοτικότητα με την οποία αναγνωρίζεται ένα φωτόνιο (photon identification efficiency) μεταξύ των πραγματικών δεδομένων και των δεδομένων προσομοίωσης λαμβάνονται υπόψιν. Ο αριθμός των γεγονότων που αντιστοιχεί στη συγκεκριμένη γεωμετρική αποδοχή κανονικοποιείται με βάση το λόγο της αποδοτικότητας εύρεσης φωτονίων μεταξύ πραγματικών και προσομοιωμένων δεδομένων. Αυτό επιτυγχάνεται κάνοντας χρήση των ηλεκτρονίων $Z \to ee$ που ικανοποιούν τα κριτήρια αναγνώρισης που έχουν τεθεί [74].

Ανάμεσα στις θεωρητικές αβεβαιότητες συγκαταλέγονται οι αβεβαιότητες της ενεργούς διατομής και των PDF. Η τελευταία ποικίλει μεταξύ 0.03% και 78% ανάλογα με τις μάζες των Υπερσυμμετρικών σημάτων (αυξάνεται με την ταυτόχρονη αύξηση των μαζών των gluino και squark).

Προχωράμε στον υπολογισμό των ανώτατων ορίων για τα Υπερσυμμετρικά σημεία GGM για τα bino και wino-like neutralinos. Η ερμηνεία των αποτελεσμάτων γίνεται στο φασικό χώρο μαζών των gluino-squark (και οι δύο μάζες παίρνουν τιμές μεταξύ 400-2000 GeV με βήμα 80 GeV) για δεδομένη μάζα neutralino (375 GeV). Επιπλέον στην περίπτωση bino-like neutralinos, παρατίθεται ερμηνεία και στο φασικό χώρο μαζών gluino-neutralino. Σε αυτήν την περίπτωση η μάζα του gluino έχει τιμές μεταξύ 160-2000 GeV (με βήμα 80 GeV), ενώ η μάζα του neutralino βρίσκεται μεταξύ 150-1050 GeV (βήμα 100 GeV), με δεδομένη μάζα squark (2500 GeV).

Πίνακας 7: Σύνοψη των συστηματικών αβεβαιοτήτων

Πηγή	**Αβεβαιότητα στην ενεργό διατομή**		
Luminosity	2.2%		
Jet energy scale	2%		
Photon efficiency	4%		
Acceptance PDF uncertainty	0.03 - 78%		
	Αβεβαιότητα ως προς το υπόβαθρο		
	80-100 GeV	100-120 GeV	> 120 GeV
JGB uncertainty	39%	38%	32%
$f_{e \to \gamma}$	1%	2%	10%

Ένα σημείο (signal point) απορρίπτεται όταν η αναμενόμενη ενεργός διατομή υπερβαίνει το ανώτατο όριο. Προκειμένου να επιτευχθεί καλή ευαισθησία σήματος (good signal sensitivity), τα όρια υπολογίζονται για τρεις διαφορετικές διαμερίσεις (bins) σε GeV: [80,100), [100,120), [120,inf). Στη συνέχεια συνδυάζονται τα αποτελέσματα που προκύπτουν από αυτή τη διαμέριση λαμβάνοντας υπόψην τη σημαντικότητα (significance) της κάθε διαμέρισης και τα αντίστοιχα συστηματικά. Αν και η ευαισθησία (sensitivity) προέρχεται κατά κύριο λόγο από τα γεγονότα της πιο μεγάλης διαμέρισης του JGB, μερικές περιοχές του πιθανού σήματος ίσως να εποφελούνται από άλλες διαμερίσεις και ως εκ τούτου από τον συνδυασμό των διαμερίσεων.

Τα όρια υπολογίζονται με βάση τη σύγκριση μεταξύ αναμενόμενης και παρατηρούμενης ενεργού διατομής (95% CL upper limits). Στο Σχήμα 10 και Σχήμα 8.4 απεικονίζονται τα σχετικά όρια για την περίπτωση wino και bino-like neutralino. Το αναμενόμενο όριο που υπολογίζεται με τη μέθοδο isolation-sideband που περιγράφεται στις δημοδιεύσεις [72, 74] είναι επίσης σχεδιασμένο στο ίδιο σύστημα αξόνων (πράσινη διακεκομμένη γραμμή, SUS-12-001). Η μπάντα που αντιστοιχεί στα πειραματικά σφάλματα (experimental error band) αναπαριστάται γύρω από το αναμενόμενο όριο, και αντιστοιχεί στις πειραματικές αβεβαιότητες που αναφέρονται στον Πίνακα 7), ενώ η μπάντα των θεωρητικών σφαλμάτων (theoretical error band) αντιπροσωπεύει την αβεβαιότητα στην NLO ενεργό διατομή. Τα όρια που προκύπτουν (95% CL limits) από αυτά τα διαγράμματα για το σενάριο bino και wino-like neutralino (με δεδομένη μάζα neutralino) συνοψίζονται παρακάτω.

- Για το bino-like σενάριο με δεδομένη μάζα neutralino στα 375 GeV, μπορούν να αποκλειστούν οι μάζες squark μέχρι ~ 900 GeV και μάζες gluino μέχρι ~ 920 GeV.
- Για το σενάριο wino-like με μάζα neutralino στα 375 GeV, αποκλείονται οι μάζες squark μέχρι ~ 870 GeV και οι μάζες gluino μέχρι ~ 770 GeV.

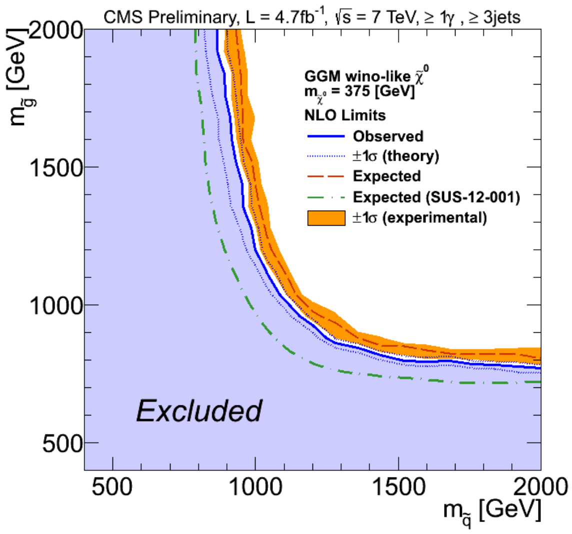

Σχήμα 10: Υπολογισμένα όρια (95% CL) για την περίπτωση wino- (αριστερά) και bino-like (δεξιά) neutralino στο σύστημα αξόνων μάζας squark-gluino.

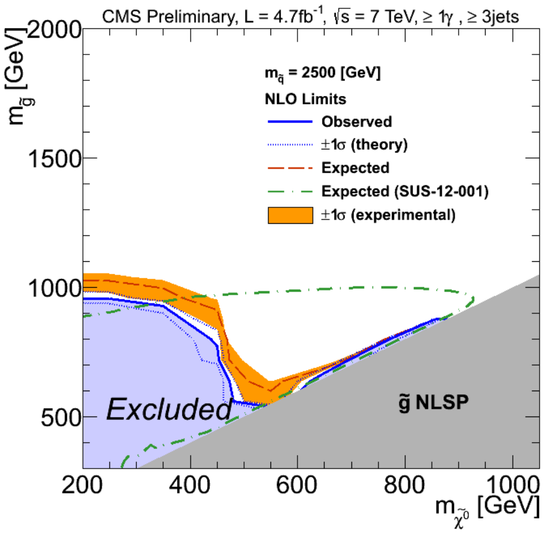

Σχήμα 11: Υπολογισμένα όρια (95% CL) για την περίπτωση bino-like neutralino στο σύστημα αξόνων μάζας neutralino-gluino.

Abstract

The Standard Model (SM) of particle physics has emerged through tremendous successes of experimental and theoretical physics to describe the complexity around us with fundamental particles and interactions. It has been precise in its predictions, as many particles were discovered after they were predicted by the SM. It still remains the most complete model that gives us an understanding of our universe, even though it is far from being a complete theory. SM is based on gauge symmetry with a problem still remaining to solve: “Why the elementary particles carry mass?”. The gauge group theory on which SM is based forbids masses for all particles. The Higgs mechanism was introduced in the SM to provide masses to the Vector Bosons (W, Z) and the whole spectrum of the elementary particles as part of their interaction while keeping the photon massless. Although it is a very elegant theory, the Higgs particle has not yet been confirmed with the past and current high energy physics experiments and it remains as the most exciting motivation of the LHC collider experiments. Nevertheless, recent results of the LHC experiments, point to the observation of a boson likely to be the Higgs. Even if the Higgs particle is found, SM is believed to be only a fraction of the big picture. There are strong indications of new symmetries, new particles and new theories that try to unify fundamental laws including gravity, and all need to have experimental observations from the new generation collider experiments. It falls short of being a complete theory of fundamental interactions because it incorporate the physics of only 4% of the universe leaving aside the dark matter and the dark energy while in addition gravity remains outside this framework. The theory does not contain any viable dark matter particle that possesses all of the required properties deduced from observational cosmology. It also does not correctly account for neutrino oscillations (and their non-zero masses). Although the Standard Model is believed to be theoretically self-consistent, it has several apparently unnatural properties giving rise to puzzles like the strong CP problem and the hierarchy problem.

Nevertheless, the SM is important to theoretical and experimental particle physicists alike. For theorists, it is used as a basis for building more exotic models that incorporate hypothetical particles, extra dimensions, and elaborate symmetries (such as supersymmetry) in an attempt to explain experimental

results at variance with the Standard Model, such as the existence of dark matter and neutrino oscillations. On the other hand, experimenters have incorporated the Standard Model into simulators to help search for new physics beyond the Standard Model.

The Large Hadron Collider (LHC) was built at the European Organization for Nuclear Search (CERN) in Geneva, in order to access the energy at which the more fundamental theory can be revealed. The results from past experiments and new theoretical predictions imply the new generation of colliders. To probe the energy scales of possible new physics one has to build accelerators with high energies and high luminosities to collide particles harder and collect as much as possible events of the interesting process. Although the experience to measure mass values, jets and missing energy from the past experiments is very useful, there are challenges that new collider projects has to be aware of. The collision rate in LHC is very high and in the collision environment there are more secondary particles to deal with from each collision. These facts require more sophisticated selection devices and algorithms and fast processing (data acquisition). The LHC project with its detectors, is being built to fulfil these requirements. One of the two multi purpose detectors at the LHC is the Compact Muon Solenoid (CMS) and this thesis is based on the analysis of the data taken from this experiment. The most favored extension to the SM is supersymmetry (SUSY). It doubles the number of particles by predicting a supersymmetric partner to all SM particles, but can solve many problems of the SM in an elegant way. There are different possibilities in which SUSY can be realized. This thesis presents an analysis to find supersymmetry, which is based on general concepts of General Gauge-Mediation (GGM) SUSY scenarios for the symmetry breaking, in the photon(s)+jets+missing transverse energy (E_T^{miss}) final state produced by events in 7 TeV pp interactions. This is an experimentally well accessible channel since photons can be identified with high efficiency and purity at the collider experiments. Additionally, in SUSY scenarios, we expect events with missing transverse energy, thus largely suppressing the Standard Model backgrounds.

In Chapter 1 there's an introduction to SM and SUSY, followed by a brief overview of the LHC and the CMS experiment (Chapter 2) with a special reference on the trigger system and more specifically on the global trigger processor emulator; an apparatus designed, developed and tested at N.C.S.R. Demokritos. In Chapter 3 there's a summary of the gaseous detectors history and principles with emphasis on the micromegas detector along with its possible use in the upgrade of LHC. Afterwards (Chapter 4) there are details about the event simulation used for validity tests of the novel method described here, to establish the presence of the signal over background. Chapter 5 has a presentation of the objects definition and the relevant event selection while in Chapter 6 there is a presentation of the background estimation method along with tests of the method's validity using simulated events (Monte Carlo closure tests), followed by the relevant results of the method's application on the data collected by the CMS detector (7). The thesis will finish with a synopsis including conclusions and outlook. Additionally in the Appendixes can be found comparison plots between data and MC (Appendix A), event displays from the most interesting events in Appendix B, along with a short review of the filters used for the analysis procedure (Appendix C), and lastly a description of our study on the energy recovery of the Dead Channels of the Electromagnetic Calorimeter in CMS (Appendix D).

Contents

List of Figures

List of Tables

Chapter 1

Theoretical overview

> *By convention there is color, by convention sweetness, by convention bitterness. But in reality nothing exists except atoms and empty space; everything else is opinion.*
>
> -Democritus-

Particle physics, at its heart, concerns itself with two very fundamental questions: What are the ultimate building blocks of matter? And how do these fundamental constituents interact? It began as what might generously be described as a philosophical tradition studied by ancient Greek philosophers such as Leucippus, Democritus, and Epicurus; and early modern European physicists such as John Dalton, Robert Boyle, and Isaac Newton. Democritus first suggested the existence of the atom but it took almost two millennia before the atom was placed on a solid foothold as a fundamental chemical object by John Dalton. Through his work on stoichiometry, he concluded that each element of nature was composed of a single, unique type of particle. Dalton and his contemporaries believed these were the fundamental particles of nature and thus named them atoms, after the Greek word atomos, meaning "indivisible". However, near the end of the century, physicists discovered that atoms are not, in fact, the fundamental particles of nature, but conglomerates of even smaller particles. Quantum field theory (for example [3]) is the language of particle physics. All particles are represented by excitations in a quantized field, and their interactions are mediated by other, force-carrying particles. According to current knowledge, field theories have been very successful at describing three of the four known fundamental forces: electromagnetism, the weak interaction, and the strong interaction, with gravity being the only holdout. These theories are collectively referred to as the Standard Model (SM). In fact, all three of these forces are described by a particular type of quantum field theory, known as gauge theories due to their symmetry under gauge transformations. In each case, the force between particles is caused by the exchange of force carriers called gauge bosons.

In electromagnetism, the force carrier is the photon (γ). The weak force is carried by two vector bosons, the $W^{\pm}$ and the Z^0 , and the strong force is carried by the gluons (g).

1.1 The Standard Model of Particle Physics

1.1.1 Historical approach

Elementary particle physics was born in 1897, with the discovery of the electron by J.J. Thomson's. He imagined a *plum pudding model* where the atom is composed of electrons that are suspended in a heavy, positively charged paste, like the plumps in a pudding. His model was repudiated by Rutherford's famous scattering experiment in 1909, which showed the positive charge and most of the mass, was concentrated in a tiny core, known as the nucleus, at the center of the atom. The nucleus of the lightest atom, the hydrogen, was given the name *proton*, by Rutherford. Five years later, Niels Bohr proposed a model of hydrogen consisting of a single electron circling the proton, held in orbit by the mutual attraction of opposite charges. This model appeared to be one step toward the right direction (e.g. calculation of hydrogen's spectrum in agreement with experiment). The proton's discovery by Rutheroford (1919) and neutron's discovery by Chadwick (1932), put the final touch on the *classical period* in elementary particle physics. The *middle period* (1930-1960) in particle physics, was dominated by Yukawa's meson (the π), Dirac's positron and Pauli's neutrino.

These discoveries were naturally followed by the question of what holds the nucleus in place as it contains several tightly-packed positive charged protons. Yukawa assumed the existence of a force field binding the particles together, and a mediator particle being the carrier of that force. The existence of the pion as well as the muon, was revealed by Cosmic ray experiments.

In 1964, Gell-Mann and Zweig independently proposed that all hadrons are composed of even more elementary constituents, called quarks. The quarks come in three types (flavors); up, down and strange (u, d, s). To each quark (q) corresponds an aniquark ($\bar{q}$), with the opposite charge and strangeness. According to the quark model, every baryon is composed of three quarks (likewise every antibaryon is composed of three antiquarks), while every meson is composed of a quark and an antiquark. All baryon and meson combinations are known as hadrons. However, there were two theoretical objections to the quark model, the experimental absence of free quarks and the incosistency with the Pauli exclusion principle (Δ^{++}(uuu)). The same year (1964), O. W. Greenberg proposed a way to overcome this problem. His suggestion was that quarks not only come in three flavors but also in three colors (red, green and blue). The particles responsible for keeping the quarks together inside baryons and mesons were called *gluons*.

Curiously, what gave the model more credibility, was not the discovery of free quarks, or an explanation of quark confinement, or the confirmation of the color hypothesis, but the discovery of the J/ψ meson (1974) representing a bound state of a new quark, the charm (c) and its antiquark ($\bar{c}$). One year later (1975), a new lepton (the tau, τ) was discovered, spoiling Glashow's symmetry, which was restored two years later, with the discovery of a new heavy meson (the upsilon, Υ) - recognised as the carrier of the beauty (or bottom) quark (b): $\Upsilon = b\bar{b}$.

As it was mentioned before, in the 1930s, physicists were led to assume the existence of one more particle, the neutrino, because of the inconsistencies with the energy and momentum conservation in beta decay experiments. In 1942 Wang Ganchang first proposed the use of beta-capture to experimentally detect neutrinos. In 1956, Clyde Cowan, Frederick Reines, F. B. Harrison, H. W. Kruse, and A. D. McGuire published confirmation that they had detected the neutrino, a result that was rewarded almost forty years later with the 1995 Nobel Prize. In this experiment, now known as the Cowan–Reines neutrino experiment, antineutrinos created in a nuclear reactor by beta decay reacted with protons producing neutrons and positrons. The actual beta decay mechanism was explained by the assumption that this weak interaction was mediated by the exchange of some particle. The mediator came to be known as *intermediate vector boson*. The challenge for the experimentalists was to produce one intermediate vector boson, and for the theorists to predict its properties. In 1968, the theoretical framework predicting these intermediate vector bosons was introduced by Sheldon Glashow, Abdus Salam and Steven Weinberg (GSW) who provided a unified description of the electromagnetic and weak forces. Experimentally, the existence of the electroweak interactions was verified in two stages, both of them at CERN. The discovery of neutral currents in neutrino scattering, in the Gargamelle bubble chamber (1973), and lastly the discovery of the W and the Z gauge bosons in proton-antiproton collisions at the Super Proton Synchrotron accelerator by Carlo's Rubia group (1983).

1.1.2 Standard Model - description

The SM of particle physics describes almost all fundamental particles and interactions. It can be divided into three parts: The first part is composed by the fundamental matter particles, which are fermions with spin-1/2 and can be distinguished into two types: quarks (Table 1.1) and leptons (Table 1.2) and arranged in three generations of increasing mass. The particles of higher generations decay via weak interactions to particles of the first generation. This explains why everyday matter comprises only of first generation particles. There are also six flavors of quarks known at present: the up (u), charm (c), top (t) quarks carry a +2/3 electric charge, the down (d), strange (s), bottom (b) quarks carry a -1/3 charge. Futhermore there are six flavors of leptons, the electron (e), muon (μ) and tau (τ) leptons which carry a +1 electric charge, each accompanied by their neutrino. In the framework of the Standard Model, neutrinos have zero charge and were initially believed to be massless. However, recent observations from neutrino flavor oscillation experiments [1], implying small neutrino masses, might give rise to changes. Each one of the twelve particles is also accompanied by their antiparticle carrying opposite charges.

Table 1.1: Quarks overview

	Quarks	
First generation	up (u)	down (d)
Second generation	charm (c)	strange (s)
Third generation	top (t)	bottom (b)

Table 1.2: Leptons overview

	Leptons	
First generation	electron (e)	electron neutrino (ν_e)
Second generation	muon (μ)	muon neutrino (ν_μ)
Third generation	tau (τ)	tau neutrino (ν_τ)

Table 1.3: Fundamental interactions overview

Interaction	**Strength**	**Theory**	**Mediator boson**	**Charge**
Strong	1	Chromodynamics	8 colored gluons	0
Electromagnetic	10^{-2}	Electrodynamics	γ	0
Weak	10^{-7}	Flavordynamics	W^+ W^- Z	+1 -1 0
Gravitational	10^{-39}	Genaral Relativity	Graviton	0

The second part contains the carriers of the fundamental forces (Table 1.3, [4]), which are spin-1 bosons. These forces work over different ranges and have different strenghts. In order of decreasing force strength the relevant carriers are: the gluons for the strong force, the photon for the electromagnetic, the two W's and the Z for the weak force and the postulated graviton for gravity. The SM includes the electromagnetic, strong and weak forces and all their carrier particles and gives an extremely good explanation about the way these forces act on all the matter particles. However, gravity, the most familiar force in our everyday life, is not part of the SM. Until now, the quantum theory used to describe the micro world and the general theory of relativity used to describe the macro world, are

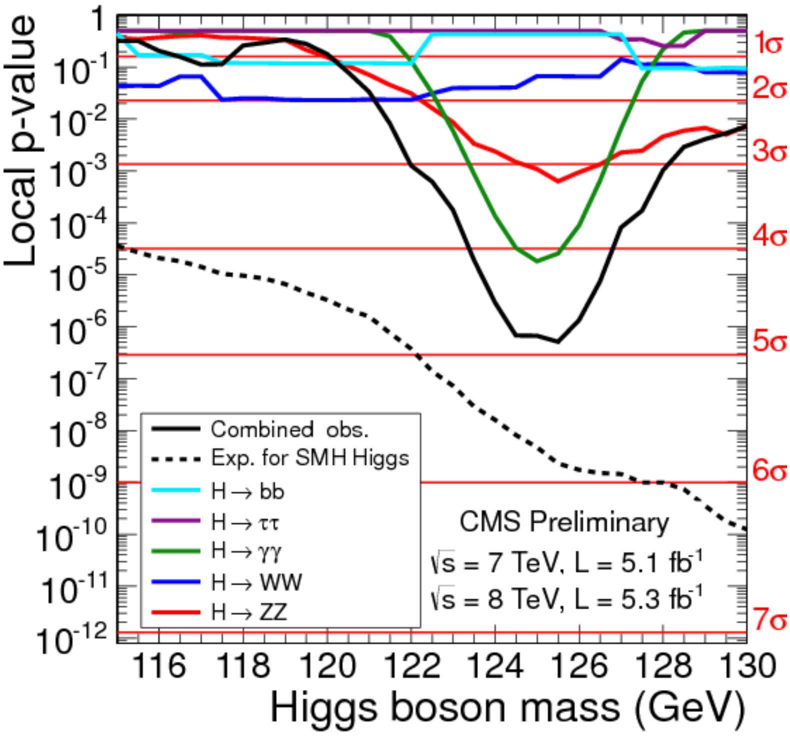

Figure 1.1: The observed probability (local p-value) that the background-only hypothesis would yield the same or more events as are seen in the CMS data, as a function of the SM Higgs boson mass for the five channels considered. The solid black line shows the combined local p-value for all channels.

not mathematically compatible in the context of the SM. But luckily enough, the effects of gravity in particle physics experiments is so weak as to be negligible. Only in cases of matter in bulk, the gravity is observed to dominate. Despite its reluctant exclusion of one of the fundamental forces, the SM still works well.

Lastly comes the Higgs mechanism -introduced by Englert and Brout (1964), and Higgs (1964)- which allows particles to gather mass depending on each particle's interaction with the Higgs field. The masses are determined by the strength of their couplings to the Higgs field. It predicts a spin-0 Higgs boson that has not yet been observed, but recent results of the LHC experiments, point to the observation of a boson likely to be the Higgs [7, 8]. Figure 1.1 shows the observed probability (local p-value) that the background-only hypothesis would yield the same or more events (collected by the CMS detector), as a function of the SM Higgs boson mass for the five considered channels (H→bb, H→ $\tau\tau$, H→ $\gamma\gamma$, H→WW and H→ZZ). An excess near 125 GeV is clearly visible.

The Higgs boson is a consequence of electroweak symmetry breaking that is believed to be responsible for generating the masses of the $W^{\pm}$ and Z^0 bosons from their couplings to this field, whereas the corresponding carriers of the

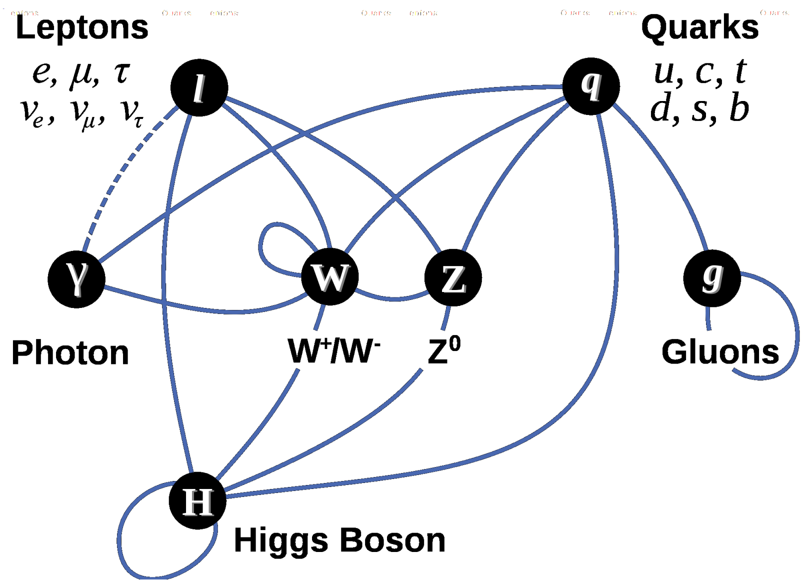

Figure 1.2: Summary of interactions between particles described in SM.

electromagnetic force (photons) remain massless since they have no couplings to the Higgs field.

Particle Physics studies the elementary particles that constitute matter and describes the interactions between them. Figure 1.2, provides a visual overview of the possible interactions between particles in the SM.

Within the -extremely successful experimentally- description of the interactions of the fundamental components of matter known as SM, the existence of the gauge bosons and the form of their interactions are dictated by local gauge invariance. In fact, gauge bosons are a manifestation of the Standard Model's symmetry group,

$$G_{SM} = SU(3)_C \bigotimes SU(2)_L \bigotimes U(1)_Y \tag{1.1}$$

where:

- $SU(3)_C$ is the non-abelian gauge symmetry group which describes the strong interactions. C stands for the color quantum number. Such a structure involves eight independent matrices, which are the generators of the group (3^2−1 parameters, hence eight generators), reflecting the fact that the strong interaction is carried by eight vector bosons, the gluons. The gluons are massless, electrically neutral and carry the charge of strong interactions, known as "color". The strong interactions are well-described by the theory of quantum chromodynamics (QCD).

- $SU(2)_L \bigotimes U(1)_Y$ is the weak isospin symmetry group which describes the electromagnetic and weak interactions together (electroweak interaction). L stands for the left-handed chirality (weak isospin) and Y for the hypercharge.

The mediators of the weak interactions are massive particles and can interact among themselves. $W^{\pm}$ have electrical charges of $Q = \pm 1$ respectively, while Z^0 is electrically neutral (charges are given in units of the elementary charge, e). The photon -mediator of the electromagnetic interactions- is massless, chargeless and does not interact with itself.

The SM can be described by the Langrangian:

$$\mathcal{L}_{SM} = \mathcal{L}_{EW} + \mathcal{L}_{QCD} + \mathcal{L}_{Higgs} + \mathcal{L}_{Yukawa} \tag{1.2}$$

where:

- $\mathcal{L}_{EW}$ and $\mathcal{L}_{QCD}$ describe free fermions, free gauge bosons associated with the $SU(2)_L \bigotimes U(1)_Y$ and $SU(3)_C$ gauge symmetries, along with the interactions between fermions and gauge bosons as well as among gauge bosons.

- $\mathcal{L}_{Higgs}$ describe the Higgs particle and the electroweak symmetry breaking.

- $\mathcal{L}_{Yukawa}$ describes the flavor physics.

1.2 Extensions of the Standard Model

1.2.1 Motivation for Supersymmetry

In the previous section we discussed in brief, the Standard Model. It describes with a very good precision, the behavior of the elementary components of nature, up to distances of $\sim 10^{-18}$ m, but it is also known that it does not give a complete description of the nature. It can not explain the repeating pattern of the three observed generations in matter or questions like why the masses of the particles are what they are. Furthermore it fails to embody a theory of the gravitational interactions. A better understanding of the Universe, often comes when connections between separate entities are found. The theory for the electromagnetic force (developed in 1860s by James Clerk Maxwell) was a major breakthrough. A century later comes an other breakthrough of similar importance; the links between electromagnetism and the weak force (in high energies only). Here comes the question: are there any other connections between the forces? Experiments have already shown that with increasing energies, the effect of the strong force becomes weaker. This is a good indication that the electromagnetic, weak and strong forces could be merged to one single interaction in a incredibly high energy environment; the idea of Grand Unified Theories (GUTs). Supersymmetry (SUSY) is a very popular theory that allows the strong and electroweak forces to unite and become a single interaction at a common energy. It arose from the attempt to describe both matter particles and force carriers using the same mathematics, and it is characterized by one gauge symmetry and therefore one unified coupling constant rather than three independent ones. The convergence of the three constant couplings is illustrated in Figure 1.3.

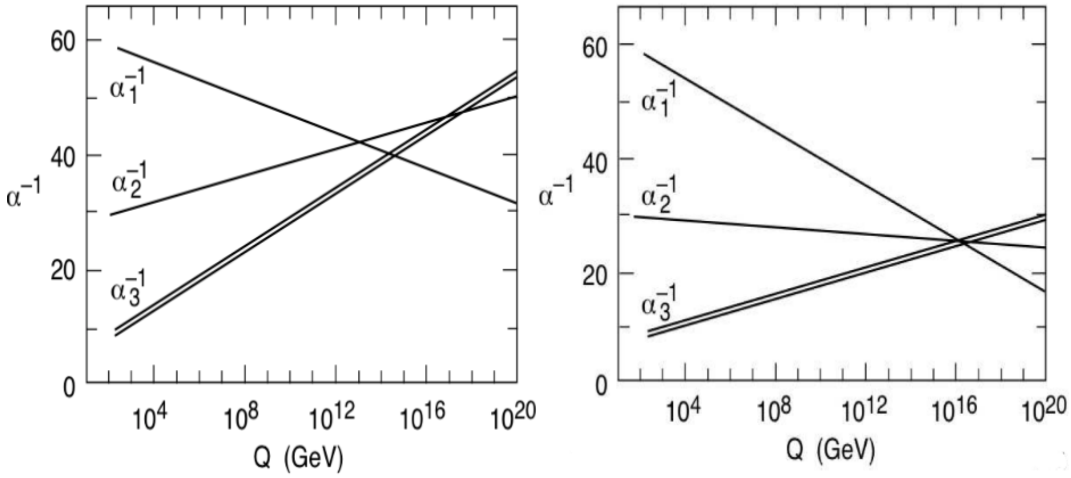

Figure 1.3: Evolution of the gauge couplings to high energy scales without (left) and with (right) the use of the renormalization group equation of the supersymmetric generalization of the SM. The double line for α_3 indicates the experimental error.

Furthermore SUSY helps to explain some of the inconsistencies of the Standard Model such as the infamous "hierarchy problem"; the vast discrepancy between aspects of the weak nuclear force and gravity. For instance, the masses of the W and Z particles, the force carriers of the weak nuclear force, are about $\sim 10^{16}$ times smaller than the reduced Planck scale (M$_{Planck} = 1/\sqrt{8\pi G_{Newton}} \sim 10^{18}$) [5].

Figure 1.4: One-loop quantum corrections to the Higgs boson's squared mass m$_H^2$, due to a Dirac fermion f (left) and a scalar S (right).

The "hierarchy problem" is related to the Higgs mass stability under radiative corrections. The Higgs boson interacts with every particle with mass, and without an incredible fine-tuning of parameters, loop-order quantum effects from these particles would give enormous corrections to the Higgs mass, driving it from the electroweak scale up to the Planck scale. For example in Figure 1.4 (left), the correction to the Higgs squared mass (m_H^2) from a loop containing a Dirac fermion is given by:

$$\Delta m_H^2 = -\frac{|\lambda_f|^2}{8\pi^2}\Lambda_{UV}^2 + ... \tag{1.3}$$

while the relevant correction in case of the scalar S (Figure 1.4 (right)) is:

$$\Delta m_H^2 = \frac{\lambda_S}{16\pi^2}[\Lambda_{UV}^2 - 2m_S^2 ln(\Lambda_{UV}/m_S) + ...] \tag{1.4}$$

where λ_f is the fermion coupling to the Higgs boson and Λ_{UV} is an ultraviolet momentum cutoff used to regulate the loop integral (it should be interpreted as the least energy scale at which new physics enters to alter the high-energy behaviour of the theory. The role of f can be played by each of the leptons and quarks; for quarks eq. 1.3 should be multiplied by 3 to account for color). If Λ_{UV} is of the order of the reduced Planck scale, the correction Δm_H^2 should be several orders of magnitude larger than the expected value for the Higgs mass. Thus several fine tuning of parameters -or in other words cancellations between the various contributions to Δm_H^2- are required in order to adjust the electroweak scale to much smaller than the Planck scale. The systematic cancellation of the "dangerous" contributions can be achieved by symmetries. Comparing eq. 1.3 and eq. 1.4 it naturally comes that a symmetry between fermions and bosons is needed, because of the relative minus sign between fermion and boson loop contributions to Δm_H^2. Assuming $\lambda_S = |\lambda_f|^2$, then the Λ_{UV}^2 contributions will neatly cancel and this is where quantum field's theory success lies; no dependence on the parameter Λ_{UV}^2, but rather on other physical quantities that can be measured. The existence of a boson state corresponding to each fermion state would imply the presence of a symmetry. Supersymmetry is one of the most famous scenarios presenting a solution like this.

The existence of dark matter, which makes up approximately one quarter of the energy density of the universe, is an other theoretical argument that cannot be explained within the Standard Model of particle physics and thus implies the existense of new physics (like Supersymmetry) at the TeV scale.

But here comes the question: why haven't we seen any SUSY particle? A possible answer is that SUSY is a broken symmetry, meaning that sparticles are much heavier and less stable than their counterparts. But in case SUSY particles exist at energy scales compatible with the Large Hadron Collider (LHC) environment, we will be able to produce and study them.

1.2.2 Supersymmetry

As it was already mentioned, supersymmetry -being one of the well developed theories for physics beyond the SM- is a symmetry between matter and force particles (fermions and bosons). Supersymmetry suggests that both could be described by the same system, but only if each has a counterpart of the opposite type; a spin-1/2 partner for force particles and whole unit spin partner for the matter particles. Thus SUSY provides a symmetry between matter and forces, and predicts that for each known particle there is a "supersymmetric" partner (see for example [2]). This means a doubling of every SM particle (Table 1.4). Matter partners are given an "s" (for example the partners of electrons are called "selectrons"), while force partners are given an "ino" (for example "gluino" for the gluon). This was not the first time the number of the known particles was doubled. In the 1930s Paul Dirac doubled it by suggesting an "antiparticle" to each known particle.

Table 1.4: SM and SUSY particles

		SM particles				**SUSY particles**	
	spin	**Name**	**Symbols**		**Name**	**Symbols**	**spin**
Fermions	1/2	leptons	e, ν_e μ, ν_μ τ, ν_τ	**Bosons**	sleptons	$\tilde{e}$, $\tilde{\nu_e}$ $\tilde{\mu}$, $\tilde{\nu_\mu}$ $\tilde{\tau}$, $\tilde{\nu_\tau}$	0
	1/2	quarks	u,d c,s t,b		squarks	$\tilde{u}$, $\tilde{d}$ $\tilde{c}$, $\tilde{s}$ $\tilde{t}$, $\tilde{b}$	0
Bosons	1	gluons	g	**Fermions**	gluinos	$\tilde{g}$	1/2
	1	EW bosons	γ,Z^0,W$^\pm$		winos	$\tilde{W}^\pm$, $\tilde{W}^0$	1/2
					bino	$\tilde{B}^0$	1/2
	0	higgs	H$_u$, H$_d$		higgsinos	$\tilde{H}_u$, $\tilde{H}_d$	1/2

Formally construction of supersymmetry rules is beyond the scope of this thesis, but some general rules will be stated. A generator (Q) of supersymmetry is an operator that commutes with the Hamiltonian and converts a bosonic into a fermionic state and vice versa:

$$Q|Boson\rangle = |Fermion\rangle \tag{1.5}$$

$$Q|Fermion\rangle = |Boson\rangle \tag{1.6}$$

Since the generator Q changes the spin of a field by 1/2, it must be a fermionic spinor, carrying an intrinsic angular momentum of 1/2. Single-particle states in a supersymmetric theory are grouped into irreducible representations of the supersymmetric algebra, called supermultiplets, with each supermultiplet containing both fermion and boson states, called superpartners of each other. The supermultiplets can be divided into two categories; chiral supermultiplets and gauge supermultiplets (see for example [2]).

Chiral supermultiplets classify leptons, quarks, Higgs bosons and their superpartners as well (see Table 1.5). SM fermions (left or right handed) couple differently under different gauge fields. Thus, they should have separate complex scalar partners. The scalar partners of the SM fermions have the same gauge interactions as their partners. The Higgs boson (spin-0) should also reside in a chiral multiplet. The Higgs multiplet giving mass to the up-type quarks could not give mass to the down-type quarks. Thus, two Higgs chiral supermultiplets are needed to have proper Yukawa couplings [3] with up-type and down-type quarks. Furthermore, if there was only one Higgs chiral supermultiplet, the electroweak gauge symmetry would most probably be inconsistent as a quantum theory because of the triangle loop diagrams involving chiral fermions (triangle gauge anomaly).

Gauge supermultiplets classify the gauge bosons and their superpartners (see Table 1.6). If the theory is to be renormalizable[1], it should be a gauge boson which is massless, at least before the gauge symmetry is spontaneously broken. Since a massless boson (spin-1) has two helicity states, the number of bosonic degrees of freedom is n_B=2. Its superpartner is a massless fermion (spin-1/2; if it was a fermion with spin-3/2, the theory would not be renormalizable), again with two helicity states, thus n_F=2. Gauge bosons must transform like the adjoint representation of the gauge group and thus their fermionic partners must also. Since the adjoint representation of a gauge group is always its own conjugate, this implies that these fermions must have the same gauge transformation properties for left and right handed components. A combination like this, with a spin-1/2 gauginos and spin-1 gauge bosons is called a gauge or vector supermultiplet.

Members of the same supermultiplet can be transformed to each other by invoking Q and $Q^\dagger$. Furthermore since the generators of supersymmetry commute with the spacetime momentum, they also commute with $P^\mu P_\mu$ which is proportional to the mass. Lastly, they commute with the generators of gauge symmetries, as well. Suppose two states $|b\rangle$ and $|f\rangle$, with masses m_b and m_f respectively, are members of the same supermultiplet.

Without spinor indices, the supersymmetry algebra [6] gives:

$$\{Q, Q^\dagger\} = P^\mu \tag{1.7}$$

---

[1] Renormalization is a method for consistently removing the infinities and divergences that arise in field theory calculations.

Table 1.5: The MSSM chiral supermultiplets

Names		**spin-0**	**spin-1/2**	**SU(3)$_C$**	**SU(2)$_L$**	**U(1)$_Y$**
squarks, quarks	Q	$(\tilde{u}_L\ \tilde{d}_L)$	$(\mathrm{u}_L\ \mathrm{d}_L)$	3	2	$\frac{1}{6}$
(×3 families)	$\bar{u}$	$\tilde{u}_R^*$	$u_R^\dagger$	$\bar{3}$	1	-$\frac{2}{3}$
	$\bar{d}$	$\tilde{d}_R^*$	$d_R^\dagger$	$\bar{3}$	1	$\frac{1}{3}$
sleptons,leptons	L	$(\tilde{\nu}\ \tilde{e}_L)$	$(\nu\ \mathrm{e}_L)$	1	2	-$\frac{1}{2}$
(×3 families)	$\bar{e}$	$\tilde{e}_R^*$	$e_R^\dagger$	1	1	1
Higgs, higgsinos	H$_u$	$(\mathrm{H}_u^+\ \mathrm{H}_u^0)$	$(\tilde{H}_u^+\ \tilde{H}_u^0)$	1	2	$\frac{1}{2}$
	H$_d$	$(\mathrm{H}_d^0\ \mathrm{H}_d^-)$	$(\tilde{H}_d^0\ \tilde{H}_d^-)$	1	2	-$\frac{1}{2}$

Table 1.6: The MSSM gauge supermultiplets

Names	**spin-1/2**	**spin-1**	**SU(3)$_C$**	**SU(2)$_L$**	**U(1)$_Y$**
gluino, gluon	$\tilde{g}$	g	8	1	0
winos, W bosons	$\tilde{W}^\pm\ \tilde{W}^0$	$W^\pm\ W^0$	1	3	0
bino, B boson	$\tilde{B}^0$	B^0	1	1	0

$$\{Q, Q\} = \{Q^\dagger, Q^\dagger\} = 0 \tag{1.8}$$

$$[P^\mu, Q] = [P^\mu, Q^\dagger] = 0 \tag{1.9}$$

where P$^\mu$ is the four-momentum generator of spacetime translations. Since $P^\mu P_\mu|b\rangle = m_b^2|b\rangle$ and $P^\mu P_\mu|f\rangle = m_f^2|f\rangle$ and considering the previous relations, we have:

$$\begin{aligned} P^\mu P_\mu Q|b\rangle &= P^\mu P_\mu|f\rangle = m_f^2|f\rangle & (1.10)\\ &= QP^\mu P_\mu|b\rangle = m_b^2 Q|b\rangle = m_b^2|f\rangle & (1.11) \end{aligned}$$

and from 1.10 and 1.11 it follows:

$$\Rightarrow m_b = m_f \tag{1.12}$$

which points that in supersymmetry, superpartners must have equal masses. The supersymmetry generators Q, Q† also commute with the generators of gauge transformations and therefore particles in the same supermultiplet must also have the same electric charge, weak isospin and color degrees of freedom. Since the superpartners of the Standard Model particles have not been observed, supersymmetry, if it exists, must be a broken symmetry, allowing the superparticles to be heavier than the corresponding Standard Model particles in much the same way that electroweak symmetry breaking gives rise to the masses of the gauge bosons. Nevertheless it is possible to break supersymmetry without spoiling attractive cancellation of quadratic divergences. This kind of breaking is called soft breaking and yields heavy superpartners in a natural way. These arguments show that broken supersymmetry might be relevant to nature, thus posing the problem of how it is broken [13].

In the Standard Model, baryon (B) and lepton (L) numbers are conserved because of global gauge invariance. Supersymmetric theories have terms that violate these numbers. Nevertheless, it is possible to construct renormalizable operators consistent with SM gauge symmetries. This is done with the introduction of a new symmetry known as R-parity and defined for each particle as:

$$P_R = (-1)^{3(B-L)+2s} \tag{1.13}$$

where s is the spin of the particle. All of the SM particles and the Higgs bosons have even R-parity (P_R=+1), while all of the squarks, sleptons, gauginos and higgsinos have odd parity (P_R=-1), a fact that makes R-parity assignment a very useful definition for phenomenology. Particles with odd parity are known as "supersymmetric particles" or "sparticles". Assuming R-parity conservation, there can be no mixing between the sparticles and the particles with even R-parity. Furthermore, every interaction vertex in the theory contains an even number of sparticles (odd R-parity), leading to three very important phenomenological consequences:

- The lightest sparticle (P_R=-1), known as the lightest supersymmetric particle (LSP), has to be absolutely stable, and must be produced eventually at the end of a decay chain of a heavy unstable supersymmetric particle. If it is electrically neutral, it is weakly interacting with ordinary matter, and thus can be an attractive candidate for the non-baryonic dark matter that seems to be a cosmology requirement.

- Each sparticle apart from LSP, must eventually decay into a state that contains an odd number of LSPs.

- In collider experiments, sparticles can only be pair produced.

1.2.3 The Minimal Supersymmetric Standard Model

The Minimal Supersymmetric Standard Model (MSSM) is usually considered as a low energy theory describing phenomenology of supersymmetric models (see for example [13, 17]. It is the simplest extension to the Standard Model originally proposed in 1981 to stabilize the weak scale, solving the hierarchy problem. It assumes minimal particle content, R-parity conservation and Poincaré and gauge invariance. As it is already mentioned, the MSSM introduces supermultiplets in which there is a partner for every particle in SM with the same internal quantum numbers but a spin difference of 1/2. Like any other supersymmetric theory, the MSSM should have the same number of bosonic and fermionic degrees of freedom. It should also be consistent with the known features of the Standard Model, including the presence of chiral fermions and parity violation.

The Higgs boson mass of the SM is unstable to quantum corrections and the theory predicts that weak scale should be much weaker than what is observed to be. In the MSSM, the Higgs boson has a fermionic superpartner, the Higgsino, that has the same mass as it would if supersymmetry was an exact symmetry. However in MSSM there is a need for more than one Higgs field.

The Langrangian of the MSSM can be written in the form:

$$\mathcal{L}_{MSSM} = \mathcal{L}_{SUSY} + \mathcal{L}_{Breaking} \tag{1.14}$$

where $\mathcal{L}_{SUSY}$ is the SUSY generalization and contains all the gauge and Yukawa interactions and preserves supersymmetry invariance, and $\mathcal{L}_{Breaking}$ describes the SUSY breaking.

The parameters of the MSSM can be described by considering separately the supersymmetry-conserving sector and the supersymmetry-breaking sector. The parameters of the supersymmetry-conserving sector consists of: i) gauge couplings (g_s, g and g$'$, corresponding to the Standard Model gauge group $SU(3) \bigotimes SU(2) \bigotimes U(1)$ respectively); ii) a supersymmetry-conserving higgsino mass parameter (μ); and iii) Higgs-fermion Yukawa coupling constants (λ_u, λ_d and λ_e, corresponding to the coupling of one generation of left- and right-handed quarks and leptons and their superpartners to the Higgs bosons and higgsinos).

The supersymmetry-breaking sector contains the following parameters: i) gaugino Majorana masses (M_3, M_2, and M_1 associated with SU(3), SU(2), and U(1) subgroups of the Standard Model); ii) five scalar squared-mass parameters for the squarks and sleptons ($M^2_{\tilde{Q}}$, $M^2_{\tilde{U}}$, $M^2_{\tilde{D}}$, $M^2_{\tilde{L}}$ and $M^2_{\tilde{E}}$ corresponding to the five electroweak gauge multiplets); iii) Higgs-squark-squark and Higgs-slepton-slepton trilinear interaction terms (with coefficients $\lambda_u A_U$, $\lambda_d A_D$, and $\lambda_e A_E$, which define the so-called *A-parameters*) and iv) three scalar squared-mass parameters -two of which ($m_1^2 + m_2^2$) contribute to the diagonal Higgs squared-masses, given by $m_1^2 + |\mu|^2$ and $m_2^2 + |\mu|^2$, and a third which contributes to the off-diagonal Higgs squared-mass term, ($m_{12}^2 := B_\mu$, which defines the *B-parameter*).

The breaking of the electroweak symmetry $SU(2) \times U(1)$ to $U(1)_{EM}$ is only possible after introducing the supersymmetry-breaking Higgs squared-mass parameters.

To summarize, MSSM incorporates supersymmetry into the Standard Model by making "minimal" additions; absolutely necessary for changing SM into a Supersymmetric theory:

- Adds superpartners to the gauge field bosons (gauginos).

- Adds superpartners to the fermions (sparticles).
- Adds superpartners to the Higgs field, usually more than one (higgsinos).
- Adds some soft-symmetry breaking terms.
- Adds a second Higgs doublet.

Tables 1.5 and 1.6 present the gauge eigenstates of the MSSM. In general, mixing can occur between gauginos and higgsinos with the same charge and between various sets of sfermions with the same charge, as well. In SUSY scenarios only the gluino is exempt from this, as its color charge prohibits it from mixing with any other particles.

The neutral higgsinos ($\tilde{H}_u^0$ and $\tilde{H}_d^0$) combine with the neutral gauginos ($\tilde{B}^0$ and $\tilde{W}^0$) to form four mass eigenstates known as *neutralinos* ($\tilde{\chi}_i^0$, i=1, 2, 3, 4). The charged higgsinos ($\tilde{H}_u^+$ and $\tilde{H}_d^-$) combine with the charged winos ($\tilde{W}^{\pm}$) to form two mass eigenstates known as *charginos* ($\tilde{\chi}_i^{\pm}$, i=1, 2).

1.2.4 Gauge Mediation Supersymmetry Breaking scenario

In the previous section it was discussed the need for transmitting SUSY breaking to the MSSM. The most common scenarios are: Gauge Mediation (GMSB) [9, 10, 11], Gravity Mediation (mSUGRA) [14], Gaugino Mediation [15] and Anomaly Mediation (AMSB) [16]. In this thesis we concentrate on the first one.

Gauge mediated Supersymmetry Breaking scenario is one of the oldest, simplest, and most robust ways of transmitting SUSY breaking to the MSSM. It is of particular theoretical interest for new physics as it not only stabilizes the mass of the SM Higgs boson and drives the grand unification of forces, but also avoids the large flavor-changing neutral currents that trouble other SUSY-breaking scenarios. The universality of the fundamental soft-supersymmetry breaking squark and slepton squared-mass parameters is guaranteed in gauge-mediated supersymmetry breaking scenarios, because the supersymmetry breaking is communicated to the sector of MSSM fields via gauge interactions. Three sectors are included:

- The *visible* sector containing particles of MSSM (quarks, leptons and two Higgs doublets along with their supersymmetric particles).
- The *hidden* sector that is responsible for the SUSY breaking. It contains a collection of yet unobserved superfields and the corresponding hypothetical

particles which do not interact via the SM force messengers (e.g. gluons, photons, and W/Z bosons).

- The *messenger* sector, formed by some new superfields Φ and $\bar{\Phi}$. These superfields interact with MSSM via $SU(3)_C \bigotimes SU(2)_L \bigotimes U(1)_Y$ and couple to a chiral superfield X of the hidden sector at tree level, via some Yukawa interaction.

Thus, a typical structure of gauge-mediated supersymmetry breaking models, involves a hidden sector where supersymmetry is broken, a messenger sector consisting of particles (messengers) with $SU(3)_C \bigotimes SU(2)_L \bigotimes U(1)_Y$ quantum numbers, and the visisble sector consisting of the fields of the MSSM. The direct coupling of the messengers to the hidden sector generates a supersymmetry-breaking spectrum in the messenger sector. Finally, supersymmetry breaking is transmitted to the MSSM via the virtual exchange of the messengers.

GMSB has a number of virtues, for instance guaranteeing flavor universality among the MSSM sfermion masses, and thus solving the SUSY Flavor Changing Neutral Currents (FCNC) problem[2] in a universal way, since the soft supersymmetry breaking is communicated to the visible sector via gauge interactions. Unfortunately, even with the inherent simplicity of gauge mediation there is a veritable cornucopia of models. These models have a wide variety of features, and often it is unclear which features are model specific and which are generic to gauge mediation.

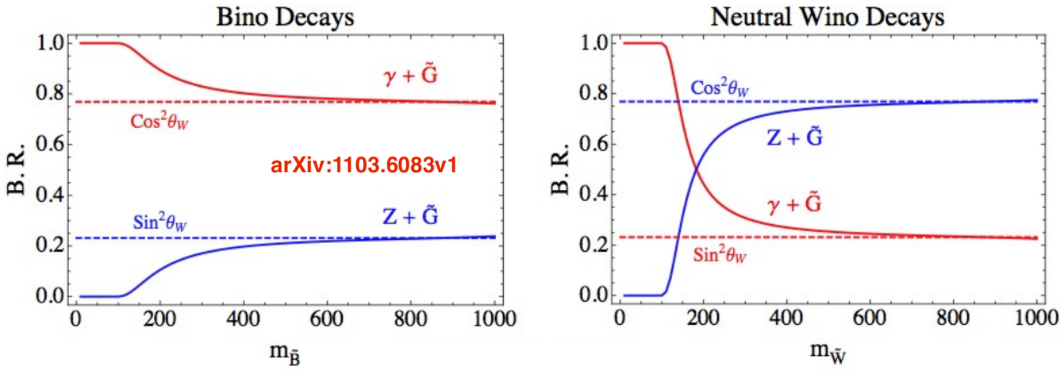

Figure 1.5: Branching ratio of bino and wino like neutralino to photons and Z bosons in dependence of the neutralino mass

In the GMSB scenario, the lightest supersymmetric particle is the gravitino $\tilde{G}$, while the next-to-lightest supersymmetric particle is the neutralino $\tilde{\chi}_1^0$. In case of gaugino-like NLSP, the neutralino consists predominantly of either the bino, the

---

[2] flavor-changing neutral currents (FCNCs) are expressions that change the flavor of a fermion current without altering its electric charge.

superpartner of the U(1) gauge field, or the wino, the superpartner of the SU(2) gauge fields.

A bino-like neutralino decays predominantly into a gravitino and a photon with a branching fraction $\sim \cos^2\theta_{\mathrm{w}}$ (Figure 1.5), while the decay to a gravitino and a Z boson is sub-dominant ($\sim \sin^2\theta_{\mathrm{w}}$). In case of a wino-like neutralino, the spliting between the charged and the neutral wino is in general small. Thus the neutral and charged winos become co-NLSPs. The charged wino will decay directly into the gravitino and a $\mathrm{W}^{\pm}$ as well, while the neutral will decay dominantly to a gravitino and a Z boson ($\sim \cos^2\theta_{\mathrm{w}}$) and sub-dominantly to a gravitino and a photon ($\sim \sin^2\theta_{\mathrm{w}}$). Yet for wino masses below ~200 GeV the $\gamma + \tilde{G}$ decay is dominant.

1.3 Creating events with γ + jets + $\mathrm{E}_{\mathrm{T}}^{\mathrm{miss}}$ final state

In order to search for interesting events such as possible supersymmetric particles, two intense proton beams, with opposite directions, are created. Each time the two beams are crossing, proton-proton collisions are produced and collected by the giant detectors that have been built in the four collision points.

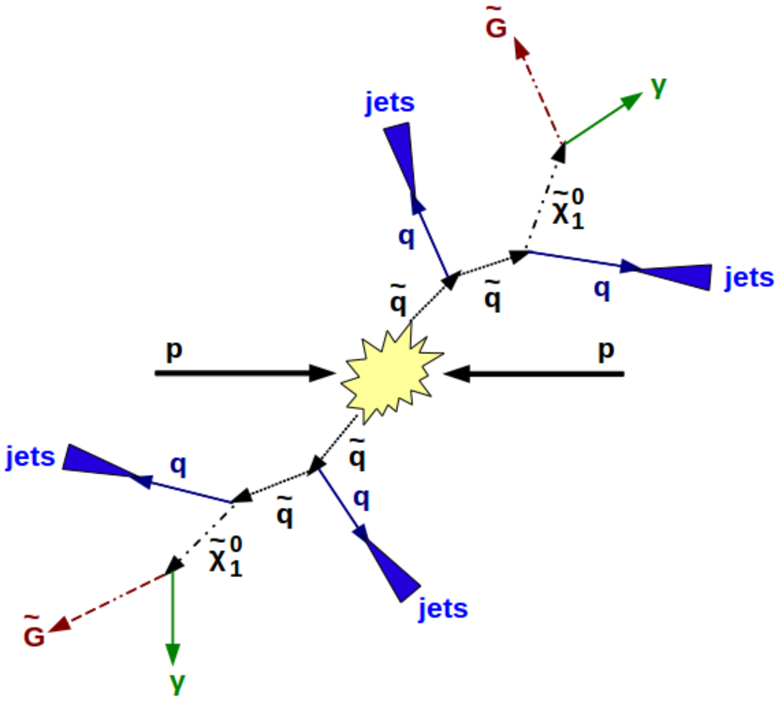

Figure 1.6: Schematic view of pp colission resulting to an event with two photons, jets and Gravitino according to the GMSB scenario.

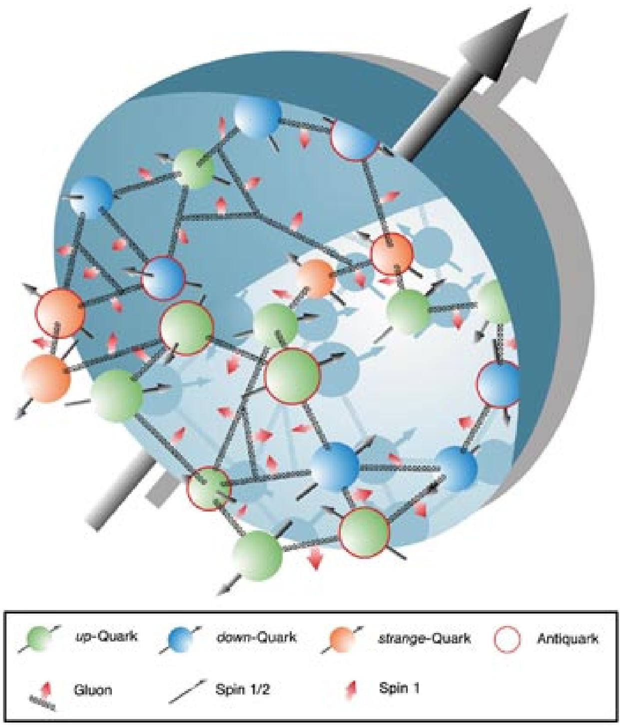

Figure 1.7: Schematic showing the proton's structure; valence quarks, gluons and sea quark-antiquark pairs.

In the standard model of particle physics, the proton is a hadron, composed of quarks. The two up quarks and one down quark of the proton are held together by the strong force, mediated by gluons. However, the real picture is more complicated; the proton is composed of the valence quarks (up, down), the gluons, and transitory pairs of sea quarks (see Figure 1.7). As sea quarks are known virtual quark-antiquark pairs. They are formed when a gluon of the hadron's color field splits; this process also works in reverse in that the annihilation of two sea quarks produces a gluon. Sea quarks are much less stable than their valence counterparts, and they typically annihilate each other within the interior of the hadron. Despite this, sea quarks can hadronize into baryonic or mesonic particles under certain circumstances. All particles inside a proton (real or virtual) are collectively called partons. A parton distribution function is defined as the probability density for finding inside the proton a particle with a certain longitudinal momentum fraction at a given momentum transfer Q^2. Because of the inherent non-perturbative effect in a QCD binding state, parton distribution functions cannot be obtained by perturbative QCD. Due to the limitations in present lattice QCD calculations, the known parton distribution functions are instead obtained by studing experimental data.

In the previous section we discussed about decays that can give as products, final states with at least one photon, jets and supersymmetric particles. For this reason, we only consider cases in which at least one of the neutralinos decays promptly to a gravitino and a photon. Since the gravitino escapes detection, it leads to missing transverse energy in the event. Assuming R-parity conservation, SUSY particles are pair produced at the LHC. Those particles are dominantly strongly interacting with decay chains including one or several quarks/gluons. Therefore, events with a pure bino-like neutralino are expected to contain two photons and two gravitinos plus additional Standard Model particles in the final states. The created Standard Model particles are either a photon or a Z or a Higgs boson if the mass difference between the NLSP and the LSP allows it kinematically. A second signature, with just one photon, is possible if one of the NLSPs decays into a Z boson instead of a photon. In Figure 1.8 is illustrated an example of a Feynman diagram of single-photon final state, while Figure 1.9 shows an example of a Feynman diagram of a typical di-photon final state. Lastly in the case of a wino-like neutralino, the di-photon final state is quite suppressed but single-photon final states may be significant (Figure 1.10).

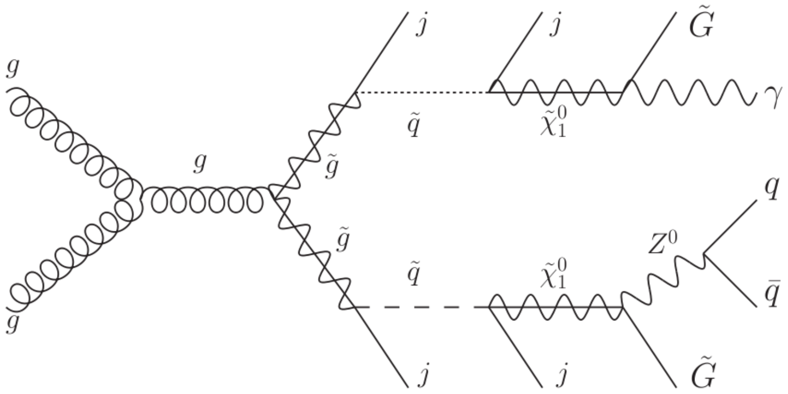

Figure 1.8: Sample of Feynman diagrams of a typical single photon final state expected within the GGM framework for a bino-like neutralino

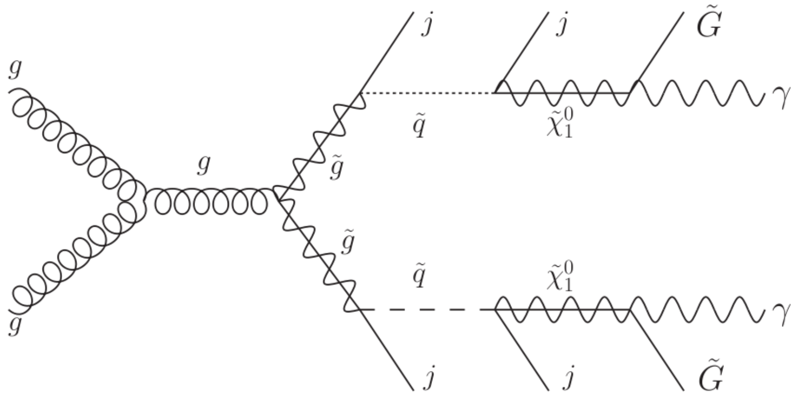

Figure 1.9: Sample of Feynman diagrams of a typical double photon final state expected within the GGM framework for a bino-like neutralino

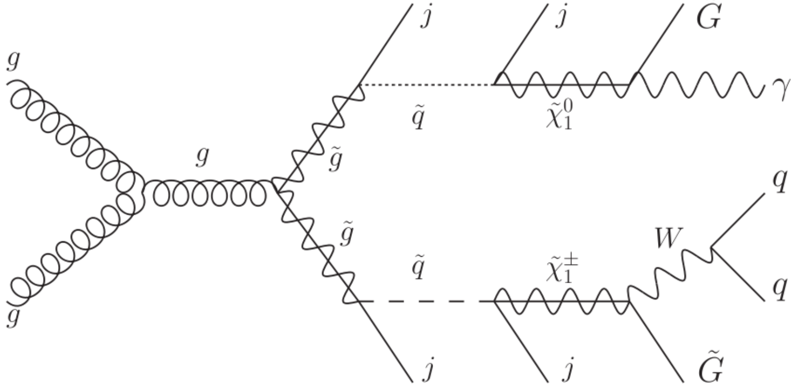

Figure 1.10: Sample of Feynman diagrams of a typical single photon final state expected within the GGM framework for a wino-like neutralino.

Chapter 2

The Compact Muon Solenoid experiment

> *An experiment is a question which science poses to Nature, and a measurement is the recording of Nature's answer.*
>
> -Max Planck-

The Large Hadron Collider at the European Center for Nuclear Research was build to answer questions about fundamental particle physics, at the TeV energy scale. This Chapter describes the LHC and the Compact Muon Solenoid that is one of the four detectors placed along the accelarator circumference.

2.1 European Center for Nuclear Research

The European Organization for Nuclear Research (CERN) is one of the largest and most respected centres for scientific research in the world. The convention establishing CERN was ratified in 1954 by 12 countries in Western Europe (Greece was one of them). Today it has 20 European member states and noumerous experiments following international collaborations. CERN's main function is to provide all the necessary tools (particle accelerators and detectors) for studing fundamental physics, finding out what the Universe is made of and how it works. CERN is also the birthplace of the World Wide Web.

Figure 2.1: CERN's logo.

2.2 The Large Hadron Collider

The Large Hadron Collider (LHC) [18, 19, 20, 21] is a two-ring hadron accelerator and collider in the 26.7 km circumference tunnel formerly used by the Large Electron-Positron collider (LEP) at CERN. It lies beneath the Franco-Swiss border near Geneva, Switzerland at a depth ranging from 45 to 170 m below the earth's surface (Fig. 2.2).

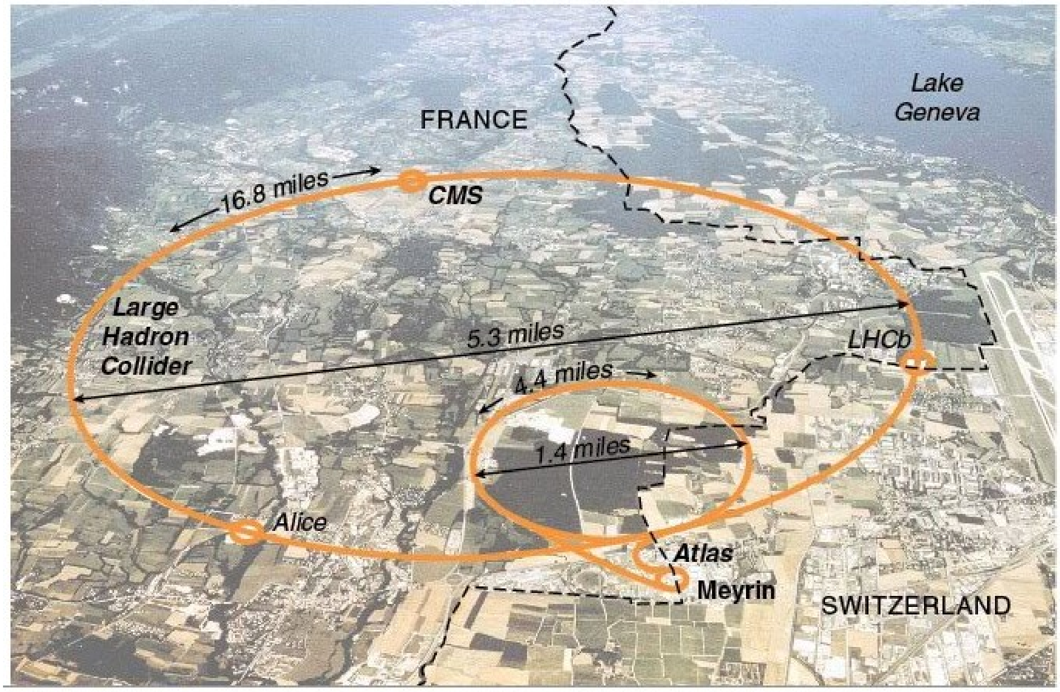

Figure 2.2: Panoramic view of the Franco-Swiss border, where LHC lies beneath the earth's surface, in a 27 km circumference tunnel at a depth ranging from 45 to 170 m.

The prime motivation is to elucidate the nature of electroweak symmetry breaking for which the Higgs mechanism is presumed to be responsible. Furthermore the experimental study of the Higgs mechanism, can shed light on the mathematical consistency of the Standard Model at energy scales above $\simeq$ 1 TeV. Various alternatives to the Standard Model invoke new symmetries, new forces or consistencies. There are also, high hopes for discoveries that could pave the way toward a unified theory. Supersymmetry could be among these discoveries. LHC is designed to collide proton beams and heavy (Pb) ions but also as recently conceived proton-Pb ions collisions. The two beams rotate in opposite directions and collide in four interaction points where four experiments have been built; CMS, ATLAS, ALICE and LHCb. CMS [53] and ATLAS [52] are located in opposite positions along the ring and are general-

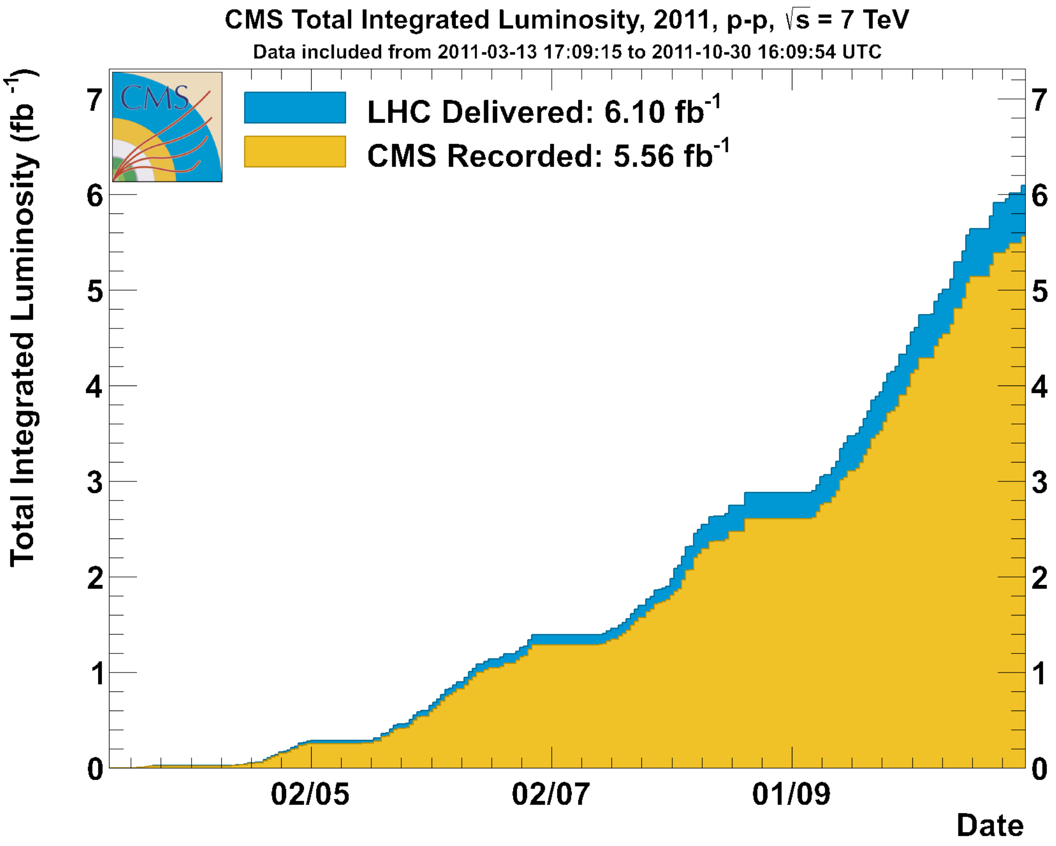

Figure 2.3: Total Integrated luminosity as a function of time delivered (blue) to, and recorded (yellow) by the CMS detector during stable beams for pp running at 7 TeV centre-of-mass energy in 2011.

purpose experiments studying general SM processes and looking for new physics, the ALICE [54] experiment investigates heavy-ion collisions and LHCb [55] is dedicated to precision measurements of CP violation and rare decays of B hadrons.

The design collision energy (for the proton beams), projected to be reached after 2012, is $\sqrt{s} = 13 - 14$ TeV. During the 2011 running period the collision energy was $\sqrt{s} = 7$ TeV, while in 2012 it increased to $\sqrt{s} = 8$ TeV. The number of events per second generated in the LHC collisions is given by:

$$N_{event} = \mathcal{L}\sigma_{event} \tag{2.1}$$

where σ_{event} is the cross section for the event under study and $\mathcal{L}$ the machine luminosity. The luminosity is the number of collisions per unit-time and cross-sectional area of the beams and depends only on the collider parameters. The design luminosity is $\mathcal{L} = 10^{34}$ cm^{-2}s^{-1}. For a beam with Gaussian kinematic distribution, the luminosity is given by:

$$\mathcal{L} = \frac{N_b^2 n_b f_{rev} \gamma_r}{4\pi \epsilon_n \beta*} F \tag{2.2}$$

where N_b is the number of particles per bunch, n_b is the number of bunches per beam, f_{rev} the revolution frequency, γ_r the relativistic gamma factor, ϵ_n the normalized transverse beam emittance, $\beta*$ the beta function at the collider point and F the geometric luminosity reduction factor due to the crossing angle at the interaction point (IP). Usually, the integrated luminosity $L = \int \mathcal{L}\mathrm{d}t$ is used to express the amount of available collision data. During the 2011 running, the LHC delivered 6.10 fb^{-1} of collision data. The CMS experiment recorded 5.56 fb^{-1} of these, and after quality checks approximately 5.05 fb^{-1} of collision data were approved for analysis.

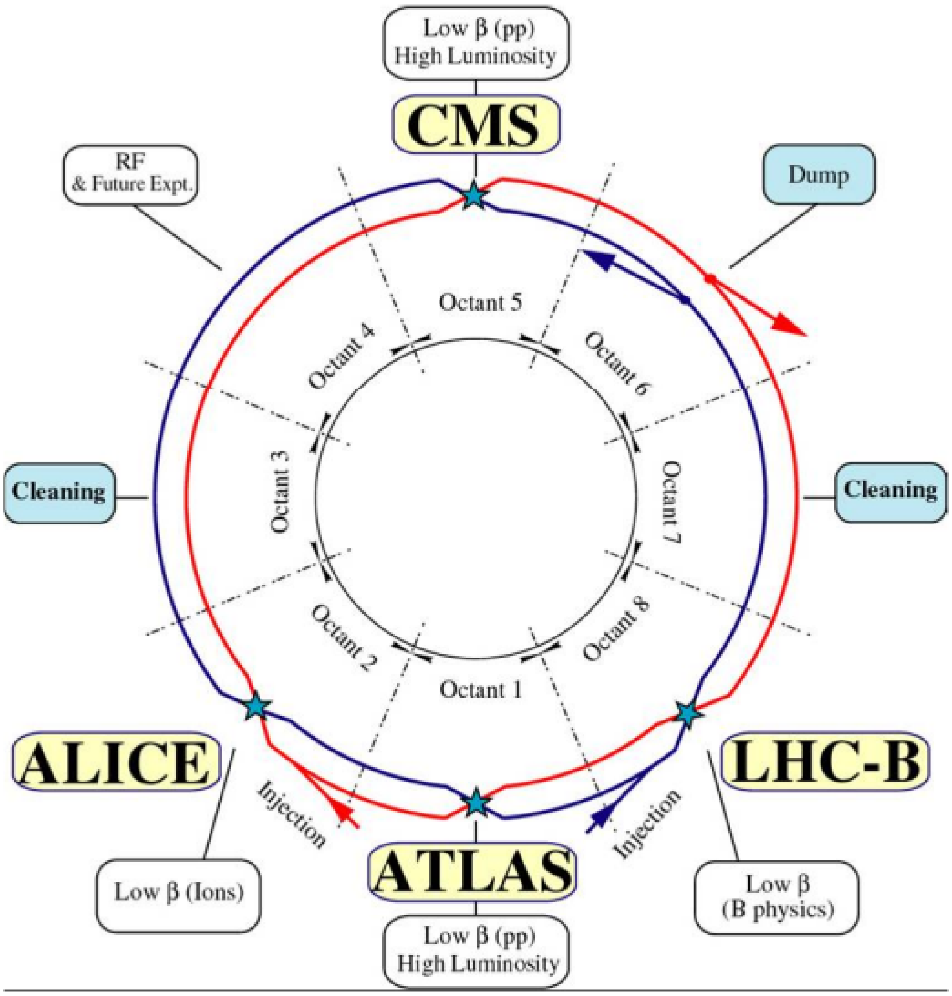

Figure 2.4: Schematic layout of the LHC. Beam 1 (red line) - clockwise, Beam 2 (blue line) counterclockwise.

As it is previously mentioned, the LHC has two separate parallel rings, each containing a proton beam. These beams rotate in oppposite directions and require opposite magnetic dipole fields and thus two sets of dipole magnets and two separate vacuum systems within the same structure (Fig. 2.4). The ring contains 1232 superconducting dipole magnets operating at 1.9 K deliver the nominal 8.33 T magnetic field required to steer the beam along the beam pipes (Fig. 2.5). Additionally, there are 392 quadrupole magnets whose function is to collimate the beams in order to maximize the probability of interactions at the intersection points.

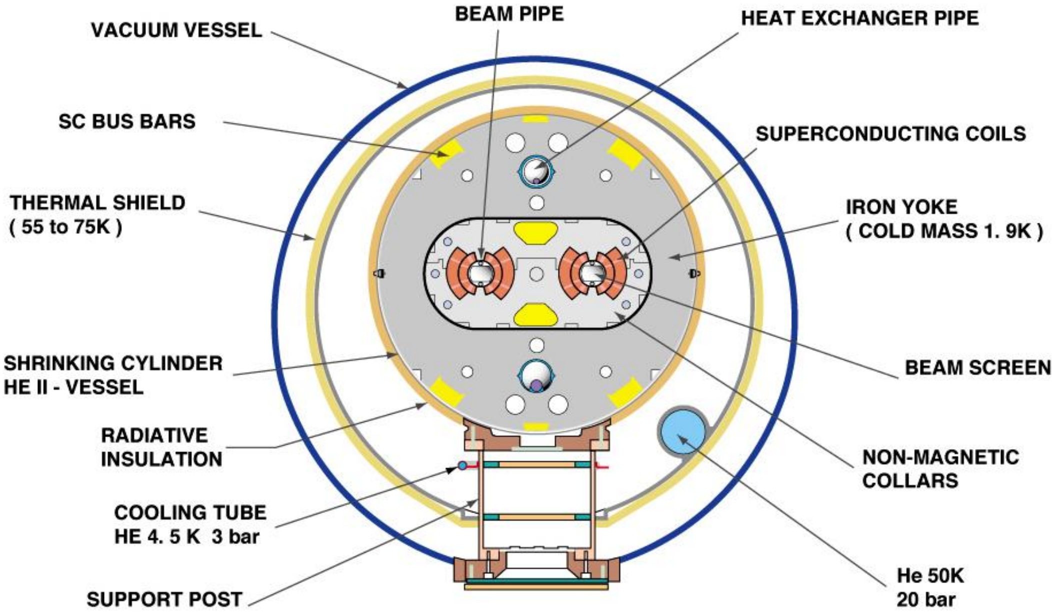

Figure 2.5: Cross section of LHC dipole magnet.

The LHC is supplied with protons acquired by stripping electrons from hydrogen atoms. The beams (protons or heavy ions) are accelerated in stages, with the linear accelerator (LINAC2) first generating 50 MeV protons. The Proton Synchrotron Booster (PSB) increases their energy to 1.4 GeV and then the beam is fed to the Proton Synchrotron (PS) where it is accelerated to 25 GeV before they reach the Super Proton Synchrotron (SPS) and 450 GeV, the energy they carry as they are injected in the main ring of the LHC where they are finally accelerated to their peak beam energy (Fig. 2.6). The protons arrive in the LHC in bunches of approximately 10^{11} protons, with a bunch spacing of 25 ns, resulting in 2808 bunches in total. The operation of the LHC begins with the injection of the proton bunches into the LHC, which typically takes 20 minutes. In order to reach its operational energy, it takes another 20 minutes. Once the beams reach the desirable energy, the optics are changed to squeeze the beams at the interaction points, and the magnets separating the beams are squized off, resulting in collisions. If the beams remain stable, the collision phase lasts approximately 10 hours, during which time the luminosity is constantly decreasing. Eventually, the luminosity decreases to the point that it becomes advantageous to dump the beam, at which point the process can start over with new beams. Thus, faster turn-around time (limited by magnet hysteresis, injection, ramping, and squeezing) makes it possible to have shorter runs with higher-luminosity beams.

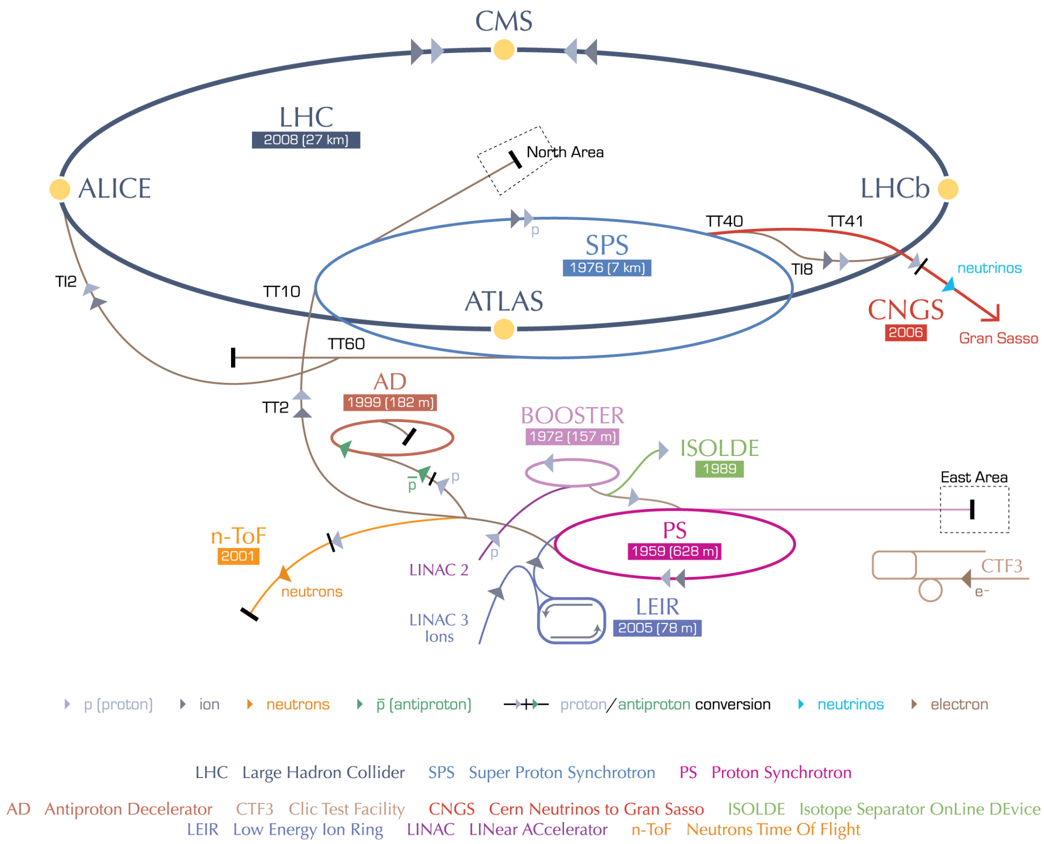

Figure 2.6: CERN's Machine Complex.

2.3 The Compact Muon Solenoid

The Compact Muon Solenoid (CMS) is a general-purpose particle detector installed at Interaction Point 5 of the LHC ring, near the village of Cessy in France. Its design began in the early 90's, followed by the development phase and the construction of the subsystems. Its assembly and commissioning spanned the last decade up to the start of LHC operations in November 2009.

The large flux of particles coming from the interaction region leads to high radiation levels, requiring radiation-hard detectors and front-end electronics. In order to meet its physics goals, the detector requirements for CMS are:

- Good muon identification and momentum resolution over a wide range of momenta and angles, good dimuon mass resolution ($\simeq$ 1% at 100 GeV/c^2), and the ability to determine unambiguously the charge of muons with p<1 TeV/c.
- Good charged-particle momentum resolution and reconstruction efficiency in the inner tracker.
- Good electromagnetic energy resolution, good diphoton and dielectron mass resolution ($\simeq$ 1% at 100 GeV), wide geometric coverage, π^0 rejection, and efficient photon and lepton isolation at high luminosities.
- Good missing-transverse-energy $\mathrm{E_T^{miss}}$ and dijet-mass resolution, requiring hadron calorimeters with a large hermetic geometric coverage and with fine lateral segmentation.

The design of CMS meets these requirements. The main distinguishing features of CMS are a high-filed solenoid, a full-silicon based inner tracking system, and a homogeneous scintillating-crystals-based electromagnetic calorimeter. The overall design is shown in Figure 2.7. By convention, we use a coordinate system with the origin located in the center of the detector at the collision point. The x-axis points radially inward toward the center of LHC (horizontally south), the y-axis points vertically upward and thus the z-axis points along the beam direction toward the Jura mountains (west). We may define a polar angle θ with respect to the z axis, with θ=0 lying along the positive z-axis and $\theta = \pi$ along the negative z-axis and an azimuthal angle ϕ in the xy-plane, where ϕ=0 is along the positive x-axis and $\phi = \pi/2$ is along the positive y-axis. Instead of using the polar angle, positions within the detector are generally defined in terms of the pseudorapidity (η):

$$\eta = -\ln(\tan\frac{\theta}{2}) \tag{2.3}$$

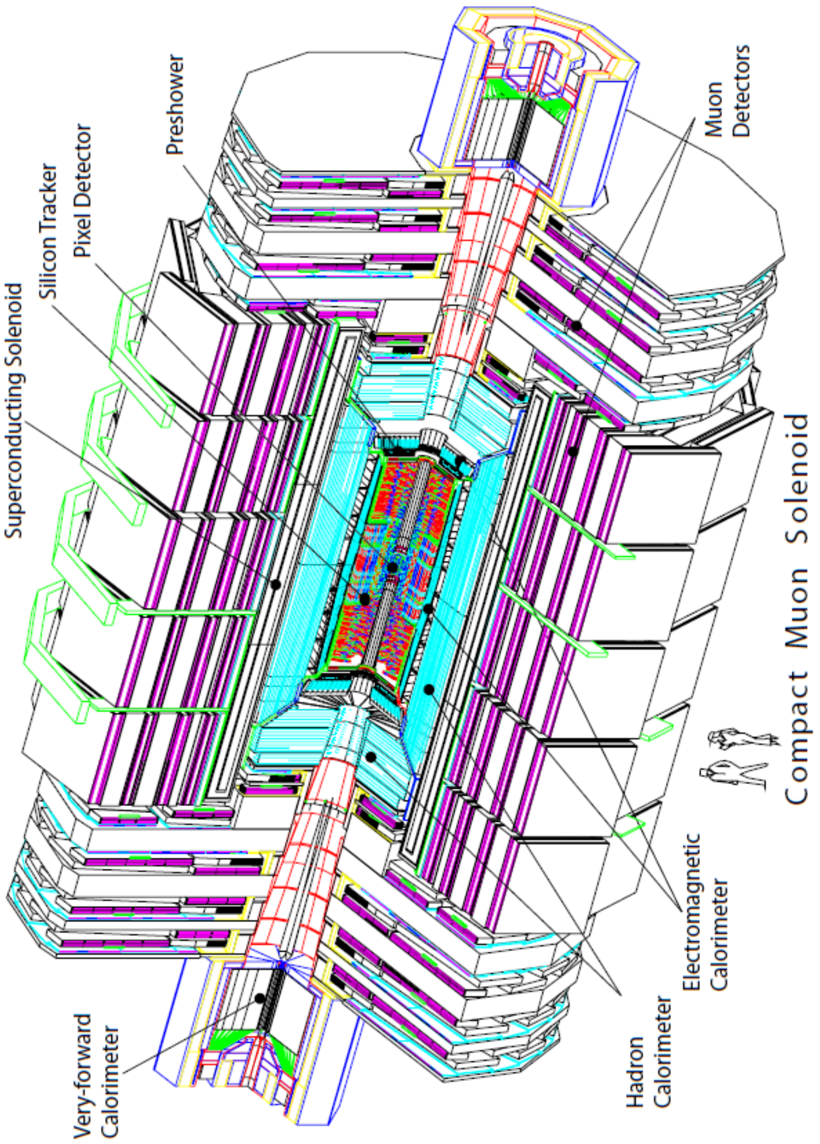

Figure 2.7: A perspective view of the CMS detector and its components. The human figures demonstrate the size of the detector.

2.3.1 The superconducting magnet

The superconducting solenoid magnet of the CMS detector has been designed to reach a 4 T field (currently operates at 3.8 TeV to increase the lifetime of the magnet) in a free bore of 6 m diameter and 12.5 m lenght. The flux is returned through a 10 000 t yoke comprising 5 wheels and 2 endcaps, composed of three disks each (Fig. 2.8). The distinctive feature of the 220 t cold mass is the 4-layer winding made from a stabilized reinforced NbTi conductor. The ratio between stored energy and cold mass is high (11.6 kJ/kg).

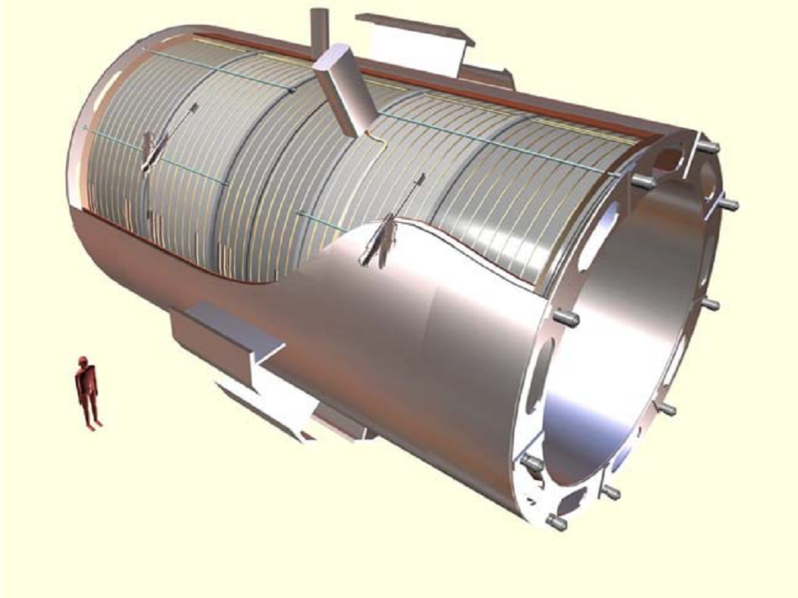

Figure 2.8: A perspective view of the solenoid.

2.3.2 The Inner tracking system

The CMS Inner tracking system surrounds the interaction point and is designed to provide a precise and efficient measurement of the trajectories of charged particles (electrons, muons and hadrons) originating from the LHC collisions, as well as a precise reconstruction of primary and secondary interaction vertices. Its length is 5.8 m and the diameter 2.5 m and it is embedded in the strong magnetic field of the solenoid. At the LHC design luminosity, about 1000 particles from more than 20 overlapping proton-proton interactions are expected to traverse the tracker for each bunch crossing. Therefore a detector technology with high granularity and fast response is required, so that the trajectories can be identified reliably and attributed to the correct bunch crossing. These features imply high power density of the on-detector electronics which require efficient cooling, but this is in conflict with the aim of keeping the amount of material

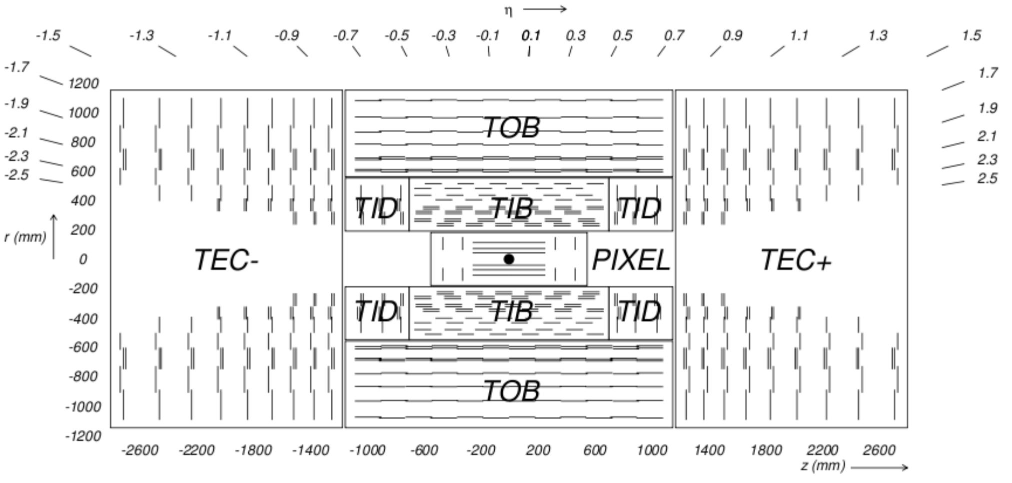

Figure 2.9: Schematic cross section of the CMS tracker. Each line represents a detector module. Double lines indicate back-to back modules which deliver stereo hits.

to minimum in order to limit undesirable interaction effects (multiple scattering, bremsstrahlung, photon conversion and nuclear interactions). The final decision was a compromise between these aspects and the challenge of a tracker able to operate in the intense radiation environment for about ten years.

All these requirements lead to a tracker design entirely based on silicon detector technology. The CMS tracker (Fig. 2.9) is composed of a pixel detector with three barrel layers at radii 4.4 cm, 7.3 cm and 10.2 cm and a silicon strip tracker with 10 barrel detection layers extending outwards to a radius of 1.1 m. Each system is completed by endcaps which consist of two disks in the pixel detector and 3 plus 9 disks in the strip tracker on each side of the barrel, extending the acceptance of the tracker up to a pseudorapidity of $|\eta|$ <2.5. With about 200 m^2 of active silicon area the CMS tracker is the largest silicon tracker ever built. Figure 2.10 shows the material budget of the CMS tracker in units of radiation length X/X_0. At $\eta \simeq 0$ starts at about 0.4 X_0, reaching a maximum of about $1.8X_0$ at an $|\eta| \simeq 1.4$ due to the presence of cabling and other auxiliary services to fall again to about 1 radiation length at $|\eta| \simeq 2.5$

2.3.2.1 The pixel detector

The pixel system is the part of the tracking system that is closest to the interaction region. It measures points in $(r - \phi, z)$, and its components arrangement; three layers of pixel modules (BPix) and two disks at each endcap (FPix), ensures that there are at least three tracking points over the full η-range for each charged

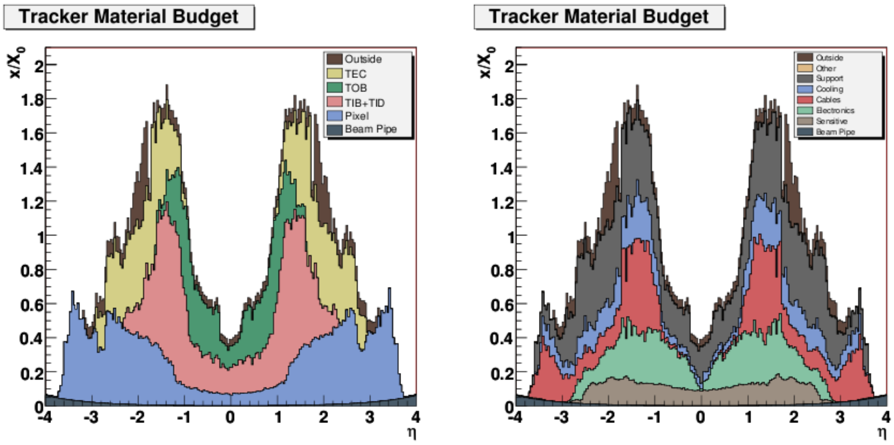

Figure 2.10: Material budget in units of radiation length as a function of pseudorapidity η for the different sub-detectors (left) and functional contributions (right).

particle trajectory (Fig. 2.12). The pixel system contains about 66 million pixels covering an area of $\simeq 1$ m^2. Each pixel cell has a size of 100 μm $\times$ 150 μm and a thickness of 300 μm. In more details, the BPix layers are 53 cm long, placed at radii of 4.4, 7.3 and 10.2 cm away from the beam axis, and contain a total of 48 million pixels. The FPix disks have a radius of 6-15 cm, are placed at z=±34.5 and 46.5 cm and contain 18 million pixels. The detector covers an area of pseudorapidity $|\eta| < 2.5$ and the spatial resolution obtained for the z measurement is in the range of 15-20 μm.

2.3.2.2 The silicon strip tracker

The particle flux decreases with increasing radius, so it becomes possible to achieve the required granularity with silicon microstrip detectors. The silicon strip tracker is a sub-detector, based on micro-strip silicon devices. It comprises of three subsystems; tracker inner barrel and tracker inner disks (TIB/TID), tracker outer barrel (TOB) and tracker endcaps (TEC), and ensures the measurement of nine hits for each charged trajectory, with at least four of them being two-dimensional. It has about 9.3 millions of strips, arranged in ten barrel layers covering an area of 198 m^2. The entire silicon strip tracker contains about 15400 highly sensitive modules, each one consists of three elements: a set of sensors, its mechanical support structure and readout electronics. The mechanical support is achieved by a carbon-fiber or graphite frame, with a kapton layer to isolate the silicon and provide the electrical connections to the sensor backplane. The readout and auxiliary chips are housed on a ceramic multiplayer hybrid, and a glass pitch adapter between the hybrid and the sensor, brings the signals from

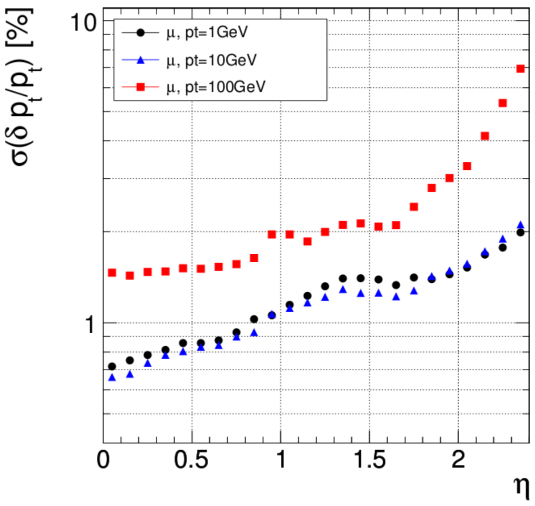

Figure 2.11: Transverse momentum resolution for single muons with transverse momenta of 1, 10 and 100 GeV.

the sensor strips to the readout input pads.

The TIB includes four layers, where the strips are placed parallel to the beam and the pitch is larger in the two outer layers, while the TID includes three disks at each endcap, with the strips placed radially. The TOB surrounds the inner detector and its six barrel layers provide six measurements in r-ϕ. It extends up to a radius of 116 cm, between z=±118 cm and consists of strips with a thickness of 500 μm. The tracker endcaps (TEC+, TEC-) cover a range of $22.5 < r < 113.5$ cm and $124 < |z| < 282$ cm and provide up to nine measurements in r-ϕ. Each Endcap comprises of nine disks, each of them holding up to seven rings of radial strips. Their thickness is 320 μm on the four innermost rings and 500 μm on the rest. In addition to these systems, a second micro-strip system is attached to some of their modules. This system is attached to the first two layers and rings, respectively, of TIB, TID and TOB, as well as to rings 1, 2, and 5 of each TEC. These extra modules are mounted back-to-back, with a stereo angle of 100 mrad, in order to provide a measurement of z in the barrel and r on the disks. The achieved single point resolution of this system is 230 μm and 530 μm in TIB and TOB respectively.

Roughly half of the modules in the tracker layout are in fact double-sided modules, made of two independent single-sided modules glued together back-to-back with a relative rotation of 100 mrad with respect to each other. This allows a determination of the ionization in the z coordinate in the barrel modules, and in the r coordinate in the disks. These double-sided modules are mounted in the first two layers of the TIB and TOB, in the first two TID rings, and in rings 1, 2 and 5 of the TEC (Fig. 2.9) [22].

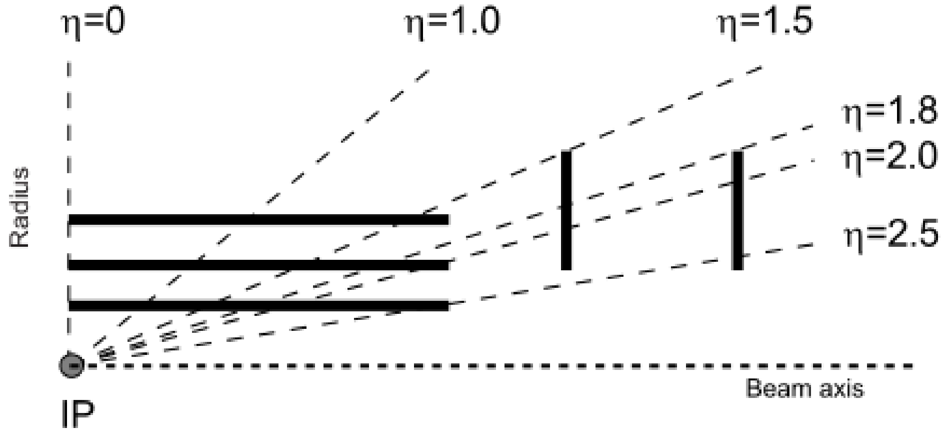

Figure 2.12: Geometrical layout of the pixel detector and hit coverage.

2.3.3 The calorimeter system

2.3.3.1 The electromagnetic calorimeter

Many interesting physics signatures involve photons or electrons in the final state. The electromagnetic calorimeter (ECAL) [56] of the CMS detector is a hermetic homogeneous calorimeter (Fig. 2.13). The choice of the materials and the geometric design have been optimized for the reconstruction of electromagnetic objects, with energies relevant for Higgs boson decays, at the intermediate region of Higgs boson mass values and it was based on the following considerations: $PbW0_4$ has a small radiation length (0.89 cm), small Molière radius[1] (2.19 cm) and high density (8.28 g/cm^3). The scintillation decay time of these crystals is of the same order of magnitude as the LHC bunch crossing time (about 80% of the light emitted in 25 ns). These requirements led to a compact calorimeter with fast response, high granularity and good energy resolution. It has been observed that some of the crystals are problematic thus degrading the energy resolution or decreasing the geometric acceptance of the detector. For this reason we made a study including the development of algorithms that estimate the accommodated energy of such problematic crystals, when a particle impinges in their vicinity. An overview of this study can be found in Appendix D.

ECAL is divided into the barrel covering a pseudorapidity range of $|\eta| < 1.479$ and two endcaps at $1.479 < |\eta| < 3.0$. The endcap part includes a preshower detector covering the region $1.65 < |\eta| < 2.6$.

---

[1] the radius of a cylinder containing on average 90% of the shower's energy deposition.

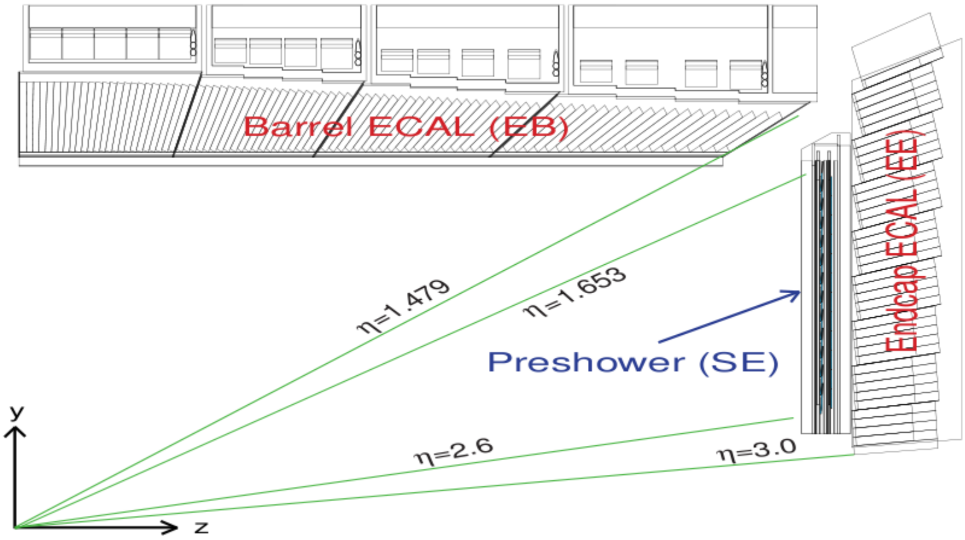

Figure 2.13: Geometrical layout of the electromagnetic calorimeter, showing the arrangement of barrel modules and supermodules, endcaps and the preshower.

The ECAL barrel (EB)

The EB forms a cylinder with an inner radius of 1.3 m and is made of 61200 lead tungstate ($PbWO_4$) crystals of a tapered shape, slightly varying with position in η. The crystals are mounted with a 3° angle with respect to the vector from the nominal interaction point in order to avoid alignment of particle trajectories with the inter-crystal gaps. These gaps, known as "crack" refer to the transition region between the barrel and the endcap and are used for cabling and other services. The crystal cross-section corresponds to approximately 22×22 mm^2 at the front face of crystal, and 26×26 mm^2 at the rear face. The crystal length is 230 mm (25.8X_0), while the barrel crystal volume is 8.14m^3 and the relevant weight is 67.4 t. EB consists of 36 supermodules each segmented into four modules across η. Furthermore, matrices of 5×5 crystals share the front-end electronics and form "trigger towers". With this topology, EB is effectively 360-fold in ϕ and (2×85)-fold in η. The EB is closed by 7324 crystals in each of the two endcaps (EE).

The ECAL endcap (EE)

The EE consists of identically shaped crystals grouped in mechanical units of 5×5 crystals (SCs) consisting of a carbon-fibre alveola structure. Each endcap is divided into two halves (Dees), while groups of 5×5 crystals form mechanical "units" called supercrystals. Each Dee consists of 3662 crystals, with a front face cross-section of 28.62×28.62 mm^2, a rear cross-section of 30×30 mm^2

and a length of 220 mm (24.7 X_0). Avalance photodiodes (APDs) are used as photodetectors (collect and amplify the scintillated light) in the barrel and vacuum phototriodes (VPTs) in the endcaps. The photodetectors need to be fast, radiation tolerant and able to operate in the longitudinal 4 T magnetic field.

The preshower detector (ES)

The ES is a sampling calorimeter with two layers: lead radiators initiate electromagnetic showers from incoming photons/electrons and silicon strip sensors placed after each radiator, which measure the deposited energy and the transverse shower profiles. Its principal aim is to identify neutral pions in the endcaps within a fiducial region $1.653 < |\eta| < 2.6$. Furthermore it helps the identification of electrons against minimum ionizing particles and improves the position determination of electrons and photons with high granularity. The total thickness of the Preshower is 20 cm. There are two lead planes (whose strips are orthogonally oriented), the first of which has a thickness of $2X_0$, while the second $1X_0$. The lead planes are arranged in two Dees, one on each side of the beam pipe, with the same orientation as the crystal Dees. Each one of the silicon sensors measures 63×63 mm^2, with an active area of 61×61 mm^2 divided into 32 strips.

For energies below 500 GeV, where shower leakage from the rear of the calorimeter starts to become significant, the energy resolution can be parametrized as:

$$\left(\frac{\sigma}{E}\right)^2 = \left(\frac{S}{\sqrt{E}}\right)^2 + \left(\frac{N}{E}\right)^2 + C^2 \tag{2.4}$$

where S is the stochastic term, N the noise term and C the constant term. The stochastic term describes the event-to-event fluctuations in the lateral shower containment, the photostatistics contribution (2.1%) and the fluctuations in the energy deposited in the preshower absorber with respect to what is measured in the preshower silicon detector. The noise term includes contributions of electronics, digitization and pileup noise, while contributions to the constant term comes from the non-uniformity of the longitudinal light collection, intercalibration errors and leakage of energy from the back of the crystal. Figure 2.14 shows the contributions from the different components of ECAL. Using test beam data [23], a typical energy resolution was found to be:

$$\left(\frac{\sigma}{E}\right)^2 = \left(\frac{2.8\%}{\sqrt{E}}\right)^2 + \left(\frac{0.12}{E}\right)^2 + (0.30\%)^2 \tag{2.5}$$

where E is in GeV.

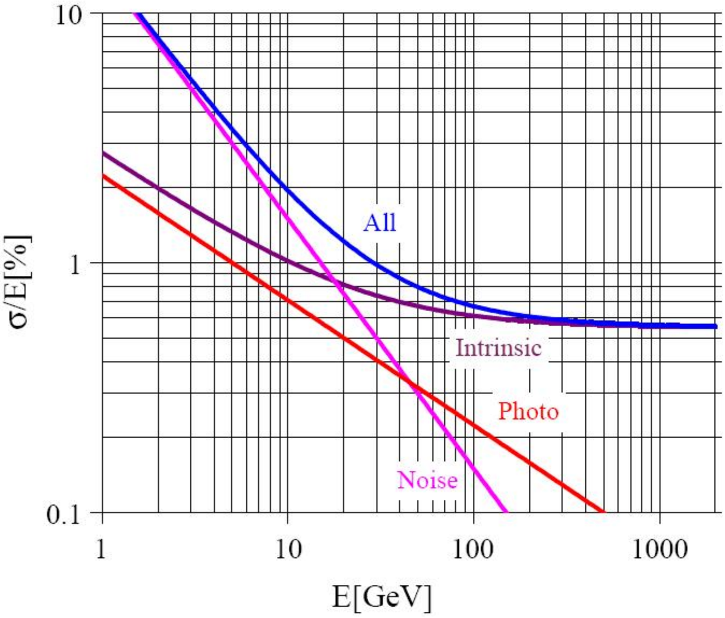

Figure 2.14: The ECAL energy resolution. The red curve ("Photo") refers to the contribution from the photo-statistics and the purple curve ("intristic") includes shower containment and the constant term.

2.3.3.2 The hadron calorimeter

The hadron calorimeter (HCAL) [57] is radially restricted between the outer extent of the ECAL and the inner extent of the magnet coil. This constrains the total amount of material which can be put in, to absorb the hadronic shower. Therefore, an outer hadron calorimeter (tail catcher) is placed outside the solenoid complementing the barrel calorimeter. Beyond $|\eta| = 3$, the forward hadron calorimeters placed at 11.2 m from the interaction point extend the pseudorapidity coverage down to $|\eta| = 5.2$ using a Cherenkov-based, radiation-hard technology.

The longitudinal view of the CMS detector is shown in Figure 2.15. The hadron calorimeters are very important for the measurement of hadron jets and neutrinos or other exotic particles resulting in apparent missing transverse energy. HCAL will also help the identification of electrons, photons and muons in conjunction with ECAL and the muon system. Thus HCAL is an essential subsystem of the CMS detector, contributing to to the most if not all of the CMS's physics studies. It is composed of four subdetectors (Barrel, Endcap, Outer and Forward).

The hadronic barrel (HB)

The HB is a sampling calorimeter located between EB and the CMS magnet. It covers a pseudorapidity range $|\eta| < 1.3$ and is divided into two half-barrel sections

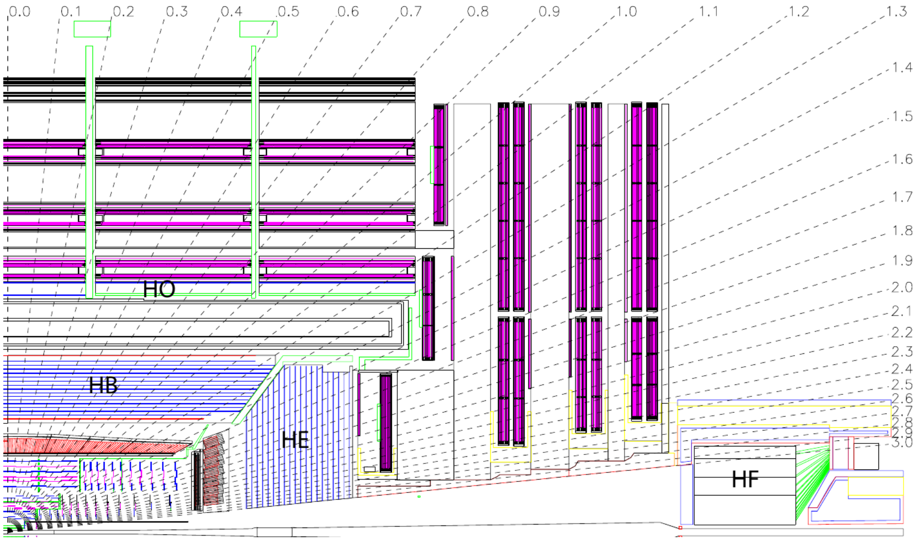

Figure 2.15: Geometrical layout of the hadron calorimeter, showing the locations of the hadron barrel (HB), endcap (HE), outer (HO) and forward (HF) calorimeters.

(HB+ and HB-) consisting of 36 identical azimuthal wedges. The wedges are constructed out of flat brass absorber plates with a thickness range of 40-75 mm and each one of them is segmented into four azimuthal angle (ϕ) sectors. The plates are bolted together in a staggered geometry resulting in a configuration that contains no projective dead material for the full radial extent of the wedge, while the wedges are bolted together in such a way as to minimize the crack between the wedges to less than 2 mm.

The hadronic endcap (HE)

The HE is placed inside the CMS magnet and for this reason it is made from non-magnetic materials. It covers a range $1.3 < |\eta| < 3$ and it consists of two endcaps attached to the muon endcap yoke, complementing HB. HE uses the same brass absorber plates with HB, but with a thickness of 79 mm. Between the absorber layers, 70 000 plastic scintillator tiles are used.

The hadronic outer detector (HO)

In the central pseudorapidity region, the combined stopping power of EB plus HB does not provide sufficient containment for hadron showers. Thus HCAL is extended outside the solenoid to ensure adequate sampling depth for $|\eta| < 1.3$. The HO uses the magnet coil as an additional absorber to identify late starting showers and to measure the shower energy deposited after HB. Outside the vacuum tank of the solenoid, the magnetic field is returned through an iron yoke consisting of five rings (along z-axis). The HO is placed as the first sensitive layer in each of these five rings. At $\eta = 0$, HB has the minimal absorber depth. Therefore, the central ring (ring 0) has two layers of HO scintillators at radial distances of 3.82 m and 4.07 m. All other rings have a single HO layer at a radial distance of 4.07 m. The total depth of the calorimeter system is thus extended to a minimum of 11.8 λ_I except at the barrel-endcap boundary region.

The forward hadronic calorimeter (HF)

The forward calorimeter (HF) is essentially a cylindrical steel structure constructed using 18 wedges, with an outer radius of 130.0 cm, located around the beam pipe at 11.2 m from the interaction point (IP), with a depth of 1.65 m and pseudorapidity range $3.0 < |\eta| < 5.0$. There are two main objectives with this detector: to improve the measurement of the missing transverse energy ($\mathrm{E}_{\mathrm{T}}^{\mathrm{miss}}$) and to enable identification and reconstruction of very forward jets. In order to withstand the extreme radiation at the high pseudorapidity region, the active medium uses quartz fibres (with fused-silica core and polymer hard-cladding) as the active medium, embedded in a copper absorber matrix at a distance of 5 mm from each other in both directions. The signal is produced via Cherenkov mechanism, when charged shower particles with energies above their respective Cherenkov threshold (e.g. 6190 keV for electrons) generate light, which is then leaded to the photomultipliers. This procedure is mostly sensitive to the electromagnetic component of showers, as it is mainly electrons which move at a speed close to that of light inside the medium. In addition, this mechanism renders the detector insensitive to the high neutron flux from showers initiated in the absorber.

The energy resolution of the CMS HCAL is parametrized as:

$$\left(\frac{\sigma}{E}\right)^2 = \left(\frac{90\%}{\sqrt{E}}\right)^2 + (4.5\%)^2 \tag{2.6}$$

$$\left(\frac{\sigma}{E}\right)^2 = \left(\frac{172\%}{\sqrt{E}}\right)^2 + (9.0\%)^2 \tag{2.7}$$

with the first equation describing the HB/HE resolution and the second the HF.

2.3.4 The muon detectors

Muon detection is a powerful tool for recognizing signatures of interesting processes over the very high background rate expected at the LHC with full luminosity. Therefore, precise and robust muon measurement was a central importance from the earliest CMS design stages. The muon system [58] performs three tasks; muon identification, momentum measurement and triggering. The muon system is designed to reconstruct the momentum and charge of muons over the entire kinematic range of the LHC and consists of three types of gaseous particle detectors; the drift tubes, the cathode strip chambers and the resistive plate chambers. It consists of about 25 000 m^2 of detection planes and about one million readout channels.

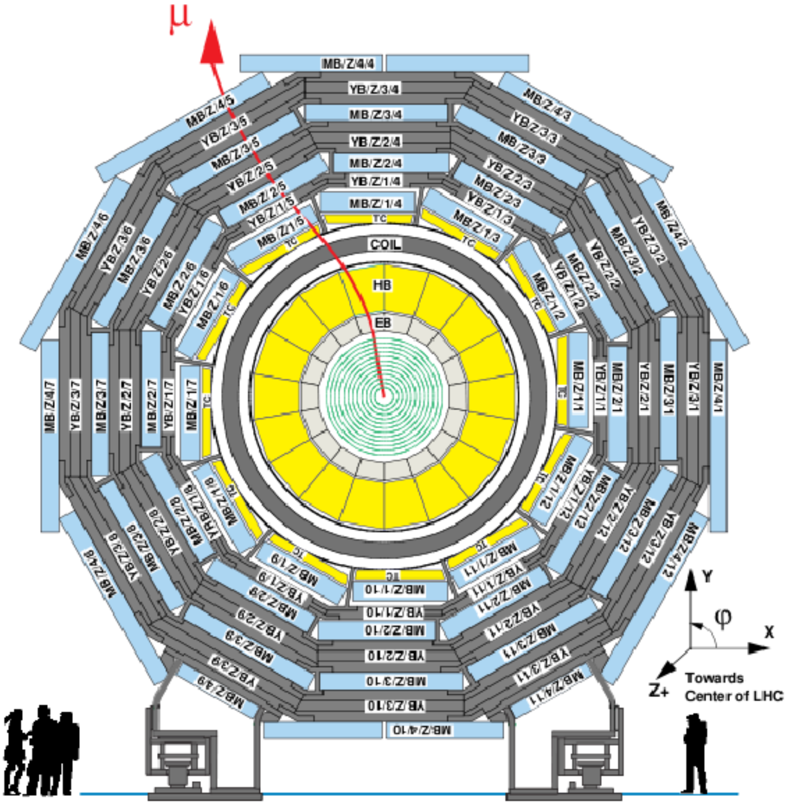

Figure 2.16: Geometrical layout of the CMS barrel muon DT chambers in one of the five wheels.

Drift tubes (DT)

The DT are located in the barrel region, where the neutron-induced background is small, the muon rate is low and the 4 T magnetic field is uniform and mostly contained in the steel yoke. They cover a pseudorapidity range of $|\eta| < 1.2$ and are organized into four stations. each one of the first three contains eight chambers (two sets of four), which measure the muon coordinate in the $r-\phi$ bending plane, and four chambers along the beam line to provide a measurement in the z direction. The fourth station does not contain the z-measuring planes. The two sets of four chambers in each station are separated as much as possible to achieve the best angular resolution. The drift cells of each chamber are offset by a half-cell width with respect to their neighbor to eliminate dead spots in the

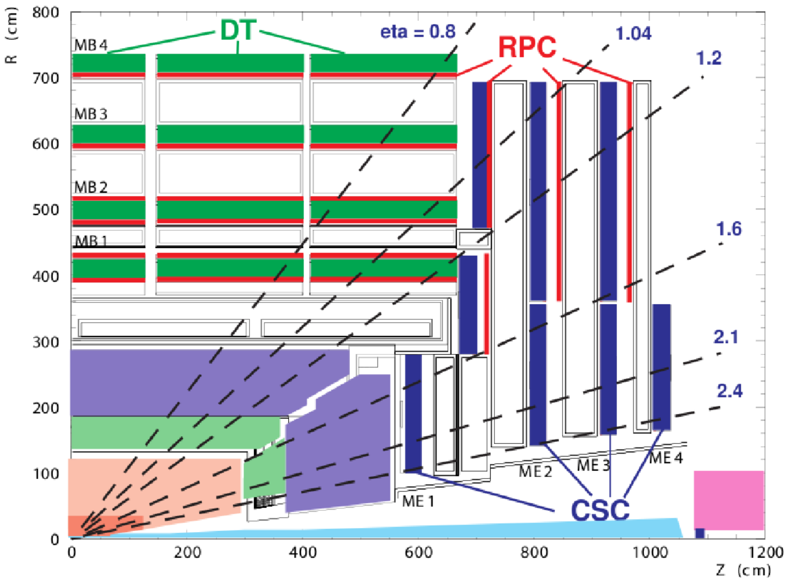

Figure 2.17: Schematic layout of one quadrant of the CMS muon system in the r-z plane showing DT, CSC and RPC subdetectors.

efficiency and providing also a convenient way to measure the muon time with excellent time resolution, using simple meantimer circuits, for efficient, standalone bunch crossing identification. The number of chambers in each station and their orientation were chosen to provide good efficiency when linking together muon hits from different stations into a single muon track and for rejecting background hits.

Cathode strip chambers (CSC)

In the two endcap regions of CMS, where the muon rates and background levels are high and the magnetic field is large and non-uniform, CSCs are used. CSCs have fast response time, fine segmentation, and radiation resistance, allowing them to identify muons in a region $0.9 < |\eta| < 2.4$. There are four stations of CSCs in each endcap, with chambers positioned perpendicular to the beam line and interspersed between the flux return plates, providing a precision measurement in the $r - \phi$ bending plane. The anode wires run approximately perpendicular to the strips and are also read out in order to provide measurements of η and the beam-crossing time of a muon. Each 6-layer CSC provides robust pattern recognition for rejection of non-muon backgrounds and efficient matching of hits to those in other stations and to the CMS inner tracker.

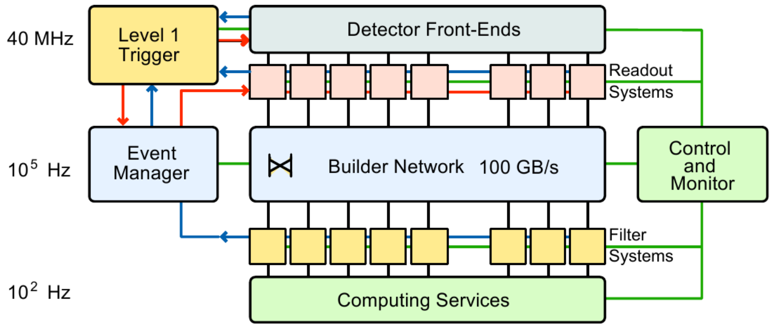

Figure 2.18: CMS Data Acquisition system architecture.

Resistive plate chambers (RPC)

Due to the uncertainty in the eventual background rates and in the ability of the muon system to measure the correct beam-crossing time at full LHC luminosity, a complementary trigger system of resistive plate chambers (RPC), gaseous parallel plate detectors was used to achieve redundancy and accurate time measurement (∼1 ns) for muon triggering. RPCs are installed both in the barrel and in the endcaps covering a region of $|\eta| < 1.6$ and providing a fast, independent, and highly-segmented trigger with a sharp p_T threshold. They also help to resolve ambiguities in attempting to make tracks from multiple hits in a chamber. A total of six layers of RPCs are embedded in the barrel muon system, two in each of the first two stations, and one in each of the last two stations. The redundancy in the first two stations allows the trigger algorithm to work even for low-p_T tracks that may stop before reaching the outer two stations. In the endcap region, there is a plane of RPCs in each of the first three stations in order for the trigger to use the coincidences between stations to reduce background, to improve the time resolution for bunch crossing identification, and to achieve a good p_T resolution. Finally, a sophisticated alignment system measures the positions of the muon detectors with respect to each other and to the inner tracker, in order to optimize the muon momentum resolution.

2.3.5 The trigger and Data Acquisition systems

The LHC provides proton-proton collisions every 25 ns, corresponding to a crossing frequency of 40 MHz. Depending on luminosity, approximately 20 pp collisions occur at each crossing of the proton bunches (or 10^9 interactions) at the nominal design luminosity of 10^{34} cm^{-2}s^{-1}. Only a small fraction of these collisions contain possible interesting events. Furthermore it is infeasible to store and process all this amount of data. Thus a drastic rate reduction has to be achieved; a task performed by the trigger system, which is the start of the physics event selection process. The rate is reduced in two steps; Level-1 Trigger [59] and High-Level Trigger [60]. The L1 trigger consists of custom-designed, largely programmable electronics, and reduces the rate to 10^5 Hz, while the HLT is a software system implemented in a filter farm of about a few thousand commercial processors, and finally reduces the rate down to the order of 100 Hz, which matches the storage capability (Fig. 2.18). This way, algorithms that are computationally expensive are only executed on interesting events.

2.3.5.1 Level-1 (L1) Trigger

The required rate reduction in the limited latency window of 3.2 μs is achieved by the L1 Trigger which uses coarsely segmented data from the calorimeters and the muon system, while holding the high-resolution data in pipe-lined memories in the front-end electronics until the L1 decision is reached.

The L1 Trigger has local, regional and global components. The Local Triggers; Trigger Primitive Generators (TPG), identify energy deposits in calorimeter trigger towers and track segments or hit patterns in muon chambers. Regional Triggers determine ranked and sorted trigger objects such as electron or muon candidates in limited spatial regions, by combining their information and using pattern logic. The Global Calorimeter (GCT) and Global Muon Triggers (GMT) determine the highest-rank calorimeter and muon objects across the entire experiment and transfer them to the Global Trigger (GT) which decides the rejection or the acceptance of an event for further evaluation by the HLT. The decision is based on algorithm calculations and on the readiness of the sub-detectors and the DAQ, which is determined by the Trigger Control System (TCS). The Level-1 Accept (L1A) decision is communicated to the sub-detectors through the Timing, Trigger and Control (TTC) system. The architecture of the L1 Trigger is shown in Figure 2.19.

Calorimeter trigger

The TPGs sum the transverse energies measured in ECAL crystals or HCAL readout towers. In a region up to $|\eta| = 1.74$ each trigger tower has an (η,ϕ)-coverage of 0.087×0.087. The TPGs are transmitted through high-speed serial links to the RCT, which determines regional candidate electrons/photons, transverse energy sums, τ-veto bits and information relevant for muons in the form of minimum-ionizing particle (MIP) and isolation (ISO) bits. The GCT determines jets, the total transverse energy ($\mathrm{E_T}$), the missing transverse energy ($\mathrm{E_T^{miss}}$), jet counts, and $\mathrm{H_T}$ (the scalar transverse energy sum of all jets above a programmable threshold). It also provides the highest-rank isolated and non-isolated electrons/photons candidates.

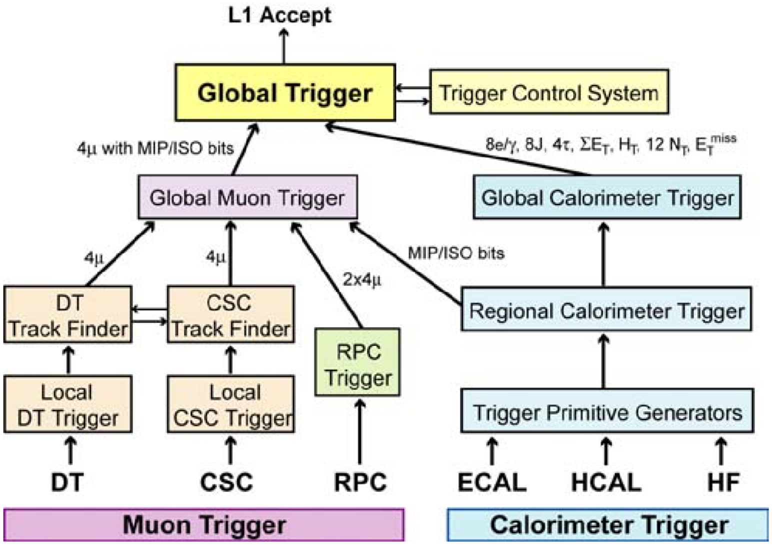

Figure 2.19: Level-1 Trigger architecture.

Muon trigger

All three muon systems (DT, CSC and RPC) take part in the trigger. The barrel DT chambers provide local trigger information in the form of track segments in the ϕ -projection and hit patterns in the η-projection. The endcap CSCs deliver 3-dimensional track segments. The bunch crossing from which an event originated is identified by all of these chamber types. The Regional Muon Trigger consists of the DT and CSC Track Finders, which join segments to reconstruct tracks. Furtheromre, the RPC trigger chambers, having an excellent timing resolution, deliver their own track candidates based on regional hit patterns. Afterwards the Global Muon Trigger combines the information from the three sub-detectors, achieving an improved momentum resolution and efficiency compared to the stand-alone systems. The pseudorapidity coverage of the muon trigger is $|\eta| \leq 2.4$.

Global Trigger

As already mentioned, the Global Trigger accepts or reject an event at L1 based on trigger objects delivered by the GCT and GMT. The GT has five basic stages: input, logic, decision, distribution and read-out. The core of the GT is the Global Trigger Logic (GTL) stage, in which algorithm calculations are performed. The most basic algorithms consist of applying p_T or E_T thresholds to single objects, or of requiring the jet multiplicities to exceed defined values. The results of the algorithm calculations are sent to the Final Decision Logic (FDL). For normal physics data taking a single trigger mask is applied, and the L1A decision is taken accordingly. A Timing Module (TIM) is also necessary to receive the

LHC machine clock and to distribute it to the boards. Finally, the Global Trigger Frontend (GTFE) board collects the GT data records, appends the GPS event time received from the machine, and sends them to the data acquisition for read-out.

Trigger Control System

The Trigger Control System (TCS) controls the delivery of the L1A signals, depending on the status of the sub-detector read-out systems and the data acquisition. The status is derived from signals provided by the Trigger Throttle System (TTS). The TCS also issues synchronization and reset commands, and controls the delivery of test and calibration triggers. It uses the Timing, Trigger and Control distribution network, which is interfaced to the LHC machine.

High Level trigger

HLT has access to the complete read-out data and can therefore perform complex calculations similar to those made by the off-line analysis software, if this is required for events with special interest. It is also divided into internal “steps”, named L-2, L-2.5 and L-3. Typically, a Level-2 trigger, which has the maximum rate of events input to it, uses only information from the calorimeter and muon detectors. In contrast. Level-2.5 triggers[2] refer to algorithms that use partial tracker information, e.g. pixel hits, for a fast confirmation of the electron candidate. "Level-3" refers to selection that includes the reconstruction of full tracks in the tracker.

2.3.5.2 The Global Trigger emulator System

In this section there is a presenation of the Global Trigger Processor Emulator System (GTPe) for the CMS Data Acquisition System (DAQ) [51, 53]; an apparatus developed and tested at Demokritos. It generates Level-1 pseudo-random triggers and exchanges information with other DAQ components. Its purpose is to decouple the Level-1 trigger system from the readout system, something that makes it an important component of the installation, testing and maintenance of the DAQ.

For every beam crossing (25 ns), the Global Trigger Processor (GTP) calculates up to 128 different trigger conditions and combines them to a Level-1 Accept (L1A) signal. The L1A signal is sent via the Timing , Trigger and Control (TTC) optical network to all the Front-End Drivers of the subdetectors. The detector Front-End electronics are read-out in parallel by multiple units which format and store the data in buffers. The buffers are connected to the processors in the High

---

[2] 2.5 attempts to indicate the intermediate nature of the selection, as one that occurs between the selection that is based solely on the calorimeter information, and the selection that is based on the full CMS detector information.

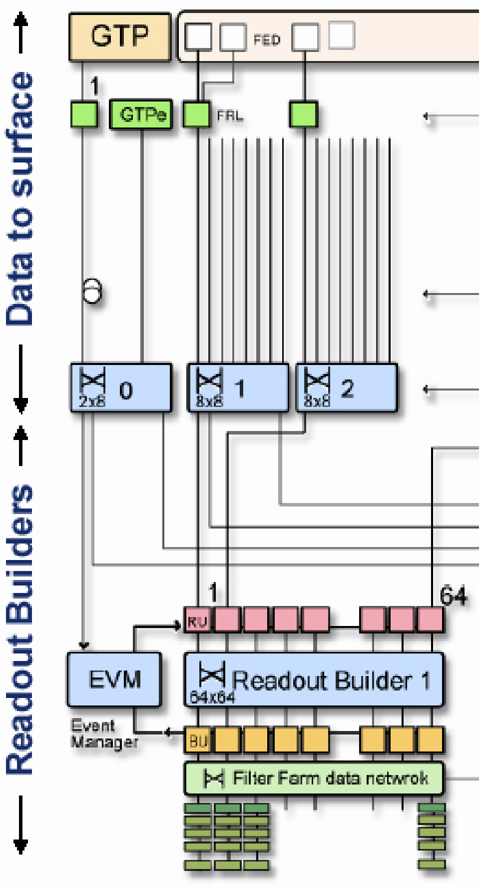

Figure 2.20: The GTP and the GTPe system in the CMS DAQ.

Level Trigger farm via the Readout Builder (switch network). Furthermore, it controls the delivery of L1A signals according to feedback signals through asynchronous (aTTS) and synchronous (sTTS) Trigger Throttling System. The data flow is completed by the Event Manager (EVM) and the Monitoring System. The EVM is responsible for the actual data flow through the DAQ, while the Monitoring System is responsible for the configuration, control and monitoring of all the elements.

As it is seen in Figure 2.18 the DAQ is composed of eight vertical slices (DAQ partitions), each of them capable of operating more or less independently from the others. The detector is divided in 32 sub-detector parts any combination of which can also form a DAQ partition. Since the system can accomodate up to eight DAQ partitions, there are eight EVM, Readout Builders etc. The GTP drives all eight DAQ partitions in parallel although only one partition is triggered (randomly according to its preset frequency) at any given time.

In order to test and commission the central DAQ system independently of the GTP and of the DAQ subdetector systems, a number of additional components, one of which is the GTPe, has been developed. During normal data taking

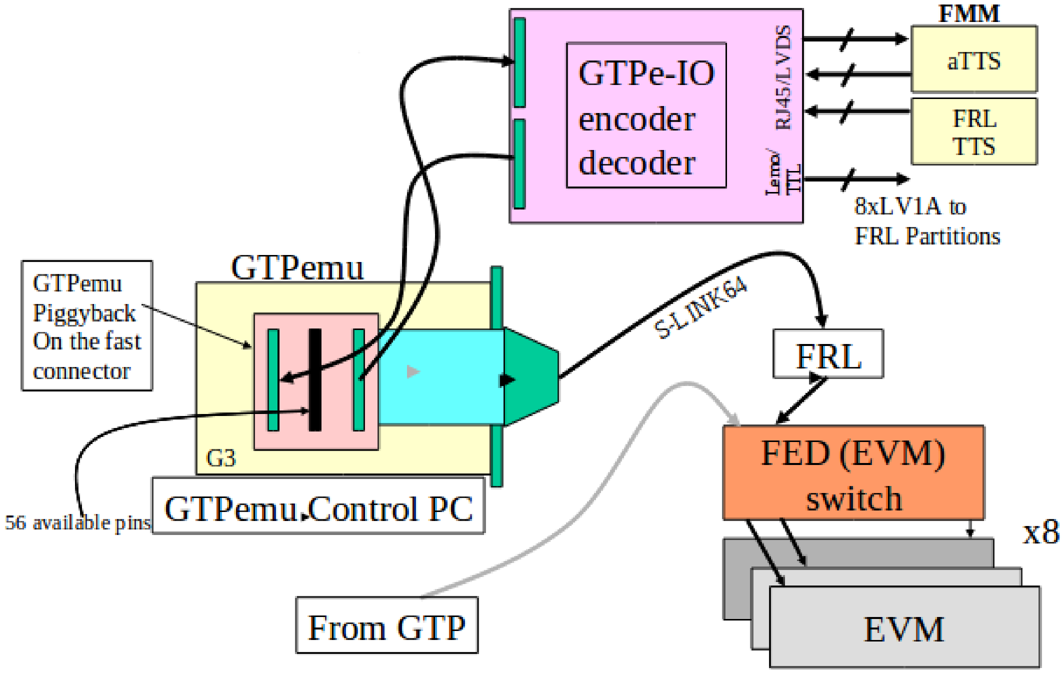

Figure 2.21: The GTPe schematics and interfaces (GTPe-IO and S-Link64 to EVM).

mode, triggers from the global trigger are distributed to the FEDs via the TTC. The GTPe is a part of the final DAQ system connected in parallel with the GTP system. It emulates the functionality of the GTP and guaranties that the sequence of L1A is compatible with the trigger rules (see Table 2.1) that lead to the minimization of the likelihood of buffer overflow of the sub-detectors.The hardware implementation is based on a generic, multi-purpose PCI card (Generic-III), specially designed for GTPe and an interface module GTPe-IO (LV1 distribution, sTTS and aTTS). The beam structure signal (BX) is fed to the Level-1 generator module (L1_Gen), which recieves the DAQ partitions definition and their associated frequency settings from the PCI bus. The DAQ partition definition specifies the sub-detector parts belonging to that partition. The L1_Gen receives feedback signals interpreted as inhibit of all L1A triggers from:

- DAQ partitions (aTTS_busy)
- Sub-detectors parts (sTTS_busy)
- The simple Link Interface in a Common Mezzanine Card (S_LINK64) controller (LFF or EVM_BUSY)
- The internal cyclic Write_Evm event buffer (WR_buf)

The PCI controller provides PCI communication plus registers for control, status, error and reset operations. For example the user can start, stop and reset the GTPe by accessing the command register (GTPe_cmd) or select the sub-detector parts belonging to a DAQ partitiom and set the trigger rate by accessing the partition definition register. The S_LINK64 protocol is used in order to transfer the GTPe data fragments. Upon the reception of the write enable S_LINK64 command from the PCI controller, the S_LINK64 controller initiates the reading of the local FIFO, so that the data start to flow to the receiver side. Backpressure signal LFF is sent to the L1_Gen module when the receiver cannot accept more data or the receiver is not running. Figure 2.21 shows the general GTPe schematic.

Table 2.1: Trigger rules

Detectors	**Trigger rules**
All sub-detectors	At least one empty BX between subsequent triggers
Pixel, Tracker, Muons, CSC	At least 2 empty BXs between subsequent triggers
HCAL	No more than 22 triggers per orbit
Pixel	Empty orbit after a period of one second
Preshower	No more than 1+13 triggers over the service time of 5.4 μs

To conclude, the GTPe performes the following tasks:

- Emulation of the LHC proton beam structure.
- Generation of trigger summary pseudo-data, encapsulated in the FED Common Data Format, to be sent to the FED Builder.
- Random or clocked generation of L1A triggers for each partition. These are generated at a user-defined frequency in a range of 0 Hz to 123 kHz, timed to coincide with non-empty beam crossings. L1A triggers are sent directly to the FRL crates via a lemo cable to a trigger distributer card which distributes the trigger over the backplane to all the FRLs in the crate.
- Partitioning. As it was mentioned above, there are eight DAQ partitions, each one of them can include any combination of subdetector's parts.
- Transmition of the GTPe data fragment over S_Link64.
- Receipt of backpressure signals from DAQ partitions (aTTS) and from sub-detectors' parts (sTTS).
- Transmission of status signals to the run control.

Figure 2.22: Picture of the GTPe modules tested at Demokritos before sending to CERN.

In this way, the GTPe is a necessary tool for the deployment of the DAQ system, particularly concerning its partitioning capabilities as well as for testing the DAQ components performance. It is also used for debugging and upgrating purposes in the final DAQ system.

Performance Tests at Demokritos

A GTPe test-bench has been set up in order to test the performance of the system. It is based on a Linux PC hosting with a PCI bus. GTPe is implemented on a specially built GIII card and pushes event fragments, via the S_LINK64 CMS cards, into a second GIII card (receiver) plugged into another similar PC.

In order to control GTPe, two applications have been developed, one based on Labview and another based on a C_language Hardware Access Library. Both applications can be used in standalone mode but the latest is more aiming at the integration in the TriDas control system.

Using this test-bench, two different sets of tests have been performed. For the first test, GTPe runs in full speed (more than 100 kHz), but with a slow readout rate limited to 20 kHz. The slow event consumption causes a highly frequent backpressure to GTPe. Data arriving via the S_LINK64 are dumped onto the receiver PC's hard disk and can be analyzed offline in order to verify that the system responds adequately to the S_LINK64 backpressure and that the LHC beam structure is reproduced correctly.

The second test includes fast readout measurements and on the fly data analysis at full speed. Trigger number, partition event number and trigger rules have been verified for a large number of accumulated events (up to 2×10^9) for trigger rates from 8 kHz to 123 kHz (per partition) and for different DAQ partition and subdetectors partition schemes (up to 8 partitions). Omitting the trigger rules, the trigger rate was pushed up to 5 MHz and no malfunction was observed, hence, the system has been proven to run properly in extreme conditions. The synchronization of the L1A signal with the corresponding events, using an event fragment has been verified using an external fast CAEN counter timer. Moreover, the event timing has been tested at various trigger rates.

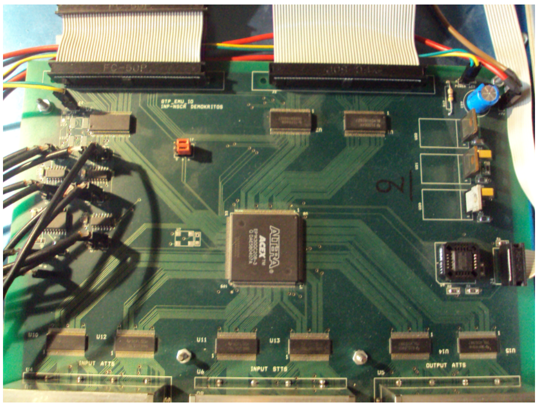

Figure 2.23: Picture of the GTPe-IO unit tested at Demokritos.

In the second test, fast readout measurements have been taken, and data are read and analyzed online at full speed. Trigger number, partition event number, and trigger rules have been verified for a large number of accumulated events (up to 4×10^9). The tests have been performed for trigger rates from 10 to 250 kHz, and for different DAQ and subdetector partition schemes.

Chapter 3

Study of the micromegas detector for the sLHC

Sometimes glass glitters more than diamonds because it has more to prove.

-Terry Pratchett-

The micromegas (MICRO MEsh GAseous Structure) detector [34] is a new generation gaseous detector with promising properties such as very good spatial ($< 100\mu$m) and time (few ns) resolutions, radiation hardness, high counting rates, good energy resolution, robustness and possibility to built large areas, which make it suitable for use in several applications. It has already been used in many particle physics experiments such as COMPASS [35], NA48 [36], nTOF [37], CAST [38] and other TPC applications [39]. R&D is carried out for using micromegas as tracking detectors (e.g. Muon Chambers) in the super LHC environment, since they are devices that would combine precision measurements and trigger functionality in the same detector.

3.1 Particle detection in gaseous detectors

The micromegas detector is a member of gaseous detectors' family [47, 48] and thus we will proceed with a brief walk through history. Details about phenomenology of particle detection in a gas can be found in Ref.[95, 96] and references within. One of the first questions that was raised since the discovery of the electromagnetic radiation, was how to detect it. The idea of gaseous detectors seems to be obvious because of the greater mobility of electrons and ions in the gas medium.

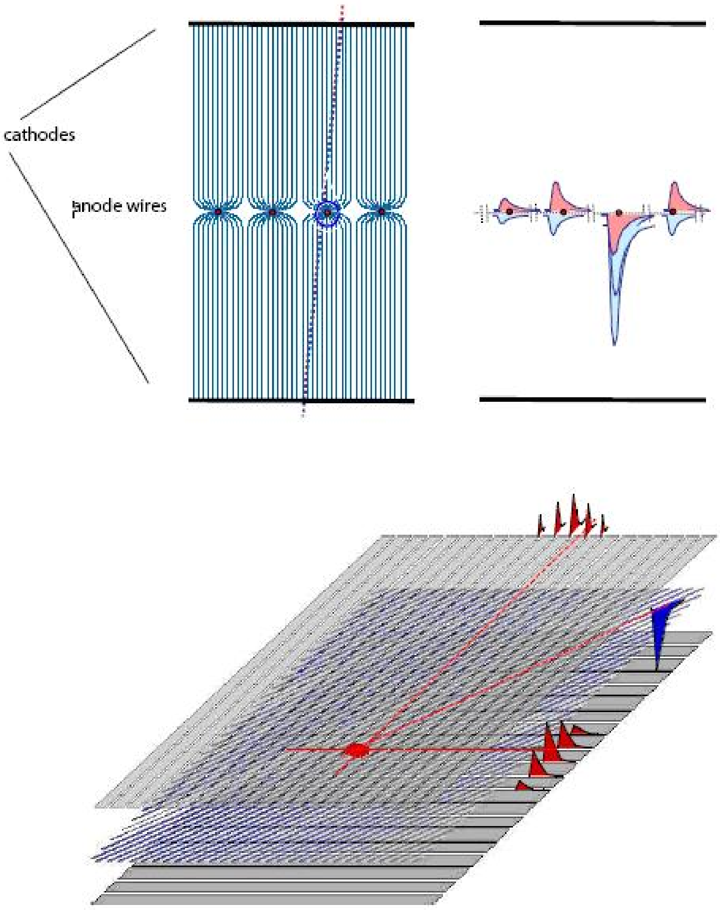

Figure 3.1: The top left figure shows the electric field lines in a MWPC (a plane of equally spaced wires placed in the middle of two cathode planes. The top right figure shows the signal induced in the closest wire as well as the neighbouring ones. The bottom figure shows that the implementation of a second plane of wires, placed perpendicular to the first, results to the increase in the spatial information

During the second half of the 20th century, three basic types of gaseous detectors were developed: the ionization chamber, the proportional counter and the Geiger Müller counter, followed by the invention of the MultiWire Proportional Chamber (MWPC) by Charpak in 1968 (Nobel Prize in 1992).

Among the main characteristics of the MWPC lies the excellent energy resolution, the good space resolution (few hundred μm) and the rate capability that is quite satisfactory with 10^4 counts mm^{-2}s^{-1}. Apart from applications in particle physics experiments, MWPC is widely used in fileds like X-rays for medical imaging, neutron and crystal diffraction studies and others.

In the top left part of Figure 3.1 we can see the electric field lines in a multiwire proportional chamber. More specifically a plane of equally spaced wires is shown. Typical distances between the anode wires are 1-4 mm, while the range between the two cathode planes varies from 5 to 15 mm. The plane is placed in the middle of two cathode planes. The electrons produced in the constant field region, drift towards the closest anode wire, where under the force of the higher field they will be accelerated and finally produce an avalanche. The top right figure illustrates the induced signal in the closest wire, where it is negative and in the neighbouring where it is positive. The figure at the bottom shows that the implementation of a second plane of wires, placed perpendicular to the first, results to the increase in the spatial information.

Triggered by MWPCs, scientists soon realized that they could get spatial information by just measuring electron's drift time (see 3.1):

$$x = \int_{t_0}^{t_1} u \mathrm{d}t \tag{3.1}$$

where t_0 is the particle's arrival time and t_1 is the moment the pulse arrives to the anode. It is more than obvious that a constant drift velocity is preferable and thus a constant electric field, since it results to a linear relation between time and distance. In the chamber shown in Figure 3.2 this is achieved with the help of additional wires between the anodes. Thus with the help of a trigger detector to signify the particle's arrival time, and measuring the drift time of the electrons, the lenght of its path could be easily deduced.

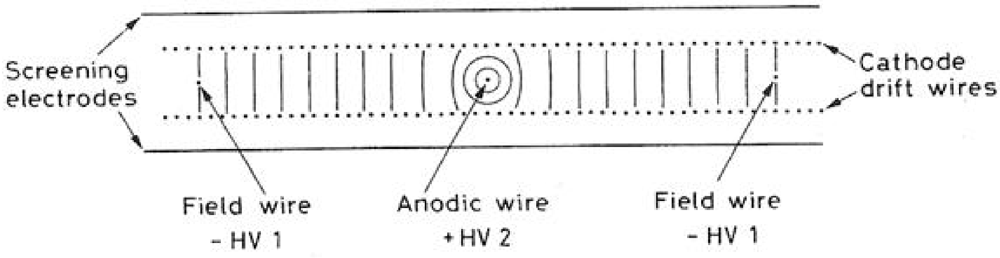

Figure 3.2: Schematics of a drift chamber. Space information is acquired by measuring electrons' drift time towards the anode.

A more sophisticated device that combines the features of both the MWPC and the drift chamber is the Time Projection Chamber (TPC) (Fig. 3.3), which gives three dimensional information of the particle. The MWPC logic with the anodes and cathodes give information on the two dimensions, while the third dimension is deduced from the drift time. The problems -with these chambers- began when better resolution and higher rate capabilities were asked, due to fundamental limitations; wires can not be placed closer without meeting functional problems and as far as rates are concerned the positive ions were not evacuated fast enough.

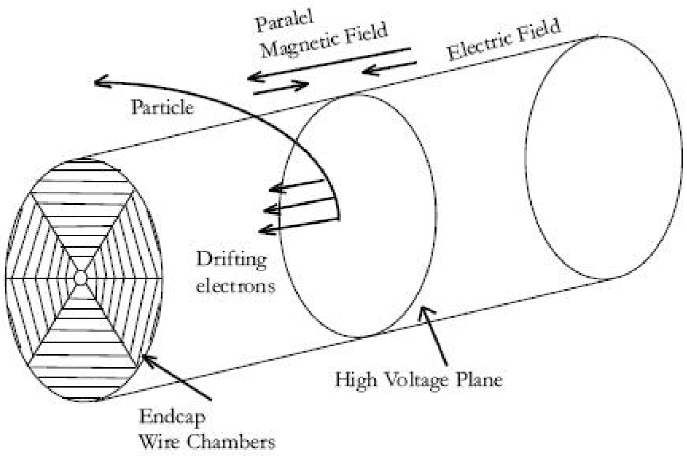

Figure 3.3: Schematics of a TPC. It is a cylinder with a thin electrode in the middle, creating a uniform electric field along the axis. To minimize diffusion, a magnetic field parallel to the electric, forces the electrons to spiral paths about the field direction.

An attempt to cover these limitations was made with the invention of Micro-Strip Gas Chambers (MSGC) [49] by Oed in 1988. The anode plate is replaced by an insulating or semi-insulating substratum plate with an engraved structure of very thin metallic strips. Because of the form of the electric field, the ions produced by the avalance are rapidly evacuated, increasing the counting capacity of the chamber 100 times above the relevant achieved by the MWPC. They were used in many high-luminosity experiments, but they were susceptible to aging effects and discharge damages.

Micro-Pattern detectors were the next step, which took advantage of the new technology in micro-electronics and photolithography. In this category belongs the micromegas detector (1996) invented by I. Giomataris and J. Collar.

3.2 Principles of operation

The micromegas detector is a high gain gaseous detector. The most important difference between this detector and the previous is the micromesh; the two well distinguished regions (conversion and amplification gap) are no longer separated by a plane of wires but by a micromesh.

A schematic view of the detector is illustrated in Figure 3.6. The operation principle can be described as follows. As it is clearly seen in this figure, the drift electrode is the first part that a particle has to cross. As soon as a particle passes it, it is already inside the *conversion* region (with typical distances 3-5 mm), which

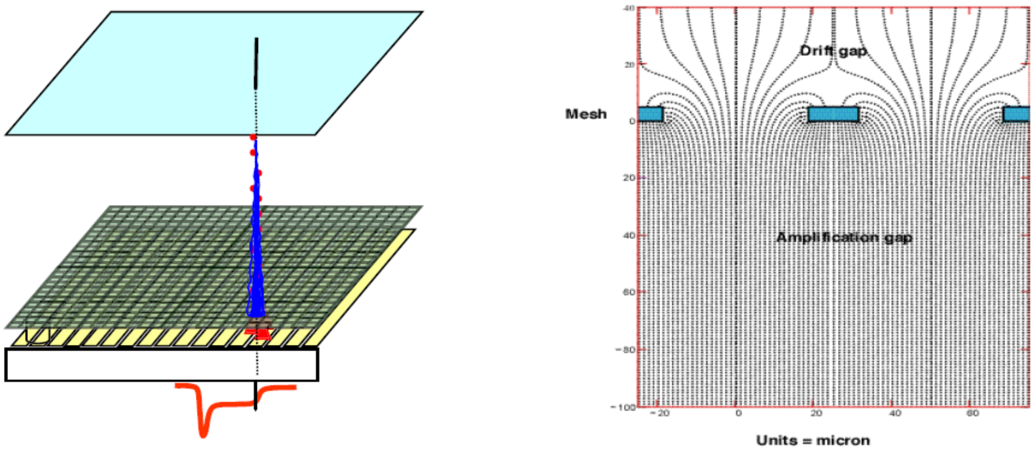

Figure 3.4: Principle of a micromegas detector; Schematic representation of the passage of a particle passing through the detector's volume (left) and Map of the electric field lines around the micromesh (right).

stretches up to some mm until the micromesh, with a rather weak electric field (of the order of 1 kV/cm). This is the region where the primary ion-electron pair production takes place. The next region is the *amplification* gap (with typical distances of the order of 100 μm) that is separated from the conversion region by the micromesh. However the role of the micromesh is more important than this. It is made of copper with a process relying on photolothography. Figure 3.5 (right) shows a picture of a micromesh taken with a microscope; 25 μm openings with a pitch of 50 μm. The voltage applied to it has to be high enough (up to 500 V) to result a big enough ratio between the electric field in the amplification gap over the relevant in the conversion gap. A big enough but appropriate ratio guarantees the higher electron transmission to the amplification gap, where the process of avalanche starts. The electric field achieved here is very high (up to 50 kV/cm). Providing a smooth way for the electrons to the amplification

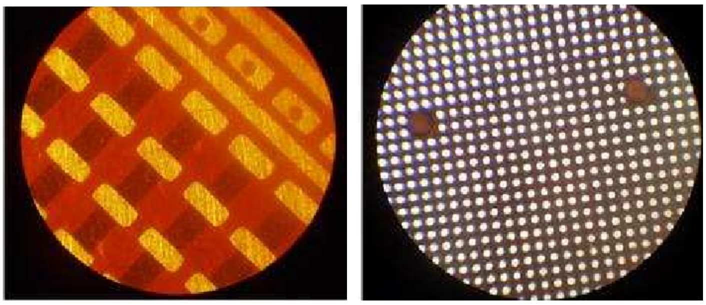

Figure 3.5: Pictures of the strips (left) and the mesh (right) taken with a microscope.

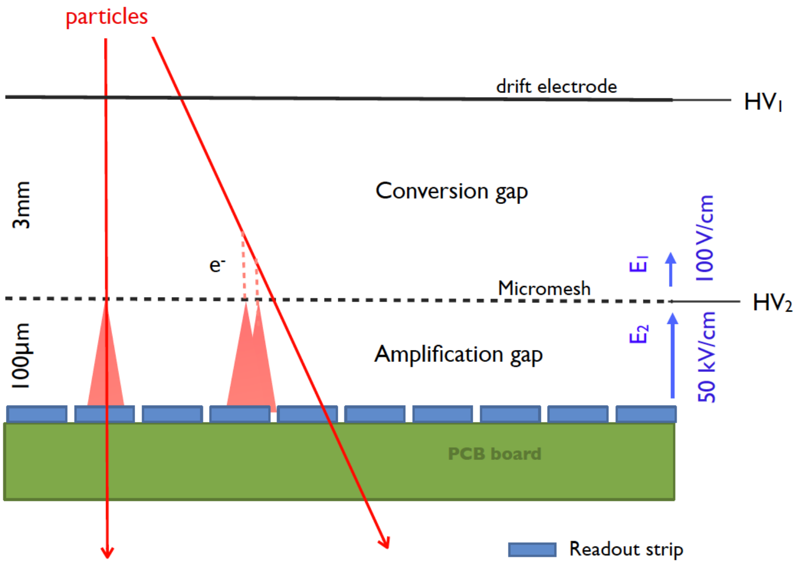

Figure 3.6: Schematic view of a micromegas detector.

gap, the micromesh also prevents the ions produced by the avalance to enter the conversion gap. Finally the electrons end up to the anode electrode. The anode electrode consists of cooper strips grounded through low-noise charge preamplifiers of high gain to an isolating layer usually made of kapton.

To sum up, the introduction of the micromegas detectors includes the following advantages:

- Very good spatial resolution ($< 100\mu$m).
- Fast response. Due to the strong electric field and the very small amplification gap, the ions are rapidly collected, suppressing any space-charge effects.
- High counting rates (of the order of 10^6 Hz mm^{-2}) due to the fast evacuation of the ions and the high granularity of the mesh.
- Radiation hardness.
- Good energy resolution.
- Robustness.
- Possibility to built large areas.
- As a result of the constant field along the amplification region, the signal detected in the anode is equally due to the ions and the electrons, contrary to the wire chambers.

- Any mechanical imperfection on the stretching of the micromesh above the strips is compensated, leading to essentially steady gain. The following relation gives an approximation of the change in the amplification factor M for a given amplification gap d:

$$\frac{\delta M}{M} = Pd(1 - \frac{Bd}{V})\frac{\delta d}{d} \tag{3.2}$$

where P is the pressure, V the applied voltage and B a constant depending on the gas used. For d decreasing and constant pressure, the multiplication factor increases up to a maximum and then decreases for higher values of d. The combination of the amplification gap and the applied voltage in the Micromegas detectors is such, that the multiplication factor is maximized, so fluctuations due to defects of flatness between the mesh and the anode plane are canceled.

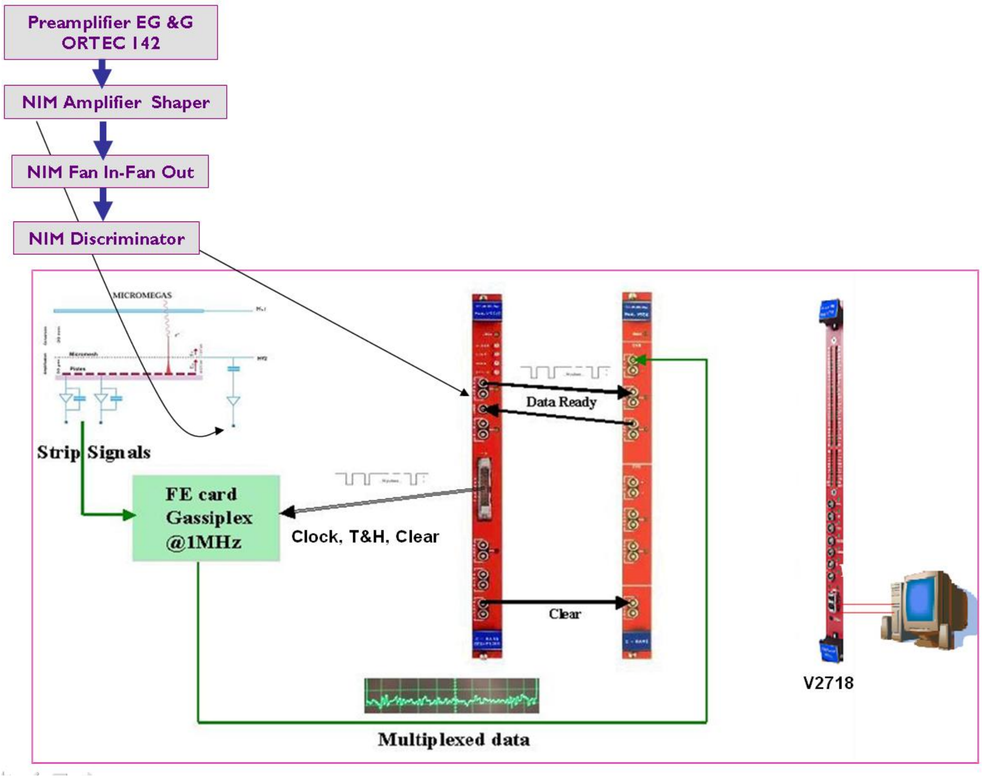

Figure 3.7: A simplified Trigger and Readout logic is depicted.

3.3 Readout electronics and the Data Acquisition (DAQ)

The trigger and Readout logic is depicted in Figure 3.7. In order to proceed to the different tests, the Micromegas detector mesh was connected to a preamplifier (EG&G ORTEC 142IH). The amplifier gives a pulse which is lead to a Fan In - Fan Out module. From this module two signals can be taken, one for the energy measurement and another which is lead to a discriminator (N96). The discriminator gives a NIM pulse (-0.8 V) that is used as a trigger to the Data Acquisition System. The trigger signal is received by a sequencer (V551B) [42] which produces control signals (Clock, Track & Hold, Clear) for the Gassiplexes and also produces the control signals for the CRAMs (V550) [41]. It receives a Data Ready signal if there are data on the CRAMS and clears the CRAMS modules at the end of the readout of an event. The CRAMs modules store the data in FIFOs and they can also apply a threshold cut and a pedestal subtraction per individual channel. The control signals of the Gassiplexes come from the Sequencer through a NIM-TTL-NIM level adapter (N89). Another very important module for this set up, is the module V2718 which is a 1-unit wide 6U VME master module, able to be interfaced to the CONET (Chainable Optical NETwork) and is controlled by a standard PC equipped with the PCI card CAEN Mod. A2818. The A2818 is a 32-bit 33 MHz PCI card (from which the data are taken) and the communication path uses optical fiber cables as the physical transmission line [44].

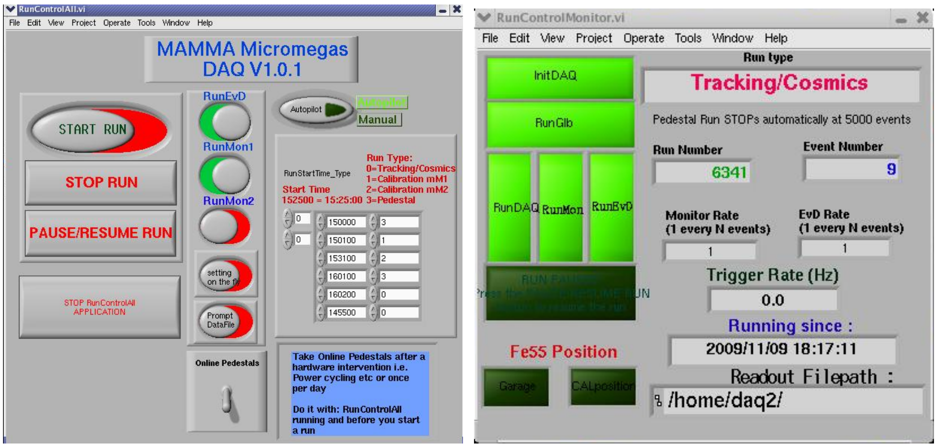

RunStartTime_Type

Start Time
152500 = 15:25:00

Run Type:
0=Tracking/Cosmics
1=Calibration mM1
2=Calibration mM2
3=Pedestal

0 150000 3
0 150100 1
153100 2
160100 3
160200 0
145500 0

Take Online Pedestals after a hardware intervention i.e. Power cycling etc or once per day

Do it with: RunControlAll running and before you start a run

Run type: Tracking/Cosmics

Pedestal Run STOPs automatically at 5000 events

Run Number: 6341

Event Number: 9

Monitor Rate (1 every N events): 1

EvD Rate (1 every N events): 1

Trigger Rate (Hz): 0.0

Running since : 2009/11/09 18:17:11

Readout Filepath : /home/daq2/

Figure 3.8: The control panel of the Data Aquisition System based on Labview.

The data acquisition and monitoring (see Fig. 3.8 and Fig. 3.9) system is based on the LabView software package of National Instruments [46] and it can run on a PC with either a Linux or a Windows (2000, XP) operating system. The data acquisition performs 3 tasks: 1) recording the events (all strip charges),

2) displaying the events and 3) online monitoring. A more detailed description of the Data acquisition system can be found in Ref. [96] Another system was also used in order to digitize the mesh signal, based on a Multichannel Analyzer, which was consequently analyzed with the ADMCA software and the Root analysis CERN package.

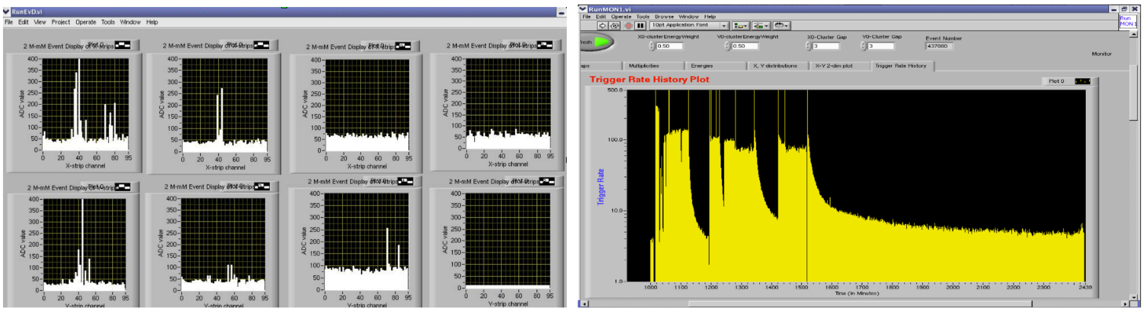

Figure 3.9: The left picture shows the event display diagrams (ADC value per strip for each one the four CRAMs - two channels per CRAM - thus this acquisition system can deal with 8 detectors) and the right shows the trigger rate history.

3.4 R&D on micromegas detectors

The micromegas detectors are proposed as one of the options to upgrade tracking detectors (e.g. Muon Chambers in the very forward/backward region) in the super LHC (sLHC) environment. In the High Luminosity LHC project, the luminosity upgrade is expected to be in two stages: phase-I with the luminosity increasing by a factor of three in a collision rate 3×10^{34} cm^{-2}s^{-1} and phase-II with a factor of ten. Thus the background (photons, neutrons, etc.) and the event pile-up probability are expected to increase in proportion in the different experiments, especially in the forward regions like, for instance, the muons chambers. This particular harsh background environment places a number of severe constraints on the performance of such detectors. For example counting rates will grow up to 20 kHz/cm^2 in the most unfavourable regions of the ATLAS muon system (Ref. [33] and references within). Based on background estimations at sLHC, a list of requirements for these new detectors has been established:

- High counting rate capability, including dense ionization.
- High single plane detection efficiency ($\geq$98%).
- Spatial resolution better than 100 μm, possibly up to large incident angles (45^o).
- Second coordinate measurement with a few mm precision.

Considering micromegas properties, detectors based on the micromegas principle should be a good altrenative for the detector upgrade in the high luminosity LHC framework. In the following two sections there's a presentation of some of the studies made in a high flux neutron environment at NCSR Demokritos and high flux hadron environment at CERN.

3.4.1 Study of a micromegas detector in a neutron beam

A study of a tracking micromegas detector with high flux neutrons, focusing on the sparking properties, is performed for the first time. The neutrons are supplied by the Tandem accelerator, at the N.C.S.R. "Demokritos" in Athens, which can provide quasi monochromatic neutrons with energies up to 25.7 MeV. The first results of this study are presented [31, 32].

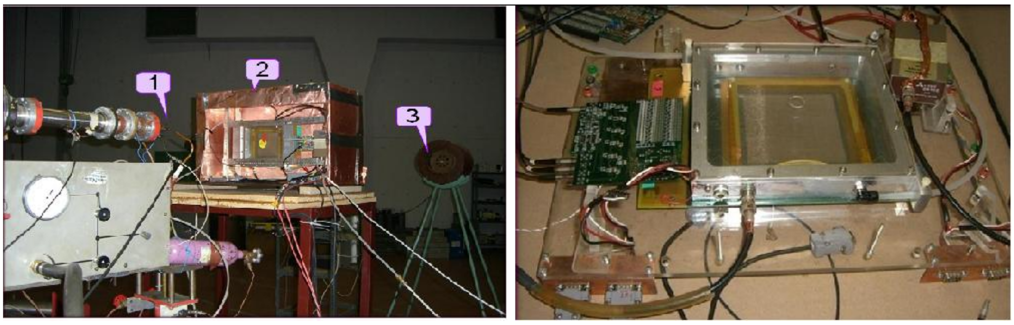

Figure 3.10: Part of the set up. The deuterium gas cell (1), the Faraday cage, the micromegas detector (2) and the neutron counter BF3 (3) are shown in this picture (left). The micromegas detector is shown. The preamplifier, the gas inlet and outlet pipes, the HV supplies and the gassiplex readout card are also visible (right).

This study refers to a prototype micromegas detector, in the framework of this R&D, which was tested in a neutron beam. The neutrons were produced through the reaction [D(d,n)^{3}He] and the Deuteron energies that were used were 2.8 MeV, 3.2 MeV, 3.7 MeV, 4 MeV and 4.3 MeV with corresponding neutron energies: 5.5 MeV, 5.9 MeV, 6.5 MeV, 6.8 MeV and 7.1 MeV respectively. The flux range was 2.4×10^5 cm^{-2} s^{-1} to 7.7×10^5 cm^{-2} s^{-1}. The detector shown in Figure 3.10 (left), consists of an aluminum frame and a 10×10 cm^2 bulk micromegas readout plane [40] with a one dimensional structure of 96 strips with a 1 mm pitch. The detector was enclosed in a Faraday cage when used in the neutron beam. The experimental setup in the beam area is illustrated in Figure 3.10.

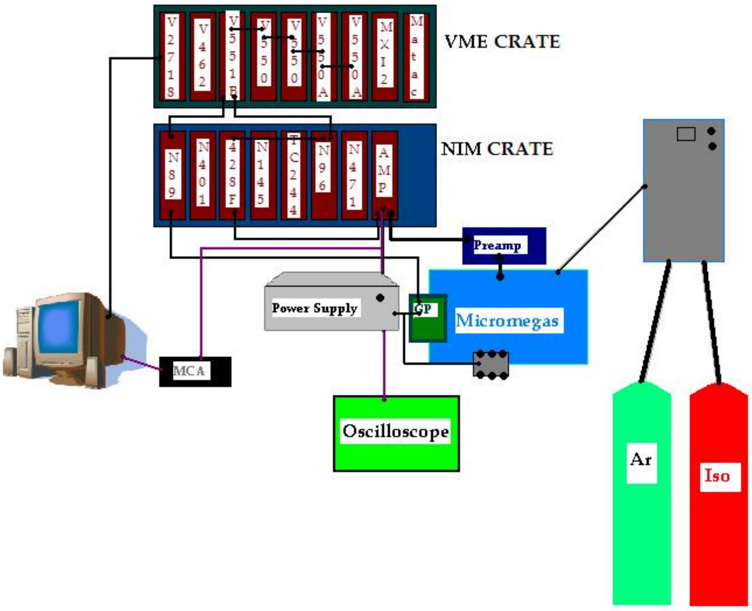

Figure 3.11: The schematic of the set-up is shown.

The detector is operated with an Argon/Isobutane (95% / 5%) gas mixture and is read out with the help of an electronic card using the Gassiplex chip and a VME based data acquisition system using a CAEN sequencer with four CRAM modules. The LabView software is used to control the Data acquisition and the monitoring of the detector performance. The detector was first studied with ^{55}Fe and ^{109}Cd sources and it was found to have a linear response and an energy resolution of about 30% FWHM at 5.9 keV. It was operated, for the neutron studies, with a gain of about 2000. The geometrical characteristics of the micromegas detector under test are listed in Table 3.1.

Table 3.1: The geometrical characteristics of the micromegas detector.

Strip lenght	10 cm
Strip pitch	1 mm
Strip width	0.9 mm
Amplification gap	128 μm
Conversion region	5 mm

A schematic of the general set up of the micromegas detector in the neutron beam is shown in Figure 3.11. Neutrons interact in the Micromegas chamber via very different processes (e.g. elastic scattering with Ar, C, H, inelastic (n,g), (n,n) processes, etc).

The recoil nuclei produce a high number of primary electrons that are amplified by a multiplication factor (Gain) of about 2000. The current of the mesh of the

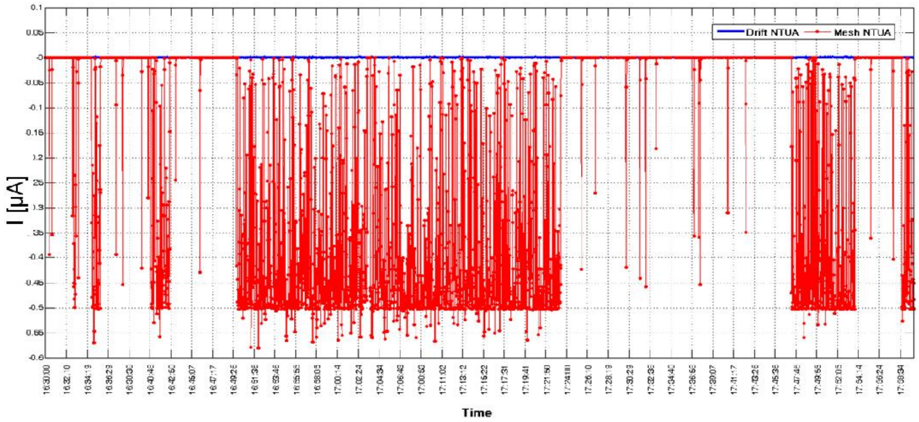

Figure 3.12: Monitoring of the mesh and drift current. Since the detector draws current, it was concluded that further development was needed for the design of the appropriate micromegas detector.

micromegas detector was monitored by FieldPoint (cFP-1804, cFP-AI-110 and cFP-CB-2) modules from National Instruments via the supervisory control & Data Acquisition (PVSS) software. The diagram in Figure 3.12 shows that the corresponding current, when the beam is on, is about 0.2 mA. This detector draws current and cannot operate efficiently. These results leaded to the conclusion that further development was needed for the design of the appropriate micromegas detector.The histogram illustrated in Figure 3.13 shows the rate of neutrons identified by a BF3 neutron counter, in a typical run. and it is clearly seen that the beam was very stable as a function of time. Since the frame of our detector was made of Aluminum, during the beam-on period we expected the Aluminum to be activated; the "deactivation" was observed after the end of the neutron radiation.

The diagram in Figure 3.14 illustrates the relevant measurement. The two exponential factors (t = 10.2±1.4 min and t = 2.3±0.2 min) correspond to the lifetimes of ^{27}Mg (9.46 min ^{27}Al(n,p)^{27}Mg) and ^{28}Al (2.24 min) from the (n,g) reaction respectively. Several fast de-excitation components are included in the first few bins and for this reason they are not included in the fitting. Figure 3.15 shows the energy spectra (mesh signal) that were acquired with a Multichannel Analyzer, after subtracting a fitted exponential contribution, attributed to photons. The yellow and black histograms correspond to calibration with ^{55}Fe (5.899 keV) and ^{109}Cd (weighted mean of K_{a1} and K_{a2} 22.103 keV), respectively. We have also taken measurements with and without deuteron target in the gas cell, in order to avoid parasitic neutrons[1]. The blue, green and violet (bottom to top) histograms correspond to the net neutron contribution (measurement of the chamber with

---

[1] neutrons produced via deuteron interactions with the materials of the gas cell

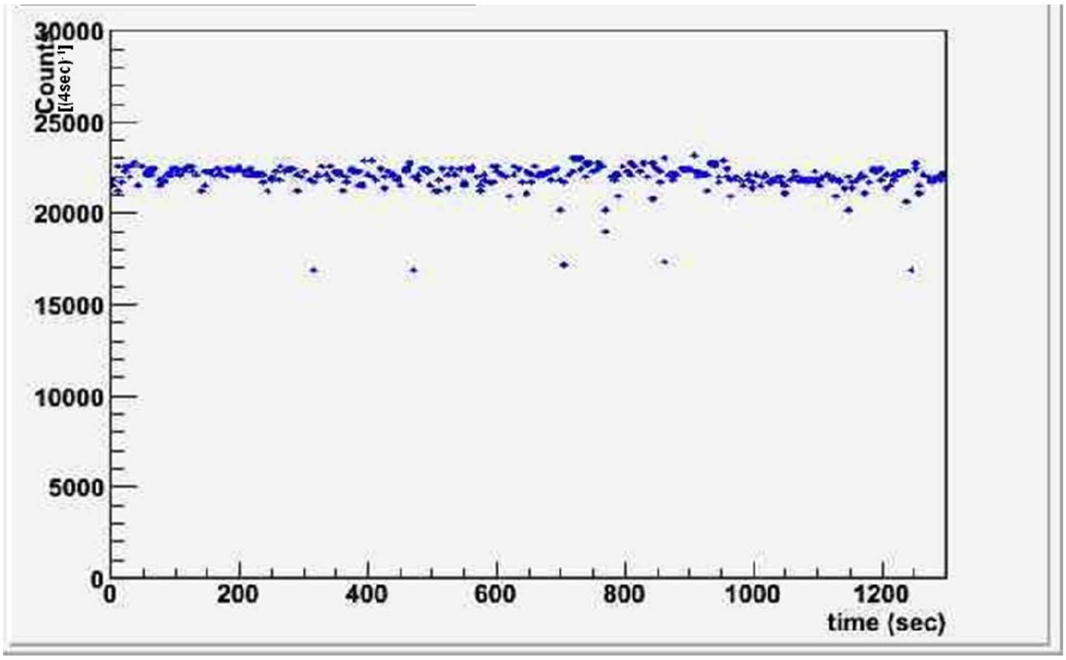

Figure 3.13: The number of neutrons per 4 seconds is identified by a BF3 neutron counter as a function of time.

deuteron target after subtracting the data without deuteron target) for various neutron beam energies. These curves represent the energy loss due to the elastic scattering of the neutrons off the detector gas nuclei. The average energy of the Ar ions is about 250 keV corresponding to about 500 µm mean path before it deposits all its energy into the gas chamber volume, thus it lies outside the current electronics dynamic range. As a result we only record the energy loss of the minimum ionizing particles. As the energy of incident neutrons is increased, the peak of the spectra is decreased as expected because of the dE/dx energy loss of the ions (mainly protons) into the chamber gas.

3.5 Study of resistive-anodes micromegas detectors

The aim of the study described in this section is to demonstrate that it is possible to reduce the discharge probability and protect the chamber and the electronics by using a resistive anode plane in a high flux hadrons environment [33]. Several prototypes of 10×10 cm^2, with different pitches (0.25 to 2 mm) and different resistive layers have been tested at CERN (π^+ at SPS). Several tests have been performed with a telescope at different voltages to assess the performances of the detectors in terms of position resolution and efficiency. The spark behaviour in these conditions has also been evaluated. Resistive coating has been shown to be a successful method to reduce the effect of sparks on the efficiency of micromegas.

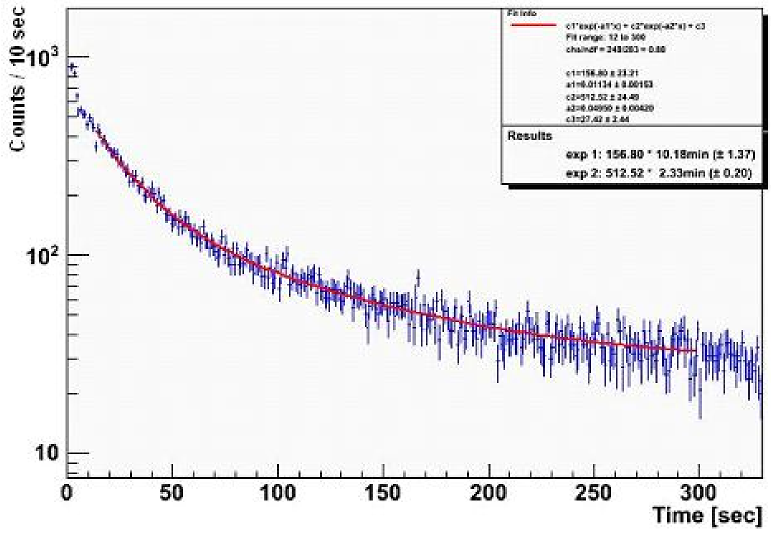

Figure 3.14: Micromegas chamber counting during the "deactivation" period. The 2 exponentials of the fitted red line are consistent with excitation of the ^{27}Al(n,g)^{28}Al (2.24 min) and ^{27}Al(n,p)^{27}Mg (9.46 min).

A good spatial resolution ($\sim 80\mu$m) can be reached with a resistive strip coating detector of 1 mm pitch and a high efficiency (>98%) can be achieved with resistive anode micromegas detector.

In standard micromegas detectors, as already discussed in section 3.2, a very high amplification field is applied in a very thin gap. In the sLHC environment, the high flux of hadrons can produce highly ionizing events that leads to large energy deposit and an increasing probability for sparks occurance. The problem with the sparks does not lie on the detector robustness or the electronics on which we can have a suitable protection, but on the dead time induced by the discarge of the whole micromesh. The dead time varies between 1 to 2 ms to recover the nominal voltage.

Resistive coatings on top of the read-out strips is one of the suggested solutions for reducing the effect of sparks. This technology was first used for the readout of Time Projection Chambers to spread out the signal of the avalanche and reduce the number of electronic channels. The micromegas structure is then built on top of the resistive strips or layer. During this test three different resistive-anodes and geometries configurations were studied:

- **Carbon-Loaded Kapton**: The plane of strips is covered with an insulating layer of 75 μm thickness, on which is glued a foil of carbon-loaded kapton. The strip pitch is 2.0 mm (Fig. 3.16-R10)
- **Resistive strip to ground**: The plane of the strips is covered with an

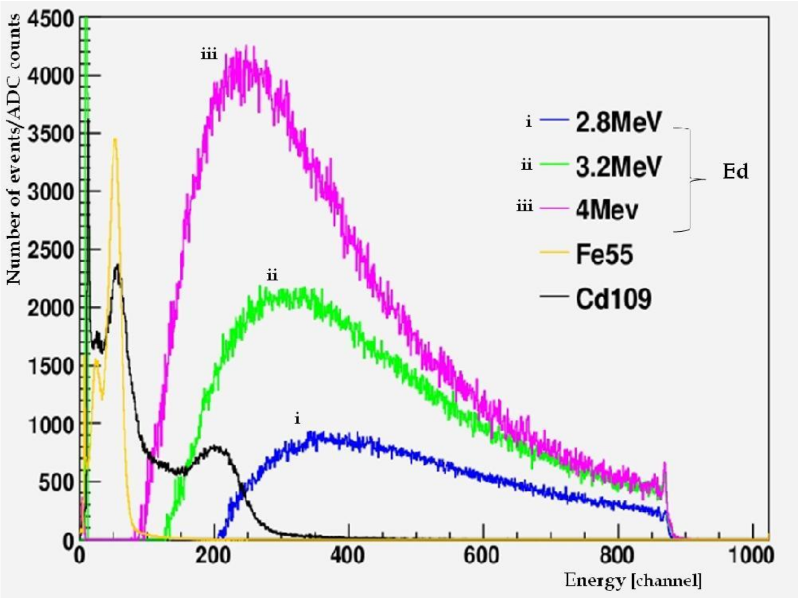

Figure 3.15: Energy spectra corresponding to the net neutron contribution and to the superimposed calibration with ^{55}Fe and ^{109}Cd. The lower energy peaks of the calibration spectra are due to fluorescence from the detector materials (Cu and Fe) and the Argon escape.

insulating layer of 64 μm thickness, on which resistive strips, matching the geometry of the copper strips, are deposited using a resistive ink. Each strip (strip pitch: 1.0 mm) is grounded through a resistor of 30 MΩ and the resistor along the strips is 250 MΩ (Fig. 3.16-R17)

- **Resistive strips**: On each copper-strip anode is deposited a resistive coating. The resistor along the strips is 300 kΩ (Fig. 3.16R12 (with strip pitch 0.5 mm) and R14 (with strip pitch 1.0 mm))

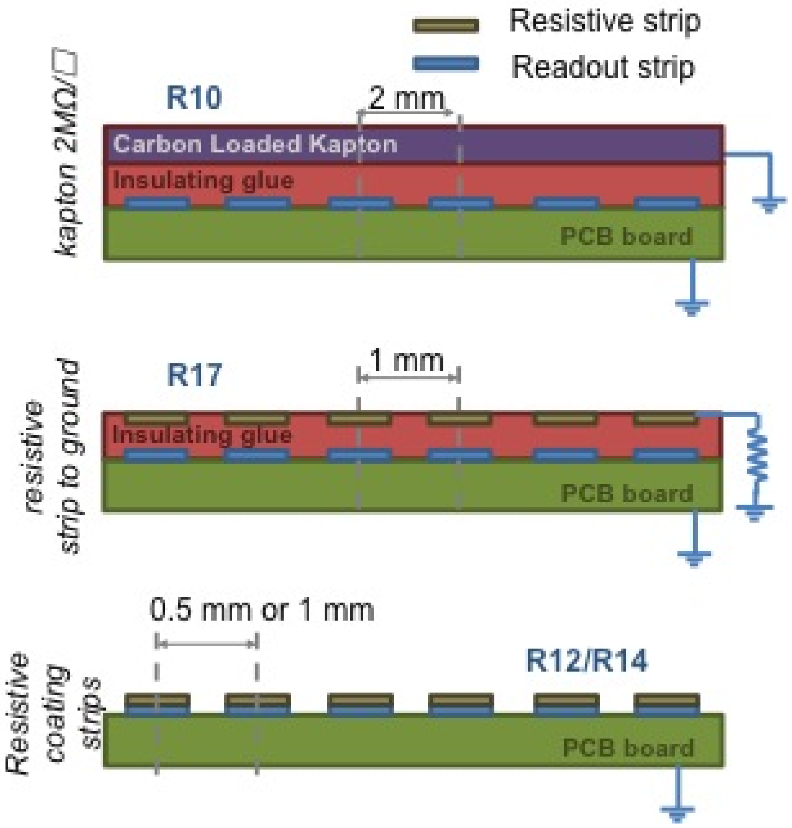

Figure 3.16: Geometry of the different resistive anodes technologies.

Part of this beam test setup is presented in Figure 3.17. The resistive anodes detectors, previously described, were exposed to 120 GeV/c pions beam at CERN SPS H6 area, during two weeks in autumn of 2010. A telescope consisting of 3 (X-Y) planes of standard micromegas was used to give an external reference measurement, on the plane normal to the beam direction. Additionally four resistive detectors were tested in a two (X-Y) configuration.

During the test beam, two different gas mixtures were used: 95%Ar + 2%C_4H_{10} + 3%CF_4 for the resistive chambers and 98%Ar + 2%C_4H_{10} for the telescope. The resistive detectors were tested with different high voltage values and mounted on a rotating structure, in order to collect data with different beam angle. The signal readout was performed with Gassiplexes electronics, with 96 channels multiplexed and a peaking time of 1.2 μs. The data acquisition system was based again on 4 C-RAMS modules driven by a sequencer from CAEN (see Section 3.3). The goal of these tests was to evaluate the performances of the resistive-anodes detectors and check the influence of resistive material on the spatial resolution and efficiency of the detector.

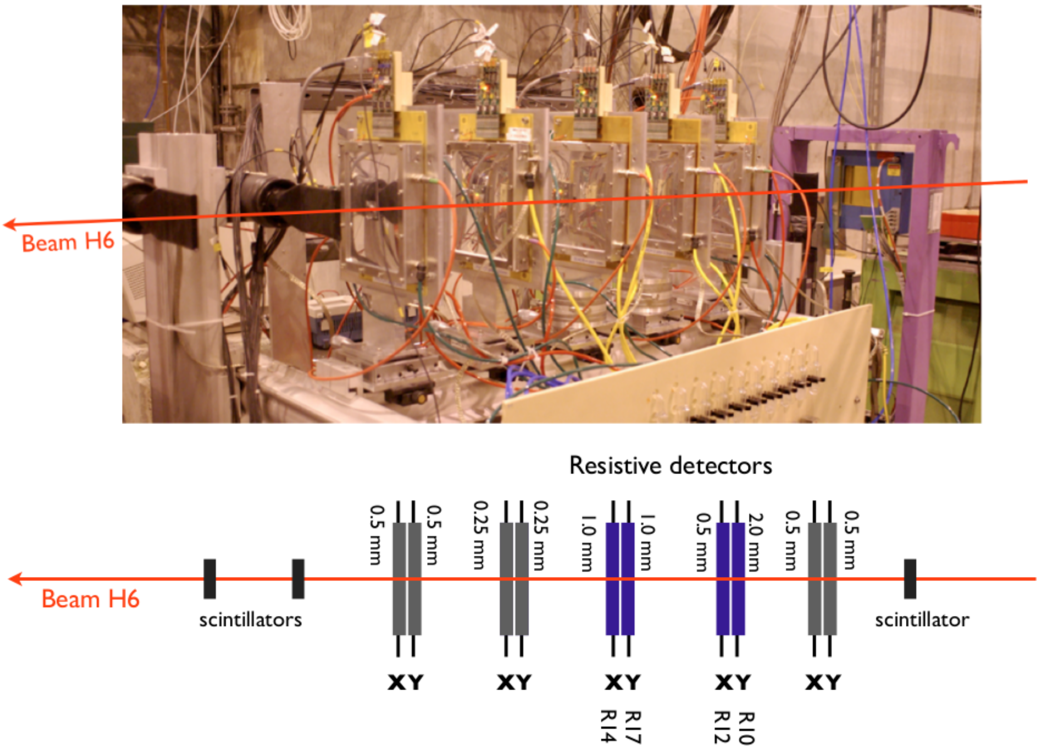

Figure 3.17: Picture and scheme of the test beam setup. The beam direction is indicated. The telescope is made of 3(X-Y) planes and 4 detectors are tested.

Spatial Resolution

The spatial resolution is calculated using reference tracks given by the telescope. The results plotted in the Fig. 3.18 are obtained by extrapolating these tracks at the level of the detector of interest. Then the distribution of the difference between the position measured and the position extrapolated is fitted by a gaussian curve of which the r.m.s. is the spatial resolution. This is clearly related to the pitch of the strips and the best resolution (88.1±0.7 μm) is obtained for a pitch of 0.5 mm.

Efficiency

The detector is considered as efficient when the measured position is within a window of $\pm 5\sigma_{mM}$ around the extrapolated position from the reference track of the telescope. The detection efficiency increases with the mesh voltage up to 98%, as it is seen in Figure 3.19 (left). From this plot it is clear that the detector with the resistive strips connected to the ground (R17) present the best efficiency results.

In order to get tracks with different incidence angles the detectors were

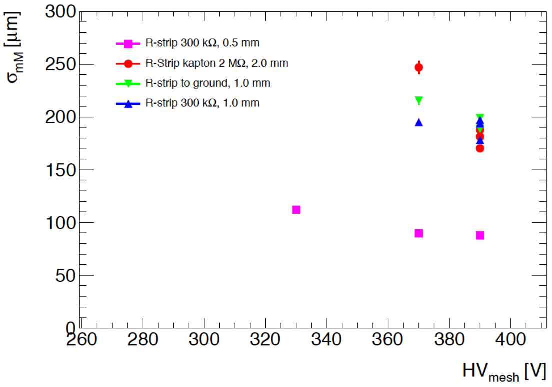

Figure 3.18: Spatial resolution as a function of micromesh voltages for four different resistive technologies.

rotated. As it is already discussed in Section 3.2, the signal is spread on several strips (depending on the strip's pitch) and this is one impact that deserves further study. Figure 3.19 (right) shows the efficiency at different voltages on the micromesh and incidence track angle, for the R-strip to the ground detector (R17). For normal incidence tracks, the efficiency is around 98%. For inclined tracks, the efficiency is of the same order and can be even better for low voltage values, because for inclined tracks the depth of gas is more important leading to more primary electron-ion pairs.

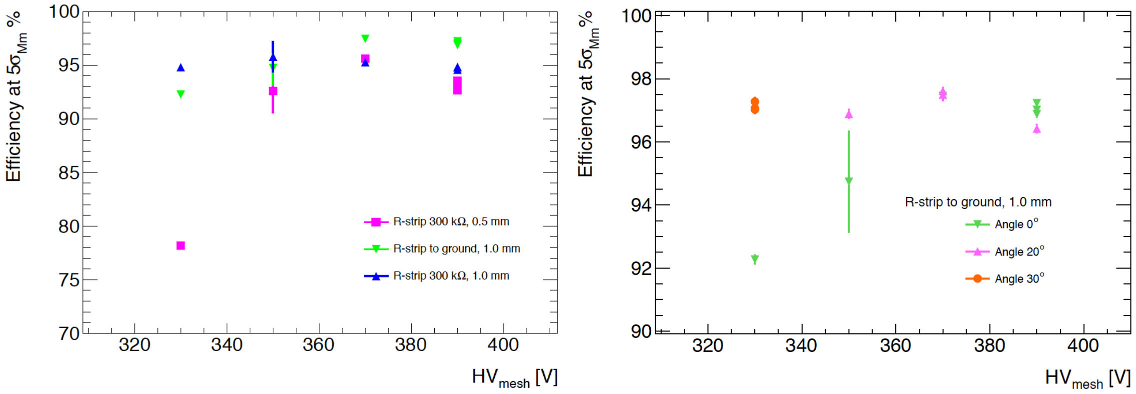

Figure 3.19: Efficiency as a function of micromesh voltages for an acceptance window of $5\sigma_{mM}$, for the different resistive technologies (left). Efficiency as a function of micromesh voltages at several incidence angles for the R-strip to the ground detector (right).

Sparks behaviour

During the ten days of the beam test, the voltages and currents were monitored by the power supply (CAEN SY2527). The results for the voltage and current on the mesh are given on Figure 3.20. For a standard Micromegas detector - on the left - many current peaks and so many sparks are visible (red curve). The current can go up to 1 or 2 μA and are related to many voltage drops (blue curve) of 10 to 20 V, that lead to a loss of efficiency of this detector. On the right, the same curves for the R-strip to ground detector (R17) show few sparks and very low current mainly corresponding to the charging up of the micro-mesh. For this detector there is no voltage drop thus no dead time and no loss of efficiency.

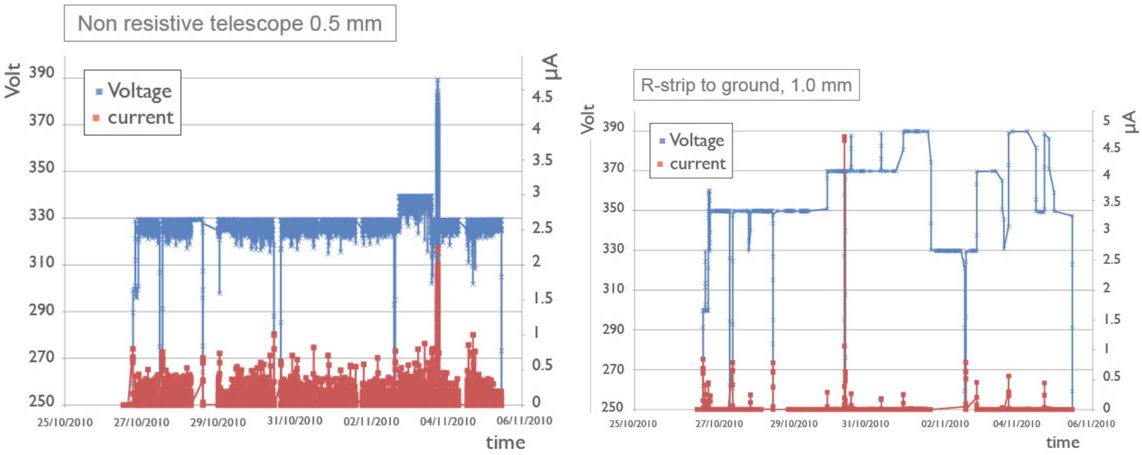

Figure 3.20: Monitoring of the micromesh voltages and currents of a standard (left) and the R-strip to the ground (right) detector for a ten days period.

To summarize, the different anode-resistive technologies that have been tested show very good performances, with a good spatial resolution (better than 100 μm for a pitch of 0.5 mm), a good efficiency (better than 95%) and an efficient reduction of sparks effects. The R-strip-to-ground technology (R17) seems to be the best candidate for the sLHC environment since it presents a better efficiency, a very good spark reduction (localization of the spark effect with no voltage drop and no dead time), a good spatial resolution achievable with a pitch of 0.5 mm, a better robustness (compared to R-coating) and no charging effect (compared to Carbon-Loaded-Kapton).

CMS Physics Analysis on final states with photons

Chapter 4

Event Simulation

> *You can avoid reality, but you cannot avoid the consequences of avoiding reality.*
>
> -Ayn Rand-

Simulated events are of great importance in checking and/or correcting for non-trivial or unforeseen detector or physics effects, as well as comparing the detector's performance with expectations. With the possible exception of the under study effect, simulated events should be as close as possible to real data events. Hence the primary goal of the simulation programme is to model closely the physical interactions involved, the detector performance, and the event reconstruction.

4.1 Monte Carlo Event Generators

Monte Carlo[1] simulation is a very important tool for designing particle detectors and for defining strategies in order to find signatures experimentally. Thus accurate simulation of both signal and background will play a key role in making discoveries at the LHC. The need for better simulation tools has spurred an intense activity that has resulted in several important advances in our ability to accurately simulate hard interactions. The full simulation chain of a collision at CMS consists of three steps:

- Event generation. It includes simulation of collisions produced by proton-proton interactions until the production of the final decay products. This includes modeling the subatomic makeup of a proton, the calculation of scattering amplitudes, the decay of unstable particles, and the hadronization of quarks and gluons into jets.

---

[1] named for the city because of its worldwide affiliation with gambling

- Detector simulation. It includes accurate description of the experimental setup (both in terms of materials and geometry). Furthermore the interactions between particles and matter must be simulated by taking into account all possible physics processes, for the whole energy range.
- Digitization. This step emulates the detector's electronics response.

4.1.1 Event generation

At the most basic level a Monte Carlo event generator is a program which produces particle physics events with the same probability as they occur in nature (virtual collider). Any production's cross section calculation, requires knowledge of the distribution of the momentum fraction x of the partons in the incoming hadrons in the relevant kinematic range. The probability of finding a proton constituent with a momentum fraction x, is described by the *Parton Distribution Functions* (PDFs). The particles of interest for the event (e.g. heavy quarks or hypothetical new particles, etc.) are generated by a simulated collision between individual partons which is referred as *hard process*. The production of these particles along with their subsequent decays, are described by *matrix elements*. The first step of the generation chain is the calculation of these matrix elements according to the Feynman rules in quantum field theory and afterwards the cross section of the under study hard process. The accelerated colored particles produce QCD radiation, resulting in *parton showers* called initial state radiation (ISR) -in case it originates from incoming partons- and final state radiation (FSR) -in case it originates from outgoing partons.

Due to color confinement, outgoing partons produced in the hard process cannot exist as free particles. Their kinetic energy is transferred to the color field, producing additional partons from vacuum. As a consequence parton showers, are grouped together into colorless hadrons -known as jets (details about the jet definition can be found afterwards in Section 5.1)- by means of a mechanism called *hadronization*. Apart from the hard scatter that creates the process of interest, the remaining partons of the incoming hard interaction protons along with additional pp interactions in the same beam crossing, represent the *underlying event* and contribute to what is called as background to our measurement.

During the previous steps, many of the produced particles are unstable, decaying into stable ones. Short-lived particles are decayed by the generator, while particles with longer lifetimes (enough to reach the detector) are left undecayed and passed as input to the next step. A schematic representation of a generated event is illustrated in Figure 4.1.

The event generators can be distinguished between "Automatized Matrix Element generators" (e.g. MadGraph) and "Parton Shower MC event generators" (e.g. PYTHIA). In the Table 4.1 there's a brief comparison between Matrix

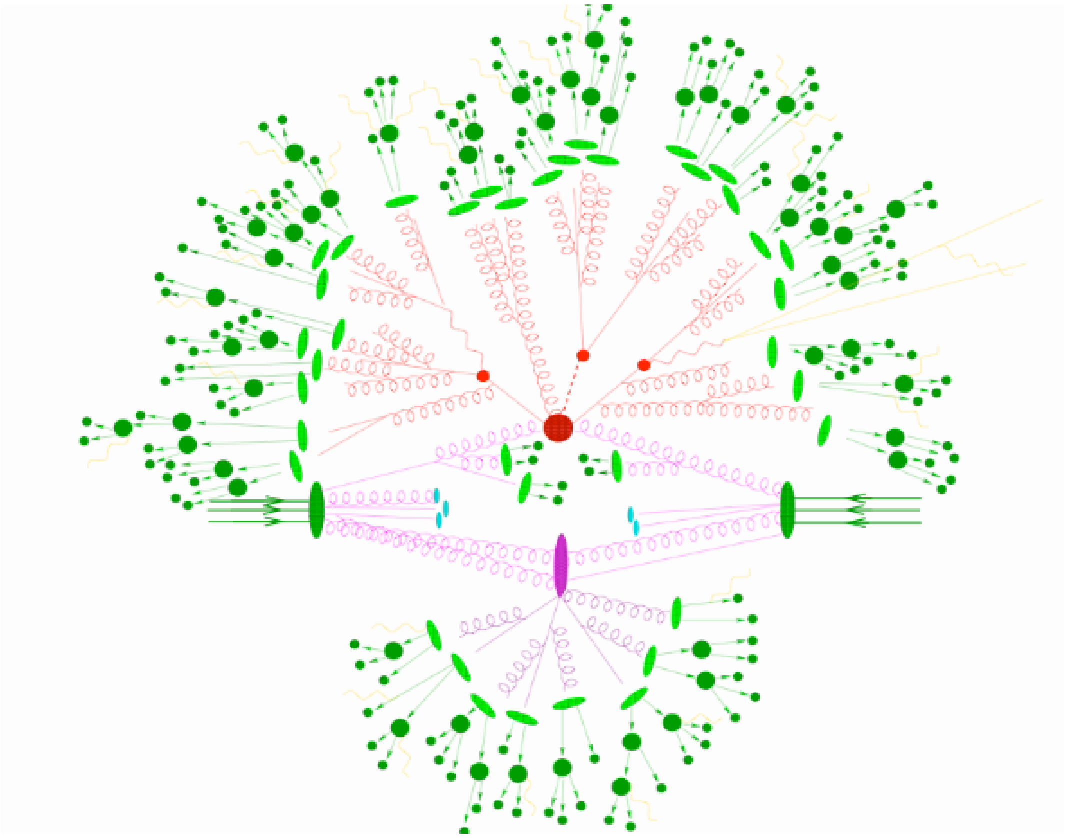

Figure 4.1: Schematic representation of a generated event. This includes hard collisions (red), soft multiple interactions (magenta), quarks and gluons hadronization and decays (green) and beam remnants (light blue).

Element and Parton Shower generators. Parton Shower generators, simulate every step of the event, including the initial interactions, parton showers, the underlying event, hadronization and lastly decays to final state particles. Cross sections are calculated to leading order (LO) only and generators like these are most suitable for processes with not more than two final state particles. On the other hand, Matrix Element generators are used for processes with complex multi-particle final states. They are specialized in modeling hard interactions and are capable of calculating next-to-leading order (NLO) corrections to matrix-elements. However, since they do not include hadronization, they have to be interfaced with other generators in order to produce the full event.

The PYTHIA generation

PYTHIA [27] is a general purpose event generator software program that contains theory and models and uses leading-order matrix elements to simulate a number of physics aspects, including hard and soft interactions, parton distributions,

Table 4.1: Comparison between Matrix Element and Parton Shower generators.

Matrix Elements	Parton Shower
Fixed order calculation	Resums large logs to all orders
Computationally expensive	Computationally cheap
Limited number of particles	No limit on particle multiplicity
Valid when partons are hard and well separated	Valid when partons are collinear and/or soft
Quantum interference correct	Only partial interference (through angular ordering)
Needed for multi-jet description	Needed for hadronization

initial and final state parton showers, multiple interactions, fragmentation and decays.

The MadGraph/MadEvent generation

MadGraph is a Matrix Element calculator [28] that allows us to generate amplitudes and events for any process in any model. Standard Model, Higgs effective couplings and MSSM are among the implemented models. It is also interefaced with a range of tools, including PYTHIA and PGS (detector simulation) as well as a Root event analysis package. The event generation with the MadGraph/MadEvent generator is divided in four steps: code creation, parton-level event, hadron-level event and reconstructed object generation.

Given a process, MadGraph/MadEvent returns a list of all contributing subprocesses along with Feynman diagrams for each subprocess. It automatically creates the amplitudes for all the relevant subprocesses and produces the mappings for the integration over the phase space. It allows the calculation of event cross sections and the generation of unweighted events for "any" tree-level processes. The event information of the generated events (particle IDs, momenta, spin etc.) is passed to CMSSW as parton level files in the standard Les Houches format (LHE). LHE files are passed to CMSSW through a MadGraphIntrerface. Within the interface package, PYTHIA takes care of the matching procedure of matrix elements to parton shower and of the fragmentation before passing the events to the simulation.

4.1.2 Detector simulation

After the simulation of the hard scattering event to final-state particles, it is necessary to model the detector's response to the produced particles. The simulation of the CMS detector is based on a toolkit called GEANT4 [29] used to model the interactions of the particles in the detector. The algorithm relies on a detailed description of the hierarchy of the subdetectors volumes and materials as well as magnetic fields. It knows which parts form the “sensitive“ detector (e.g. parts equipped with readout sensors) and which are the “dead parts“ (e.g. cables and cooling materials) and uses these information to determine the detector’s response to the simulated particles.

4.2 Standard Model Backgrounds of the “Photon(s)+ Jets+MET“ final state

A new approach is used to establish the presence of the signal over background and estimate the background from the data, the Jet-Gamma Balance (JGB) method, which is explained in more details in Chapter 6. Our topology of interest is at least one isolated photon, jets and $\mathrm{E}_{\mathrm{T}}^{\mathrm{miss}}$. This signature of SUSY signal events can be mimicked by various backgrounds. Processes with rare reconstruction effects but with huge cross sections, such as QCD photons plus jets, can give apparent $\mathrm{E}_{\mathrm{T}}^{\mathrm{miss}}$ due to detector resolution (poorly measured hadronic activity in the event, or missing particles in the pipeline or generally speaking outside the detector sensitive volume).

Another kind of background comes from processes with real $\mathrm{E}_{\mathrm{T}}^{\mathrm{miss}}$. For example processes like $t\bar{t}$ or electroweak events with a leptonic $W \rightarrow e\nu$ decay, where one electron can be misidentified as a photon and $\mathrm{E}_{\mathrm{T}}^{\mathrm{miss}}$ is produced due to neutrinos. Since the photon is expected to behave almost identically to an electron in the electromagnetic calorimeter, electrons can be mistaken as photons except that electrons have hits matching the particle track in the pixel detector. Drell Yan events can also contribute to this kind of backgrounds. Additional backgrounds can occur due to initial and final state radiation of photons. The dominant contribution is coming from $t\bar{t}$ or W/Z events with one or more neutrinos in the final state, while events where the W/Z bosons decay hadronically usually do not pass the Jet-Gamma Balance (JGB) requirement.

Although this analysis uses methods based on data to estimate the background components, simulated samples are used to validate the performance of the background estimation from data and to model the new physics signals. Details about the Background Monte Carlo samples are listed in Table 4.3.

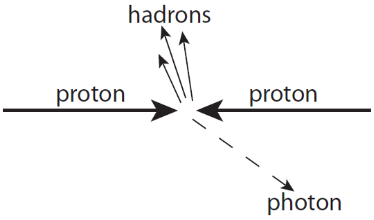

Figure 4.2: Schematic showing a collision between two protons resultion to a high energy photon and hadrons.

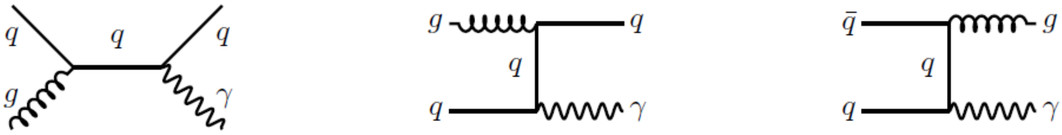

Figure 4.3: Samples of Feynman diagrams contributing to $\gamma +$ jets final state. The first two (left, middle) represent quark-gluon compton scattering, while the last one (right) is quark anti-quark annihilation.

Standard Model Backgrounds:

- γ + **jets/multi jets**: Dominant Standard Model background that can give apparent $\mathrm{E}_{\mathrm{T}}^{\mathrm{miss}}$ due to detector resolution (Fig. 4.2). There are several types of hard-scattering interactions contributing to direct creation of photons. These include gluon compton scattering and quark anti-quark annihilation (Fig. 4.3).

- **W + jets**: This background along with $t\bar{t}$ + jets and Drell-Yan is sub-dominant and it includes processes with real $\mathrm{E}_{\mathrm{T}}^{\mathrm{miss}}$. The decays of the charged $\mathrm{W}^{+/-}$ bosons that may contribute to our standard model background are: W → eν where the electron may fake the photon and W → $\tau\nu$ when $\tau \to e\nu\nu$, or $\tau \to h \geq 1\pi^0\nu$.

- **$\mathbf{t\bar{t}}$ + jets**: The only known way that a top quark can decay is through the weak interaction producing a W-boson and a down-type quark (principally bottom but also down and strange quark)[24]. The produced Ws may induce a background to our signal due to the electron (to photon) mistagging and the escaping neutrino.

- γ + **W/Z + jets**: The presence of W/Zs may also induce a background, where the missing transverse energy is produced due to neutrinos.

- **Drell Yan + jets**: In proton – proton collisions, $q\bar{q}$ interaction may produce Z^0 or $\gamma^\star$ which subsequently decay to a lepton antilepton pair. This process, known as Drell-Yan process is a potential background for our signal (Fig. 4.4).

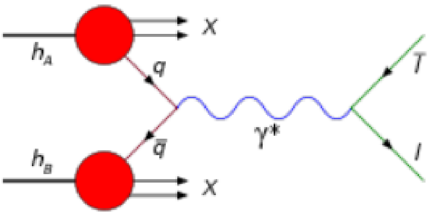

Figure 4.4: Schematic showing a Drell Yan process in proton proton scattering. It takes place when a quark of one hadron and an antiquark of another hadron annihilate, creating a virtual photon (or Z boson) which then decays into a pair of oppositely-charged leptons.

Signal scenarios considered in this study:

The simulated samples used in this search are produced with the PYTHIA event generator. Because of the large number of individual simulated samples required in the new physics parameter space, a fast detector simulation [83] based on a full description of the CMS detector geometry, and a parameterization of single-particle showers and response, is utilized to reduce the computation time for those samples. Event "pileup"[2] corresponding to the luminosity profile of the analyzed data is also added and the generated events are subsequently reconstructed using the same software program as for the collision data.

As already discussed, General gauge-mediated SUSY breaking requires the LSP to be a gravitino, and the NLSP to be a bino- or wino-like neutralino to produce final states with photon(s), jets and $\mathrm{E}_{\mathrm{T}}^{\mathrm{miss}}$. Hence three different signal scenarios have been used as benchmarks, two bino-like and one wino-like neutralino. Table 4.2 shows the mass parameters varied in the GGM planes investigated in this analysis. For the first bino-like scenario, the neutralino mass was fixed to 375 GeV and the squark as well as the gluino masses were varying from 400 to 2000 GeV, while for the second the mass of the squark was fixed to 2500 GeV and the neutralino and gluino masses were varying. The last scenario was for a wino-like neutralino with fixed neutralino mass (375 GeV) and varying squark and gluino masses.

The method's validity is checked in MC simulation samples produced with the MadGraph generator. As already mentioned, the simulated events are subsequently reconstructed (with $CMSSW$4_2_8) and analyzed using the same tools as for the collision data.

---

[2] In high-luminosity colliders, there is a non-negligible probability that one single bunch crossing may produce several separate events, so-called "pileup" events.

Table 4.2: Summary of studied GGM benchmark scenarios

	$m_{neutralino}$ [GeV]	m_{squark} [GeV]	m_{gluino} [GeV]
bino-like	375	400-2000	400-2000
bino-like	150-1050	2500	160-2000
wino-like	375	400-2000	400-2000

Table 4.3: List of Monte Carlo samples and corresponding cross-section used in the analysis.

Process	Sample name	σ [pb]	Gen. Events
γ + Jets	/GJets_TuneZ2_HT_200_ 7TeV-madgraph/Fall11-PU_S6_ START42_V14B-v1/AODSIM	798.3 (LO)	6458757
W + Jets	/WjetsToLNu_300_HT_inf_TuneZ2_ 7TeV-madgraph-tauola/Fall11-PU_S6 _START42_V14B-v1/AODSIM	48.49 (LO)	5363746
$t\bar{t}$ + Jets	/TTJets_TuneZ2_7TeV- madgraph-tauola/Fall11-PU_S6_ START42_V14B-v1/AODSIM	165.0 (NLO)	3501947
Drell Jets	/DYJetsToLL_TuneZ2_M-50_ 7TeV-madgraph-tauola/Fall11-PU_S6_ START42_V14B-v1/AODSIM	3048.0 (NLO)	27020594
γ + W/Z + Jets	/GVJets_7TeV-madgraph /Fall11-PU_S6_START42 _V14B-v1/AODSIM	56.64 (LO)	947879

The list of Monte Carlo samples (official CMS production) used in this analysis, is shown in Table 4.3, together with their cross-sections (LO or NLO if available) and the number of generated events. Monte Carlo events are re-weighted to reflect the data Luminosity and are also corrected for “pileup“ effects. The relevant event weight is equal to:

$$w_i = \frac{PUweight \times \sigma_i \times Lumi}{N_{tot}}$$

where $PUweight$ is a weight factor calculated per event according to the official instructions, N_{tot} is the generated number of events and σ_i is the theoretical cross section of the simulated process.

In order to demonstrate that a signal will not be missed and calibrated away by the control regions, as well as for comparisons with Standard Model expectations, GGM Signal MC samples with bino-like NLSP have been produced. The studied GGM benchmark scenarios are summarized in Table 4.4. Each GGM parameter point corresponds to 25000 generated events.

Table 4.4: Summary of studied GGM benchmark scenarios

m_{squark} [GeV]	m_{gluino} [GeV]	$m_{\text{neutralino}}$ [GeV]	xsec [pb] (LO from pythia)
750	700	225	3.844×10^{-1}
750	1200	225	1.153×10^{-1}
1250	700	225	7.801×10^{-2}
1250	1200	225	4.885×10^{-3}
1250	700	375	5.135×10^{-3}

Chapter 5

Object Definitions and Event Selection

Something unknown is doing we don't know what.

-Sir Arthur Eddington-

This chapter describes the criteria for the identification of the objects involved in the under study final state. Furthemore there's a description of the selection requirements that are applied in order to find events of interest in the recorded collision data. The event selection is done in two steps. First of all CMS trigger provides a first level of filtering and then offline cuts contribute to further improvement of the sample purity.

5.1 Object definitions and event reconstruction

5.1.1 Photons

The CMS electromagnetic crystal calorimeter (ECAL) was designed to have both excellent energy resolution and high granularity, making it a powerful instrument to measure photons with high precision at the LHC. Photon showers deposit their energy in several crystals in the ECAL and thus photon objects are created based on these depositions[61]. The collection of adjacent ECAL crystals that are used to reconstruct the energy and the direction of a particle is commonly referred as *basic cluster*. Approximately 94% of the incident energy of a single electron or photon is contained within a 3×3 grid and 97% within a 5×5 grid. Each supercluster (deposits of energy in the ECAL that are clusters of basic-clusters) is potentially a photon candidate. Because of the existence of material in front of the calorimeter, conversion of photons and bremsstrahlung from electrons and positrons is likely to happen. The strong magnetic field may lead the energy flow associated to primary electrons or converted primary photons, to a spread in ϕ

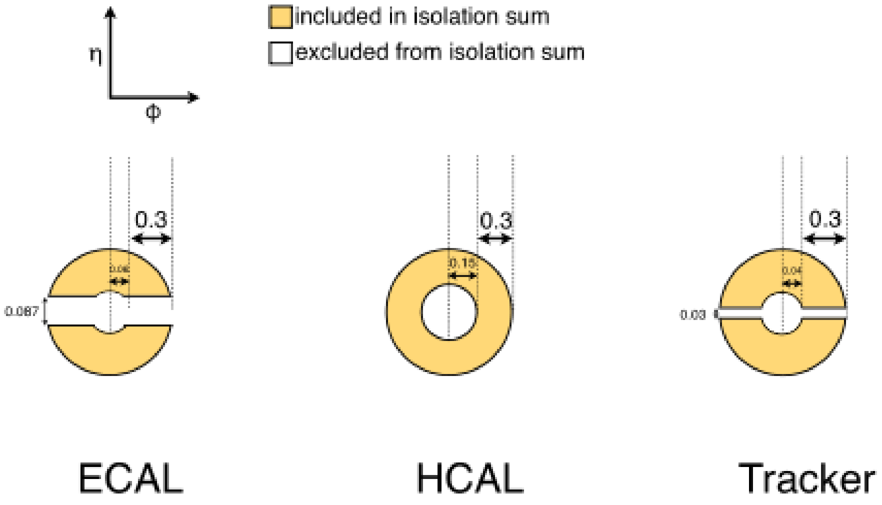

Figure 5.1: Illustration of isolation cone sums of radius ΔR=0.3.

with increasing distances from the collision vertex within the tracker volume. To collect the photon energy in the ECAL, local deposits (basic-clusters) are summed into superclusters which are extended in ϕ. After applying the appropriate energy corrections, the superclusters are used to reconstuct the photon objects, assigning the candidate momentum to the location of the reconstructed primary vertex. In order to determine if a photon is converted or not, a variable called $R9$ is used. It is estimated by the energy of each photon candidate and it corresponds to the ratio of the energy contained within the 3×3 array of crystals centered on the seed crystal of the photon candidate's supercluster to the total energy contained in the supercluster. For R9 values above 0.94 in the barrel, the energy of the 5×5 crystals ($E_{5\times5}$) around the highest energy crystal is used, or else the supercluster energy is used instead. To increase the purity of the photon sample, additional isolation and identification requirements are applied [64]. Photon candidates should be isolated from other activity in the ECAL, HCAL and tracker. A cone of $\Delta R = \sqrt{(\Delta\phi)^2 + (\Delta\eta)^2} = 0.3$ is constructed around the direction of the photon candidate, and the scalar sums of transverse energies of tracks and calorimeter deposits within this ΔR cone are determined, after excluding the contribution from the photon candidate itself. Illustration of the isolation cone sums is shown in Figure 5.1. The identification criteria are listed above:

- **PixelSeedVeto**: The supercluster is required not to match pixel hits consistent with a track from the interaction region. This prevents misidentification of electrons as photons.

- **Hadronic energy fraction (H/E)**: the ratio between the HCAL energy in a annular region around the photon with outer radious $\Delta R = 0.15$ and the ECAL super-cluster energy.

- $\sigma_{i\eta i\eta}$: calorimeter shower shape variable which describes the width of the ECAL cluster along the η direction computed for all the crystals centred on the highest energy crystal of the seed cluster. It is defined as:

$$\sigma^2_{i\eta i\eta} = \frac{\sum_{i=1}^{25} w_i(i\eta_i - i\eta_{seed})^2}{\sum_{i=1}^{25} w_i}, w_i = max(0, 4.7 + \ln(\frac{E_i}{E_{5\times5}})) \qquad (5.1)$$

  where E_i and $\mathrm{i}\eta_i$ are the energy and η index of the i^{th} crystal within the 5×5 electromagnetic cluster, $\mathrm{E}_{5\times5}$ is the energy of the 5×5 crystals around the seed crystal, and $\mathrm{i}\eta_{seed}$ is the η index of the seed crystal.

- **ECAL Isolation**: the sum of ECAL $\mathrm{E}_\mathrm{T}^\mathrm{miss}$ around the photon candidate in an annular region of inner radius $\Delta R = 0.06$ and outer radius 0.3. Three-crystal wide strip along ϕ is excluded.

- **HCAL Isolation**: the sum of HCAL $\mathrm{E}_\mathrm{T}^\mathrm{miss}$ around the photon candidate in an annular region of inner radius $\Delta R = 0.15$ and outer radius 0.3.

- **Tracking Isolation**: the scalar sum of p_T of tracks consistent with the primary vertex in a hollow cone around the photon candidate in an annular region of inner radius $\Delta R = 0.04$ and outer radius 0.3. The inner radius is chosen to avoid counting the momentum of photon conversion tracks in the isolation sum.

- **Combined Isolation**: Sum of the individual ECAL, HCAL and Tracking Isolations.

5.1.2 Jets

In proton-proton collisions in the LHC environment, initial state radiation is always present and at the same time partons existing in the final state contribute to the formation of high-p_T tight cones of particles (baryons, mesons, etc) called *jets*. Due to color confinement, outgoing partons in jets cannot exist as free particles. If two colored particles separate more than a certain distance, quark-antiquark pairs are created. Jets mainly deposit their energy on the CMS calorimeters through electromagnetic and hadronic interactions and afterwards the collected information is used to produce detector-level jets.

CMS uses three different jet reconstruction algorithms: Calorimeter Jets (CaloJets) that are reconstructed using only the energy deposits in the calorimeter towers, Jet-Plus-Track Jets (JPTJets) [66] which are reconstructed with an algorithm that utilizes the transverse momentum of well measured tracks in the inner tracker and removes the corresponding expected calorimeter deposits from the calculation and lastly Particle-Flow Jets (PFJets) [68].

Clustering the deposits of energy or tracker-measured momentum vectors from a large collection of particles into one or more jets is done by jet clustering algorithms. There are different jet clustering algorithms that are used from CMS [65]. Regarding the reconstuction approach, they can be classified into two groups. Sequential recombination clustering algorithms (e.g. k_t) and Cone Clustering algorithms (such as the Fixed Cone algorithm, the Iterative cone, the MidPoint and Seedless infrared safe cone algorithms (e.g. anti-k_t)).

Besides good correspondence to the parton-level and hadron-level, a successful jet algorithm should fulfill two important requirements: infrared safe and collinear safe. The first requirement refers to the need for stability of the jet finding against the addition of soft particles. The algorithm should also be collinear-safe, such that the outcome remains unchanged if e.g. the energy carried by a single particle is instead distributed among two collinear particles.

The Particle-Flow algorithm

PFJets are reconstructed by clustering four-momentum vectors of particle-flow candidates utilizing all detector components. The aim of the particle-flow algorithm is to reconstruct and identify all stable particles in the event; photons, charged hadrons, neutral hadrons, muons and electrons. This is done by combining all CMS sub-detectors (inner tracker, the muon chambers, and all the calorimeters) towards an optimal determination of their direction, energy and type. This list of individual particles is then used, as if it came from a Monte-Carlo event generator, to build jets (from which the quark and gluon energies and directions are inferred), to determine the missing transverse energy, to reconstruct and identify taus from their decay products, to quantify charged lepton isolation with respect to other particles, to tag b-jets, etc (Fig. 5.2).

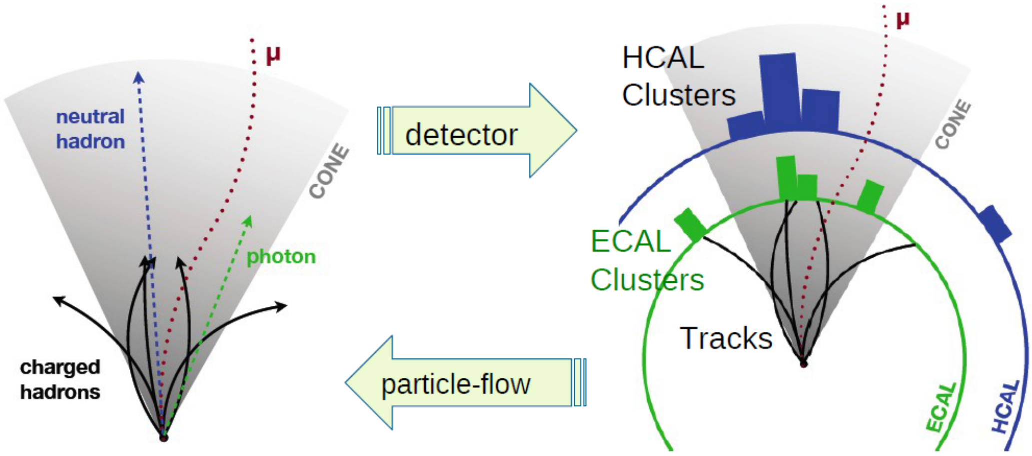

Figure 5.2: Overview of the Particle-Flow algorithm. The list of individual particles is used to build jets, determine E_T^{miss} , etc.

The design of CMS detector is almost ideally suited to attempt particle-flow event reconstruction at LHC; the large magnetic field, the possibility of having large tracking efficiency while keeping a low fake rate, the fine electromagnetic calorimeter granularity and near-hermetic coverage of the detector as well as the ability to reconstruct all muons with high purity have been shown to be key elements in this respect. The particle flow blocks are in the form of charged tracks, calorimeter clusters and muon tracks. The algorithm proceeds seperately for each block. The first step includes muon identification. If a muon's combined momentum is compatible with the determined one from the sole tracker, then it is called "particle-flow muon" and the corresponding track is removed from the block. The second step comes with the electron's reconstruction and identification. The remaining elements may give rise to charged hadrons, photons or neutral hadrons, and more rarely to additional muons. Each of the remaining tracks in the block gives rise to a “particle-flow charged hadron”, the momentum and energy of which are taken directly from the track momentum. If the calibrated calorimetric energy is compatible with the track momentum, the charged-hadron momenta are redefined by a fit of the measurements in the tracker and the calorimeters. On the other hand, it may well be that the calibrated energy of the closest ECAL and HCAL clusters linked to the track(s) be significantly larger than the total associated charged-particle momentum. If the relative energy excess is found to be larger than the expected calorimeter energy resolution, it gives rise to a “particle-flow photon”, and possibly to a “particle-flow neutral hadron”. The remaining ECAL and HCAL clusters, that are not linked to any track or for which the link was disabled, also give rise to a “particle-flow photon” and a “particle-flow neutral hadron”, respectively. The neutral-hadron energies are determined by applying the calibration procedure to the HCAL clusters only.

The anti-kt jet clustering algorithm

The anti-kt algorithm is a subset of the seedless infrared safe cone algorithms and provides both infrared and collinear safety while being of equal performance in terms of processing speed as cone-based algorithms. It takes the locally highest momentum particle and clusters nearby particles into a jet around it, based on their proximity in both position and momentum space. As each new particle is added, the resulting pseudojet is adjusted based on the resulting momentum and position. In this algorithm, one can introduce distances d$_{ij}$ between any two entities (particles, pseudojets) i and j and d$_{iB}$ between entity i and the beam (B). The definition of these distances is:

$$d_{ij} = min(k_{ti}^{2p}, k_{tj}^{2p})\frac{\Delta_{ij}^2}{R^2} \tag{5.2}$$

$$d_{iB} = k_{ti}^{2p} \tag{5.3}$$

where $\Delta_{ij}^2 = (y_i - y_j)^2 + (\phi_i - \phi_j)^2$ and k_{ti}, y_i and ϕ_i are respectively the transverse momentum, rapidity and azimuth of particle i. R stands for the radius of the cone used in the clustering algorithm (for this analysis the cone size used is $R = 0.5$) and the parameter p governs the relative power of the energy versus geometrical (Δ_{ij}) scales. For $p = 1$ one recovers the inclusive k_t algorithm, for $p > 0$ the behaviour of the jet algorithm with respect to soft radiation is rather similar to that observed for the k_t algorithm, the case of $p = 0$ corresponds to the inclusive Cambridge/Aachen algorithm, while the case of $p = -1$ corresponds to the anti-k_t jet-clustering algorithm.

If the smallest distance is d_{ij}, i and j are recombined into a single pseudojet, with the position weigheted by the momenta of the entities. On the other hand, if the smallest distance is d_{iB}, i is defined as a jet and it is removed from the list of entries. This procedure is iterated until no entry remains.

The kt and Cambridge/Aachen inclusive jet finding algorithms for hadron-hadron collisions can be seen as belonging to a broader class of sequential recombination jet algorithms, parametrised by the power of the energy scale in the distance measure. The anti-k_t algorithm essentially behaves like an idealised cone algorithm, in that jets with only soft fragmentation are conical. Softer particles tend to cluster with harder particles. In the case of a hard particle with no other hard particles nearby, it will cluster all the soft particles around it, resulting to a jet of radius R. On the other hand, in the case of the presence of another hard particle in a region $R < \Delta_{ij} < 2R$, the softer particles surrounding them will be split between the two; weighted by the relative momenta of each hard particle. If two hard particles exist in a region $\Delta_{ij} < R$, the algorithm will combine them into a single jet with a center weighted by the relative momenta of the two particles. A more detailed description of the anti-k_t algorithm can be found in Ref. [25]

Jet Energy Corrections

Generally, the measured energy by the CMS detector is different from the true particle-level jet energy. Primarily this is caused by the non-uniform and non-linear response of the calorimeters to the energy deposited by particles. Furthermore the presence of noise from electronics and additional proton collisions in the same bunch crossing makes things worse. Thus it is not straightforward to get the true energy of the particle by the measured energy. To overcome this problem, CMS uses a set of jet energy corrections, where each level of correction deals with a different effect. L1, L2 and L3 corrections are applied to both data and MC simulation, while the last one (Residual Corrections) are applied additionally only to data [69].

- **L1 Offset Correction**: This correction is applied to remove the energy that is uncorrelated with high p_T scattering. The excess energy includes contributions from “pileup“ events as well as electronics noise. CMS has developed three approaches for the offset correction: the jet area, the average offset and the hybrid jet area [69]. Here, the first approach (L1Fast) is applied.

- **L2 Relative Jet Correction**: This correction is applied in order to remove the dependence of the response of jets with pseudo-rapidity. The uniformity in pseudorapidity is achieved by correcting each jet in arbitrary η relative to a jet in the central region of the detector.
- **L3 Absolute Jet Correction**: This correction is to make the jet response flat versus p_T . Once a jet has been corrected for η dependence, it is corrected back to the hadron level.
- **Residual Correction**: This correction account for the small differences between data and MC simulation and are applied only to data.

5.1.3 Electrons

In this analysis, electrons are used to estimate the backgrounds from processes with non-symmetric JGB distribution . These processes include neutrinos in the final states, like W + jets → lepton + ν + jets where the lepton could be an electron that might be misidentified as a photon. Thus, for our study, the definition of an electron is similar to that of a photon except from the requirement of the pixel seed veto, which is inverted.

5.1.4 Missing Transverse Energy

As previously noted, the particles in the CMS detector are seen as tracks and energy depositions. The PF algorithm attempts to identify all stable particles existing in an event, by combining information from all CMS subdetectors, thereby allowing precise corrections to object energies and also providing a significant degree of redundancy which renders the MET measurement relatively less sensitive to the calibration of the calorimetry.

An accurate determination of E_T^{miss} , both for events without missing energy (due to detector resolution and reconstruction effects), typical for standard model backgrounds, and for events with missing energy, often characterizing new physics, is a major asset for the separation of the two types of events. As discussed in Chapter 1, the lightest supersymmetric particle in most supersymmetric models interact only weakly with matter and thus leaving no signature to the CMS subdetectors. Here comes the most important role of missing transverse energy, making possible to detect SUSY particle’s presence, in the form of E_T^{miss} . Determination of E_T^{miss} using the particle-flow event reconstruction, is formed by the transverse momentum vector sum over all reconstructed particles in the event and then taking the opposite of this azimuthal, momentum two-vector. The $\mathrm{E}_{\mathrm{T}}^{\mathrm{miss}}$ is the modulus of this vector.

$$\mathrm{E}_{\mathrm{T}}^{\mathrm{miss}} = | - \sum_{i}^{n} \overrightarrow{\mathrm{p}_{\mathrm{Ti}}} | \tag{5.4}$$

where i stands for the index of each particle-flow object.

Table 5.1: List of data samples used in this analysis

PhotonHad/Run2011A-May10ReReco-v1/AOD
PhotonHad/Run2011A-PromptReco-v4/AOD
PhotonHad/Run2011A-05Aug2011-v1/AOD
PhotonHad/Run2011A-PromptReco-v6/AOD

Table 5.2: List of JSON files used

Cert_160404-163869_7TeV_May10ReReco_Collisions11_JSON_v3.txt
Cert_170249-172619_7TeV_ReReco5Aug_Collisions11_JSON_v2.txt
Cert_160404-180252_7TeV_PromptReco_Collisions11_JSON.txt

5.2 Event Selection

The first step of the analysis is the selection of events based on the reconstructed physics objects defined in Section 5.1. The purpose of the selection is to attempt to exctract, from all the events, a small set of data likely to be the signal. For the first part of this analysis, only certified runs and luminosity sections as defined in the JSON[1] files (see Table 5.2), were processed. The datasets were collected from April to November of 2011 in pp collisions at $\sqrt{s}$=7 TeV.

Data are sorted into primary datasets (PD) with respect to the type of trigger they were accumulated with, as shown in Table 5.1. The set of triggers used in these PD require a single photon with $\mathrm{p}_{\mathrm{T}} \geq 70$ GeV and a minimum of hadronic transverse energy H_{T} cut, where H_{T} is defined as the scalar p_{T} sum of all the calorimetric jets passing the JetID requirement (p_{T} >40 GeV, n90Hits$\geq$ 2 and $|\eta| \geq$ 3). The H_{T} in the last runs is 400 GeV. The trigger path used in this analysis was chosen as the logical OR of the paths listed in Table 5.3 and the Trigger efficiencies of the H_{T} and photon leg of the used Photon-H_{T} triggers are illustrated in Figure 5.3 [97]. All triggers use spike cleaning. The requirements on *_CaloIdL_* are: H/E< 0.15 and $\sigma_{i\eta i\eta}$ <0.014 for ECAL Barrel (EB). The offline cuts meet

---

[1] JSON files are lists of the runs for which the entire CMS detector was fully operational

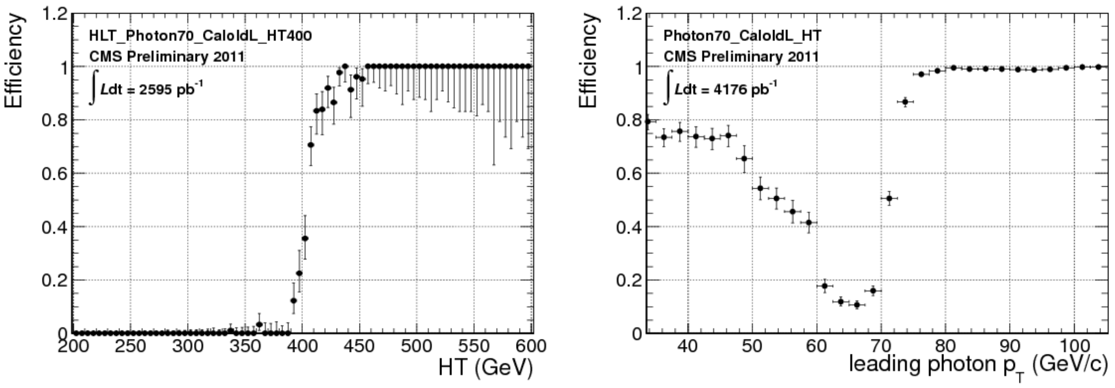

Figure 5.3: Trigger Efficiency of the H_T and Photon p_T leg[1] of the HLT_Photon70-_CaloIdL_HT400 trigger.

the trigger requirements and they are optimized for maximum efficiency. The corresponding luminosity is 5.051 fb^{-1}, but approximately 350 pb^{-1} are excluded, due to a different definition in H_T calculation in the triggers (One of the cuts included in the H_T calculation is on the number of calorimeter towers carrying 90% of the jet energy (n90 $\geq$ 2). For the run numbers after 165970 this cut was replaced by a cut on the number of calorimeter hits carrying 90% of the jet energy (n90Hits $\geq$ 2)). Thus this analysis is using data samples with an integrated luminosity of 4.7 fb^{-1} .

Table 5.3: List of triggers used in each of the data streams

Stream	**Trigger path**
PhotonHad	HLT_Photon70_CaloIdL_HT300_v(1-6)
PhotonHad	HLT_Photon70_CaloIdL_HT400_v(1-3)
PhotonHad	HLT_Photon70_CaloIdXL_HT400_v(1-3)

As previously noted in Section 5.1, the photon candidates are reconstructed from clusters of energy in the CMS electromagnetic crystal calorimeter (ECAL). To collect the photon energy in the ECAL, local deposits are summed into superclusters. A supercluster passing a list of identification and quality criteria (e.g. shower shape) is promoted to a photon. Thus we apply the following cuts: R9<1.0, H/E<0.05, $\sigma_{i\eta i\eta}$ <0.011. In addition, the absence of a pixel tracker hits matching to the supercluster is required to descriminate photons from electrons.

---

[1] The odd low pt behavior is caused by the base trigger. Photon70_CaloId_HT_XXX triggers not only barrel photons but also endcap. Given Photon50 base trigger, there could be good (but low p_T) barrel photons reconstructed as well as the endcap photon event (responsible for triggering). Thus, the low activity corresponds to low p_T photons not responsible for triggering events.

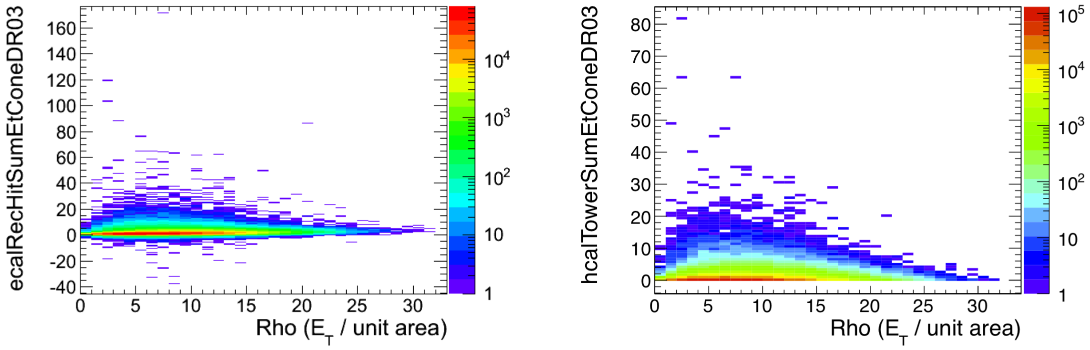

Figure 5.4: ECAL (left) and HCAL (right) isolation sums versus ρ for probe electrons

To increase the purity of the photon sample, isolation requirements are applied using combined information from ECAL, HCAL and the tracker.

With increasing Luminosity, the “pileup“ increases as well. This leads to increasing energy found in the isolation cones of photons. For this reason, “pileup“ corrections are applied as an effort to subtract the “pileup“ related deposits and minimize the “pileup“ dependence of the photon identification. Only the ECAL and HCAL isolation sums are corrected.

$$Iso_{ECAL}^{Corr} = Iso_{ECAL} - Aeff_{ECAL} \times \rho$$

$$Iso_{\mathrm{Hcal}}^{Corr} = Iso_{\mathrm{Hcal}} - Aeff_{\mathrm{Hcal}} \times \rho$$

where $Aeff_{ECAL} = 0.093$ and $Aeff_{HCAL} = 0.02808$. The ρ variable describes the amount of transverse momentum added to the event per unit area (e.g. by minimum bias particles) [30]. Briefly, in events with two electrons that pass the tag and probe criteria (Tab. 5.4), the ECAL and HCAL reconstructed photon isolations as a function of ρ, for the probe electron are plotted. These plots can be found in Figure 5.4. A_{eff} corresponds to an effective area determined from the slope of a linear fit of the average isolation versus ρ. These fits can be found in Figure 5.5.

Thus the “pileup“ corrected combined Isolation is defined as:

$$Iso_{Comb}^{Corr} = Iso_{ECAL}^{Corr} + Iso_{HCAL}^{Corr} + Iso_{Track}$$

In total, not more than 6 GeV “pileup“ subtracted [30] energy deposit is allowed within a cone of $\Delta R = \sqrt{\Delta\phi^2 + \Delta\eta^2}$=0.3. Additional “pileup“ corrections are applied to the used MC simulated events. The MC samples have been generated with a “pileup“ distribution approximately similar to the “pileup“ conditions for the 2011 data. However, since the final distribution of data is sensitive to the details of the underlying event, it is possible to be biased by the

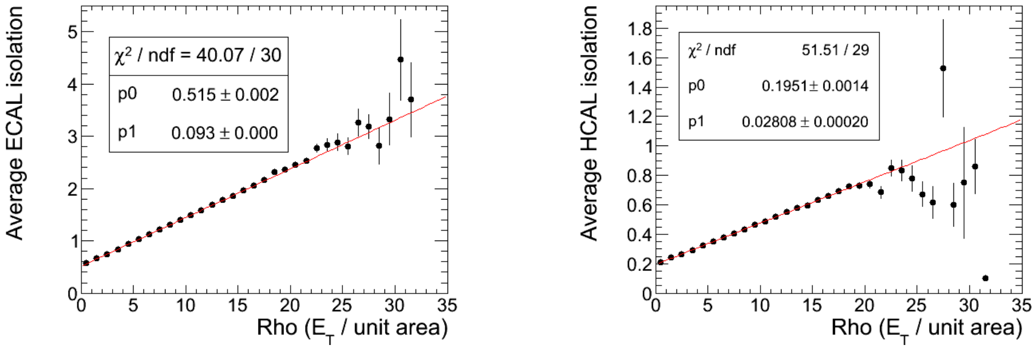

Figure 5.5: Average ECAL (left) and HCAL (right) isolation sums versus ρ for probe electrons

application of the offline event selection and trigger requirements. For this reason the number of generated primary vertices in the simulated samples is reweighted to match the distribution obtained in the used datasets.

The definition of an electron is similar to that of a photon except for the requirement of hits on the pixel tracker matching to the supercluster. Electrons are used to estimate the backgrounds from processes with an electron misidentified as photon and real E_T^{miss} (e.g. $W \rightarrow e\nu$) similarly to [74] and references within.

Jets are clustered with the anti-k$_T$ clustering algorithm [25] with a size parameter $R = 0.5$ and reconstructed with the Particle-Flow reconstruction algorithm [68]. Energy scale corrections are applied in the jet to take into account the non-linear jet energy response [69]. For the H_T offline selection, calorimeter jets (jets reconstructed using only the energy deposits in the calorimeter towers) are used in order to follow the online selection. Within the Particle-Flow framework the E_T^{miss} is the p_T of the negative vector sum of all reconstructed particles [68].

The offline cuts for the event selection are listed below. Those cuts meet the trigger requirements and they are optimized for maximum efficiency.

- at least one photon with p_T >80 GeV, $|\eta|$ <1.4442
- at least three jets with p_T >100 GeV, $|\eta| < 2.6$ with a distance $\Delta R > 0.4$ from the photon candidate
- H_T >460 GeV.

Furthermore, in order to avoid problematic events, such as HCAL noise or deposits in masked ECAL cells, we are also applying filters for HCAL and ECAL (see Appendix C).

Table 5.4: Selection criteria for tag and probe electrons and extra cuts for tag electrons as used for the “pileup“ ρ compensation study.

Common Cuts		**Value**
Good Vertices in event	$\geq$	1
$\lvert\eta\rvert$	$<$	1.4442
R9	$<$	0.98
H/E	$<$	0.05
$\sigma_{i\eta i\eta}$	$<$	0.014
$nPixelSeeds$	$\geq$	1
$R9$	$>$	1.0
or		
EcalIsoDR03	$<$	$6.0 + 0.012 \times E_T$
HcalIsoDR03	$<$	$4.0 + 0.005 \times E_T$
TrackIsoDR03	$<$	$4.0 + 0.002 \times E_T$
Extra Tag Cuts		**Value**
$\sigma_{i\eta i\eta}$	$<$	0.011
EcalIsoDR03+HcalIsoDR03+TrackIsoDR03	$<$	6.0
$\mathrm{E_T}$	$>$	25

Chapter 6

SM Background estimation

> *Once you eliminate the impossible, whatever remains, no matter how improbable, must be the truth.*
>
> -Sir Arthur Conan Doyle-

Since mismeasured E_T^{miss} can mimic signal events, our ability to establish the presence of a signal over background relies on accurate prediction of the missing energy "tail" of this background. The rate of the mismeasured background is difficult to be estimated by just using Monte Carlo samples. In this chapter we will present a deployment of a data-driven approach with the symmetric background determination inspired by the SUSY leptonic searches in Z+jets+E_T^{miss} final state [90, 91, 63, 94] and the asymmetric ones treated with a method especially developed for this analysis. The Jet-Gamma Balance (JGB) method has been devised to predict the E_T^{miss} contribution from mismeasured γ+jets events [93, 88].

6.1 The Jet-Gamma Balance method

It has been already noted that the analysis described in this thesis, uses jet and E_T^{miss} reconstruction based on the particle flow technique, which improves the resolution of the JGB observable with respect to the conventional construction using pure calorimetric deposits. The JGB observable is defined as:

$$JGB = |\sum \overrightarrow{p_T^{jets}}| - |\overrightarrow{p_T^{\gamma}}| = |\overrightarrow{E_T^{miss}} + \overrightarrow{p_T^{\gamma}}| - |\overrightarrow{p_T^{\gamma}}| \tag{6.1}$$

A high positive value of JGB favors events with a photon produced at the end of a decay chain (of cascaded supersymmetric decays in that case). Photons produced closer to the primary vertex are kinematically balanced and tend to produce JGB close to zero. We classify the background to symmetric and asymmetric with respect to JGB:

- Symmetric background: The method exploits the property of a quasi symmetric JGB distribution around zero for standard model processes with only instrumental E_T^{miss} (due to detector resolution), due to the fact that the direction of the E_T^{miss} vector is random, especially if the number of jets is large. Thus the region with JGB < 0 gives a good estimate of the background yield expected in JGB > 0. This constitutes a major component of the total background.

- Asymmetric background: Standard model processes with real E_T^{miss} and asymmetric JGB, such as W+jets and $t\bar{t}$, tend to have more events in the positive tail. In this kind of background the electron is misidentified as a photon and the neutrino leads to E_T^{miss} . The background contribution to the high JGB (signal region) is estimated using a data driven technique based on electrons + jets + E_T^{miss} selection and the estimated fake rate. For electrons with $p_T > 80\ GeV$ the relevant probability for an electron to be misidentified as a photon was found $\sim 0.006 \pm 0.0025$. As seen in Ref.[72, 89, 92] there is a good aggrement between data and MC on the mistag rate and a flat mistag rate is shown up to ~ 140 GeV. The JGB distribution for these events is calculated. The difference between the population of the negative side of JGB from the corresponding on the positive side, gives the additional background contribution from these processes.

On the other hand, in the case of events with SUSY processes, the JGB >0 region is much more populated than the JGB <0.This is confirmed by the Monte Carlo simulation for the relevant backgrounds and the SUSY benchmarks as well (Figure 6.1).

In single jet events the shape of the JGB distribution represents the jet energy response over the mean p_T spectrum of the photon production in this region of phase space. Events with an overestimated jet energy measurement will populate the JGB > 0 region, while events with an underestimated jet energy are located in JGB < 0. In multijet events the shape of the JGB distribution is the convolution of a multi jet energy measurement over the mean p_T spectrum of the photon production in a different region of phase space with respect to the exclusive one jet bin. Events with underestimated jets, do not necessarily populate the JGB < 0 region, due to vectorial addition of the jet momenta.

To summarize, the JGB variable can be used in two ways. Firstly it can be used just like an ordinary E_T^{miss} selection. Furthemore an event selection requiring positive values of JGB already rejects $\sim 50\%$ of the SM background, while retaining $\sim 70\%$ of the signal 6.1. The JGB method gives a good estimate of the total background yield expected in JGB >0, without relying on MC simulation. This is done by subtracting the JGB <0 distribution from the JGB >0 for the events with at least one electron and at least three jets, weighted by the fake rate.

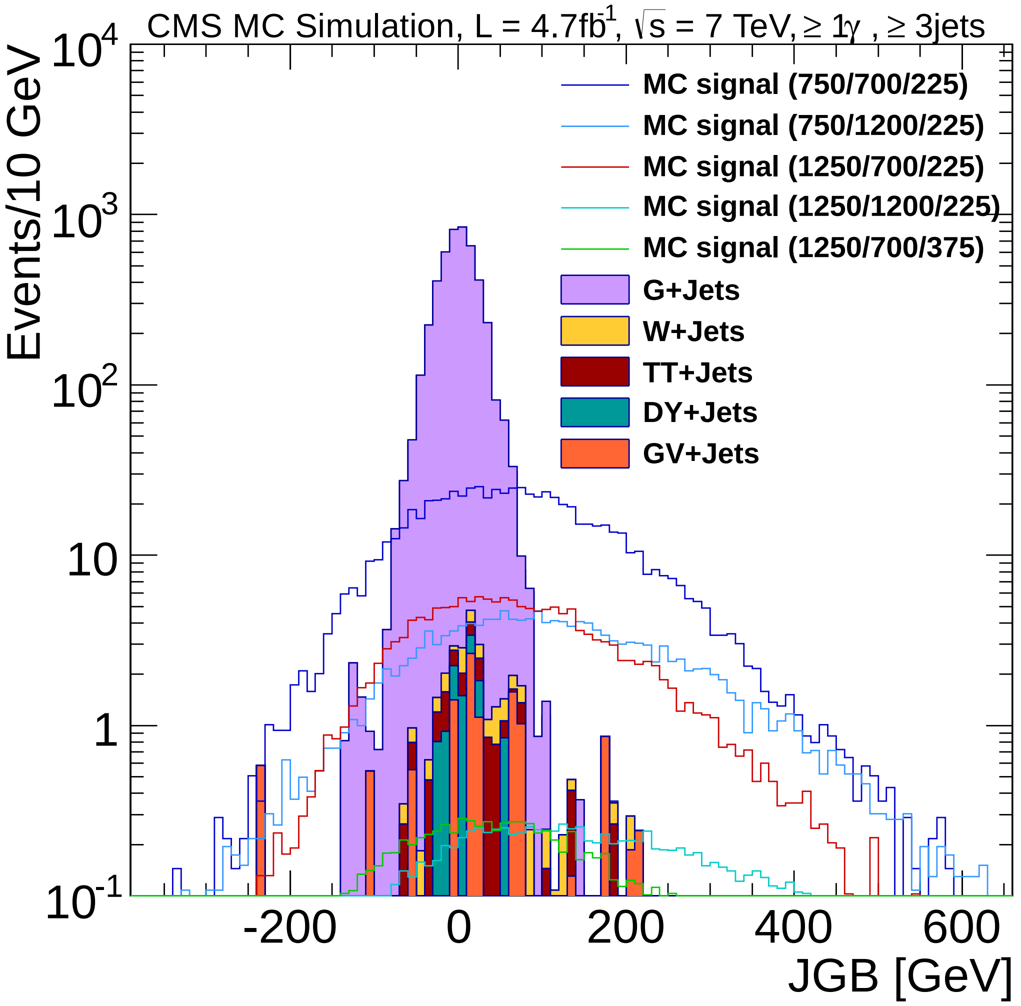

Figure 6.1: The JGB distribution in MC simulation for five different signal scenarios (Table 4.4) and the most important SM backgrounds ($\geq 1\gamma, \geq 3jets$).

Then we add to this result the JGB <0 distribution for the events with at least one photon and at least three jets.

6.1.1 Response Correction

In the JGB analysis, the hadronic recoil is estimated using particle-flow E_T^{miss} and photon's four-momentum (see eq. 6.1). The response is defined as the p_T ratio of the hadronic recoil over photon's p_T . Studying the particle flow response as a function of the photon's momentum, a reconstruction bias $\sim$ 5% for data and $\sim$ 4% in Monte Carlo was found and events are corrected for it (Figure 6.2).

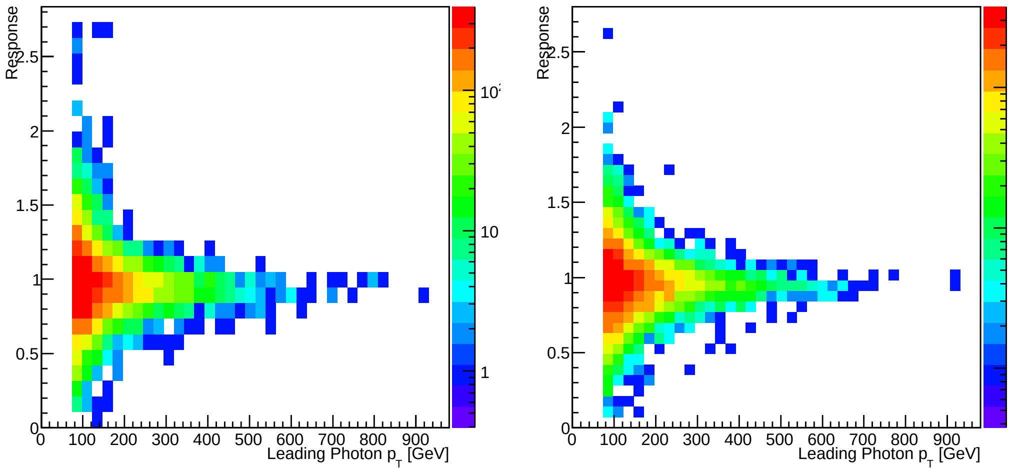

Figure 6.2: Response measured ($\geq 1\gamma, \geq 3jets$) in data (left) and Monte Carlo simulation (right).

6.1.2 Analysis closure test in MC

The comparison between predicted and observed JGB distributions is shown in Figure 6.3. It is shown that the predicted background distribution agrees with the observed. The discrepancy is accounted for by a systematic uncertainty of 40% reflected in the signal region, based on the under study MC simulation samples (MC are analyzed exactly the same way as data). In Appendix A.1 and A.2 there are comparison plots between data and MC samples. Jet resolution has been taken into account for the bin intervals definition in the high JGB region (JGB > 100 GeV).

6.1.3 Sensitivity of the JGB method to discover a signal

The closure test is also repeated by mixing background with a SUSY benchmark signal (m$_{squark}$:750 GeV / m$_{gluino}$:700 GeV / m$_{neutralino}$:225 GeV, cross section: 0.3844 pb) and performing a signal+background hypothesis test in order to demonstrate that a signal will not be missed and calibrated away by the signal presence in the control region (JGB < 0). The following plots (Figure 6.4) demonstrate qualitevely the sensitivity of JGB method, since the excess of events over the predicted background is clearly visible.

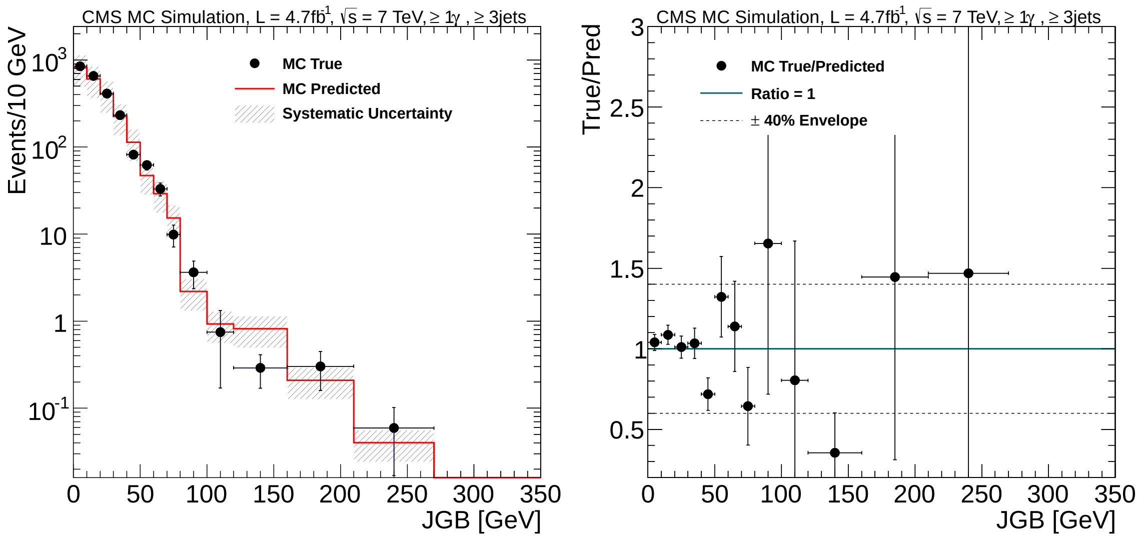

Figure 6.3: Monte Carlo closure test in a SM background only hypothesis ($\geq 1\gamma, \geq 3jets$). Comparison between the predicted and observed JGB distribution (left) and the ratio of the observed values versus the predicted values (right).

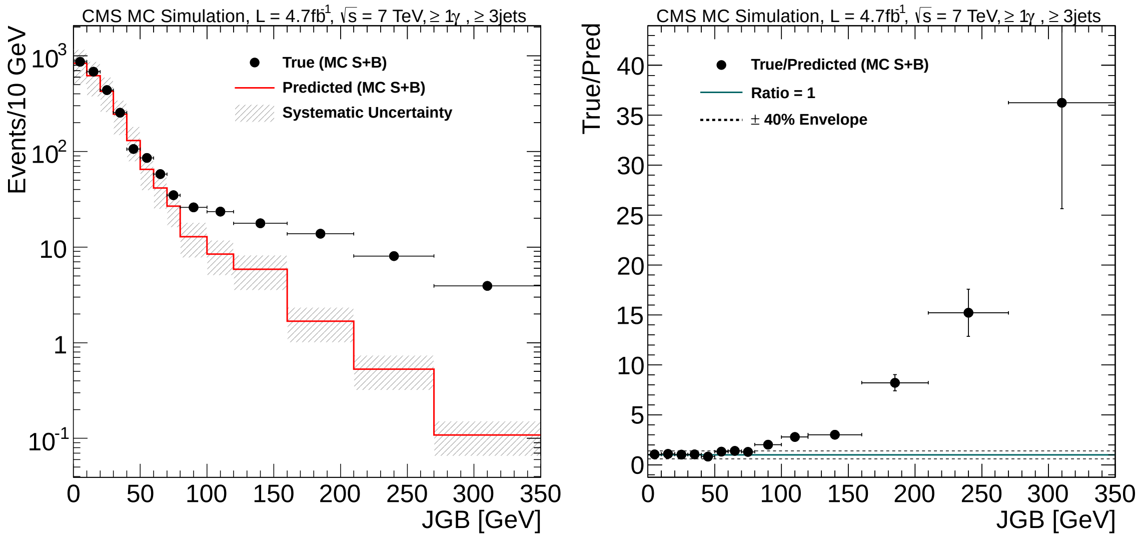

Figure 6.4: The JGB distribution for a MC backgrounds + signal hypothesis (left) and the ratio of the observed values vs the predicted values (right) ($\geq 1\gamma, \geq 3jets$).

Chapter 7

Analysis

> *I often say that when you can measure what you are speaking about, and express it in numbers, you know something about it, but when you cannot measure it, when you cannot express it in numbers, your knowledge is of a mearge and unsatisfactory kind.*
>
> -Lord Kelvin-

7.1 Background estimate in the data

In this section the same analysis steps are applied on data. Figure 7.1 shows the application of the JGB method on data. In general there is a good agreement between observed and predicted values. The left plot of Figure 7.1, shows the comparison between background prediction and observed events in the JGB > 0 region, while the right plot illustrates the ratio of the observed to the predicted number of events. The integrated number of observed and predicted events for three different signal regions (80$\leq$JGB$<$100 GeV, 100$\leq$JGB$<$120 GeV and JGB$\geq$120 GeV), are summarized in Table 7.1. More details about the integrals in different signal regions are summarized in Appendix A. The event yields correspond to 4.7 fb^{-1} of data. The systematic uncertainties accounted for standard model background contributions, are $\pm$40%. The calculation of the exclusion limits on physics beyond the standard model, along with the relevant interpretation is discussed in the following session.

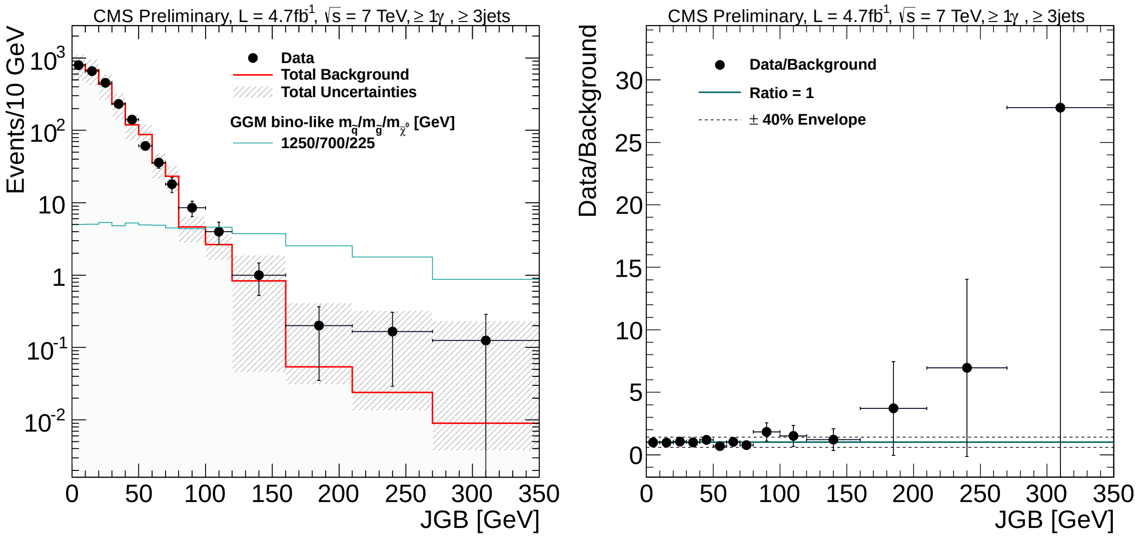

Figure 7.1: The JGB distribution for Data ($\geq 1\gamma, \geq 3jets$). Comparison between Observed and Predicted values (left) and the relevant ratio (right).

Table 7.1: Total number of events observed and corresponding background prediction, in bins of JGB

4.7 fb^{-1}	**80-100 GeV**			**100-120 GeV**			**>120 GeV**		
$\geq 1\gamma, \geq$ 3jets		**stat.**	**sys.**		**stat.**	**sys.**		**stat.**	**sys.**
SM estimation (JGB<0)	9	$^{+4.1}_{-2.9}$	±3.6	5	$^{+3.4}_{-2.2}$	±2.0	3	$^{+2.9}_{-1.6}$	±1.2
SM estimation ($f_{e\rightarrow\gamma}$)	0.3	±0.04	±0.1	0.3	±0.04	±0.1	0.9	±0.07	±0.4
Total SM estimation	9.3	$^{+4.1}_{-2.9}$	±3.6	5.3	$^{+3.4}_{-2.2}$	±2.0	3.9	$^{+2.9}_{-1.6}$	±1.3
data	16			8			8		

7.2 Results

The goal of this analysis is to find evidence for the production of new physics by observing an excess of events above the Standard Model background in the high JGB region. The resulting event yields for data and background prediction (combined and separate) for the three signal regions are summarized in Table 7.1. The systematic uncertainties accounted for standard model background contributions, are ±40%. Taking into considerartion the errors, no excess is observed since the data are in satisfactory agreement with the standard model expectation. Hence upper limits are derived on potential signals of new physics models (GMSB).

The calculation of the exclusion limits on physics beyond the standard model, along with the relevant interpretation is discussed in the following section.

7.3 Interpretation

When the background is estimated from data-driven methods, the interpretation of the analysis results in terms of upper limits in the signal cross section is a non trivial issue, since the signal always contaminates the control region.

We estimate the signal events by subtracting the predicted events (event yield in the control region) from the events observed in the signal region.

$$\hat{S} = (S + B) - (S' + B')$$

where (S+B) are the observed events in the signal region and S' + B' are the predicted events.

Before the calculation of the exclusion limits, it is very important to calculate the possible signal's strength that should be greater than unit and it is defined as:

$$Signal\_strength = (S + B)/(S' + B')$$

The signal + background hypothesis test that is shown in Figure 6.4, gives the signal's strength for the case of a SUSY benchmark signal (m_{squark}:750 GeV / m_{gluino}:700 GeV / $m_{neutralino}$:225 GeV). The ratio True/Pred is exactly this strength. In case of signal's absence like in the MC closure test for background prediction (Figure 6.3) the ratio True/Pred reduces to B/B'.

7.4 Systematic Uncertainties

The systematic uncertainties in the signal acceptance that were taken into account for the limit calculation (experimental error band) are summarized in Table 7.2. The uncertainty that comes from the JGB method is 40% and is calculated using the difference between observed and predicted integrated number of events in the signal regions of the Monte Carlo closure test. The uncertainty that comes from the electron misidentification rate $f_{e\to\gamma}$ is 34% [72, 89, 92].

The systematic uncertainty that corresponds to Luminosity is 2.2% [84] while the relevant uncertainty in the Jet energy scale is 2% [67]. Possible differences in the photon identification efficiency between data and simulation are taken into account. We determine the efficiency for new physics signal events to pass our event selections by applying correction factors derived from data to the MC simulation of the signal. Since there is no large clean sample of genuine photons in the data, we rely on the similarities between the detector response to electrons and photons to extract the photon identification efficiency. The obtained number of events in acceptance is scaled by the ratio between the photon identification efficiency in data and simulation. These are obtained using $Z \to ee$ electrons in the data (or Monte Carlo respectively) satisfying photon identification selection (Ref. [74]). The photon efficiency corresponds to 4%.

The theoretical uncertainties take into account the uncertainties in the cross section (the production cross-section at NLO is calculated using PROSPINO [26]). The relevant PDF uncertainties follow the PDF4LHC recommendations, taking the calculated errors from each of the following 3 PDF's: CT10, NNPDF2.1, MRST2008. They vary between 0.03% and 78% depending on the SUSY signal masses (increasing with larger masses of both gluino and squark).

Table 7.2: List of systematic uncertainties

Source	**Uncertainty in the cross section**		
Luminosity	2.2%		
Jet energy scale	2%		
Photon efficiency	4%		
Acceptance PDF uncertainty	0.03 - 78%		
	Uncertainty in the background yield		
	80-100 GeV	100-120 GeV	>120 GeV
JGB uncertainty	39%	38%	32%
$f_{e\to\gamma}$	1%	2%	10%

7.5 Limits on physics beyond the standard model

The statistical approach used to derive the limits, constructs a test statistic as the product of likelihood ratios in bins of JGB . These likelihoods are functions of the predicted signal and background yields in each bin. Systematic uncertainties are introduced as nuisance parameters in both signal and background models. Log-normal distributions are taken as a suitable choice for the probability density distributions of the nuisance parameters in order to incorporate uncertainties in the background rates, integrated luminosity, and the signal acceptance times efficiency.

In order to compare the compatibility of the observed data with a GGM SUSY signal, an LHC-style profiled likelihood test statistics, was used [85]. In particular the modified Confidence Levels (CLs) method [86] was used, with a confidence level for excluding the possibility of simultaneous presence of new particle production and background (S+B hypothesis):

$$CL_{S+B} = P_{S+B}\left(X \leq X_{obs}\right) \tag{7.1}$$

A typical limit calculation, also involves computing the confidence level for the background alone:

$$CL_{B} = P_{B}\left(X \leq X_{obs}\right) \tag{7.2}$$

where the probability sum assumes the presence only of the background. This confidence level is used to quantify the confidence of a potential discovery, since it is an expression of the probability of a background process with fewer or equal number to the observed events. Thus the Modified Frequentist confidence level CLs is computed as:

$$CL_{S} = CL_{S+B}/CL_{B} \tag{7.3}$$

For purposes of discovery, the qualifier $1 - CL_B$ indicates the probability that the background (of simulated experiments) might produce "signal" candidates like those observed in the data. The probability in the upper tail of the X distribution in the S+B hypothesis may be used to exclude a signal hypothesis since it does not predict enough signal to explain the relevant candidates in the data.

We calculate upper limits for GGM SUSY points for bino and wino-like neutralinos. The interpretation is done for gluino-squark mass space (both masses range from 400 to 2000 GeV with 80 GeV bin width) for a fixed neutralino mass (375 GeV). Furthemore, for the case of bino-like neutralinos, there's an interpretation for the gluino-neutralino mass plane. Here, the gluino mass ranges from 160 to 2000 GeV (80 GeV bin width), while the neutralino mass range is between 150-1050 GeV (100 GeV bin width), with a fixed squark mass (2500 GeV).

A signal point is excluded if the expected cross section exceeds our upper limit. In order to achieve good signal sensitivity, the limits were calculated for three distinct JGB bins in GeV: [80,100), [100,120), [120,inf). The multiple exclusion search channels in JGB are combined into one taking into account bin-to-bin correlations of the systematic uncertainties as well as the significance of each bin. Table 7.1 summarizes the observed number of events in bins of JGB as well as the corresponding background prediction with statistical and systematic uncertainties. Even though the sensitivity is dominated by the highest JGB bin, some regions of the possible signal's phase-space may also benefit from other bins and therefore from the combination of the bins.

The exclusion contours are derived from the comparsion of the expected and observed cross-sections to the 95% CL upper limits. In Figure 7.2, Figure 7.3 and Figure 7.4 there are the relevant limits for a wino-like and bino-like neutralino. The expected limit derived with the isolation sideband method ($\mathrm{E}_{\mathrm{T}}^{\mathrm{miss}}$ based), described in Ref. [72, 74], is also superimposed (green dashed line, SUS-12-001). The experimental error band displayed around the expected limit, comes from the experimental uncertainties (see Table 7.2), while the theoretical error band comes from uncertainty in the NLO cross-section. The resulting 95% CL limits from these plots for a bino and wino-like neutralino scenario (with fixed neutralino mass) are summarized below.

- For the wino-like scenario with a neutralino mass fixed to 375 GeV, squark masses up to ~ 870 GeV and gluino masses up to ~ 770 GeV can be excluded
- For the bino-like scenario with a neutralino mass fixed to 375 GeV, squark masses up to ~ 900 GeV and gluino masses up to ~ 920 GeV can be excluded

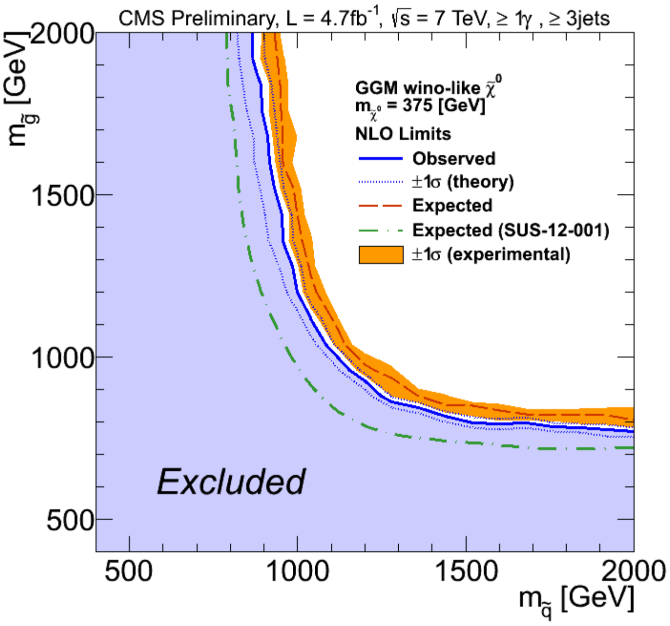

Figure 7.2: Calculated 95% CL exclusion contours for a wino-like neutralino in the squark-gluino mass plane.

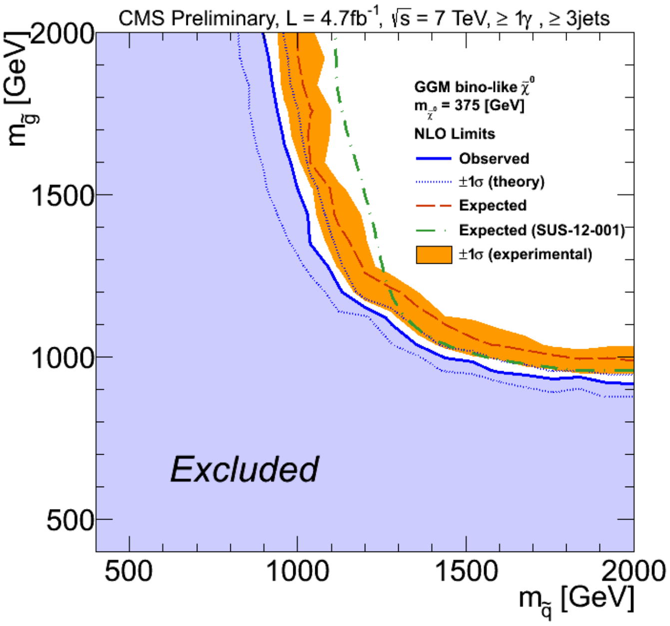

Figure 7.3: Calculated 95% CL exclusion contours for a bino-like neutralino in the squark-gluino mass plane.

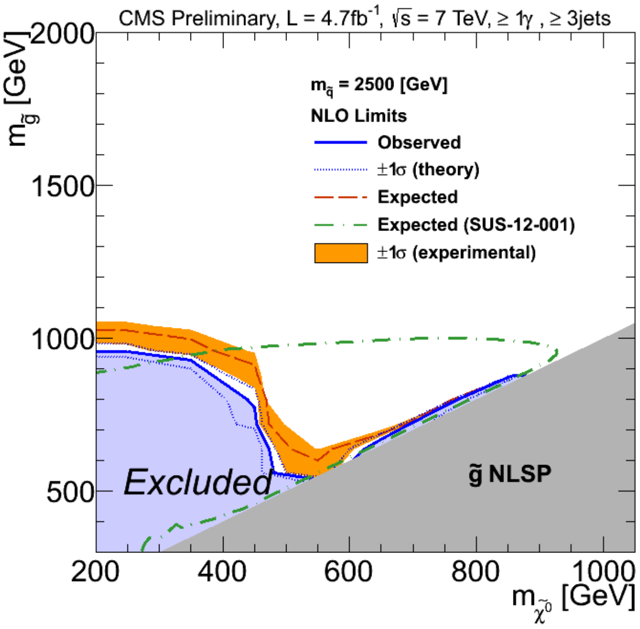

Figure 7.4: Calculated 95% CL exclusion contours for a bino-like neutralino in the neutralino-gluino mass plane.

Chapter 8

Synopsis

> *There is a theory which states that if ever anybody discovers exactly what the Universe is for and why it is here, it will instantly disappear and be replaced by something even more bizarre and inexplicable. There is another theory which states that this has already happened.*
>
> -Douglas Adams-

8.1 Conclusions

In this thesis a novel method for GGM SUSY searches in photon(s) + jets + E_T^{miss} final states using 4.7 fb^{-1} of 7 TeV pp collision data collected with the CMS detector in 2011, was described. We presented the apparatus that made this analysis possible, the CMS detector, along with a study on Micromegas detector in the framework of the sLHC. We described the reconstruction algorithms used in order to obtain higher level objects built from the raw energy deposits recorded by the various subdetectors. Afterwards we gave details about the event selection and defined the JGB variable that was used to establish the presence of the signal over background and estimate the background from the data. Monte Carlo closure tests were used to prove the method's validity and to calculate the JGB systematic uncertainty considering a non-signal case, while additional tests were also repeated by mixing background with SUSY benchmark signals to demostrate the analysis robustness under signal presence in the control region. The same analysis steps were applied on data. The total background contribution in the signal region was estimated using data control samples. Good aggrement between predicted and measured distributions was observed, both in data and MC simulation. Therefore upper limits (95% CL) were set in the GGM parameter space for several models.

Searches for new physics with this signature were previously performed at ATLAS with 36 pb^{-1} [70] and 1.1 fb^{-1} [71], CMS with 36 pb^{-1} [73], 4.7 fb^{-1} [74] of

$\sqrt{s}$ = 7 TeV pp collision data and recently with 4.04 fb^{-1} [75] of data collected at $\sqrt{s}$ = 8 TeV, as well as the Tevatron [76, 77], LEP [78, 79, 80, 81], and HERA [82].

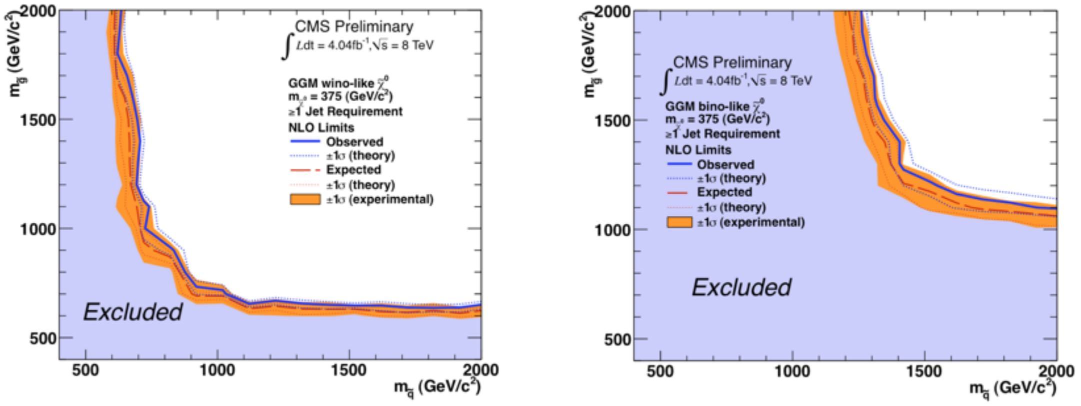

Figure 8.1: Calculated 95% CL exclusion contours for a wino- (left) and bino-like neutralino (right) in the squark-gluino mass plane for the di-photon analysis with the isolation sideband method.

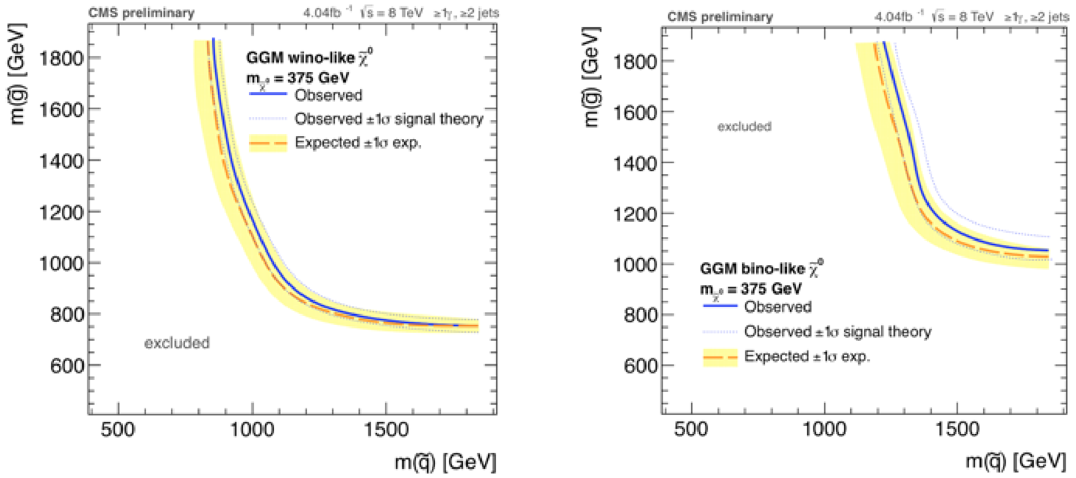

Figure 8.2: Calculated 95% CL exclusion contours for a wino- (left) and bino-like neutralino (right) in the squark-gluino mass plane for the single photon analysis with the isolation sideband method.

The most recent CMS search [74] based on 4.7 fb^{-1} of 7 TeV data, constrained the production of squarks and gluinos to masses above $\sim$ 800-1000 GeV. The other searches put constraints on the gauge boson partners, with the current best lower limit on the neutralino mass [77] of 175 GeV in a general gauge-mediation (GGM) SUSY scenario similar to what was studied here. The method that has been used from the previous CMS analyses [73, 74, 75], is based on a MET selection (isolation sideband). The first attempt was done in diphoton final states which target to the bino-like neutralinos. Figure 8.2 shows the relevant limits for the bino- (left) and wino-like (right) scenarios. Improved limits were achieved, for the wino-like neutralinos, in single photon final states (Figure 8.2). The JGB method that was discussed in the framework of this thesis, is an independent and complementary approach, providing even tighter limits for the wino-like neutralinos. Figure 8.3 (left) shows the relevant limits for the JGB method and the isolation sideband method (dashed green line), concerning the wino-like scenario.

Thus with a neutralino mass fixed to 375 GeV, squark masses up to $\sim$ 870 GeV and gluino masses up to $\sim$ 770 GeV are excluded, while for the bino-like scenario with a neutralino mass fixed to 375 GeV, squark masses up to $\sim$ 900 GeV and gluino masses up to $\sim$ 920 GeV are also excluded (Fig. 8.3 (right)). Furthermore, for the bino-like scenario with fixed squark mass (2500 GeV) and neutralino masses up to $\sim$ 350 GeV, gluino masses up to $\sim$ 950 GeV are excluded (Fig. 8.4).

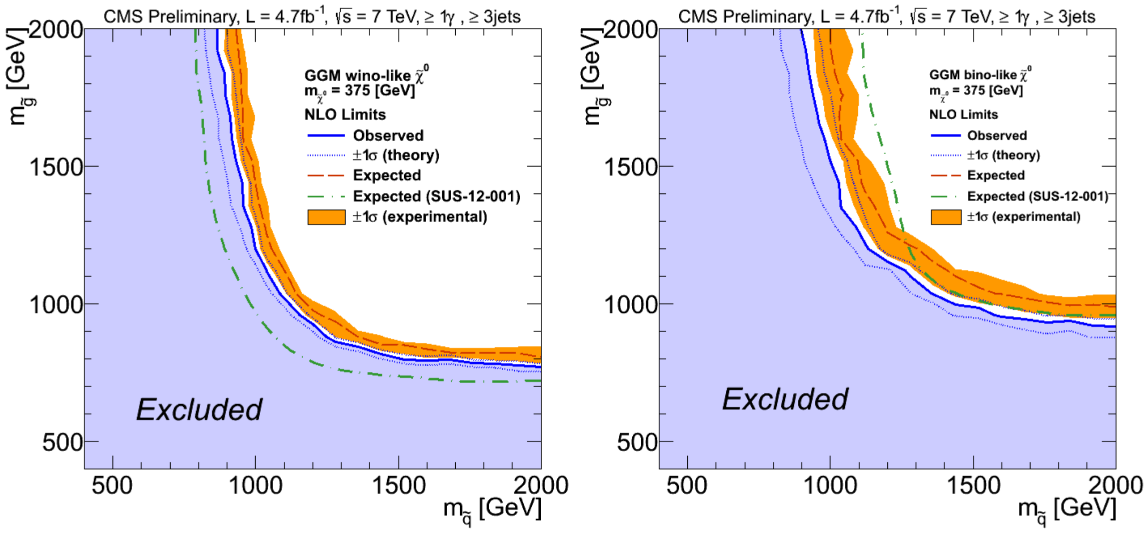

Figure 8.3: Calculated 95% CL exclusion contours for a wino- (left) and bino-like neutralino (right) in the squark-gluino mass plane.

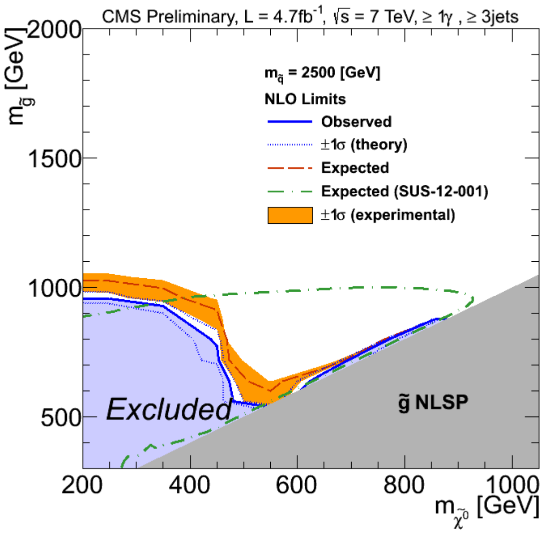

Figure 8.4: Calculated 95% CL exclusion contours for a bino-like neutralino in the neutralino-gluino mass plane.

8.2 Outlook

This analysis' prospects are considerably enhanced by the tremendous rate at which data is being taken at the LHC (by the time of this writing, an integrated luminosity of 13.92 fb^{-1} has been recorded by CMS). Future studies with this enlarged data sample will make possible higher-precision measurements and thus searches for new physics beyond the standard model in this final state will be enhanced and considerably benefit and might lead to the identification of a new particle in the SUSY framework.

Bibliography

[1] M. Maltoni, T. Schwetz, M. A. Tortola, and J. W. F. Valle. "Status of global fits to neutrino oscillations", (2004), arXiv:0405.172v6.

[2] S. P. Martin, "Supersymmetry Primer" (1997), arXiv:hep-ph/9709356.

[3] Peskin, Michael E.; Schroeder, Daniel V., "An Introduction to Quantum Field Theory" (1995), ISBN 0-201-50397-2.

[4] D. Griffiths, "Introduction to Elementary Particles", (1987), John Wiley & Sons, Inc.

[5] N. Arkani-Hamed, S. Dimopoulos, G. Dvali "The Hierarchy problem and new dimensions at a millimeter", Phys. Lett. B 429: 263–272, (1998),arXiv:hep-ph/9803315, Bibcode 1998PhLB..429..263A, doi:10.1016/S0370-2693(98)00466-3.

[6] J. Wess, J. Bagger, "Supesymmetry and Sulergravity", (1992), Princeton University Press, ISBN 0-691-08556-0.

[7] CMS Collaboration, "Observation of a new boson at a mass of 125 GeV with the CMS experiment at the LHC", Phys. Lett. B 716: 30-61, (2012).

[8] ATLAS Collaboration, "Observation of a new particle in the search for the Standard Model Higgs boson with the ATLAS detector at the LHC", Phys. Lett. B 716: 1-29, (2012).

[9] P. Meade, N. Seiberg, D. Shih, "General Gauge Mediation", (2008), arXiv:0801.3278v3.

[10] P. Meade et al., “General Gauge Mediation”, Prog. Theor. Phys. Suppl 143 (2009) doi:110.1143/PTPS.177.143.

[11] M. Buican et al., “General Gauge Mediation”, European Physical Journal 016 (2006), doi:10.1088/1126-6708/2009/03/016.

[12] Ryuichiro Kitano, Hirosi Ooguri and Yutaka Ookouchi, "Supersymmetry Breaking and Gauge Mediation", (2010), arXiv:1001.4535v2 [hep-th].

[13] S.L. Dubovsky, D.S. Gorbunov, S.V. Troitsky, "Gauge mechanism of mediation of supersymmetry breaking", High Energy Physics - Phenomenology (hep-ph), doi: 10.1070/PU1999v042n07ABEH000537, arXiv:hep -ph/9905466v1.

[14] A. H. Chamseddine, R. L. Arnowitt, and P. Nath, "Locally Supersymmetric Grand Unification," Phys.Rev.Lett. 49 (1982) 970.

[15] D. Kaplan, G. Kribs, and M. Schmaltz, "Supersymmetry breaking through transparent extra dimensions,".

[16] L. Randall and R. Sundrum, "Out of this world supersymmetry breaking," Nucl.Phys. B557 (1999) 79–118, arXiv:hep-th/9810155 [hep-th].

[17] Wess J, Bagger J, "Supersymmetry and Supergravity", Princeton Univ. Press, (1982).

[18] O.S. Bruning et al., "The LHC design report v.1: the LHC Main Ring", CERN-2004-003-V-1, (2004), `http://cdsweb.cern.ch/record/782076`.

[19] O.S. Bruning et al. "The LHC design report v.2 : the LHC Infrastructure and General Services", CERN-2004-003-V-2, (2004), `http://cdsweb.cern.ch/record/815187`.

[20] M. Benedikt et al. (eds.), "The LHC design report v.3 : the LHC Injector Chain", CERN-2004-003-V-3, (2004), `http://cdsweb.cern.ch/record/823808`.

[21] Lyndon Evans and Philip Bryant, "LHC Machine", Journal of Instrumentation, 3(08):S08001, (2008).

[22] Paolo Azzurri, "The CMS Silicon Strip Tracker", Institute of Physics Publishing Journal of Physics: Conference Series 41 (2006) 127–134, doi:10.1088/1742-6596/41/1/011.

[23] P. Adzic et al., Energy resolution of the barrel of the CMS electromagnetic calorimeter, JINST 2 P04004, (2007).

[24] A. Quadt et al., "Top quark physics at hadron colliders", European Physical Journal C (2006) doi:10.1140/epjc/s2006-02631-6.

[25] M. Cacciari, G. Salam, and G. Soyez, "The anti-kt jet clustering algorithm", Journal of High Energy Physics 04 (2008) doi:10.1088/1126-6708/2008/04/063, arXiv:0802.1189v2 [hep-ph].

[26] W. Beenakker et al., "Squark and gluino production at hadron colliders", Nucl.Phys.B492 (1997) doi:10.1016/S0550-3213(97)00084-9,arXiv:hep-ph/9610490.

[27] T. Sjostrand, S. Mrenna, and P. Z. Skands, ”PYTHIA 6.4 Physics and Manua”l, JHEP 05, 026 (2006). hep-ph/0603175.

[28] A. Johan et al., “MadGraph 5: Going Beyond”, High Energy Physics - Phenomenology (2011) doi:10.1007/JHEP06(2011)128,arXiv:1106.0522v1.

[29] S. Agostinelli et al. “G4–a simulation toolkit. Nuclear Instruments and Methods in Physics Research Section A: Accelerators, Spectrometers, Detectors and Associated Equipment“, 506(3):250–303, (2003).

[30] M. Cacciari and G. Salam, “Pileup subtraction using jet areas”, Phys. Lett. 659 (2008) doi:10.1016/j.physletb.2007.09.077.

[31] T.Alexopoulos et al., "Study of a micromegas chamber in a neutron beam”, JINST 5 (2010) P02005 doi:10.1088/1748-0221/5/02/P02005.

[32] T.Alexopoulos et al., "Micromegas study for the sLHC enviroment”, JINST 5 (2010) P02003 doi:10.1088/1748-0221/5/02/P02003.

[33] T.Alexopoulos et al., ”Performances and ageing study of resistive-anodes Micromegas detectors for HL-LHC environment”, arXiv:1201.1843v1.

[34] Y. Giomataris et al., Micromegas: A high granularity position sensitive gaseous detector for high particle flux environments, Nucl. Instrum. Meth. A 376 (1996) 29.

[35] C. Benet et al., The 40cmx40cm gaseous microstrip detector Micromegas for the high-luminosity COMPASS experiment at CERN, Nucl. Instrum. Meth. A 536 (2005) 61.

[36] B. Peyaud et al., KABES: A novel beam spectrometer for NA48, Nucl. Instrum. Meth. A 535 (2004) 247.

[37] J Pancin et al., Measurement of the nTOF beam profile with a micromegas detector, Nucl. Instrum. Meth. A 524 (2004) 102.

[38] P. Abbon et al., The Micromegas detector of the CAST experiment, New J. Phys. 9 (2007) 170.

[39] S. Anvar et al., Large bulk Micromegas detectors for TPC applications, Nucl. Instrum. Meth. A 602 (2009) 415.

[40] Y. Giomataris et al., Micromegas in a bulk, Nucl. Instrum. Meth. A 560 (2006) 405.

[41] CAEN Technical Information Manual, MOD. V550/V550 B, MOD. V550 A/V550 AB, 2 CHANNEL CRAMS, Revision n. 3 (28 August 2002).

[42] CAEN Technical Information Manual, MOD. V551 B, CRAMS, SEQUENCER, Version 1.2 (18 July 2003).

[43] CAEN Technical Information Manual, MOD. V462, Dual Gate Generator, Revision n.0 (25 January 1996).

[44] CAEN Technical Information Manual, MOD. V2718, VX2718, VN2738, VMEPCI, Optical Link Bridge, Manual Rev.7, Revision n.7 (29 March 2007).

[45] G.K. Fanourakis et al., The use of the Micromegas technology for a new imaging system, Nucl. Instrum. Meth. A 527 (2004) 62.

[46] National Instruments Corporation, LabVIEW User Manual, Part Number 320999E-01, (2003).

[47] F. Sauli, "Principles of operation of multiwire proportional and drift chambers", CERN 77-09, Geneva (1977).

[48] W. R. Leo, "Techniques for Nuclear and Particle Physics Experiments", Springer-Verlag, (1994) ISBN 3-540-57280-52.

[49] A. Oed, "Properties of micro-strip gas chambers (MSGC) and recent developments", Nucl. Instrum. Meth. A 367 (1995), doi:10.1016/0168-9002(95)00657-5.

[50] A. Oed, "Position-sensitive detector with microstrip anode for electron multiplication with gases", Nucl. Instrum. Meth. Phys. Res. A263 (1988) 351.

[51] Geralis, T.; Kyriazopoulou, S.; Markou, C.; Michailakis, I.; Zachariadou, K., The global trigger processor emulator system for the CMS experiment, doi: 10.1109/TNS.2005.852650.

[52] ATLAS Collaboration, "The ATLAS Experiment at the CERN Large Hadron Collider", Journal of Instrumentation, 3(08):S08003, (2008).

[53] CMS Collaboration, "The CMS experiment at the CERN LHC", Journal of Instrumentation, 3(08):S08004, (2008).

[54] Collaboration, "The ALICE experiment at the CERN LHC", Journal of Instrumentation, 3(08):S08002, (2008).

[55] LHCb Collaboration, "The LHCb Detector at the LHC", Journal of Instrumentation, 3(08):S08005, (2008).

[56] CMS Collaboration, "The Electromagnetic Calorimeter Technical Design Report", CERN/LHCC 97-033, CMS TDR 4, Addendum CERN/LHCC 2002-027, 1997.

[57] CMS Collaboration, "The Hadron Calorimeter Technical Design Report", CERN/LHCC 97-031, CMS TDR 2, (1997).

[58] CMS Collaboration, "The Muon Project Technical Design Report", CERN/LHCC 97-032, CMS TDR 3, (1997).

[59] CMS Collaboration, The TriDAS Project Technical Design Report, Volume 1: "The Trigger Systems", CERN/LHCC 2000-38, CMS TDR 6.1, (2000).

[60] CMS Collaboration, The TriDAS Project Technical Design Report, Volume 2: "Data Acquisition and High-Level Trigger", CERN/LHCC 2002-26, CMS TDR 6.2, (2002).

[61] CMS Collaboration, "Detector performance and software", CMS Physics Technical Design Report Volume 1, (2006).

[62] CMS Collaboration, “Search for Supersymmetry in Events with Photons, Jets and Missing Energy”, CMS Physics Analysis Summary CMS-PAS-SUS-11-009, (2011).

[63] CMS Collaboration, “Search for Physics Beyond the Standard Model in Z + jets + MET events at the LHC”, CMS Physics Analysis Summary CMS-PAS-SUS-11-012, (2011).

[64] CMS Collaboration, “Photon reconstruction and identification at sqrt(s) = 7 TeV”, CMS Physics Analysis Summary CMS-PAS-EGM-10-005, (2010).

[65] CMS Collaboration, "Performance of Jet Algorithms in CMS", CMS Physics Analysis Summary CMS-PAS-JME-07-003, (2009).

[66] CMS Collaboration, “Jet Plus Tracks Algorithm for Calorimeter Jet Energy Corrections in CMS”, CMS Physics Analysis Summary CMS-PAS-JME-09-002, (2009).

[67] CMS Collaboration, “Determination of the Jet Energy Scale in CMS with pp Colisions at $\sqrt{s}$=7 TeV”, CMS Physics Analysis Summary CMS-PAS-JME-10-010, (2010).

[68] CMS Collaboration, “Particle–Flow Event Reconstruction in CMS and Performance for miss Jets, Taus, and ET ”, CMS Physics Analysis Summary CMS-PAS-PFT-09-001 (2009).

[69] CMS Collaboration, “Determination of jet energy calibration and transverse momentum resolution in CMS”, JINST 11 (2011).

[70] ATLAS Collaboration, “Search for Diphoton Events with Large Missing Transverse Energy with 36 pb–1 of 7 TeV Proton-Proton Collision Data with the ATLAS Detector”, Eur. Phys. J. C71 (2011) 1744, doi:10.1140/epjc/s10052-011-1744-9,arXiv:1107.0561.

[71] ATLAS Collaboration, “Search for Diphoton Events with Large Missing Transverse Momentum in 1 f b– 1 of 7 TeV Proton-Proton Collision Data with the ATLAS Detector”, Phys. Lett. B710 (2012) 519, arXiv:1111.4116.

[72] CMS Collaboration, “Search for new physics in events with photons, jets and missing transverse energy in pp collisions at $\sqrt{s}$=7 TeV”, arXiv:submit/0597701 [hep-ex], (2012).

[73] CMS Collaboration, “Search for Supersymmetry in pp Collisions at $\sqrt{s} = 7$ TeV in Events with Two Photons and Missing Transverse Energy”, Phys. Rev. Lett. 106 (2011) 211802, doi:10.1103/PhysRevLett.106.211802.

[74] CMS Collaboration, “Search for New Physics in Events with Photons and Missing Transverse Energy at CMS”, CMS Physics Analysis Summary CMS-PAS-SUS-12-001, (2012).

[75] CMS Collaboration, “Search for Supersymmetry in Events with Photons and Missing Energy”, CMS Physics Analysis Summary CMS-PAS-SUS-12-018, (2012).

[76] T. Aaltonen et al., “Search for Supersymmetry with Gauge-Mediated Breaking in Diphoton Events with Missing Transverse Energy at CDF II”, Phys. Rev. Lett. 104 (2010) 011801, doi:10.1103/PhysRevLett.104.011801.

[77] V. M. Abazov et al., “Search for Diphoton Events with Large Missing Transverse Energy in 6.3 fb^{-1} of pp Collisions at $\sqrt{s} = 1.96$ TeV”, Phys. Rev. Lett. 105 (2010) 221802, doi:10.1103/PhysRevLett.105.221802.

[78] A. Heister et al., “Search for Gauge Mediated SUSY Breaking Topologies in e$^+$e$^-$ Collisions at Centre-of-Mass Energies up to 209 GeV”, Eur. Phys. J. C25 (2002) 339, doi:10.1007/s10052-002-1005-z.

[79] J. Abdallah et al., “Photon Events with Missing Energy in e+ e– Collisions at (s) = 130 to 209 GeV”, Eur. Phys. J. C38 (2005) 395, doi:10.1140/epjc/s2004-02051-8.

[80] P. Achard et al., “Single- and Multi-Photon Events with Missing Energy in e$^+$e$^-$ Collisions at LEP”, Phys. Lett. B587 (2004) 16, doi:10.1016/j.physletb.2004.01.010.

[81] G. Abbiendi et al., “Search for Gauge-Mediated Supersymmetry Breaking Topologies in e^+e^- Collisions at LEP2”, Eur. Phys. J. C46 (2006) 307, doi:10.1140/epjc/s2006-02524-8.

[82] A. Aktas et al., “Search for Light Gravitinos in Events with Photons and Missing Transverse Momentum at HERA”, Phys. Lett. B616 (2005) 31, doi:10.1016/j.physletb.2005.04.038.

[83] CMS Collaboration, “Fast simulation of the CMS detector at LHC”, J. Phys. Conf. Ser. 331 (2011), no. 3, 032049, doi:10.1088/1742-6596/331/3/032049.

[84] CMS Collaboration, “Absolute Calibration of the Luminosity Measurement at CMS: Winter 2012 Update”, CMS Physics Analysis Summary CMS-PAS-SMP-12-008, (2012).

[85] ATLAS and CMS Collaborations, LHC Higgs Combination Group, “Procedure for the LHC Higgs boson search combination in Summer 2011”, ATL-PHYS-PUB/CMS NOTE 2011-11, 2011/005, (2011).

[86] CMS Collaboration, “Confidence Level Computation for Combining Searches with Small Statistics”, Nuclear Instruments and Methods in Physics Research 434 (1999), doi:10.1016/S0168-9002(99)00498-2, arXiv:hep-ex/9902006v1.

[87] CMS Collaboration, “Search for Physics Beyond the Standard Model in Z + jets + MET events at the LHC”, CMS Physics Analysis Summary CMS-PAS-SUS-11-019, (2011).

[88] CMS Collaboration, “SUSY Search in Photon(s)+jets+E_T^{miss} final state with the Jet-Gamma Balance method”, CMS Physics Analysis Summary CMS-PAS-SUS-12-013, (2012).

[89] U. Gebbert et al., “Search for Supersymmetry in Events with one Photon, Jets and Missing Transverse Energy”, CMS Note 2011/512.

[90] M. Buchmann, P. Martinez, F. Ronga et al., “SUSY Searches in the Z + jets + MET final state in 7 TeV pp collisions with the Jet-Z Balance method”, CMS Note 2011/317.

[91] M. Buchmann, P. Martinez, F. Ronga et al., “Search for Physics Beyond the Standard Model in Z + jets + MET events at the LHC”, CMS Note 2011/345.

[92] A. Askew et al., “Search for Gauge Mediated Supersymmetry Breaking Using Two Photons and Missing Transverse Energy”, CMS Note 2011/515.

[93] E.Ntomari, T. Geralis, K. Theofilatos, "SUSY Searches in the Photon(s)+jets+E_T^{miss} final state in 7 TeV pp collisions with the JGB method", CMS Note 2012/180.

[94] K. Theofilatos, “Supersymmetric particle detection techniques and electromagnetic calorimeter testbeam analysis with the CMS detector”, PHD Thesis, National Tech.University of Athens and N.C.S.R. Demokritos.

[95] T. Dafni, "A Search for Solar Axions with the MICROMEGAS Detector in CAST, PHD Thesis, Technischen Universitat Darmstadt" (2005).

[96] E. Ntomari, "Study of a micromegas detector", Master Thesis, National Tech.University of Athens and N.C.S.R. Demokritos (2009).

[97] https://twiki.cern.ch/twiki/bin/view/CMS/RA3PhotonTriggerPerformanceV2

Appendix A

Study of the SM Backgrounds

In the tables below we can see the total number of events observed and predicted in different signal regions, for data and MC simulation as well.

Table A.1: Total number of events observed in the JGB>100 region on data and MC simulation, and corresponding background prediction

4.7 fb^{-1}, JGB>100 GeV	**Data**			**MC simulation**		
$\geq 1\gamma, \geq$ **3jets**		**stat.**	**sys.**		**stat.**	**sys.**
SM estimation (JGB<0)	8	$^{+3.9}_{-2.8}$	±3.2	6.1	±2.5	±2.4
SM estimation ($f_{e\to\gamma}$)	1.2	±0.1	±0.5	0.3	±0.1	±0.1
Total SM estimation	9.2	$^{+3.9}_{-2.8}$	±3.2	6.4	±2.5	±2.4
Observed	16			4.7	±1.5	±1.9

Table A.2: Total number of events observed in the JGB<100 region on data and MC simulation, and corresponding background prediction

4.7 fb^{-1}, JGB<100 GeV	**Data**			**MC simulation**		
$\geq 1\gamma, \geq$ **3jets**		**stat.**	**sys.**		**stat.**	**sys.**
SM estimation (JGB<0)	2428	$\pm$ 49	$\pm$ 971	2260	$\pm$ 46	$\pm$ 904
SM estimation ($f_{e\to\gamma}$)	2.1	$\pm$ 0.1	$\pm$ 0.8	3.9	$\pm$ 2.0	$\pm$ 1.6
Total SM estimation	2430	$\pm$49	$\pm$ 972	2263	$\pm$48	$\pm$ 905
Observed	2422			2346	$\pm$ 47	$\pm$ 938

Table A.3: Total number of the measured events in JGB>0 region and the corresponding background prediction

4.7 fb^{-1}	**120-160 GeV**			**160-210 GeV**			**210-270 GeV**			**270-350 GeV**		
		stat.	**sys.**		**stat.**	**sys.**		**stat.**	**sys.**		**stat.**	**sys.**
SM estimation (JGB<0)	3	$^{+4.1}_{-2.9}$	±1.2	0	$^{+1.8}_{-0}$	±0	0	$^{+1.8}_{-0}$	±0	0	$^{+1.8}_{-0}$	±0
SM estimation ($\mathbf{f}_{\mathbf{e}\to\gamma}$)	0.32	± 0.04	± 0.13	0.27	± 0.04	±0.11	0.14	± 0.03	± 0.06	0.07	± 0.02	±0.03
data	4			1			1			2		

A.0.1 Comparison of data vs MC Samples

In this section, there is a presentation of comparison plots for different kinematic distributions in data and SM MC simulation for the case of at least one photon, at least three jets and MET. MC plots are normalized to a luminosity of 4.7 fb^{-1} and are PU corrected. The systematic uncertainty on the luminosity is not accounted for in these plots. In general there is a good agreement between data and MC simulation.

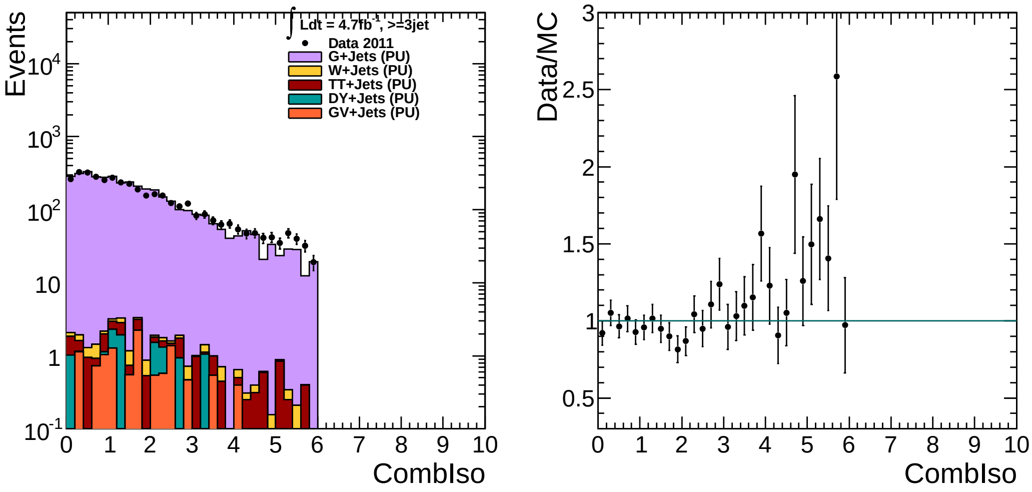

Figure A.1: The combined isolation distribution for the data and the most important SM backgrounds (left) and the ratio of data vs simulated events (right).

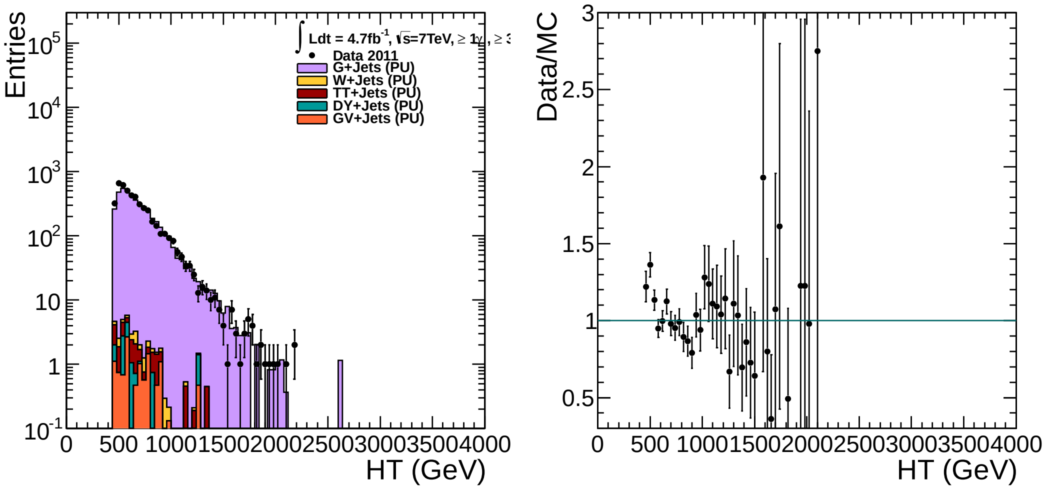

Figure A.2: The HT distribution for the data and the most important SM backgrounds (left) and the ratio of data vs simulated events (right).

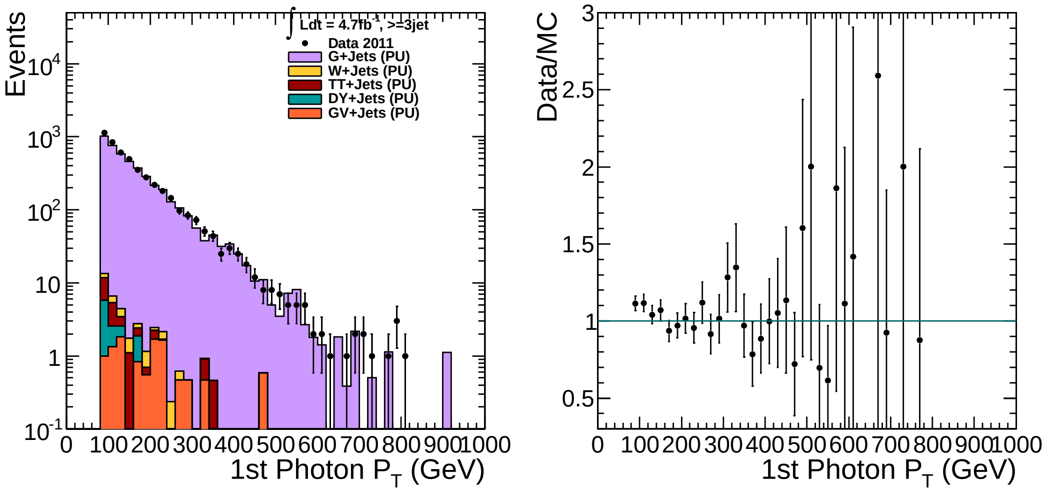

Figure A.3: The leading photon's p_T distribution for the data and the most important SM backgrounds (left) and the ratio of data vs simulated events (right).

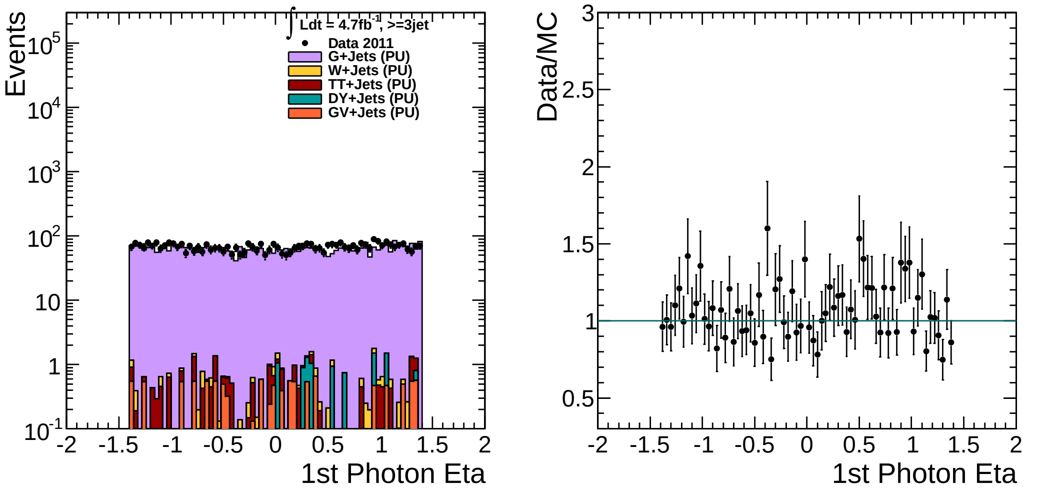

Figure A.4: The leading photon's eta distribution for the data and the most important SM backgrounds (left) and the ratio of data vs simulated events (right).

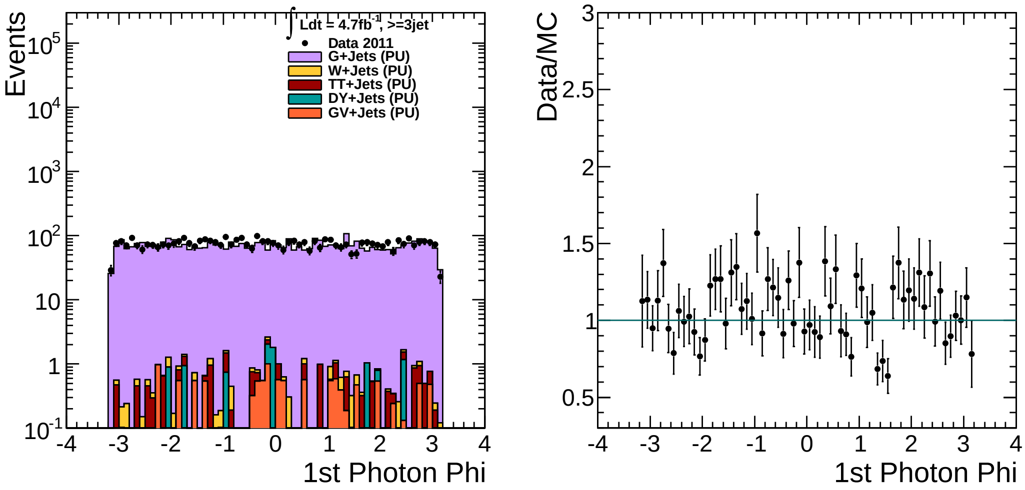

Figure A.5: The leading photon's phi distribution for the data and the most important SM backgrounds (left) and the ratio of data vs simulated events (right).

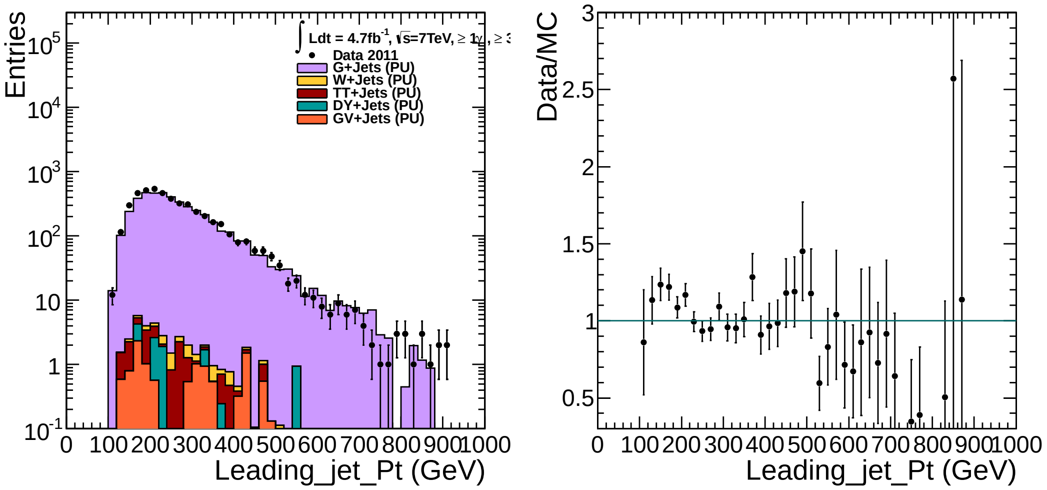

Figure A.6: The leading jet's p_T distribution for the data and the most important SM backgrounds (left) and the ratio of data vs simulated events (right).

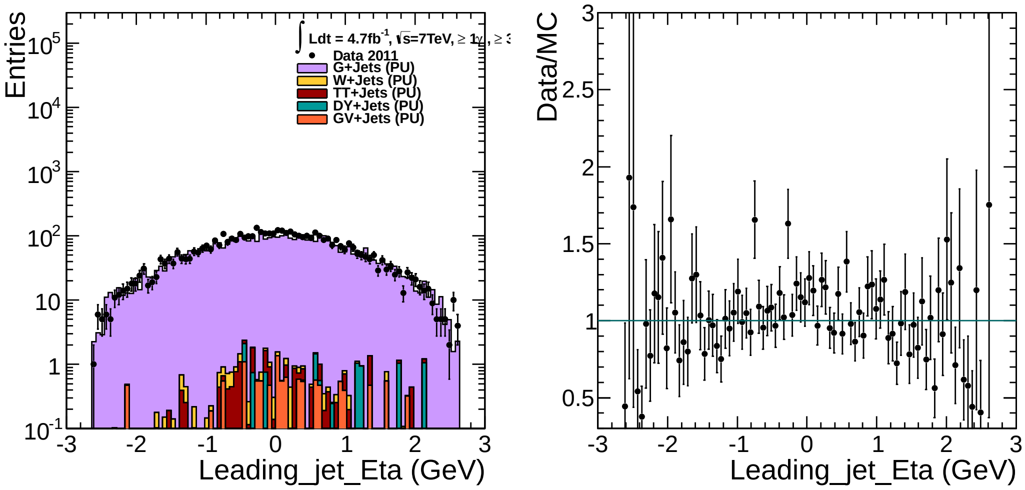

Figure A.7: The leading jet's eta distribution for the data and the most important SM backgrounds (left) and the ratio of data vs simulated events (right).

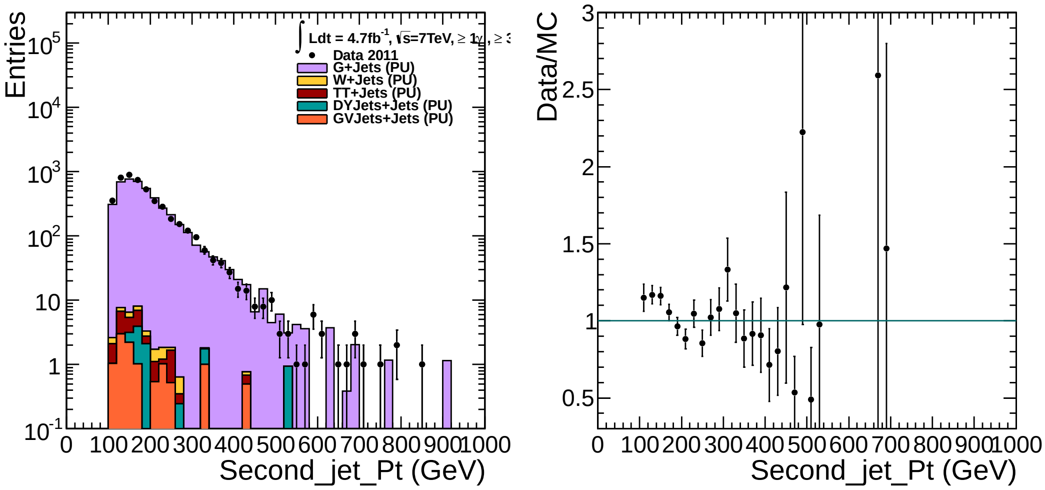

Figure A.8: The sub-leading jet's p_T distribution for the data and the most important SM backgrounds (left) and the ratio of data vs simulated events (right).

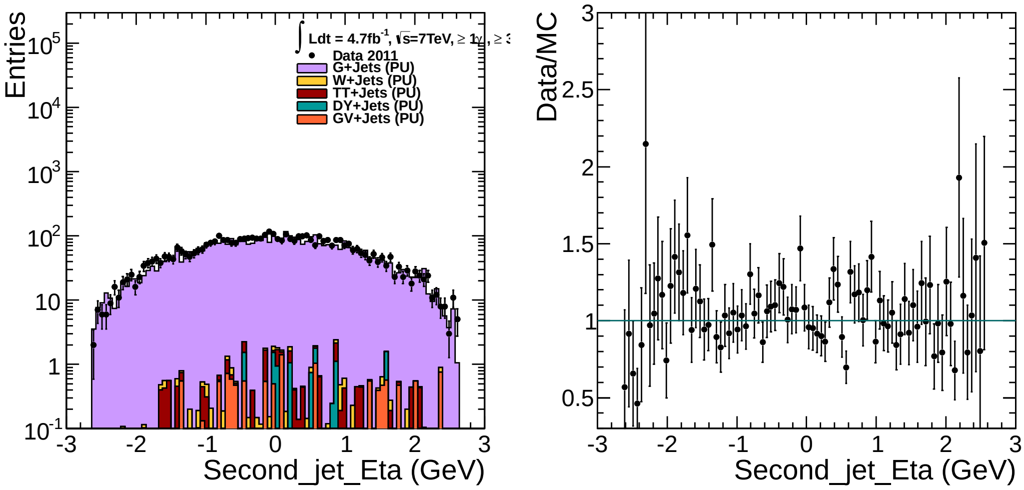

Figure A.9: The sub-leading jet's eta distribution for the data and the most important SM backgrounds (left) and the ratio of data vs simulated events (right).

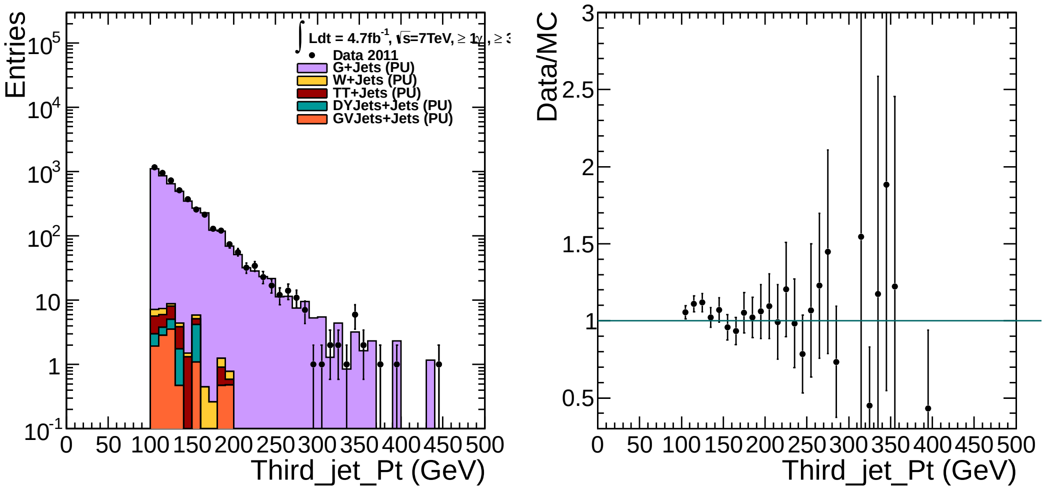

Figure A.10: The third jet's p_T distribution for the data and the most important SM backgrounds (left) and the ratio of data vs simulated events (right).

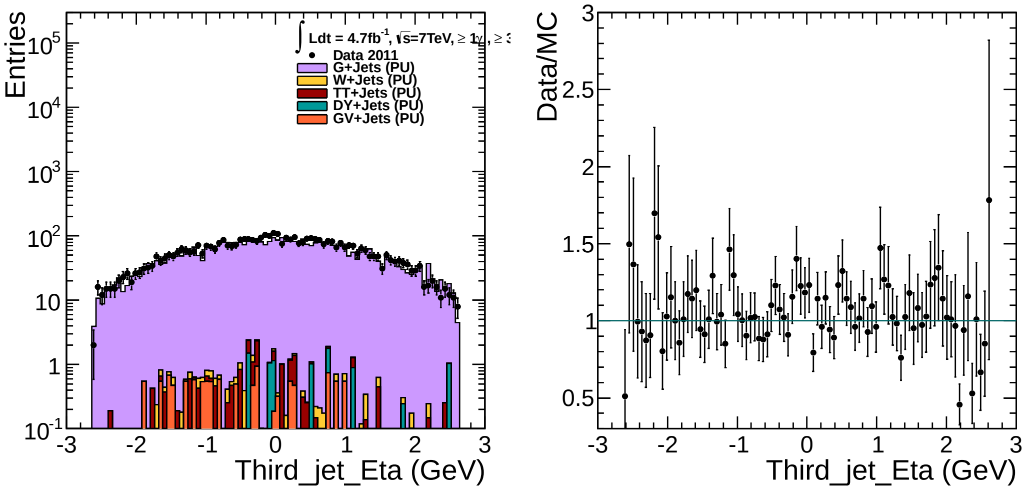

Figure A.11: The third jet's eta distribution for the data and the most important SM backgrounds (left) and the ratio of data vs simulated events (right).

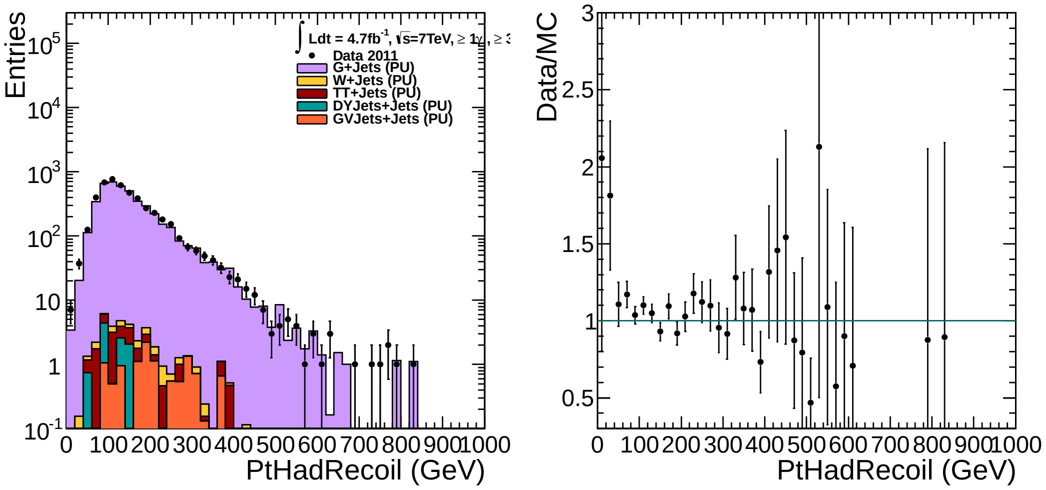

Figure A.12: The hadronic recoil distribution for the data and the most important SM backgrounds (left) and the ratio of data vs simulated events (right).

A.0.2 Comparison of data vs MC Samples for the electrons

In this section, there is a presentation of comparisons for different kinematic distributions, in data and SM MC simulation, for the case of at least least one electron (same as photons except from the requirement of the pixel seed veto, which is inverted), at least three jets and MET. MC plots are normalized to a luminosity of 4.7 fb^{-1} and are PU corrected. The systematic uncertainty on the luminosity is not accounted for in these plots. In general there is a satisfactory agreement between data and MC simulation.

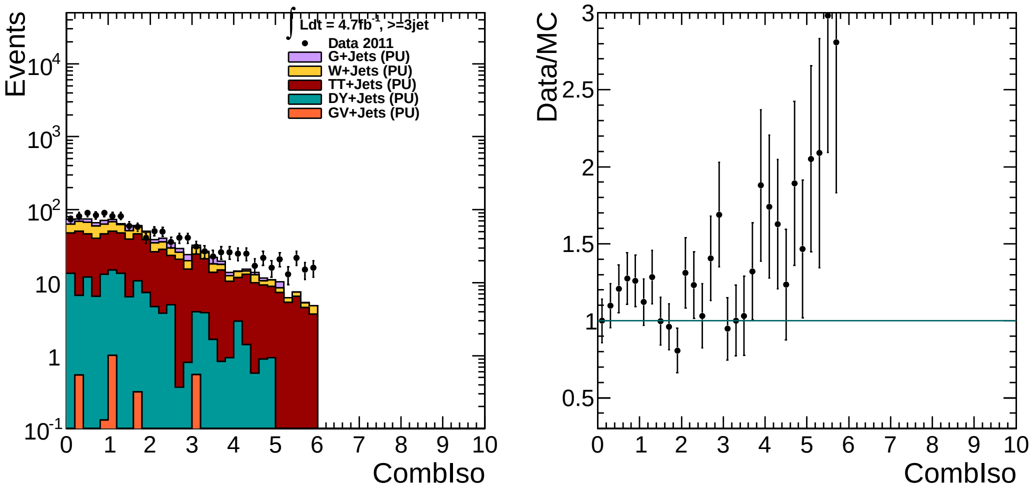

Figure A.13: The combined isolation distribution for the data and the most important SM backgrounds (left) and the ratio of data vs simulated events (right).

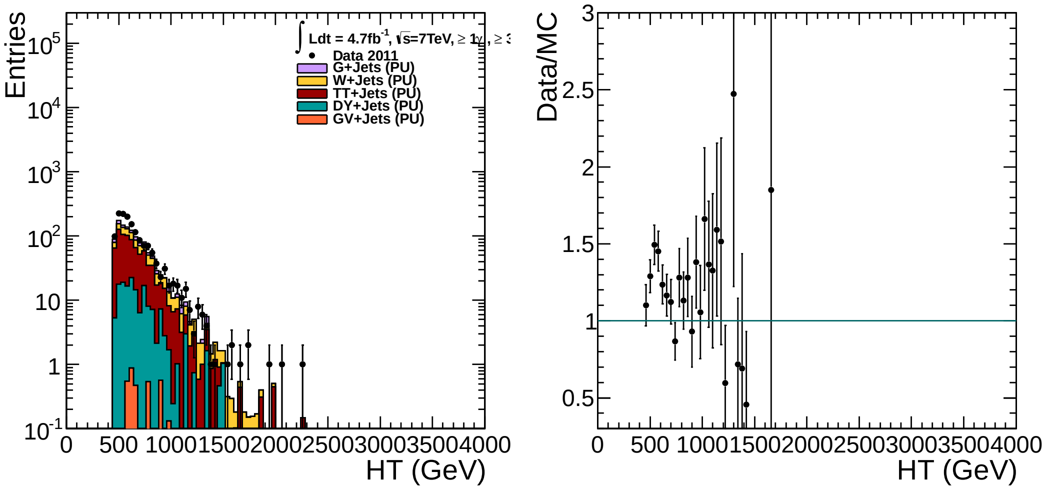

Figure A.14: The HT distribution for the data and the most important SM backgrounds (left) and the ratio of data vs simulated events (right).

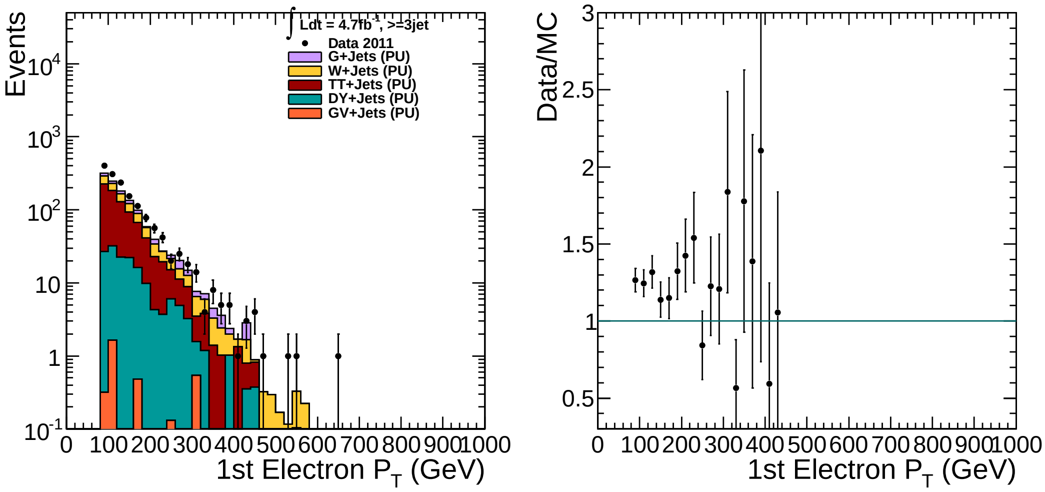

Figure A.15: The leading electron's p_T distribution for the data and the most important SM backgrounds (left) and the ratio of data vs simulated events (right).

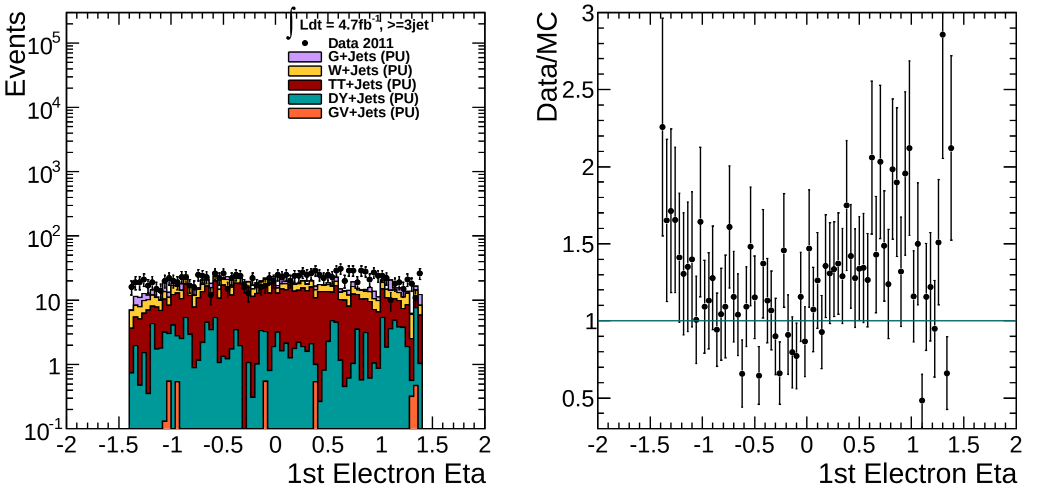

Figure A.16: The leading electron's eta distribution for the data and the most important SM backgrounds (left) and the ratio of data vs simulated events (right).

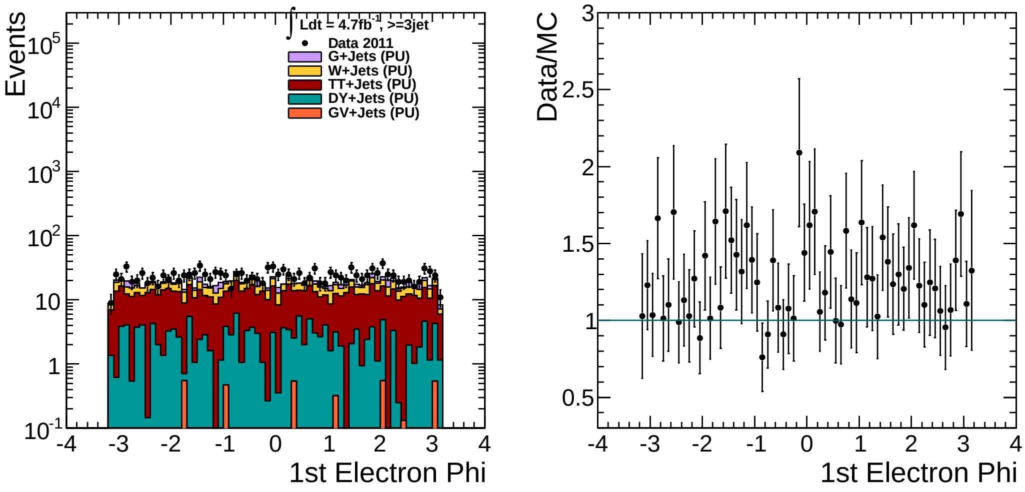

Figure A.17: The leading electron's phi distribution for the data and the most important SM backgrounds (left) and the ratio of data vs simulated events (right).

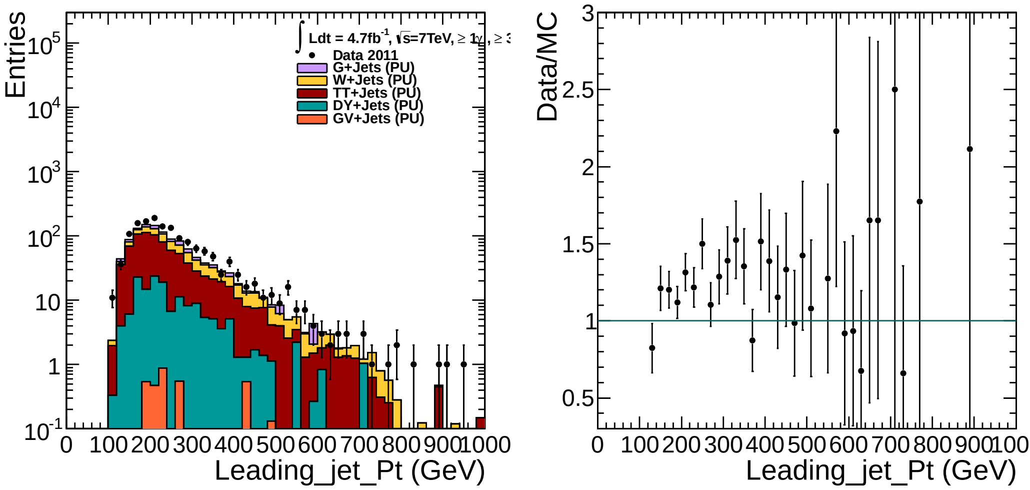

Figure A.18: The leading jet's p_T distribution for the data and the most important SM backgrounds (left) and the ratio of data vs simulated events (right).

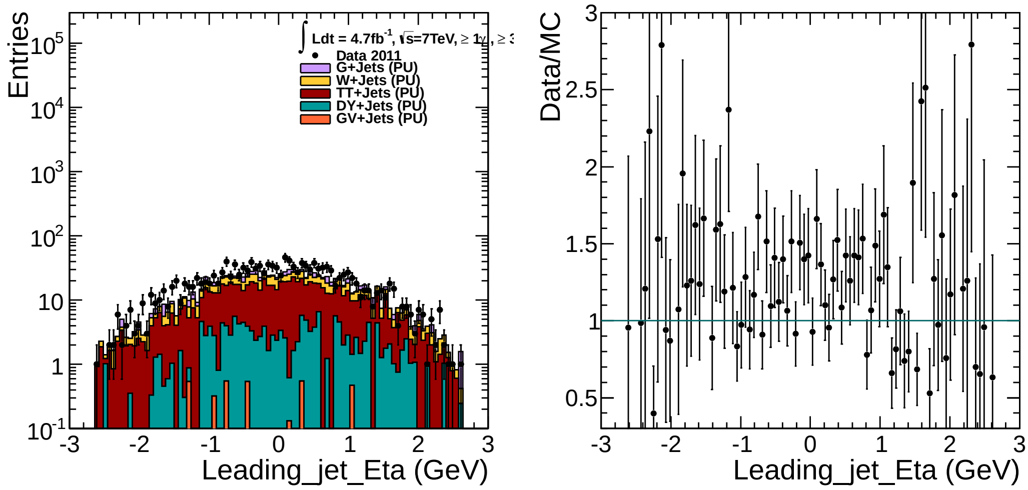

Figure A.19: The leading jet's eta distribution for the data and the most important SM backgrounds (left) and the ratio of data vs simulated events (right).

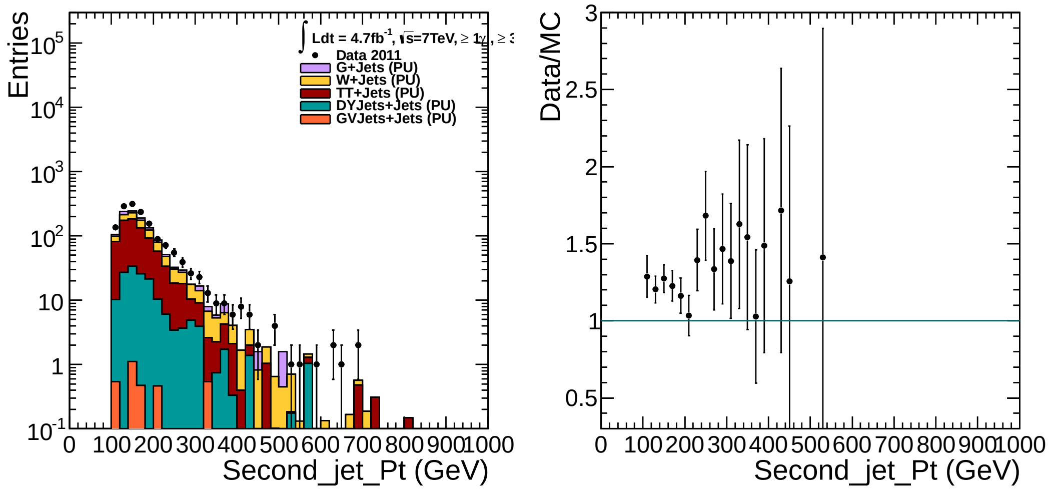

Figure A.20: The sub-leading jet's p_T distribution for the data and the most important SM backgrounds (left) and the ratio of data vs simulated events (right).

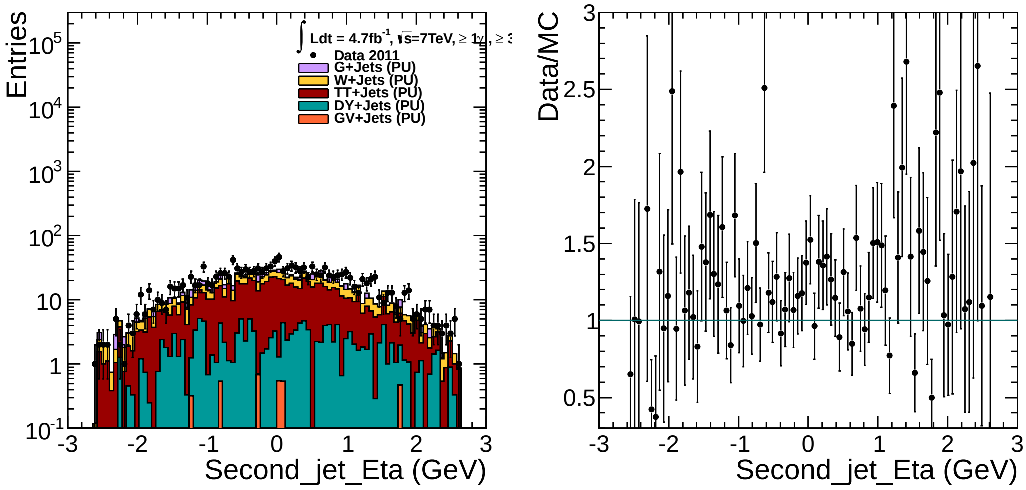

Figure A.21: The sub-leading jet's eta distribution for the data and the most important SM backgrounds (left) and the ratio of data vs simulated events (right).

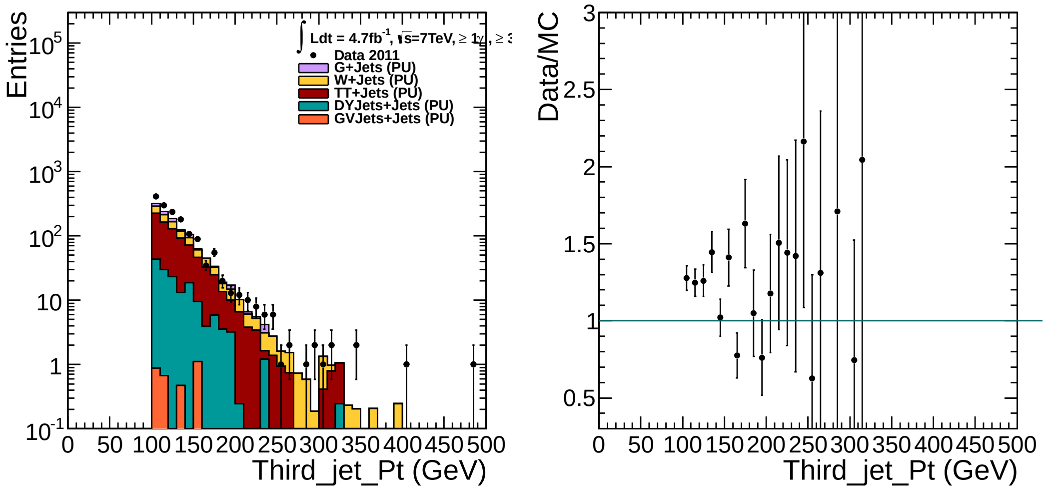

Figure A.22: The third jet's p_T distribution for the data and the most important SM backgrounds (left) and the ratio of data vs simulated events (right).

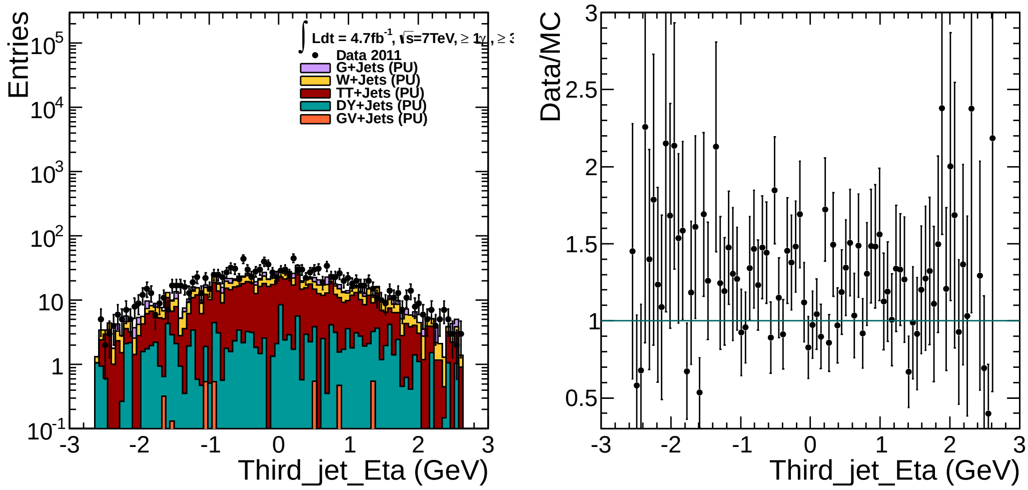

Figure A.23: The third jet's eta distribution for the data and the most important SM backgrounds (left) and the ratio of data vs simulated events (right).

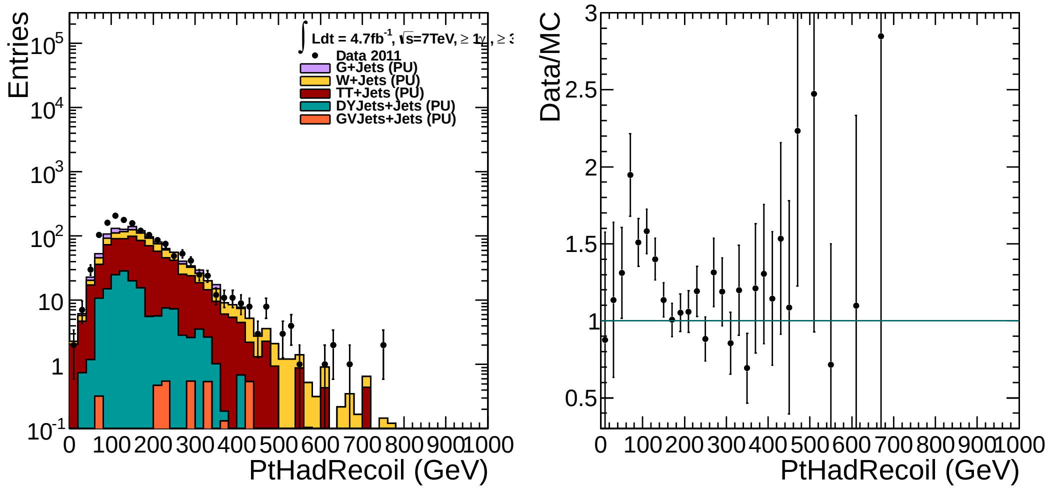

Figure A.24: The hadronic recoil distribution for the data and the most important SM backgrounds (left) and the ratio of data vs simulated events (right).

A.0.3 Comparison of observed and predicted events on data

In this section, there is a presentation of a comparison of kinematic distributions in data between the observed events in the signal region (JGB > 0) and the relevant estimated background (as it is derived from the mentioned data-driven method) for the case of at least least one photon and at least three jets. In general there is a good agreement between the observed and the predicted values.

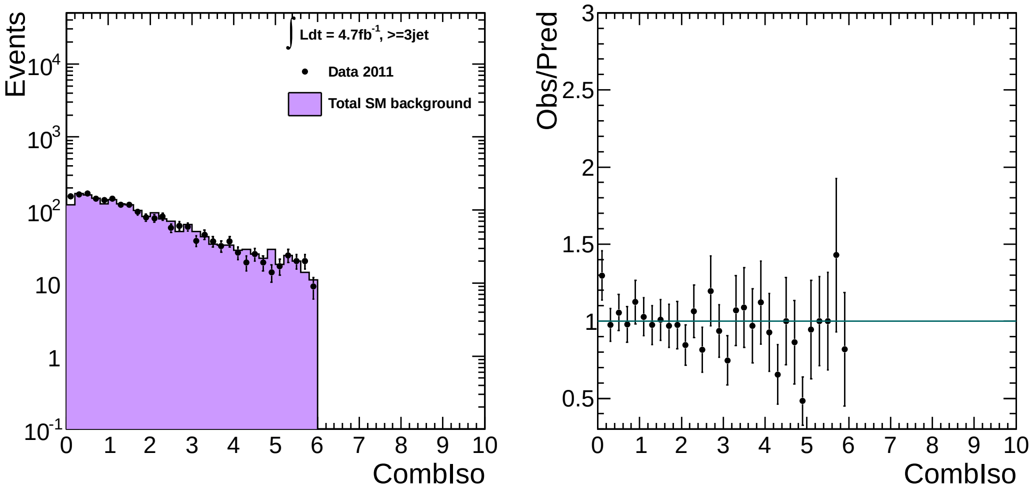

Figure A.25: The combined isolation distribution for the data and the total SM background prediction (left) and the ratio of data vs background (right).

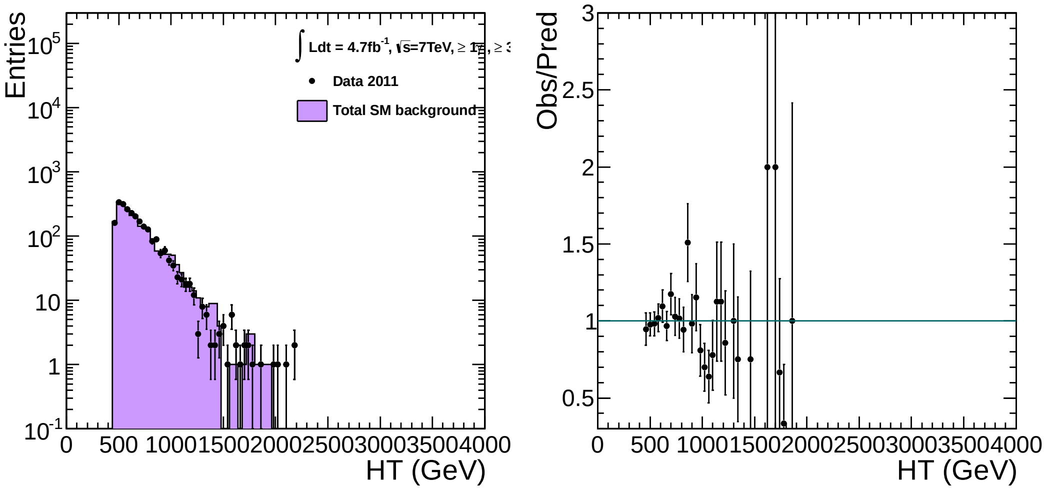

Figure A.26: The HT distribution for the data and the total SM background prediction (left) and the ratio of data vs background (right).

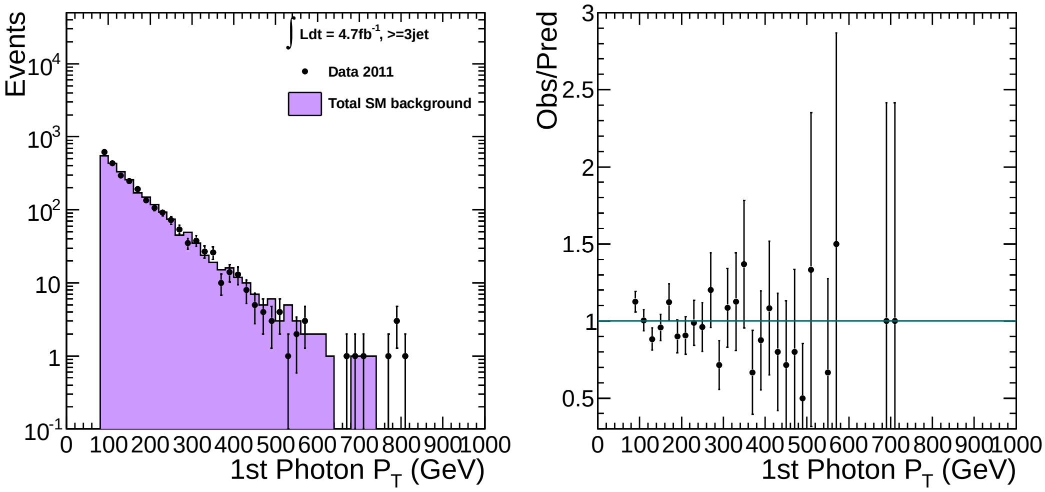

Figure A.27: The leading electron's p_T distribution for data and the most important SM backgrounds (left) and the ratio of data vs simulated events (right).

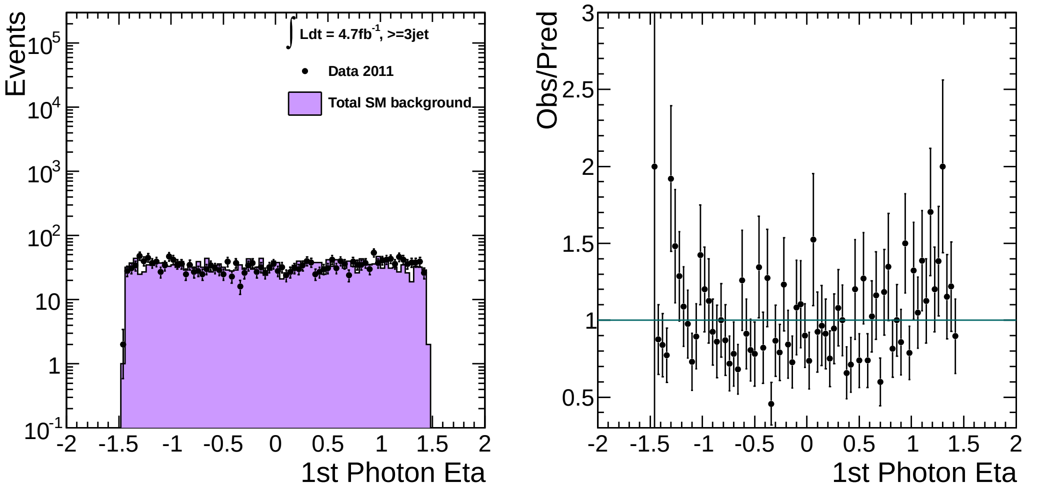

Figure A.28: The leading electron's eta distribution for the data and the total SM background prediction (left) and the ratio of data vs background (right).

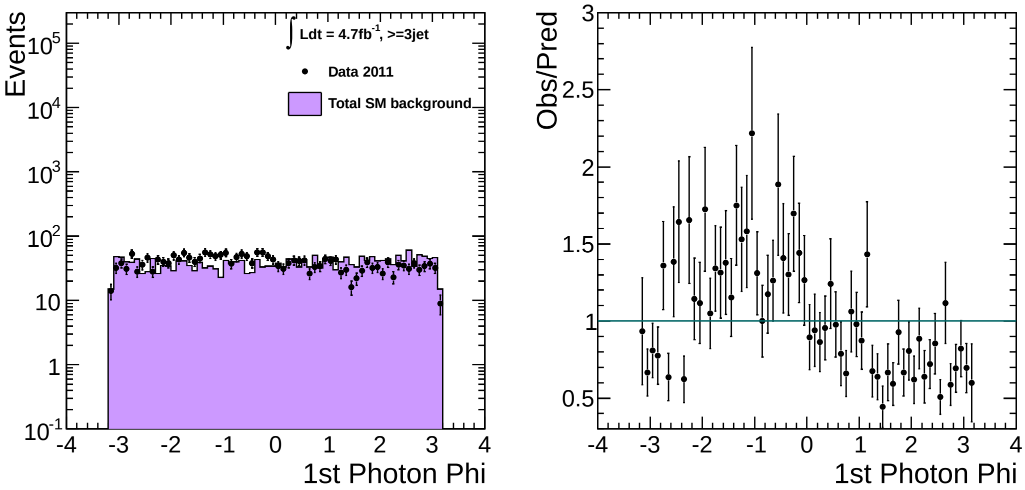

Figure A.29: The leading electron's phi distribution for the data and the total SM background prediction (left) and the ratio of data vs background (right).

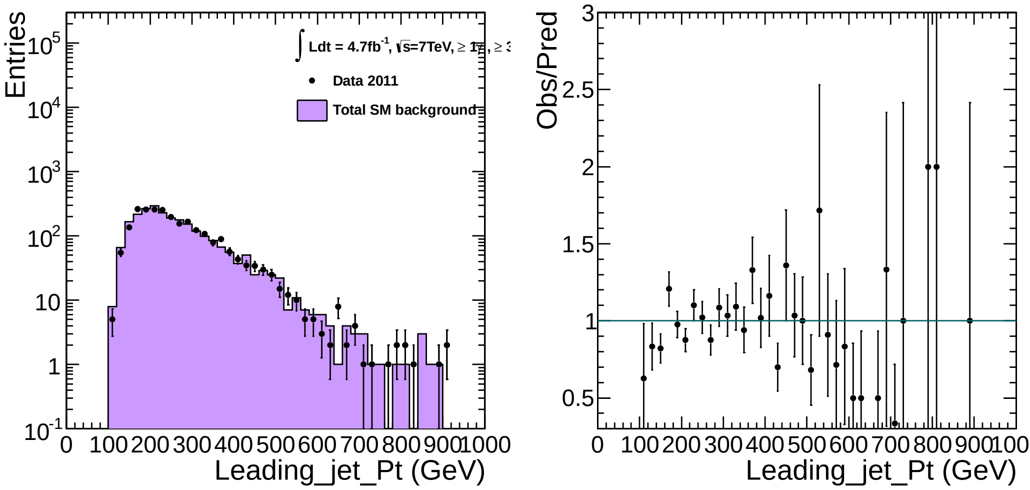

Figure A.30: The leading jet's p_T distribution for the data and the total SM background prediction (left) and the ratio of data vs background (right).

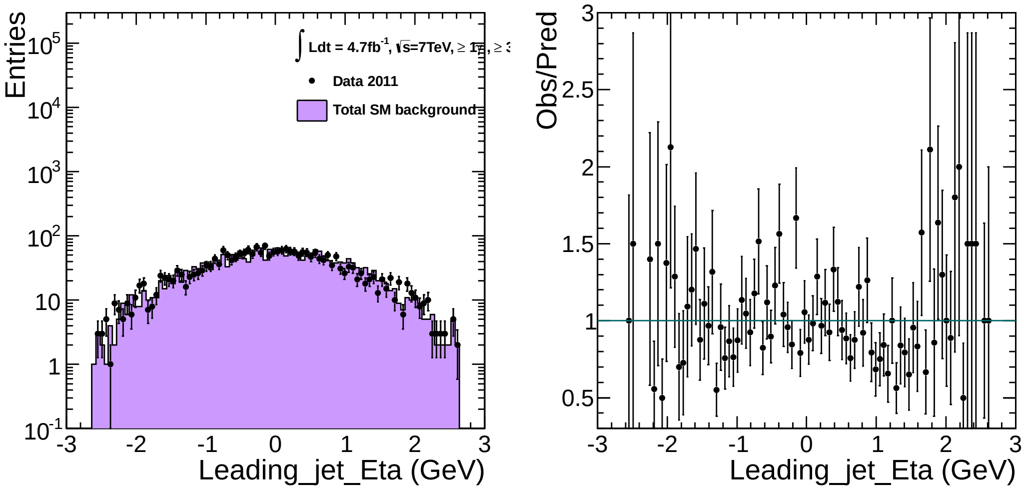

Figure A.31: The leading jet's eta distribution for the data and the total SM background prediction (left) and the ratio of data vs background (right).

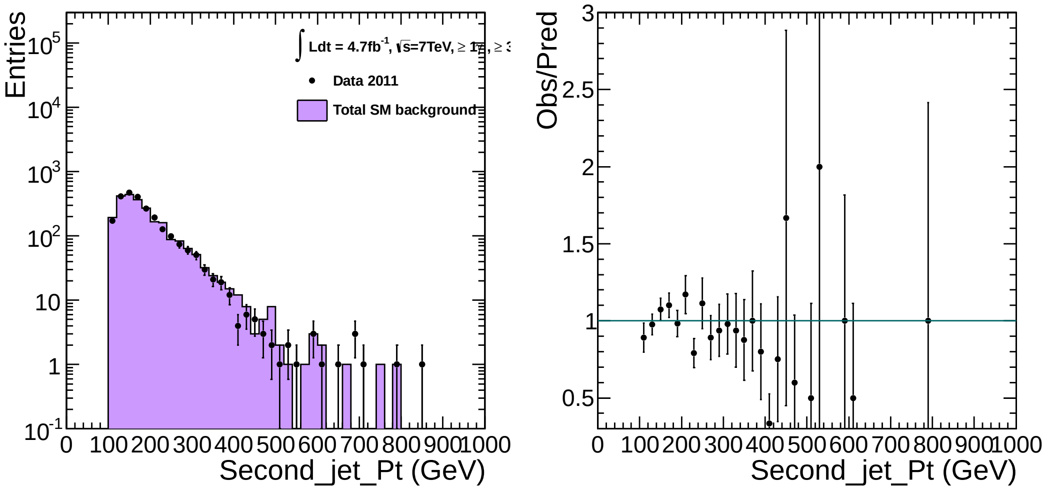

Figure A.32: The sub-leading jet's p_T distribution for the data and the total SM background prediction (left) and the ratio of data vs background (right).

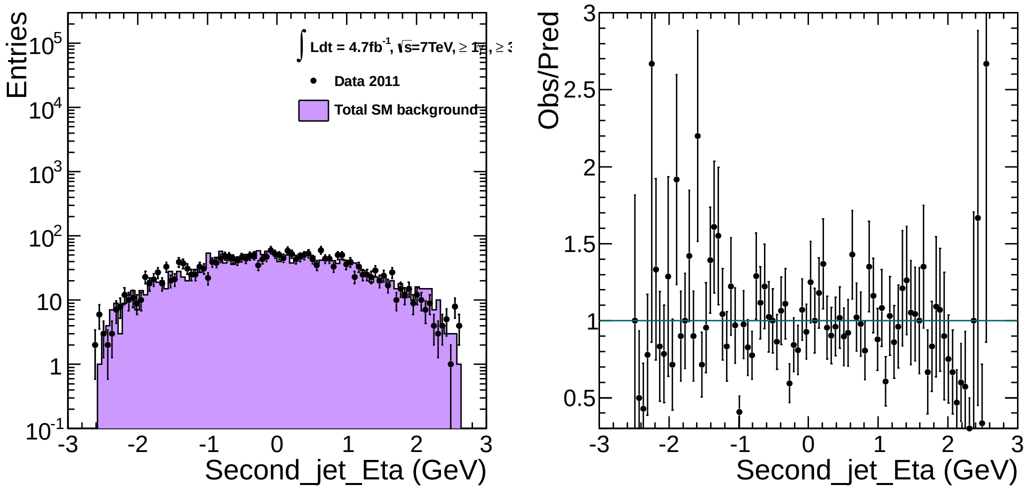

Figure A.33: The sub-leading jet's eta distribution for the data and the most important SM backgrounds (left) and the ratio of Data vs simulated events (right).

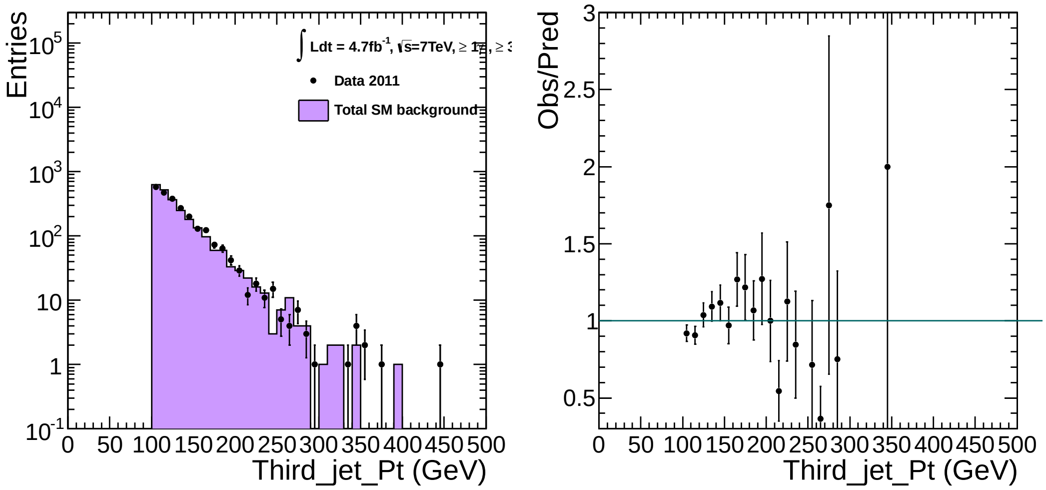

Figure A.34: The third jet's p_T distribution for the data and the total SM background prediction (left) and the ratio of data vs background (right).

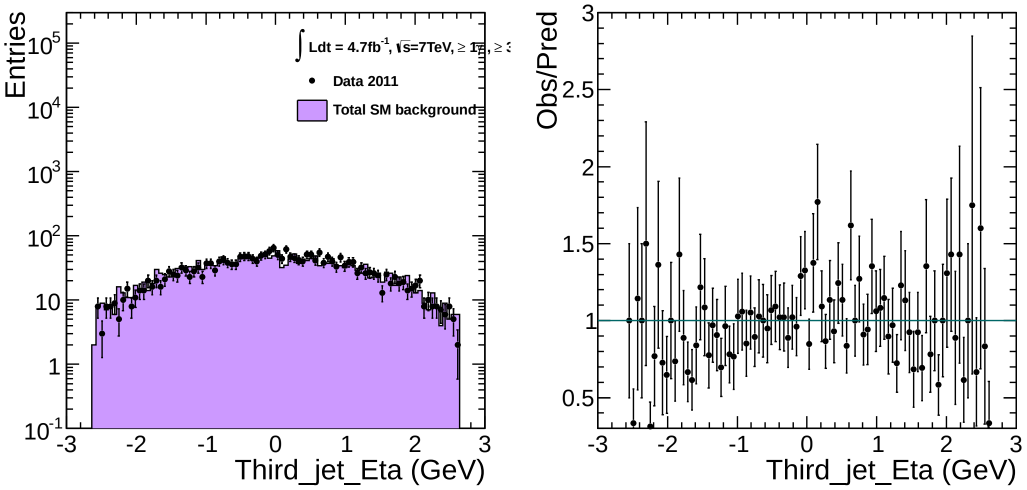

Figure A.35: The third jet's eta distribution for the data and the most important SM backgrounds (left) and the ratio of data vs simulated events (right).

Appendix B

Study of JGB tail events

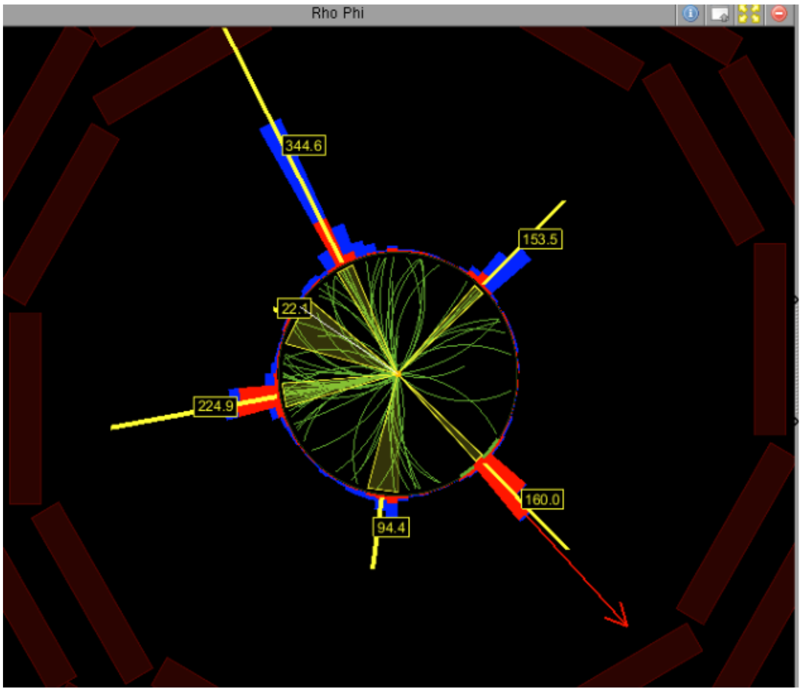

Figure B.1: Event display of the $Run = 172949$, $Lumi = 253$, $Event\_Number = 367225623$.

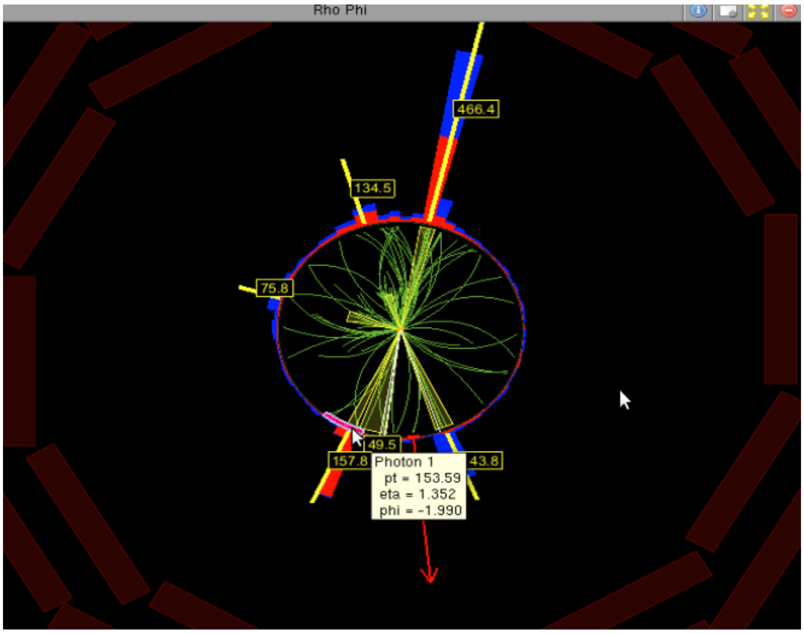

Figure B.2: Event display of the $Run = 176797$, $Lumi = 180$, $Event\_Number = 282232912$, $Bunch = 2053$.

Table B.1: Summary of high JGB events

Run:Lumi:EventNumber	**76797:180:282232912**	**172949:253:367225623**
#pfjets	5	4
#Photons	1	1
Photon p_T	153.6	165.1
Photon Eta	1.35	1.28
Photon Phi	-1.99	-0.79
pfMET	303.9	285.2
JGB	295.7	291.5
HE	0	0
sigmaietaieta	0.008	0.008
R9	0.86	0.83
EcalIso	1.44	0.12
HcalIso	0.37	0
TrkIso	0	0

Appendix C

Filters

We are applying three kind of filters. HcalNoiseFilter (HBHENoiseFilterResultProducer) checks that an event has not been flagged as HCAL noise, while EcalDeadCellFilter (ecalDeadCellTPFilter, Trigger Primitive method) flags an event if the Trigger Primitive Et of a masked ECAL cell (status 13) surpasses 63.75 GeV.

The last filter is based on the following precise map of problematic crystals using geometry and information at single crystal level.

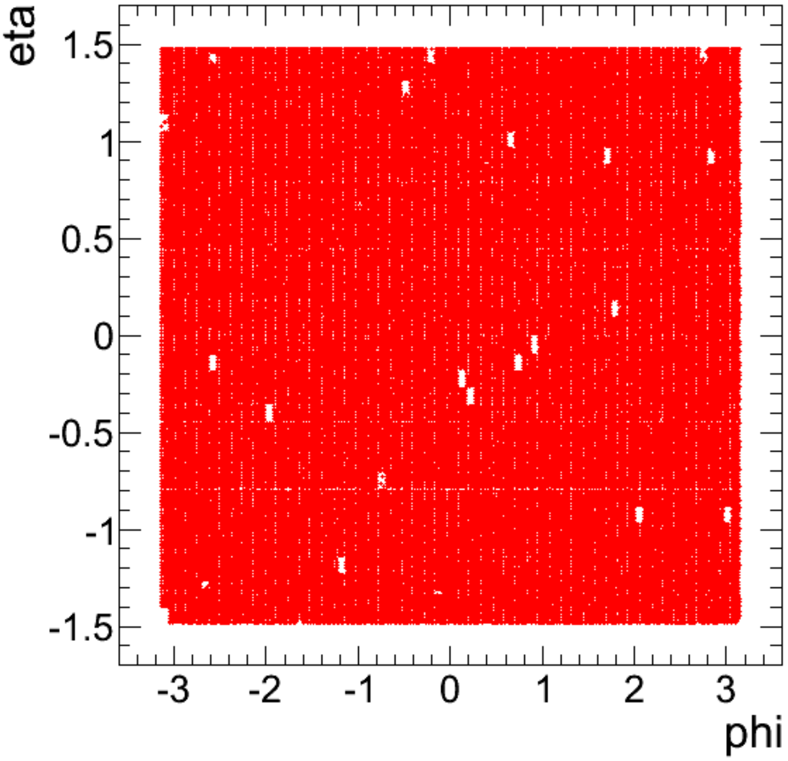

Figure C.1: Precise map of problematic crystals using geometry and information at single crystal level and an example of photon which passes ID and isolation cuts, now removed with a geometry filter.

Appendix D

Development of an algorithm for the energy estimation of problematic ECAL crystalls

As it is already discussed, the electromagnetic calorimeter of CMS is one of the most accurate subdetectors of the Compact Muon Solenoid experiment at CERN. Its characteristics were chosen to be optimized for the detection of the Higgs boson through the decay channel $H \rightarrow \gamma\gamma$. It is also very crusial for our SUSY search in photon(s)+jets+E_T^{miss} final state. It has been observed though that some crystals, that build up the calorimeter, are either noisy or non-responsive at all. These channels sum up to almost 1% of the total channels available. This chapter describes a method that has been developed to estimate the energy of such crystals making use of the remaining available information, namely the energy depositions around such problematic areas. It has been applied to data electrons in the barrel region of the ECAL. The electron samples (data and simulation) were chosen to satisfy the selection made by the Vector Boson Task Force (VBTF) group, meaning electrons originating from $W \rightarrow e\nu$ and $Z \rightarrow e^+ e^-$ decay schemes. Selection includes identification and isolation criteria and a threshold of 25 GeV in transverse energy of the involved electrons. For the purpose of this study no trigger requirements were applied. The simulated samples in use are $Z \rightarrow e^+ e^-$ events produced by PYTHIA generator with a lower cut of 20 GeV on the invariant mass of Z boson. Those simulated samples were used to build the correction functions in the Spline method.

D.1 Description of the Spline Functions Method

The method consists of two discrete steps. The exact position that the particle impinged on the central crystal, is estimated in the first step, using the energy of the remaining functioning crystals. The fraction of the energy that the problematic

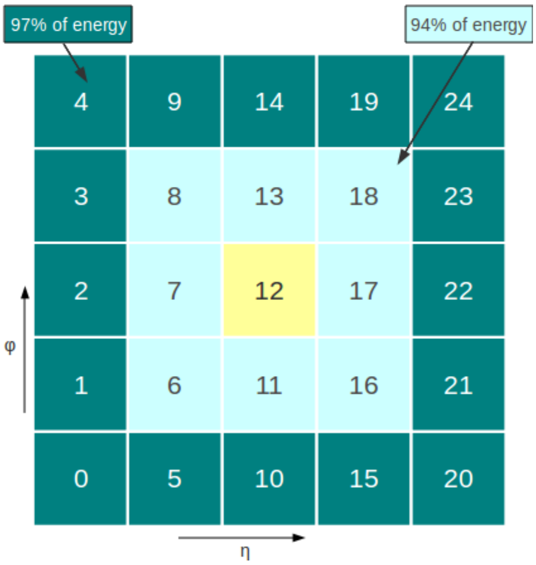

Figure D.1: Schematics of the crystals layout in a 5×5 matrix around the most energetic crystal (#12).

crystal accommodated as a function of the exact position, is estimated in the second step. In the latter step the functions in use are spline functions, hence the name of the method. In order to achieve this, areas where no problematic crystals are present are examined and build our position estimation functions. The method proceeds by building the energy correction functions. Finally those functions are applied to areas where problematic crystals are present.

D.1.1 Position Estimation

Electron and photon showers deposit their energy in several crystals in the ECAL. As already discussed, approximately 94% of the incident energy of a single electron or photon is contained in 3×3 grid of crystals, and 97% in 5×5 grid (Fig. D.1). The presence in CMS of material in front of the calorimeter results in bremsstrahlung and photon conversions. Because of the strong magnetic field the energy reaching the calorimeter is spread in ϕ, depending on the electron/photons transverse momentum. The spread energy is clustered by building a cluster of clusters, i.e. a "supercluster", which is extended in ϕ.

The position estimation of the particle impinged on the central crystal is carried out, using official CMS reconstruction quantities. In order to achieve this many quantities were studied, including the position of the supercluster and tracker information propagated to ECAL through "TransientTracks"[1]. The research concluded to use the position of the BasicSeedCluster, as it gave the

---

[1] TransientTracks are the tracks (pairs or triplets of hits) which are used for vertex reconstruction and for b/tau tagging

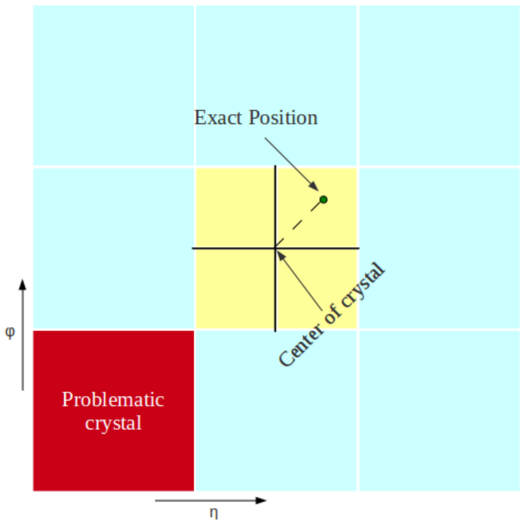

Figure D.2: Schematic diagram of a 3×3 matrix around the most energetic crystal (central).

best results and logically is the most suitable to use in this case. These positions will be called from now on true positions. Then emerges the need to construct a variable that can be estimated in cases where a problematic crystal is present. An important remark here is, that the position estimation method is needed only when dealing with photons, where information from the tracking system is not available, or when someone does not want to use the information from the Tracker in the case of electrons.

In order to estimate the electron's or photon's exact position, the central crystal is divided in 25 equally sized orthogonal boxes constructing a 5 × 5 grid inside the central crystal. Each box is associated with a pair of indexes in the range [–2, 2] in each direction. Figure D.2 explains this procedure. The following variables are constructed. X resembles η and Y resembles ϕ direction respectively.

$$estimX = \sum_{i}^{24} w_i * x_i \tag{D.1}$$

$$estimY = \sum_{i}^{24} w_i * y_i \tag{D.2}$$

where $w_i = \frac{E_i}{\sum_i^{24} E_i}$. Continuing, 2-D histograms of true-estimated vs estimated position are produced in each direction (η, ϕ). This way the S-curves that are shown in the following figure (Fig. D.3) are produced.

The goal here is to model the behavior of these S-curves in cases where problematic crystals are present. It is obvious how the shape gets distorted when some crystal is left out of the estimation. So what follows is a fit in slices in each × bin and a mapping of the undistorted shape to the distorted one. This procedure gets carried out for all possible problematic crystal positions in a 3 × 3 matrix and both directions $(\eta, -\phi)$. This way it is assured, there is always an estimation of the exact position in cases where a problematic crystal is present. These positions will be introduced later to the spline functions which estimate the fraction of the energy of the problematic crystal.

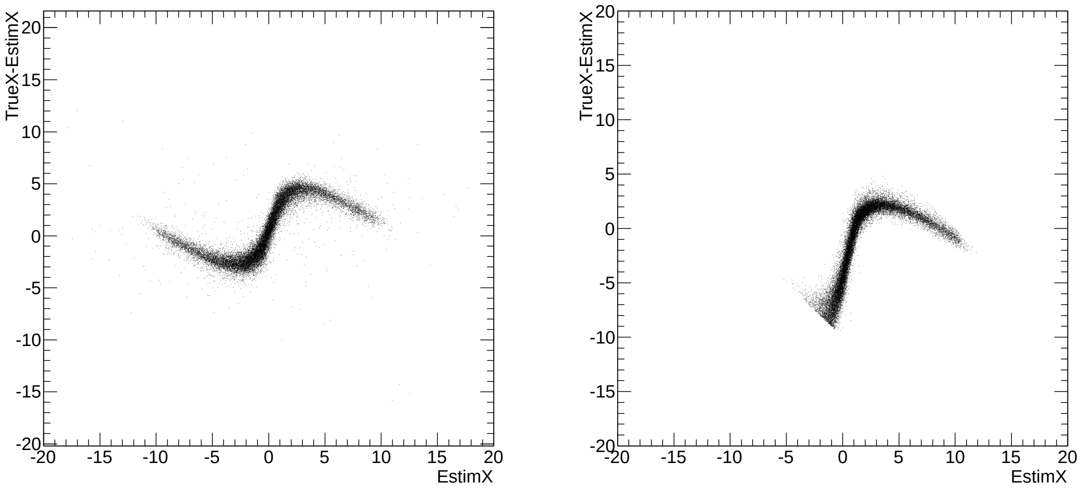

Figure D.3: Plots of S-curves in case no problematic crystal is present (left) and in case of a problematic crystal's presence (right).

The method proceeds by calculating the fraction (F) of the energy that the problematic crystal accommodated, with respect to the exact estimated position. Achieving this and making use of the following equation, the estimation of the energy of the problematic crystal (E_{pc}) can be carried out.

$$F = \frac{E_{pc}}{Sum_8 + E_{pc}} \Leftrightarrow E_{pc} = Sum_8 \times \frac{F}{1 - F} \tag{D.3}$$

where E_{pc} is the estimated energy of the problematic crystal, Sum_8 is the sum of the energies of all the crystals in the 3×3 matrix around the most energetic crystal apart from the problematic one. In order to calculate the aforementioned fraction the decision was made, to split the central crystal in 25 equally sized divisions. An assignment of a pair of indexes is made, on each division in the range [-2,2]. Plots are made of the fraction of the energy that the problematic crystal accommodated for each such division. Those plots are fitted using Gauss function. This way a mean fraction value is calculated for each division. A remark here is that the Gauss hypothesis for the fraction of each division is strong for the inner regions of the central crystal, but while moving to the border sides of the crystal, shapes involved in the plots become more complex. These values will be used later to construct the spline functions. The spline function form in use is shown in following equation.

$$f(\eta,\phi) = \sum_j \sum_i a_{ij}\eta^i\phi^j \tag{D.4}$$

where (i,j) ∈ [0,7] and (η,ϕ) ∈ [-2,2], f (η, ϕ) is the fraction of the energy, η - ϕ correspond to the internally assigned indexes and a$_{ij}$ are constants to be calculated. Using linear algebra methods those constants can be obtained by solving a set of 25 equations, each for one division. More accuratelly the following equation lies in the heart of the calculation. Brackets denote matrix formalism.

$$[F] = [\eta,\phi] \times [C] \Rightarrow [C] = [\eta,\phi]^{-1} \times [F]$$

With $[F]$ is denoted a 25×1 matrix containing the mean fraction values obtained by fitting with gauss function for each division. $[C]$ is a 25×1 matrix that denotes the constants to be calculated, while $[\eta,\phi]$ is a 25×25 matrix and denotes terms containing powers of η and ϕ from unfolding the sums involved in the spline function. What we need to do is calculate the inverse of this matrix. This is achieved by using ROOT algorithms and its linear algebra capabilities. After calculating the inverse and multiplying equation from the left side, the values of these constants are obtained, that build up energy correction functions.

After calculating the constants, the spline functions are finally constructed and can reproduce the accommodated fraction of energy with respect to the estimated position.

D.2 Results

Results of the method will be presented in tables.The corresponding plots lie in the Appendix D.3. Each cell in the table represents a possible position of a problematic crystal in a 3×3 grid around the central crystal.

D.2.1 Spline Function Results

D.2.1.1 Electrons

Table D.1: Electrons in positive η

(a) Estimated/True Energy Mean Values

1.00	0.97	0.98
1.01	N.A	0.86
0.96	0.87	0.90

(b) Estimated/True Energy RMS Values

0.26	0.41	0.30
0.24	N.A	0.29
0.21	0.49	0.25

(c) Estimated/True Cluster Raw Energy Mean Values

1.00	0.99	1.00
0.99	N.A	0.97
1.00	0.96	0.99

(d) Estimated/True Cluster Raw Energy RMS Values

0.01	0.06	0.01
0.05	N.A	0.06
0.01	0.11	0.02

Table D.2: Electrons in negative η

(a) Estimated/True Energy Mean Values

0.87	0.99	1.22
0.73	N.A	1.06
0.90	0.76	1.10

(b) Estimated/True Energy RMS Values

0.29	0.44	0.33
0.53	N.A	0.25
0.24	0.59	0.30

(c) Estimated/True Cluster Raw Energy Mean Values

0.99	0.99	1.00
0.96	N.A	0.99
1.00	0.96	1.00

(d) Estimated/True Cluster Raw Energy RMS Values

0.03	0.08	0.01
0.10	N.A	0.06
0.01	0.10	0.02

D.2.1.2 Positrons

Table D.3: Positrons in negative η

(a) Estimated/True Energy Mean Values

0.93	0.85	1.24
0.87	N.A	1.03
0.95	1.00	0.99

(b) Estimated/True Energy RMS Values

0.26	0.41	0.34
0.31	N.A	0.27
0.30	0.49	0.29

(c) Estimated/True Cluster Raw Energy Mean Values

0.99	0.97	1.00
0.97	N.A	0.99
1.00	0.99	1.00

(d) Estimated/True Cluster Raw Energy RMS Values

0.02	0.07	0.01
0.06	N.A	0.05
0.02	0.06	0.01

Table D.4: Positrons in positive η

(a) Estimated/True Energy Mean Values

0.95	0.72	0.94
0.95	N.A	0.91
0.99	1.08	0.98

(b) Estimated/True Energy RMS Values

0.26	0.46	0.25
0.25	N.A	0.29
0.27	0.46	0.29

(c) Estimated/True Cluster Raw Energy Mean Values

1.00	0.97	1.00
0.98	N.A	0.98
1.00	0.99	1.00

(d) Estimated/True Cluster Raw Energy RMS Values

0.01	0.07	0.01
0.05	N.A	0.05
0.01	0.08	0.02

D.3 Resolution plots

D.3.1 Position resolution plots for Spline method.

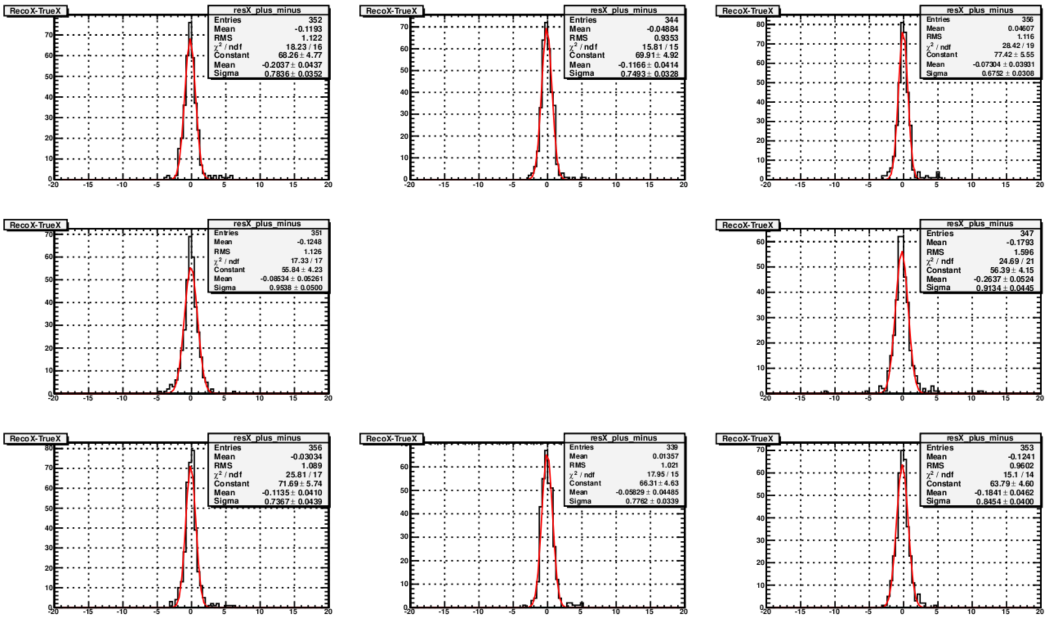

Figure D.4: Position resolution of Electrons in the positive η direction

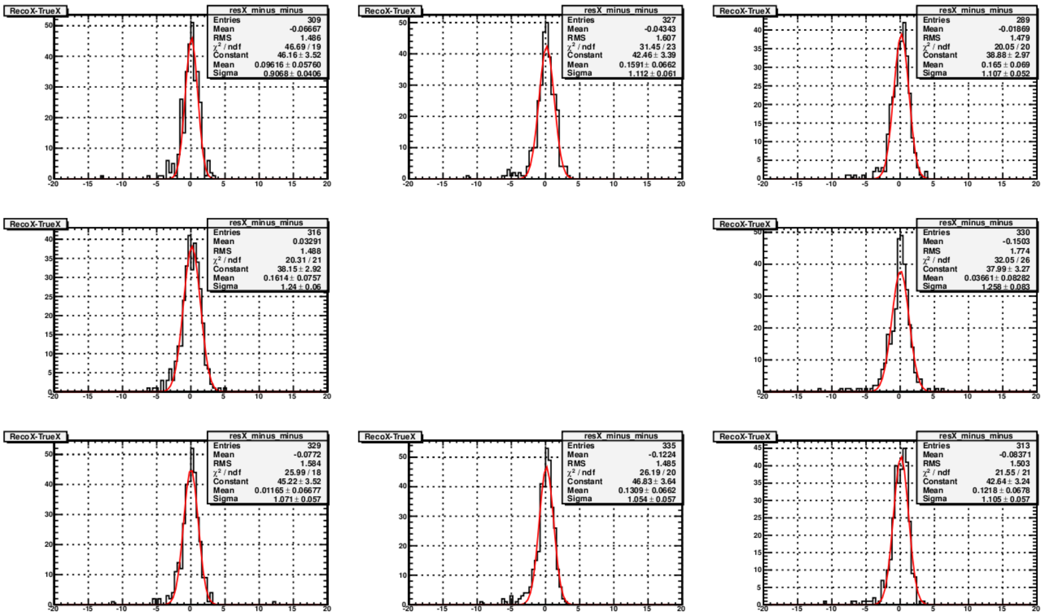

Figure D.5: Position resolution of Electrons in the negative η direction

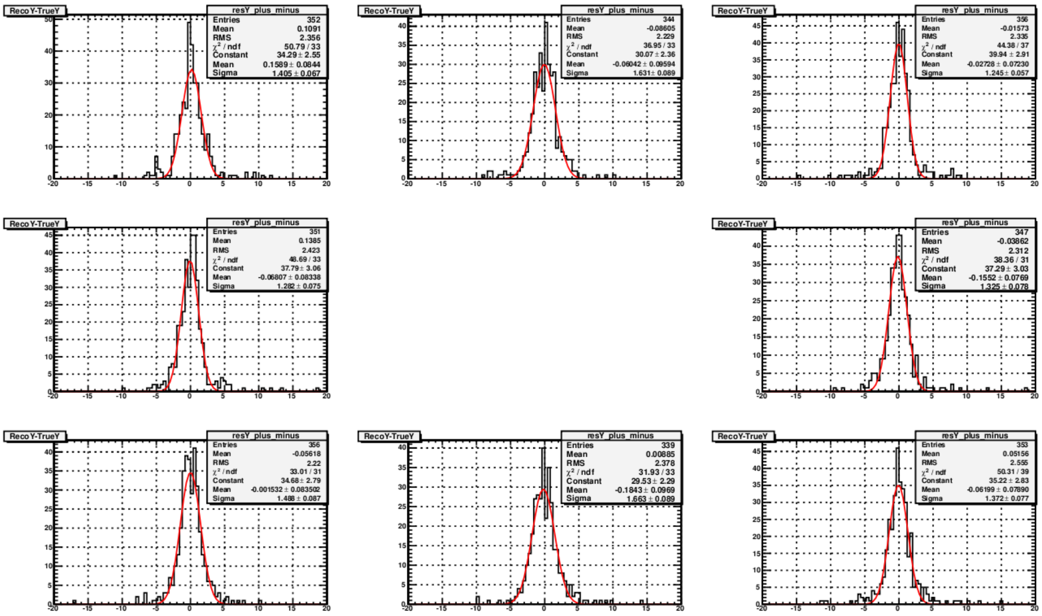

Figure D.6: Position resolution of Electrons in the positive ϕ direction

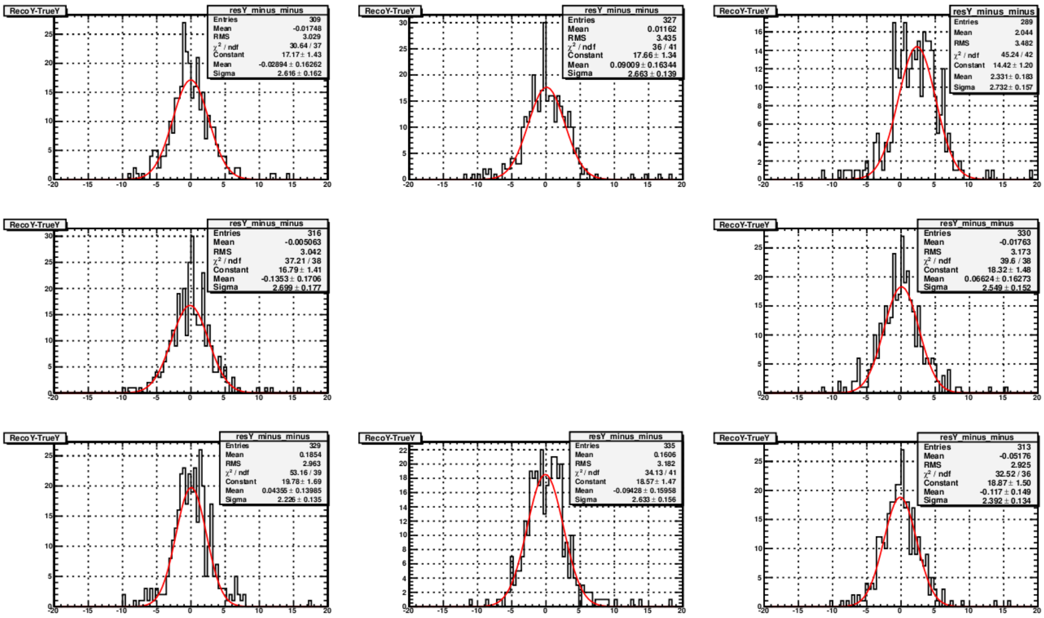

Figure D.7: Position resolution of Electrons in the negative ϕ direction

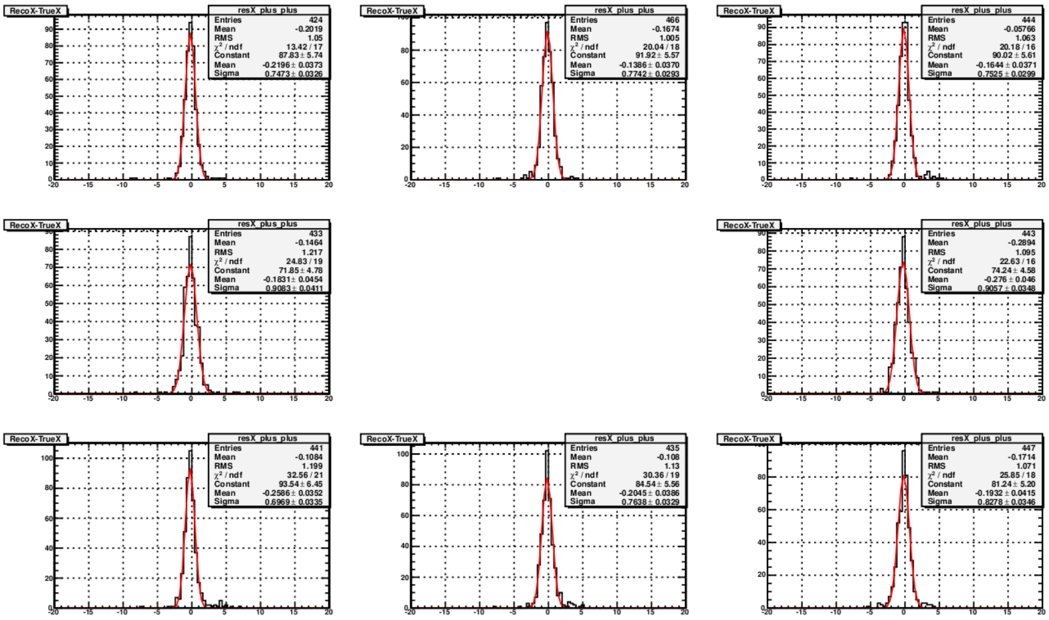

Figure D.8: Position resolution of Positrons in the positive η direction

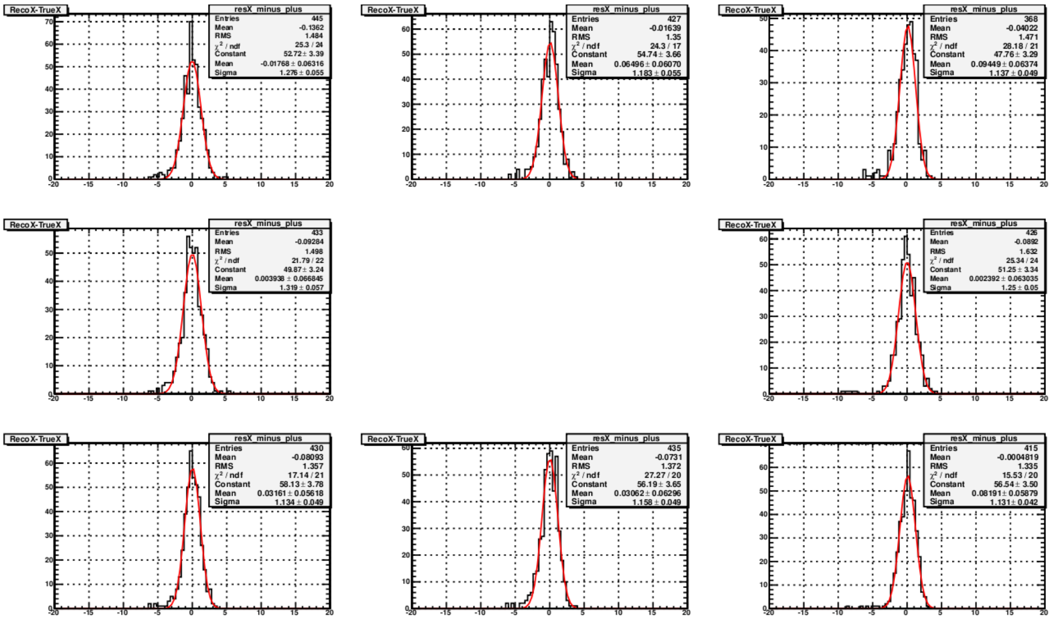

Figure D.9: Position resolution of Positrons in the negative η direction

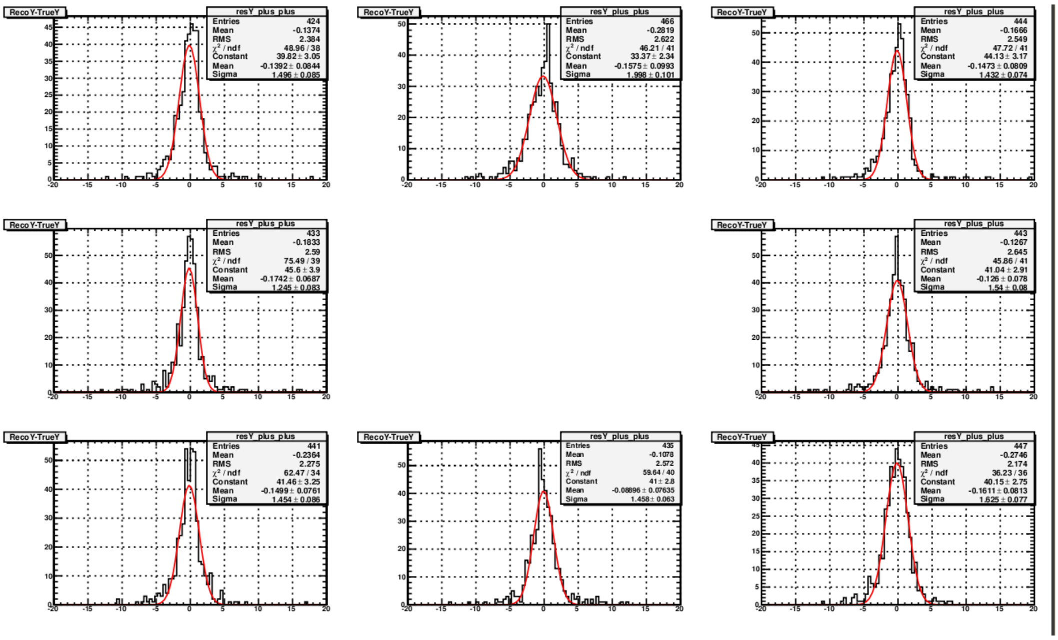

Figure D.10: Position resolution of Positrons in the positive ϕ direction

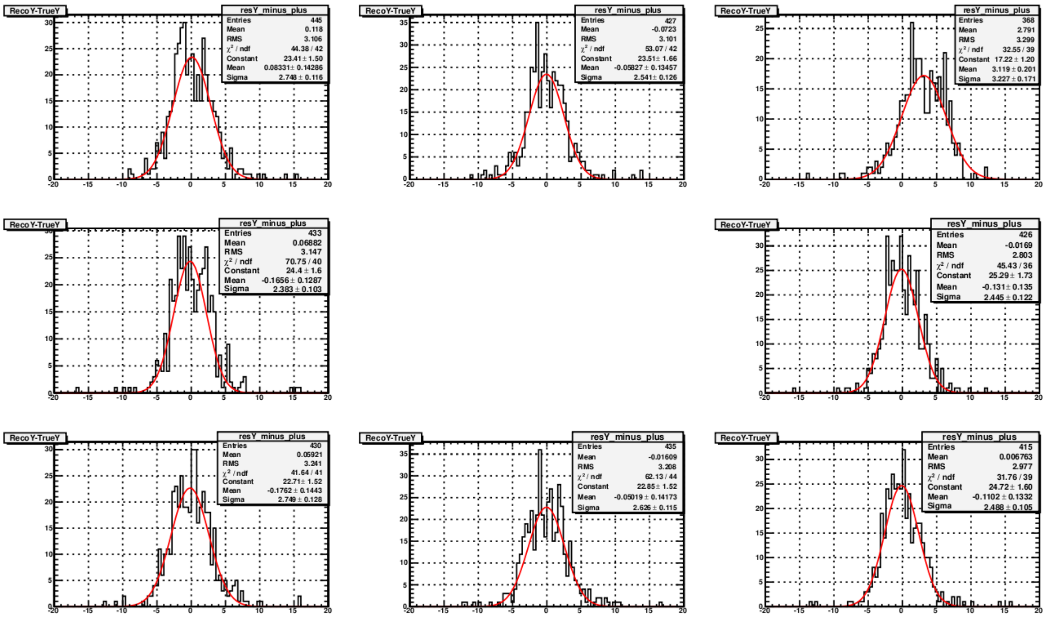

Figure D.11: Position resolution of Positrons in the negative ϕ direction

D.3.2 Crystal and Cluster Energy Resolution Plots for Spline Method.

D.3.2.1 Crystal Energy Resolution Plots

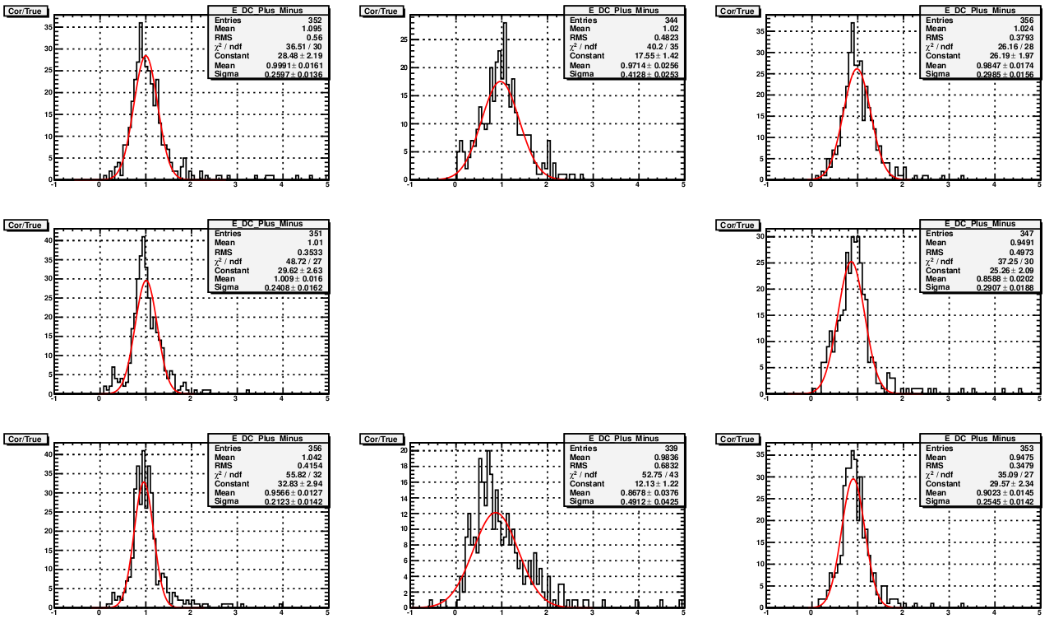

Figure D.12: Energy Resolution for Electrons in positive η

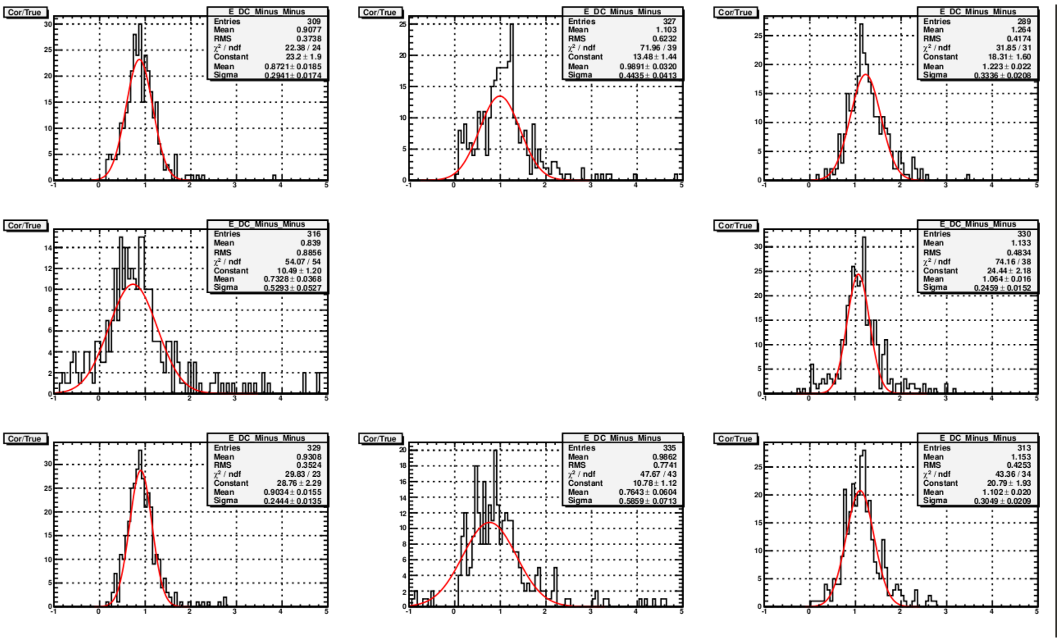

Figure D.13: Energy Resolution for Electrons in negative η

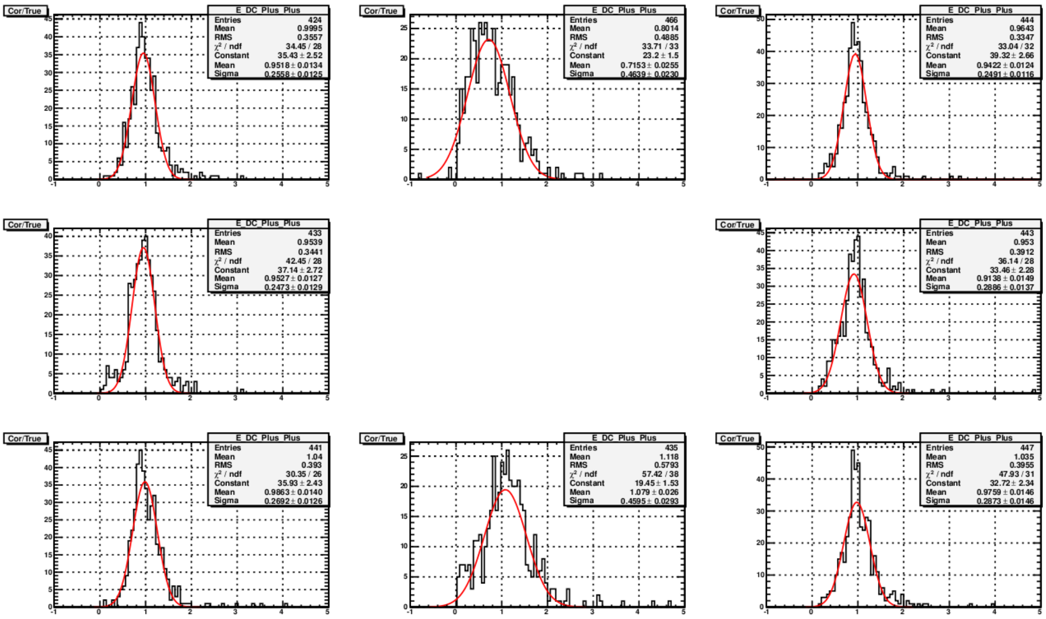

Figure D.14: Energy Resolution for Positrons in positive η

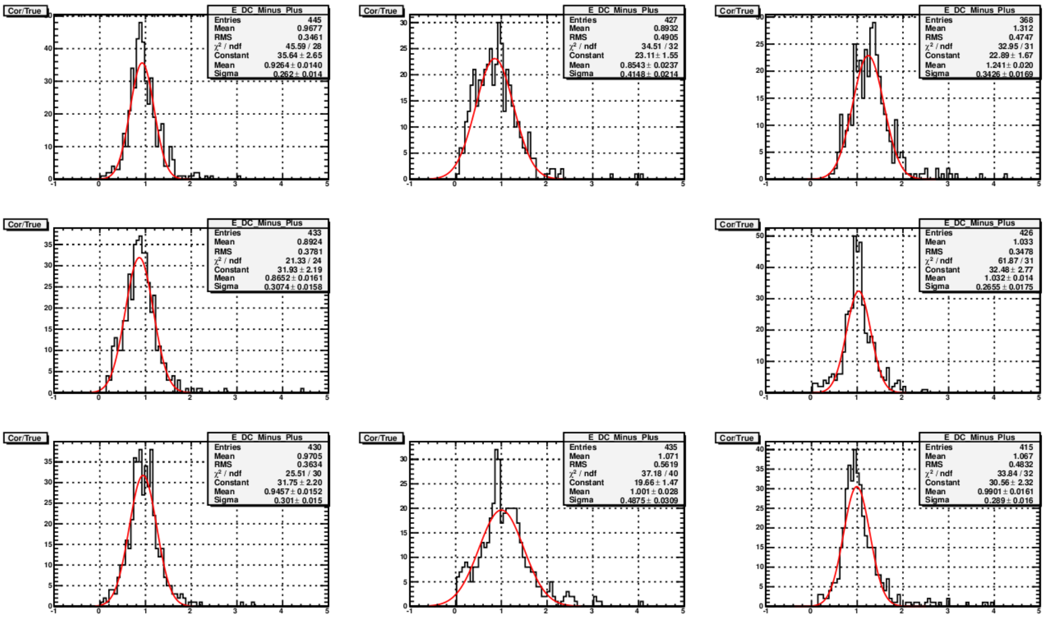

Figure D.15: Energy Resolution for Positrons in negative η

D.3.2.2 Cluster Energy Resolution Plots

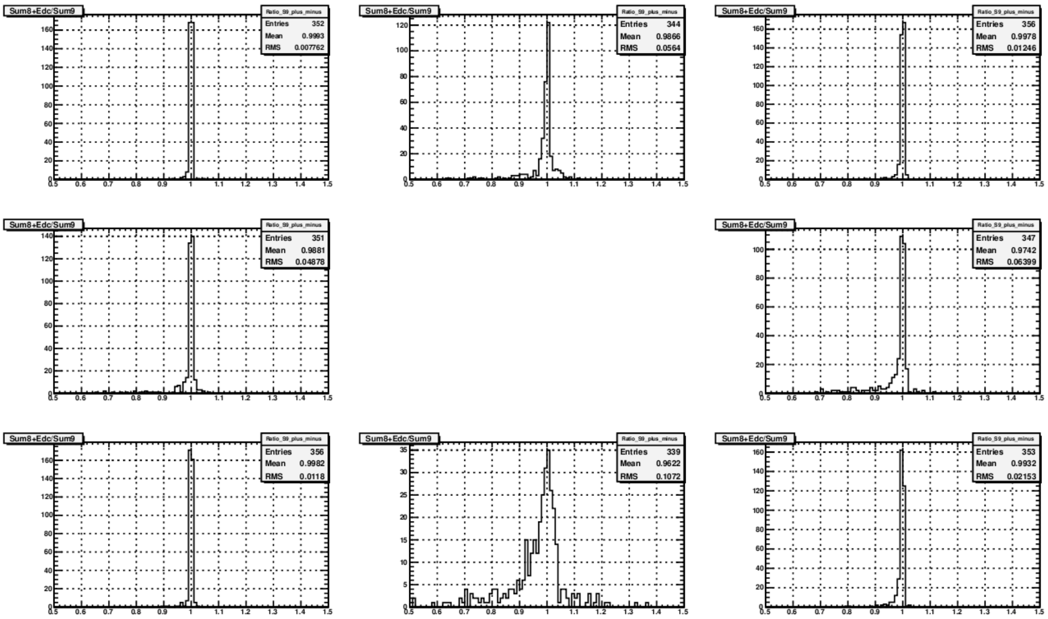

Figure D.16: Cluster Resolution for Electrons in positive η

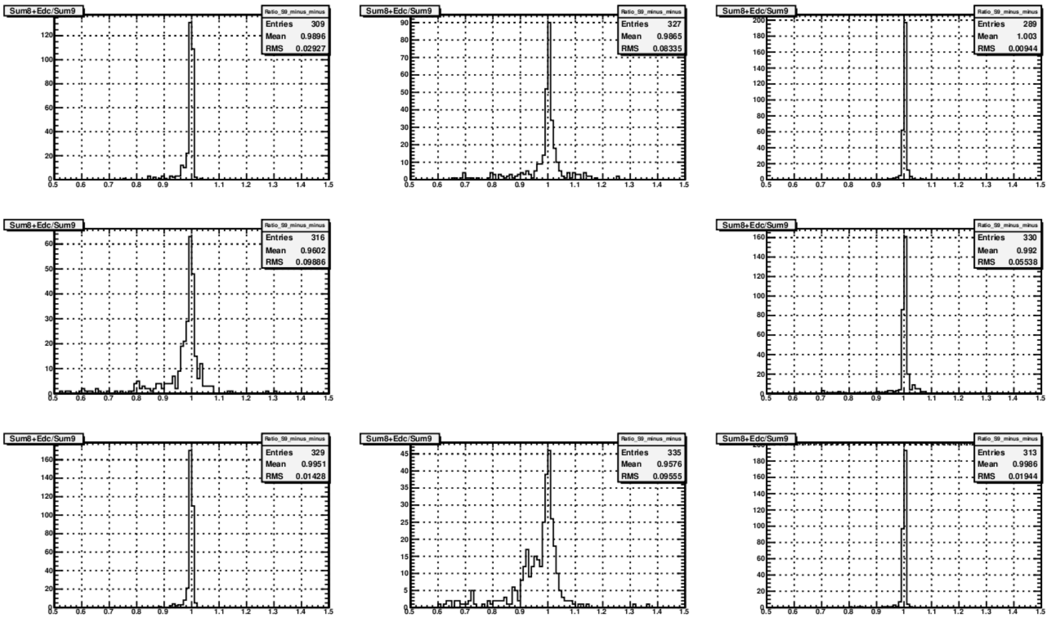

Figure D.17: Cluster Resolution for Electrons in negative η

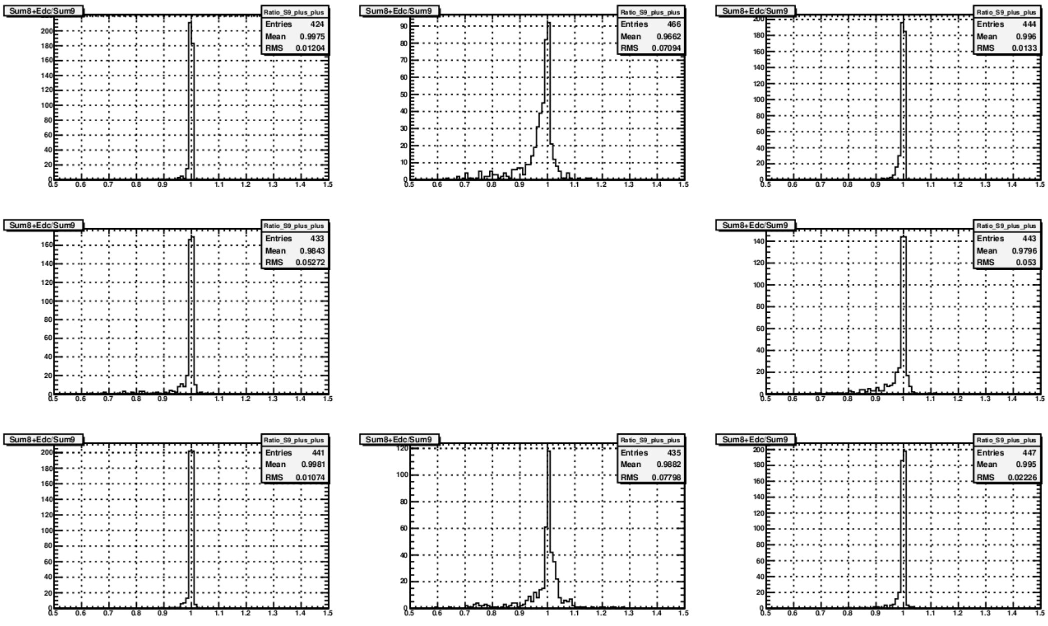

Figure D.18: Cluster Resolution for Positrons in positive η

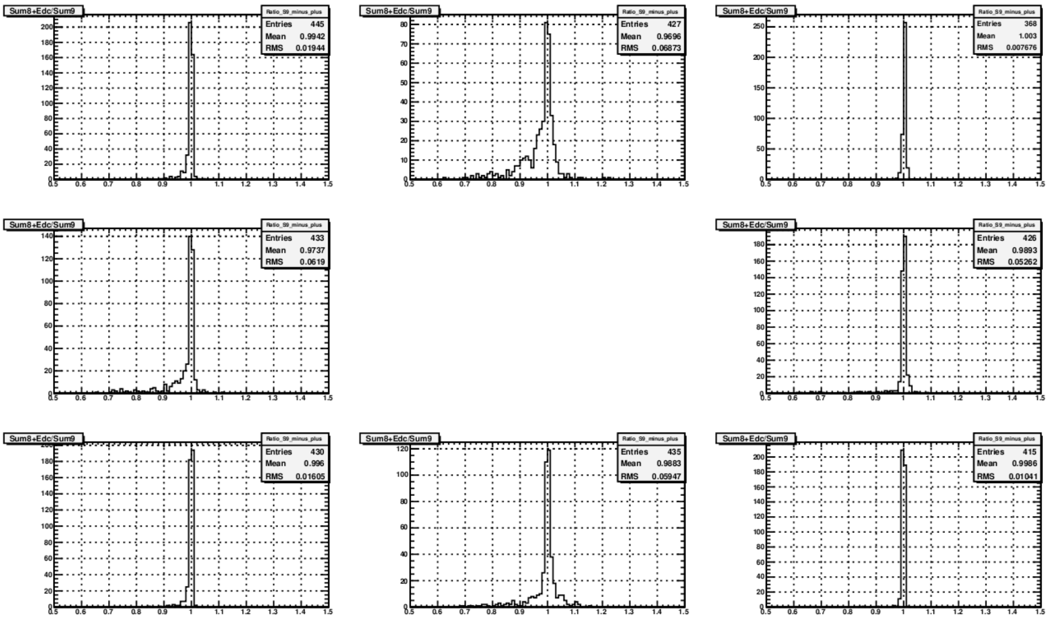

Figure D.19: Cluster Resolution for Positrons in negative η

D.3.2.3 Conclusions

To conclude, this method provides encouraging results in most of the cases, but it fails to give a correction for the case the problematic crystal is the most energetic. Moreover, if the problematic crystal is above or below the most energetic one, the energy resolution is not satisfactory either. Thus, more studies are necessary. Therefore, two other approaches were tested in our group at Demokritos, by Victoria Giakoumopoulou and Stilianos Kesisoglou. The first one is based on Pattern matching (try to match the observed energies of the good working crystals in the 3×3 grid, with a list of 3×3 grids for the cases of “healthy“ crystals and thus derive the energy corresponding to the problematic crystal), and the second one is based on neural networks. The results of these tests are very encouraging, have been already presented at CMS and soon will be implemented in the CMS framework and will be made public.